CHARACTERIZATION OF THE CYCLIC BEHAVIOR OF CORRODED STEEL BRIDGE BEARINGS AND THEIR INFLUENCE ON SEISMIC BRIDGE PERFORMANCE

by

Xiaohu Fan

A dissertation submitted in partial fulfillment
of the requirements for the degree of
Doctor of Philosophy
(Civil Engineering)
in the University of Michigan
2014

Doctoral Committee:

Assistant Professor Jason P. McCormick, Chair
Professor Carlos Cesnik
Professor Sherif El-Tawil
Professor Gustavo Parra-Montesinos, University of Wisconsin

DEDICATION

To my parents, Jingui and Xiuli, and fiancée, Qianru, for their love and support.

ACKNOWLEDGEMENT

I would like to first acknowledge the Illinois Department of Transportation for donating the bearing specimens and documentation used in the experimental and numerical studies of this dissertation.

Throughout my career in graduate school, I have been fortunate to glean mentorship, friendship, and love in addition to a doctoral degree. There have been many people who have had an influence in my five years of living in Ann Arbor, Michigan. Good times of being together always come to an end, but those dear memories will never fade and only grow stronger.

I am grateful that I get to become friends with a great advisor and person, Dr. Jason McCormick, who has offered me continuous mentorship, guidance, and friendship. His encouragement and support helped me fight through the many times when I doubted myself and even the career choice in this profession. His technical competency and scope of knowledge, exceptional work ethics, and high moral standards have all had a deep imprint in shaping the scholar that I am today. I would also like to acknowledge Dr. Cesnik, Dr. El-Tawil, and Dr. Parra-Montesinos for their commitment to my academic success. Their advice and inspiration have contributed greatly to making my doctoral dissertation stronger. I look up to them and view them as my role models based on their success in both life and career.

Without the help and expertise of the structural engineering laboratory technicians, Bob Spence, Bob Fisher, and Jan Pantolin, the experimental work in this dissertation would never be finished so smoothly and on time. I sincerely appreciate their assistance and all the interesting conversations that made the experimental work less strenuous and more fun.

I have been looked after by many great friends every time I needed help or support. Because of them, life in a different country far from home becomes lively and promising,

and that intense homesickness gradually dissolves into a fond and excitement for exploring what this great nation has to offer. Yao Zhang, Matt Fadden, Jieshi Fang, Honghao Li, Qian Zhang, Zhichao Liu, Remy Lequesne, Mike Stults, Lin Liu, Monthian Setkit, and many other have all shared with me their joy and friendship.

Even though they were not able to make it to the U.S. to share this special moment of my life, I know my parents are proud of me as they have always been. Their selfless love, support, and sacrifices are the reason that I can come this far and the motivation that I want to accomplish more.

I will always have a special sentiment for Ann Arbor because this is where I found my beloved fiancée, Qianru Guo. She has made my life so much more promising and colorful. I feel fortunate and grateful that I get to hold her hands to enjoy the beauty of life and love.

TABLE OF CONTENTS

LIST OF TABLES

LIST OF FIGURES

ABSTRACT

Steel bridge bearings are widely used in existing highway bridges in the United States to provide a load transfer mechanism and accommodate movements between the superstructure and substructure. These bearings include steel rocker (expansion) bearings and steel bolster (fixed) bearings. Steel rocker bearings accommodate both translation and rotation of the superstructure, while steel bolster bearings only permit rotation of the superstructure under vehicle braking and thermal actions. Due to a lack of regular maintenance, the in-situ condition of these steel bearings, which have typically been in service for several decades, is often severely corroded. Moreover, these steel bearings are not designed for seismic loads due to a lack of understanding of the seismic hazard posed to bridges in the Central and Eastern United States (CEUS) at the time that many of these bridges were built. As awareness of their susceptibility to corrosion and vulnerability to seismic loads increases among bridge owners and engineers, the seismic performance of steel bridge bearings and their influence on the overall bridge system performance is of major concern, particularly given the importance the highway network plays in providing safe transportation and sustaining economic prosperity. For this reason, the goal of this study is to correlate corrosion level with the performance of steel bearings under seismic loads, thereby providing a means of more accurately assessing the vulnerability of in-situ bridges.

An analytical and finite element study is first undertaken to gain a preliminary understanding of the deformation modes, stiffness, and strength of the considered steel bearings. Corrosion loss quantification and large-scale experimental testing are then conducted on 25 salvaged steel bridge bearings aiming to provide an in-depth understanding of corrosion loss distribution and its influence on the cyclic behavior of steel bearings. Cyclic behavior of steel bearings is experimentally derived for two orthogonal (longitudinal and transverse) loading directions. Further, a portfolio of constitutive models that incorporate corrosion effects is created for the steel bridge

bearings based on the experimental findings. The seismic performance of the steel bearings and the bridge systems is then numerically evaluated considering two suites of bi-directional ground motions, a design basis earthquake suite and a maximum credible earthquake suite. The bearing models and simulation results provide a quantitative understanding of how an existing continuous steel girder highway bridges using steel bearings perform under seismic loads.

Overall, the findings of this study show that significant corrosion can develop on steel bearings over their service life, which can result in major changes to the cyclic behavior of steel bearings with respect to deformation mode and failure pattern. The numerical simulations suggest that steel rocker bearings, when used in a continuous steel girder bridge, have the potential to topple in the longitudinal direction regardless of corrosion level. The bolster bearings also can lead to large forces transferred to the bridge wall piers.

CHAPTER 1 INTRODUCTION

1.1 Motivation

Data from the United States National Bridge Inventory shows that there are over 600,000 bridges that make up the United States' roadway network (FHWA 2010). Age-related deterioration of these bridges is becoming a significant concern as over half of the bridge inventory is approaching the end of its design life (AASHTO 2008). The recently released American Society of Civil Engineers (ASCE) report card gives the bridge inventory a Grade of C+ indicating a major area of need over the coming years as reflected by the fact that nearly a quarter of the bridge inventory is either structurally deficient or functionally obsolete (ASCE 2013). These findings clearly show the effect that deterioration has had on U.S. bridges, but a systematic means of addressing this problem is still lacking (AASHTO 2005, NSTPRSC 2008, and ASCE 2011). Among various phenomena associated with deterioration, corrosion of steel components of highway bridges is of particular concern due to the influence corrosion can have on component behavior and the potential large losses associated with bridge failures. For example, the 2007 collapse of the I35W bridge in Minnesota claimed 13 lives and injured 145 people (NTSB 2008). The accompanying economic and financial impact was in the millions of dollars (Xie and Levinson 2009).

Steel bearings, including rocker (expansion) and bolster (fixed) bearings (Figure 1.1), have been commonly used in highway bridges (Figure 1.2) throughout the Central and Eastern United States (Choi 2002). The main reason for their use is the relatively low cost of fabricating steel bearings and ease of installation. Deterioration in the form of corrosion of the bearing surfaces and debris buildup at the contact interfaces of steel bearings can have a significant influence on their mechanical behavior. Traffic disruption and financial losses due to past failures of ill conditioned steel bearings have emphasized

the importance of these linkages to the proper functioning of the bridge. In 2008, two spans of the Birmingham Bridge in Pittsburgh dropped up to 8 in. (200 mm) overnight and damaged the pier supporting the two spans (Splitstone et al. 2010). Forensic investigations (Modjeski and Masters Inc. 2008) found that the Birmingham Bridge failure was triggered by excessive movement in one direction of the rocker bearing system as a result of accelerated corrosion and debris buildup around the rocker bearings due to leaking expansion joints (Figure 1.3(a)). Another example of rocker bearing failure was the Dunn Memorial Bridge in Albany, New York. Two spans of the bridge dropped off the supporting rocker bearings (Figure 1.3(b)) partially due to excessive rotation caused by decades-long accumulation of debris and corrosion at the bottom contact interface of the rocker bearing, which restrained the mobility of the rocker and attracted undesired horizontal forces (NYSDOT 2005).

In addition to corrosion, the seismic hazard associated with the Central and Eastern United States (CEUS) creates another potential threat to the deteriorated bridge inventory in this region (Nielson and DesRoches 2006). The CEUS features a moderate seismicity with a long return period. Under a seismic event, the response of the older and deteriorated bridge inventory in the region is largely unknown. This lack of knowledge needs to be addressed to minimize potential loss of life and limit far reaching economic consequences of a seismic event on the transportation system. Many of these bridges depend on steel bearings to transfer loads between the superstructure and substructure and to contribute to the lateral force resistance under seismic loads. However, only a few studies in the past have considered the cyclic behavior of steel bridge bearings (Mander et al. 1996, Barker and Hartnagel 1998, and Steelman et al. 2013) as well as the seismic performance of highway bridges equipped with such bearings (DesRoches et al. 2004 and Bignell et al. 2005). The behavior of a number of steel bearing configurations still has yet to be considered under seismic loads. Moreover, among the limited literature available on steel bridge bearings, issues concerning corrosion and seismic performance are often addressed separately instead of considering the correlation between the two. As a result, there is a significant need for in-depth research on the performance of bearings and bridges under combined aging effects (i.e. corrosion) and seismic loads that quantitatively correlates corrosion level with behavior.

1.2 Research Objectives

The goal of this research is to characterize the cyclic behavior of corroded steel bridge bearings and correlate this behavior with corrosion level allowing for more accurate evaluation of the performance of in-situ bridges and leading to more robust and sustainable solutions. This is accomplished through theoretical analyses, finite element modeling, corrosion loss quantification, experimental testing of salvaged steel bridge bearings, and nonlinear time history analyses of a prototype deteriorated bridge under seismic excitations. The results from the bearing theoretical analyses, modeling, and testing provide previously non-existent information about the cyclic response of corroded steel rocker and bolster bearings. In addition to the distribution of corrosion on a bearing and among different bearing locations in a bridge system, the displacement capacity, lateral strength, and failure modes of corroded steel bearings under both monotonic and cyclic loads are obtained. The results from the nonlinear time history analyses of the bridge model are used to evaluate the effect of corrosion of the bearings on the overall bridge response leading to a better understanding of retrofit or replacement needs in areas of moderate to high seismicity.

The scope of this research focuses on evaluating the performance of steel bridge bearings typically found in the CEUS and identifying their vulnerability to the combined effects of corrosion and seismic loads allowing for the response of older in-situ steel bridges to be evaluated. Specifically, 25 steel bearings, salvaged from the Meridian Road bridge (Figure 1.2) in Rockford, IL, serve as the experimental specimens being studied. The Meridian Road bridge, chosen as the prototype bridge for this study, has four continuous spans symmetric about the middle pier wall with span lengths of 14 m and 17.8 m. The bridge superstructure consists of five parallel steel girders (W840×193 mm×kg/m) and a 178 mm thick reinforced concrete slab. More details in regard to the prototype bridge are provided in Chapter 3.

The following main tasks are conducted to achieve the goal of this research:

Task 1 – Analytical and Finite Element Modeling:

- Analytically analyze the stiffness and strength of the steel bearings using rigid body kinematics and upper bound plastic analysis.
- Establish finite element models that can accurately capture the cyclic response of steel bridge bearings, considering the intrinsic contact and friction behavior between contact surfaces, the effect of anchor bolts, and the influence of the dead load from the superstructure.
- Validate the finite element models through comparison with the theoretical analysis of steel rocker and bolster bearings.
- Characterize the hysteretic behavior of rocker and bolster bearings in the longitudinal and transverse direction through a preliminary cyclic study to obtain relevant force data for the design of the experimental test setup to be used in Task 2.

Task 2 – Experimental Testing of Salvaged Steel Bearings:

- Categorize the corrosion level of salvaged bearings that were previously installed in a bridge for over 50 years and quantify corrosion-induced weight loss and geometry changes.
- Correlate corrosion levels with location where the bearing was installed in the bridge.
- Characterize the cyclic behavior of steel rocker and bolster bearings for each corrosion category in the longitudinal and transverse directions under cyclic loading.
- Investigate the effect of removing corrosion byproducts at the bearings' surfaces on the bearing cyclic behavior.
- Identify the failure modes of the bearing-pedestal assemblage.
- Correlate corrosion level with hysteretic behavior and failure modes.

Task 3 – Nonlinear Time History Analysis of the Protype Bridge:

- Develop macro-numerical elements for steel bearings based on the results obtained from Task 1 and 2 that are capable of numerically and efficiently reproducing the steel bearing cyclic behavior and incorporating corrosion level effects.
- Implement the analytical models of the steel bridge bearings into a full bridge model to consider the effect of corroded bridge bearings on the overall seismic response of a deteriorated continuous steel girder bridge.
- Correlate the seismic performance of the bridge with the corrosion level of steel bearings to provide guidance for the seismic assessment of existing steel bridges.

1.3 Dissertation Outline

The organization of this dissertation consists of the following chapters:

Chapter 1 provides a brief introduction of the background and motivation for this research on corroded steel bridge bearings and the objectives of this project.

Chapter 2 offers a literature review of the major hazards (i.e. seismicity and corrosion) facing the highway infrastructure in the United States, steel bridge bearings and their vulnerability to corrosion, and lessons learned from the performance of bridges and their members, specifically steel bearings, during past seismic events.

Chapter 3 introduces an analytical study of the strength and stiffness of the steel bearings considered in this study. Rigid body kinematics is used to analyze the longitudinal rolling behavior and transverse instability of steel rocker bearings. Upper bounds for the steel bolster bearing strength in both longitudinal and transverse loading directions are estimated assuming a variety of failure modes including shear failure of the pintles and anchor bolts and combined tension and shear failure of the anchor bolts under rocking and prying.

Chapter 4 focuses on developing a set of finite element models for the steel bridge bearings that are capable of capturing the strength and cyclic behavior of the bearings under lateral loading. Cyclic loading protocols considering progressively increasing and constant displacement magnitudes are applied to the bearing models to examine preliminarily their cyclic behavior in both the longitudinal and transverse direction. The limitations of these models are also discussed.

Chapter 5 demonstrates the effect of corrosion on steel bearings with respect to their geometry and weight. The characteristics of atmospheric corrosion of steel bearings are discussed together with several existing corrosion loss prediction models.

Chapter 6 provides an extensive experimental program that was implemented to study the cyclic behavior of the steel bridge bearings in two orthogonal directions, longitudinal and transverse. The effect of corrosion on the bearings' lateral cyclic response is investigated and discussed. Severely corroded bearings are also retested after removing the surface rust layers to investigate further the effect of corrosion.

Chapter 7 presents a numerical study of a full-scale computational model for a representative highway bridge typical of the CEUS. The experimental findings of the steel bearings regarding their lateral cyclic behavior are used to guide the development of a set of phenomenological bearing models that can accurately reproduce the bearing cyclic response in an efficient manner.

Chapter 8 summarizes the conclusions drawn from this study and outlines future research needs.

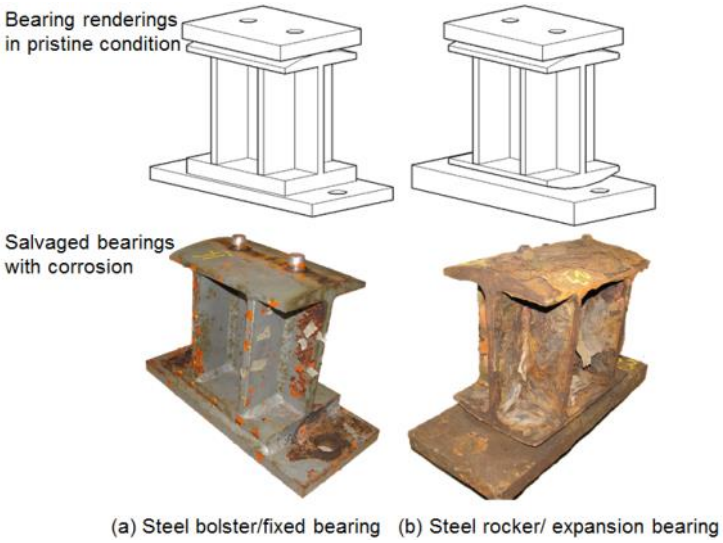

Figure 1.1 Schematic and picture showing corroded (a) bolster and (b) rocker bearings

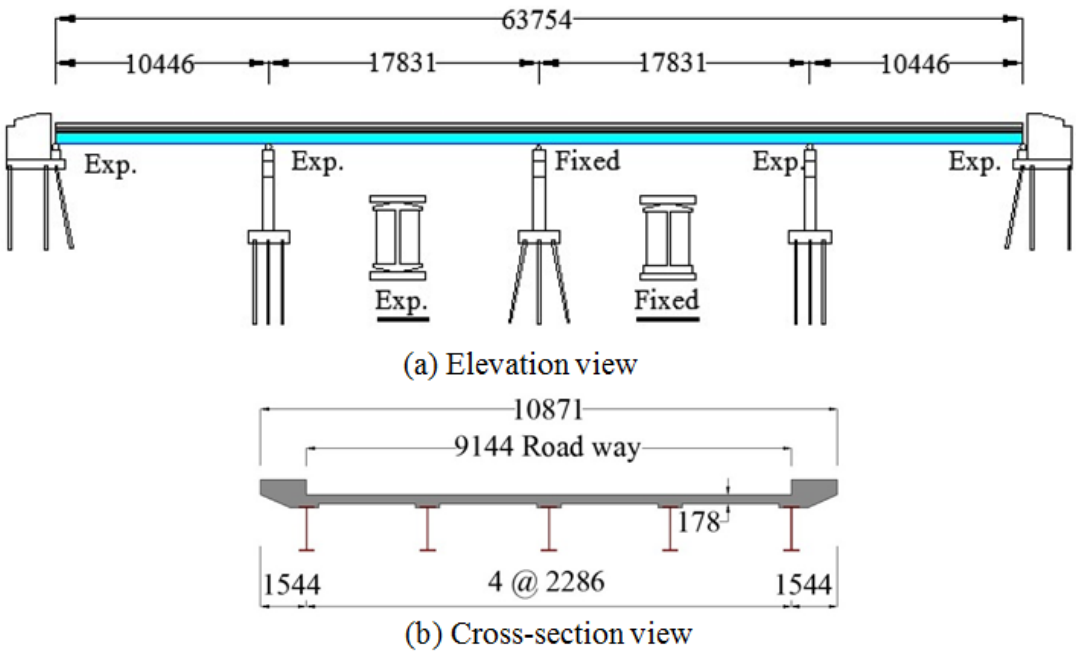

Figure 1.2 Plan drawing of the highway bridge from which the steel bearings were salvaged with all dimensions given in mm

Figure 1.3 Toppled rocker bearing failures: (a) Birmingham Bridge (Splitstone et al. 2010) and (b) Dunn Memorial Bridge (NYSDOT 2005)

CHAPTER 2 LITERATURE REVIEW

2.1 Hazards Affecting Highway Infrastructure in the CEUS

2.1.1 Seismicity in the CEUS

The New Madrid seismic zone (NMSZ) (Figure 2.1) and its extension, i.e. the Wabash Valley seismic zone (WVSZ), together with the Charleston seismic zone (CSZ) in South Carolina, are the major sources that pose a seismic threat to the CEUS (Merino et al. 2010). Seven states including Illinois, Indiana, Kentucky, Tennessee, Mississippi, Arkansas, and Missouri are located around the vicinity of the NMSZ. Between 1811 and 1812, three major earthquakes struck the area demonstrating the potential for significant seismic loads in the region. Although modern instrumentation was not available at that time, geologic evidence estimates the magnitudes of the aforementioned sequential events to be between 7.0 and 8.0, which are to date the largest known earthquakes for an intraplate seismic event (Johnston and Schweig 1996). Figure 2.2 illustrates locations and magnitudes of recorded seismic activities in the NMSZ since 1974 when modern seismological instrumentation was installed in the area. Recent studies of liquefaction features at over 250 sites across the NMSZ have suggested that the area has an average 500 year return period with an upper limit of 800 years and a lower limit of 200 years for sequential earthquake strikes resembling those events that occurred in 1811 and 1812 (Tuttle et al. 2002).

Figure 2.3 shows the current seismic hazard map of the United States. It is clear that the NMSZ and CSZ have a comparable hazard to that of the West Coast of the United States where more frequent inter-plate earthquakes occur. Moreover, a joint finding made by the Center of Earthquake Research and Information at the University of Memphis and the United States Geological Survey has estimated that the probability of an earthquake with

magnitude between 7.5 and 8.0 is 7-10% in a 50-year period for the NMSZ. For earthquakes having a magnitude of larger than 6.0, this probability increases to 25-40% (USGS 2006). Given the fact that earthquakes in the Central and Eastern United States spread much broader than those along the West Coast due to the geology of the area, a large earthquake in this region can be felt over a broad range of as many as 14 states (DesRoches et al. 2003) and has the potential for both large loss of life and significant economic impact due to the density of the highway network and the number of larger urban areas.

The above discussion illustrates the seismic threat imposed on highway bridges in the Central and Eastern United States. In general, these bridges were not designed and constructed to resist seismic loads (Dicleli and Bruneau 1995) due to a lack of understanding of the region's seismic hazard at the time. As a result, many existing highway bridges in this region are vulnerable to earthquakes because their structural members such as steel bearings are insufficient in withstanding the large lateral forces associated with earthquakes. Considering the importance of highway bridges to the economy and public safety in regards to freight transportation and commute, it is of particular concern to understand the behavior of older highway bridges under seismic loads so that feasible and sustainable retrofit schemes can be proposed to improve their survivability and serviceability during a moderate earthquake.

2.1.2 Age-related corrosion of highway infrastructure

Age-related deterioration of bridges manifests itself in a variety of forms including concrete cover spalling as a result of reinforcement corrosion, reduced capacity of steel girders due to corrosion-induced section loss, changes in the friction coefficient due to contact surface corrosion and debris buildup, and area loss of embedded anchor bolts over time. All of these forms of deterioration result from corrosion of steel components (reinforcement, connection elements, and members). Corrosion develops from the continued exposure of steel components or members to a chloride-rich environment within the presence of moisture and oxygen (Cramer et al. 2002). For highway bridges in the Central and Eastern U.S., the use of deicing solvents is a major source of chloride.

The process of corrosion generally takes years to accumulate a significant amount of corrosion byproduct and can be prevented by proper and continued maintenance i.e. painting and lubricating steel components/members. However, previous findings show that serious corrosion exists among steel members and components of highway bridges in the Central and Eastern U.S. (Kayser 1988; Lindquist 2008), which also explains the necessity of evaluating the aging bridge inventory under seismic loads for this region.

According to Fontana and Greene (1967), eight forms of corrosion are defined to categorize the corrosion phenomena with five of these specifically applying to bridge components (Kayser and Nowak 1989a).

Uniform Corrosion:

Also known as general corrosion, uniform corrosion is the most common form of corrosion and takes place over an entire exposed surface or a large area through an electrochemical reaction. Corrosion of the contact surfaces of steel bearings is an example of uniform corrosion (Figure 2.4). For a steel rocker bearing, uniform corrosion can cause buildup of debris and corrosion byproducts between the bottom contact surfaces along with a reduction of capacity and change in the behavior due to loss of surface area (Figure 1.3). As a result, corrosion can prevent movement of the rocker bearing leading to locking. Under cyclic loading, a locked rocker bearing at first performs like a fixed bearing attracting unexpected horizontal forces before the bond is broken and the ability to rotate is restored (Mander et al. 1996). The configuration of a bearing poses a challenge to continued routine maintenance of pre-painted surfaces at contact locations, which are where uniform corrosion can be most pervasive and has the largest effect on the behavior of a rocker bearing (Lindquist 2008).

Pitting:

Unlike uniform corrosion, pitting is more concentrated to a localized area. This localization of corrosion results in section loss that extends into the metal in the form of holes. Pitting is among the most destructive forms of corrosion and is difficult to detect as it is extremely localized and often concealed by corrosion byproducts. In addition, as a

result of stress concentrations, pits in high stress regions pose a serious threat to the structural stability of a component and may result in abrupt failures. Pitting can occur randomly along any surface of the bearing assemblage. However, no consensus has been achieved regarding the mechanism of pitting initiation (Lindquist-Hoeke et al. 2009).

Galvanic Corrosion:

Initiation of galvanic corrosion involves two dissimilar metals in contact with each other. The potential difference between the two metals produces an electron flow between the metals. The active metal among the two serves as the anode while the less active metal acts as the cathode. Usually the metal serving as the anode sustains severe corrosion while the other metal serving as the cathode corrodes very little or not at all. This form of corrosion can be found at bolted or welded connections where dissimilar metals may be in contact. For example, in a steel bearing assemblage, galvanic corrosion can be triggered between components made of stainless steel (i.e. anchor bolt) and carbon steel (i.e. masonry plate) (Lindquist-Hoeke et al. 2009). However, for the majority of older bridges, carbon steel typically was used throughout the entire bearing assemblage (Rashidi and Saadeghvaziri 1997).

Crevice Corrosion:

Crevice corrosion is found between surfaces in close contact or in shielded areas as a result of solutions rich in oxygen being trapped in these areas. This form of corrosion often occurs in holes, between faying surfaces, and at lap joints. Crevice corrosion often accompanies pitting as it can occur in the holes associated with pitting. For steel bearing assemblies, crevice corrosion can occur in the crevices between components of the anchor bolt (i.e. nut and washer) and between the masonry plate and the concrete pedestal (Lindquist 2008).

Stress Corrosion Cracking:

The simultaneous presence of tensile stress and a corrosive environment can induce stress corrosion cracking, which can lead to brittle failure of ductile materials (Lindquist-Hoeke et al. 2009). For mild carbon steel used in bridges, stress corrosion is usually not an issue

because the susceptibility of a steel material to stress corrosion decreases as its fracture resistance increases (Kayser and Nowak 1989b).

The above discussion briefly summarizes the common corrosion mechanisms that can lead to the deterioration of older steel bridge components. Corrosion of steel bridge components and members can result in three main outcomes including section loss, geometry changes, and buildup of debris and corrosion byproducts (Kayser and Nowak 1989a). Specifically for a steel bearing, section loss causes a reduction in the net area of the bearing available to withstand the dead load from the superstructure. Reduction of the section of a bolster bearing, particularly in the contact region, also can cause a decrease in stiffness and strength of the bearing under horizontal loads. These changes can lead to unexpected and nonuniform behavior under seismic loads. Buildup of debris and corrosion byproducts also can restrain free movement of a rocker bearing leading to adverse horizontal forces imparted to the superstructure and the substructure, unexpected behavior, and possible overturning of the rocker bearings (Figure 1.3).

Past studies have considered corroded steel girders (Kayser 1988) and corroded anchor bolts of steel bearings (Lindquist 2008). Kayser (1988) showed that corrosion can lead to a reduction in the bending, shear, and bearing resistance of steel girders as a result of thinned webs and flanges. Lindquist (2008), considering corrosion initiation mechanisms, systematically discussed the possibility of initiation of various corrosion forms for steel bearing anchor bolts. Findings of this study showed that galvanic corrosion and crevice corrosion are among the major forms of corrosion that prevail in the deterioration of anchor bolts. Neither of these studies looked at the effect of corrosion on the seismic performance of the bearings, which provide a load path for both vertical and lateral loads and accommodate relative movements between the superstructure and substructure in a bridge system. Thus, bearings deserve more research given the seismic hazard in the CEUS.

2.2 Steel Bridge Bearings

2.2.1 Overview of steel bearings

Bearings provide the connection between the superstructure and substructure of a bridge system. Under service conditions, bearings transmit the dead load and traffic load from the superstructure to the substructure while also accommodating relative movements between the superstructure and substructure caused by thermal action and vehicular braking. Bearings also provide lateral resistance in both the longitudinal and the transverse direction under extreme loads such as collisions and earthquakes (Chen and Duan 2003). A variety of bearings have been used in practice where steel rocker bearings have been used for more than 100 years (Eggert and Kauschke 2002). In the CEUS, a large number of older bridges are equipped with steel bearings due to the number of bridges constructed in the mid 20th century when steel bearings were the most popular bearing type because of their cheap fabrication cost and ease for installation (Saadeghvaziri and Rashidi 1998; AASHTO 2008). For this reason, typical steel rocker and bolster bearings will be considered in this study since no studies have previously correlated their performance under seismic loads with corrosion level. The configuration of the studied bearings is illustrated in Figure 1.1 and various bearing components are labeled in Figure 2.5.

2.2.2 Definition and AASHTO Specifications

Bolster Bearing:

Also known as a fixed bearing, a bolster bearing (Figure 2.5(a)) has a single contact interface between the sole plate and the cylindrical surface at the top of the bearing. This configuration allows for rotation of the superstructure about the transverse axis. No translation is accommodated by the bolster bearing. According to Hertz theory, the theoretical contact zone for the bolster bearing at the contact interface is a line along the transverse direction that experiences infinite stress under dead loads and subsequently will yield to a rectangular plane reducing the infinite stress to a finite stress (Ramberger 2002). The considered bolster bearing assemblage, typical of that found in Illinois, is

comprised of a sole plate, a pair of pintles, a bearing body with a cylindrical surface at the top, a masonry plate, and a pair of anchor bolts. The sole plate is typically welded to the bottom flange of a bridge girder. Inserted tightly into the bearing body, the pintles fit loosely into holes in the bottom of the sole plate. The bearing body is rigidly attached (i.e. welded) to the masonry plate which is bolted to the concrete pedestal with a thin lead plate placed in between to account for the potential non-uniform surface of the pedestal.

Rocker Bearing:

A rocker bearing, as illustrated in Figure 2.5(b), has a pair of contact interfaces at the top and bottom of the rocker body, allowing the bearing to accommodate both translation and rotation of the superstructure. The rocker bearing has a rigid body with cylindrical top and bottom surfaces. Compared to the bolster bearing, the additional degree of freedom associated with the rocker bearing is attained through the extra contact interface at the bottom of the bearing body. To avoid transverse walking or sliding of a rocker bearing, pintles are located at both the top and bottom of the bearing at the point of contact.

AASHTO Specifications

The American Association of State Highway and Transportation Officials (AASHTO) modernized its specifications for seismic design of highway bridges in 2008 by incorporating a design earthquake with a 1,000 year return period that replaced the previous 500 year return period design earthquake. The 1st edition of the AASHTO Specifications for LRFD Seismic Bridge Design was published in 2009, which combined input and findings of several organizations in the bridge engineering community including ATC-32, Caltrans, the Multidisciplinary Center for Earthquake Engineering Research (MCEER), and the South Carolina Department of Transportation.

The current AASHTO LRFD Bridge Design Specifications (2010) offers seismic provisions for bridge bearings, including rocker and bolster bearings. The adoption of rocker bearings is not recommended for new bridge construction due to their limited displacement capacity as well as tendency toward tipping under seismic loads (AASHTO 2009). For this reason, it is important to understand their behavior in evaluating in-situ

bridges, particularly under the influence of seismic loads and corrosion. The impact of these updated codes on highway bridges in the CEUS is that the new design earthquake with a 1,000 year return period requires a capacity that surpasses what most existing bridges in the NMSZ were initially designed. This increased capacity requires a better understanding of the expected performance of in-situ highway bridges and a plan for determining the need to retrofit or replace based on the bridges current condition. To address these concerns, the Illinois Department of Transportation initiated an earthquake resisting system (ERS) strategy in mid-2005 for the design and retrofit of highway bridges in Illinois to meet the new design earthquake requirements (Tobias et al. 2008). The main goal of this ERS strategy is to prevent span loss by allowing controlled damage at strategic locations in bridges such that seismic energy imparted to the bridge can be mitigated. This requires sacrificial connection elements (e.g. elastomeric bearings) between bridge superstructures and substructures that will under seismic loads act like fuses leading to prolonged periods and reduction of force demands on the substructure (Filipov et al. 2013).

2.2.3 Behavior of steel bearings

Although steel bearings have been used in bridge construction for over 100 years, research on the behavior of steel bearings is limited, particularly under large cyclic loads anticipated from an earthquake. The advent of modern aseismic bearing devices, such as base isolation systems, dampers, and active control devices, has exacerbated this situation since older steel bearings were replaced and abandoned in the traditional seismic zones along the West Coast (Mander et al. 1996). However, steel bearings are still regularly seen throughout the CEUS (Saadeghvaziri and Rashidi 1998) and their behavior under seismic loads needs to be correlated to their condition in order to properly assess these bridges and ensure the safety of the public.

The behavior of steel bearings at the contact interface is dictated by hard contact in the normal direction allowing transfer of vertical load from the superstructure to the substructure and by Coulomb friction, rolling resistance, and bearing in the tangential direction providing lateral resistance to horizontal actions (i.e. thermal action, wind,

vehicular forces, etc). A theoretical solution for normal contact pressure between two elastic bodies has been provided by Heinrich Hertz in 1881 (Ramberger 2002). Steel bearings with spherical contact surfaces have a point contact that will yield to a circular contact plane under vertical loads, while steel bearings with cylindrical contact surfaces have a line of contact that will yield to a rectangular contact plane. For sliding bearings, horizontal force resistance can be determined ideally as the product of the friction coefficient and normal force. As a result of deterioration, the contact surfaces of a steel bearing can undergo corrosion and build-up of debris, which affects the tangential behavior at the contact interfaces due to changes in the friction coefficients resulting from the condition of the contact surfaces and changes to the contact area. Thus, the behavior of steel bearings needs to be better understood for different levels and locations of corrosion.

Mazroi et al. (1983) studied a class of steel bearings including pipe roller bearings, pinned rocker bearings, and pintle rocker bearings to determine their effective friction coefficients under as-built, corroded, and in-situ conditions. A sensitivity study of pintle rocker bearing's performance to configuration variations was also conducted. The conducted tests were restricted to monotonic displacement-controlled loading under constant vertical loads. It was found that the effective coefficient of friction increased to 0.02 for corroded pinned rocker bearings and 0.09 for in-situ pinned rocker bearings compared to 0.01 for clean pinned rocker bearings. In addition, results of the sensitivity study showed a significant dependence of the behavior of pintle rocker bearings on the variation in the radius of the sole plate socket. To date, this study is one of the only to consider the effects of corrosion on the monotonic behavior of steel bridge bearings.

Mander et al. (1996) carried out one of the most comprehensive experimental studies of steel bearings by considering the cyclic behavior of salvaged steel bearings. This study used a unique experimental setup and loading scheme to characterize the behavior of salvaged steel bearings under cyclic loads. The steel bearings studied (Figure 2.6) were retrieved from two New York bridges typical of those found in the Eastern United States (EUS). Cyclic tests were performed in the longitudinal and the transverse directions to examine the influence of multi-directional ground excitations. The applied vertical load

levels were within the range of 270 kN and 356 kN calculated according to a typical highway bridge configuration in the State of New York. The test specimens comprised a variety of steel bearings including low-type sliding and fixed bearings, and high-type bolster, fixed, and rocker bearings. The configuration at the top contact interface of the high-type bearing specimens features a bearing body with a cylindrical surface being inserted into a sole plate with a cylindrical recess or socket, which differs from the typical configuration of steel bearings in Illinois as seen in Figure 2.5. Significant findings for each type of steel bearing are summarized below.

Expansion bearing:

In the longitudinal direction, quasi-rectangular hysteresis loops were observed from the test results indicating the rocker specimens obeyed a Coulomb friction law. However, for the specimens where locked-in field stresses were maintained, an increase in resistance, which progressively reduced during successive loading cycles as a result of the breakdown of debris and smoothening of the sole plate-rocker interface, was seen during the first loading cycle (Figure 2.7). A parametric study concerning the vertical load level applied to the bearing specimens was performed. The rocker bearing response exhibited an increase in resistance proportional to the vertical load as it increased from 178 kN to 356 kN to 534 kN, again emphasizing that high-type rocker bearing behavior is dictated by Coulomb friction. Such observations were also confirmed by Barker and Hartnagel (1998) who experimentally studied the cyclic behavior of 15 Missouri type-D rocker bearings in an as-received condition. These rocker specimens were grouped by corrosion levels (i.e. heavy and mild) and the test results revealed that heavily corroded bearings had equivalent friction coefficients in the range of 6.87 to 9.79 percent, while for mildly corroded bearings equivalent friction coefficients varied between 2.39 and 4.38 percent.

In the transverse direction, more rectangular hysteresis loops were observed before the rocker bearing body struck the keeper plate and after the keeper plate fractured, which demonstrated that the governing deformation mode was sliding along the sole plate (Mander et al. 1996). A sudden increase in resistance was observed as a result of bearing on the keeper plate prior to keeper plate fracture (Figure 2.8). One transverse loading test

was terminated as the rocker bearing became unstable in the longitudinal direction at 0.71 in. (18 mm) of displacement, which serves as proof of possible instability issues. This is a possible alternative explanation for toppled rocker bearings, previously attributed to inadequate seat width, found in bridge failures during past earthquakes (Bruneau et al. 1996). However, the study by Mander et al. (1996) is the only work that investigated the transverse cyclic behavior of rocker bearings, and hence further experimental studies are needed in order to adequately characterize the transverse behavior of different rocker bearing configurations with different corrosion levels.

Fixed bearings:

Mander et al. (1996) also conducted tests under longitudinal loading on fixed bearings mounted to a steel base. The results showed that rocking and prying were the predominant deformation modes at the masonry plate-pedestal interface (Figure 2.9). Moreover, the lateral stiffness of the fixed bearing was also found to be proportional with the vertical load level. In the transverse loading direction, sliding of the sole plate on the bearing body was the predominant deformation mode confirmed by the rectangular hysteresis loops after the keeper plates fractured (Figure 2.10). The experimental results also confirmed that the transverse behavior of fixed bearings obeyed the laws of Coulomb friction.

In order to check the influence of the concrete pedestal on the ability of a fixed bearing to transfer lateral forces, a number of tests were run using a reinforced concrete pedestal rather than a steel base. Experimental results (Figure 2.11) for the fixed bearings under progressively increasing loading cycles in the longitudinal direction exhibited several occurrences of damage to the concrete pedestal including concrete cover spalling, loosening of the anchor bolt nut, and pullout and bending of the anchor bolts. A dramatic decrease in stiffness and ultimate strength was shown for specimens mounted on concrete pedestals compared with those mounted on a steel base. However, better energy dissipation characteristics were seen for specimens mounted on concrete pedestals due to the deformation of the concrete pedestal and anchor bolts. In addition, an improved ductility factor of 6.0 was obtained. In the transverse direction (Figure 2.12), the original

keeper plates failed soon after loading was initiated leading to a rectangular hysteresis behavior indicating that Coulomb friction or sliding dominates the motion of the bearing body with respect to the sole plate. However, Mander et al. (1996) showed that retrofitting steel bearings with stronger keeper plates can switch the failure mode in the transverse direction from fracture of the keeper plate to deformation of the concrete pedestal and anchor bolts.

Hite et al. (2008) experimentally studied the cyclic behavior of steel pedestals (Figure 2.13) used in Georgia for elevating existing highway bridges with insufficient clearance. The experimental results revealed hysteresis loops similar to those seen for high type fixed bearings. The results demonstrated reasonable deformation and strength capacities of steel pedestals under simulated seismic loads. In addition, a set of shear failure modes reported by ACI (2005) was also observed in the tests of the steel pedestal-concrete cap beam assembly such as prying of the post-installed anchor bolts, concrete breakout, and yielding of the anchor bolts.

Steelman et al. (2014) experimentally investigated the lateral cyclic behavior of low-type steel fixed bearings under longitudinal and transverse loading. As shown in Figure 2.14, Steelman et al. (2014) found that the bearing behavior is insensitive to loading orientation when the anchor bolts are weaker than the pintles and that the bearing strength is determined by the shear capacity of the anchor bolts. This study demonstrated that low-type steel bearings can be used as fuses for aseismic purposes on highway bridges that are located in areas with a low to moderate seismic hazard such as Illinois.

As a result of the minimal experimental studies, particularly pertaining to different configurations of steel bearings, and the need to establish a correlation between corrosion level and cyclic behavior for in-situ steel bridge bearings, the cyclic behavior of steel bearings typically found in the Central United States are experimentally characterized and numerically modeled as part of this dissertation under both longitudinal and transverse loading to close the gap in knowledge of their performance and allow for more realistic representation of in situ bridge behavior in evaluating the vulnerability of older bridges.

2.3 Seismic Performance of Highway Infrastructure

Performance of highway bridges during past seismic events has been archived and studied by numerous groups (Mitchell et al. 1995; Housner and Thiel 1995; Bruneau et al. 1996; Basoz et al. 1999; Wardhana and Hadipriono 2003) since the San Fernando earthquake in 1971, which served as the pivotal point in the development of seismic design standards for bridges in North America. During that earthquake, seven bridges collapsed and sixty others suffered moderate to extensive damage. Separated hinges at expansion joints, inadequate seat widths for both the superstructure and bearings, and insufficient confinement of columns were the most common reasons for damage to bridges (Pond 1972). The San Fernando event led to a series of new seismic design provisions as well as retrofit programs being initiated by Caltrans. The 1989 Loma Prieta earthquake with a moment magnitude of 7.1 resulted in the collapse of the Cypress Viaduct of Interstate 880 and partially the Bay Bridge. An overview of bridge failures during the Loma Prieta earthquake revealed similar damage patterns to that of the San Fernando earthquake. The leading reason behind these failures was that older bridges were either not designed for seismic loads or inadequately designed to survive a large earthquake.

One significant outcome of the Loma Prieta earthquake in regard to the retrofit of bridges is the reevaluation of the retrofit program initiated after the San Fernando earthquake leading to a more concerted consideration of the whole bridge, foundation, and supporting soil (Housner et al. 1990). During the 1994 Northridge earthquake, seven bridges collapsed, of which five were scheduled for retrofit. All seven bridges were designed to the prevailing codes prior to 1971. All retrofitted and newly-constructed bridges in the Post-Loma Prieta earthquake era maintained their structural integrity with no or little damage, confirming the soundness of the post-1989 retrofit program and seismic design provisions (Housner and Thiel 1995). However, few records are available on the types of bearing failures during these earthquakes. It is worthwhile to note that the majority of the bearing failures recorded during these earthquakes were related to insufficient seat widths. Nevertheless, questions regarding the reliability of older highway

bridges under seismic loads are raised from the seismic performance of highway bridges in California during past earthquakes.

Seismic performance of steel bridges during the 1995 Kobe earthquake in Japan provided another perspective on the performance of highway bridges under large seismic loads. A number of unanticipated failure modes were observed for steel bridges including various levels of buckling of steel columns, brittle fracture of steel columns, and bearing failures. Roller bearings showed a strong tendency toward failure under seismic actions, triggering further span losses. In addition, various failure mechanisms were observed for fixed bearings ranging from failed bolted connections between the girder and the bearing to failure of the anchorage in the concrete pedestals to fracture of the keeper plates and stoppers (Bruneau et al. 1996; Sato et al. 2008). The 2011 Tohoku earthquake in Japan offered further evidence in regards to the vulnerability of steel bridge bearings to strong ground motions. Steel bearing failure modes such as sheared anchor bolts, ejected steel rollers, and unseating were observed on several older bridges (EERI 2011, Kawashima 2012). These repeated failures of steel bearings (Figure 2.15) provide solid evidence of the vulnerability of steel bridge bearings under seismic loads and justify the need to quantify their cyclic behavior.

The highway bridge inventory in the CEUS comprises a great number of older bridges equipped with steel bearings (Nielson and DesRoches 2007a). These older bridges were not designed for seismic hazard levels that are now expected. Hence, the response of such bridges under large seismic loads is unknown, particularly when coupled with corrosion-related deterioration (Ghosh and Padgett 2010). The proposed research focuses on the characterization of the cyclic behavior of corroded steel bridge bearings and thus will facilitate a better understanding of the response of older highway bridges that are prevalent in the Central and Eastern United States.

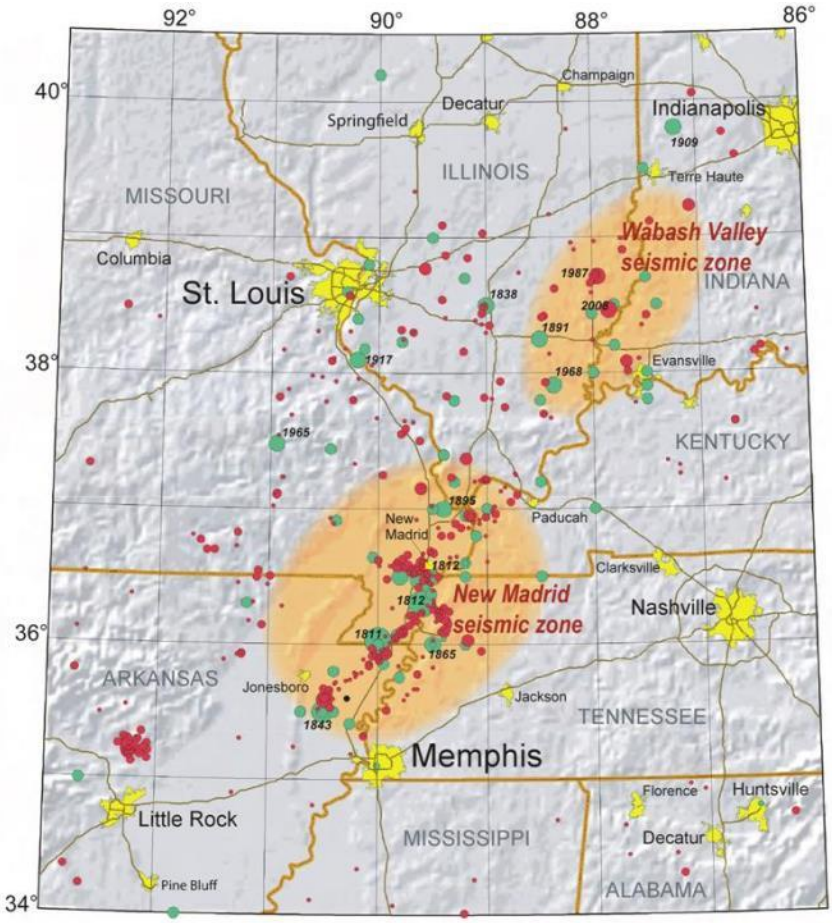

Figure 2.1 The New Madrid seismic zone with its seismicity denoted by red dots (NMSZ Expert Panel 2011)

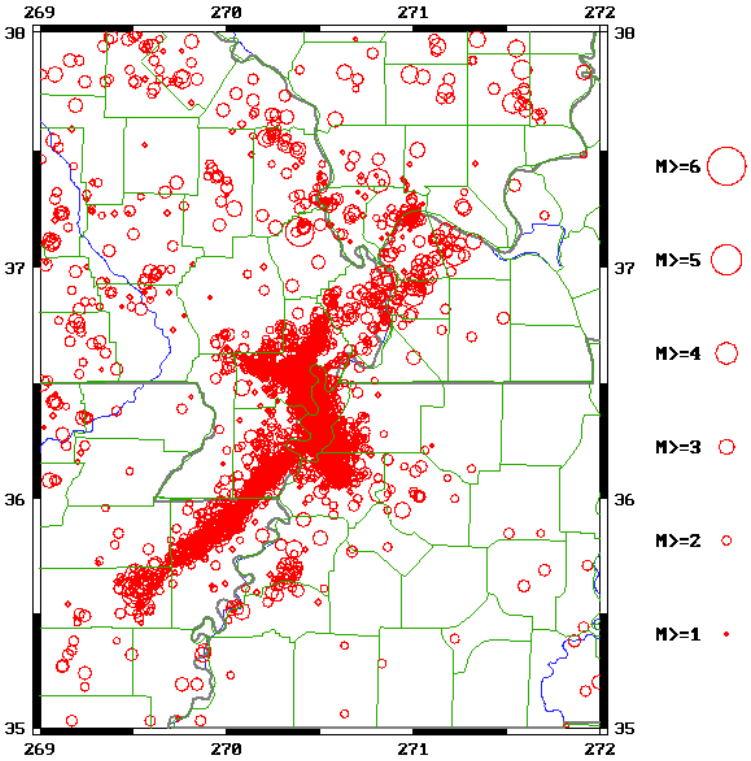

Figure 2.2 Seismic activities within the NMSZ between 1974 and 2011 (CERI 2011)

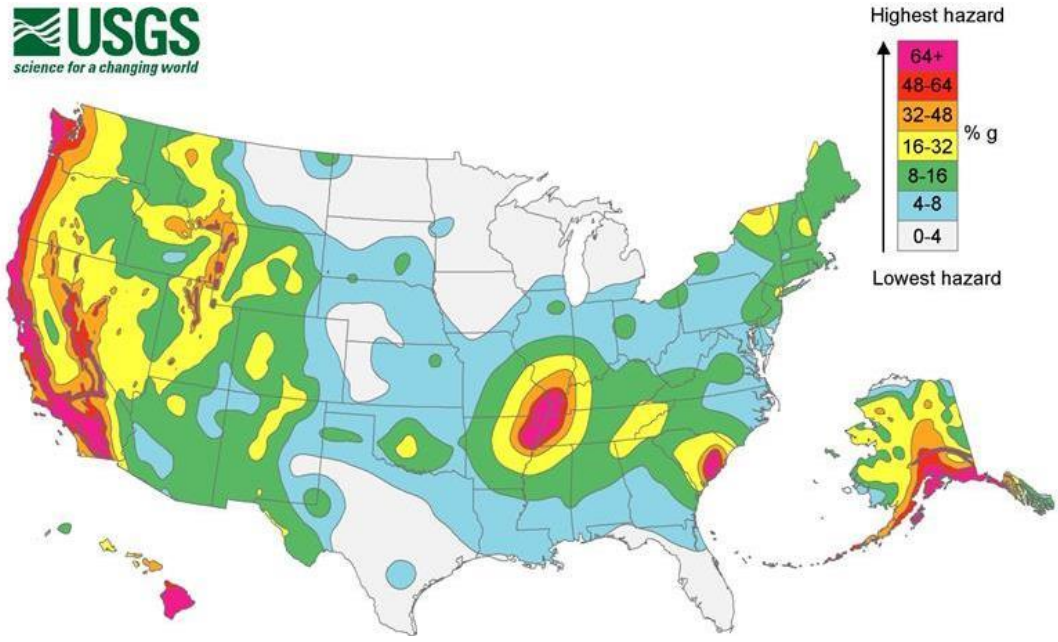

Figure 2.3 U.S. Geological Survey hazard map of the United States for a probability of exceedance of 2% in 50 years (USGS 2008)

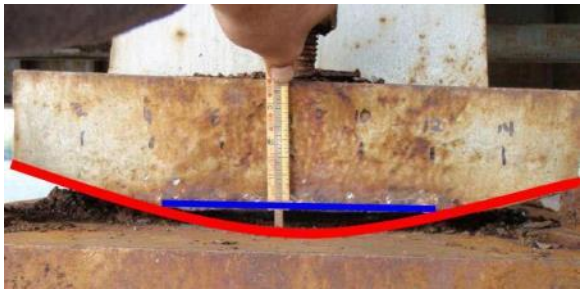

Figure 2.4 Uniform corrosion at the bottom contact surface of a rocker bearing (modified from Balassone (2010))

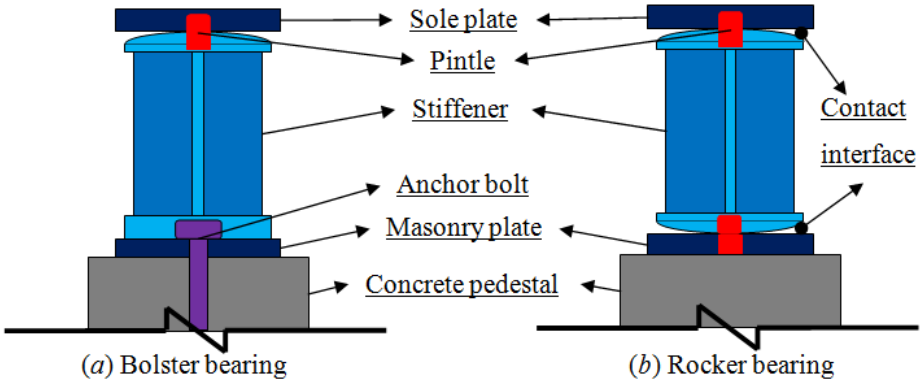

Figure 2.5 Side view of a bolster and rocker bearings found in the Central and Eastern U.S.

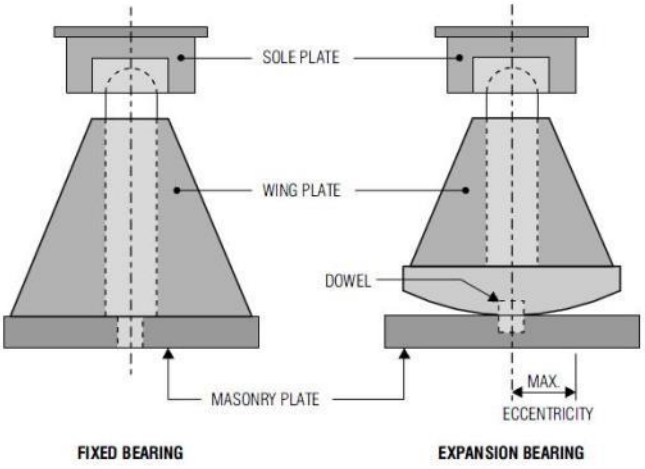

Figure 2.6 Configuration of the steel bearings studied by Mander et al. (1996)

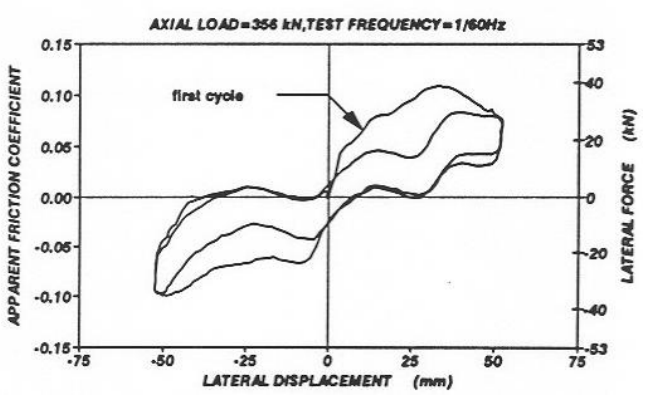

Figure 2.7 Longitudinal test results for the high type rocker bearings (Mander et al. 1996)

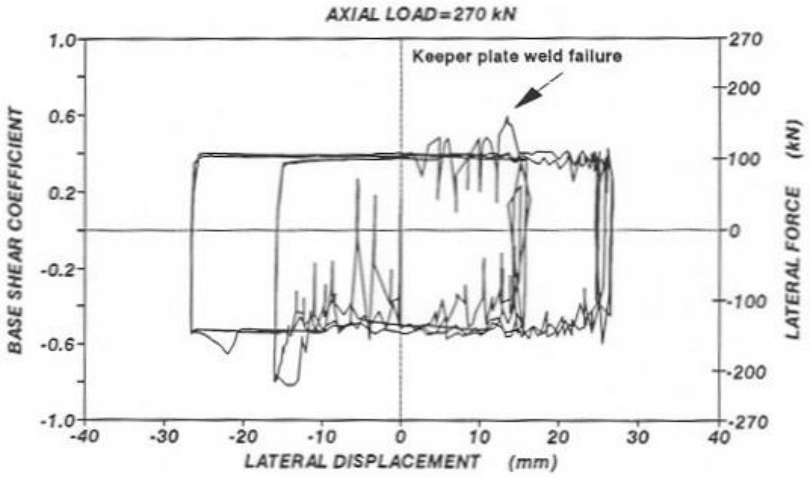

Figure 2.8 Transverse test results for the high type rocker bearings (Mander et al. 1996)

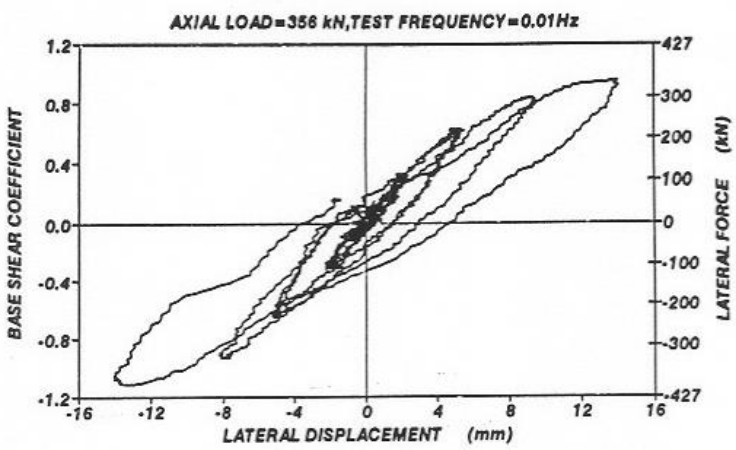

Figure 2.9 Longitudinal test results for the high type fixed bearings (Mander et al. 1996)

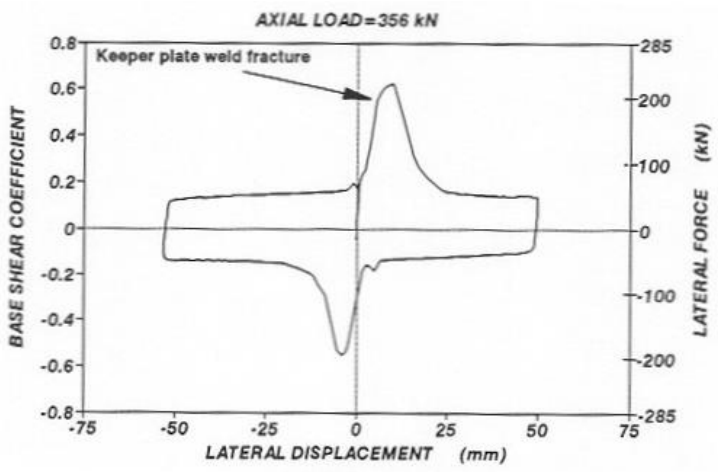

Figure 2.10 Transverse test results for the high type fixed bearings (Mander et al. 1996)

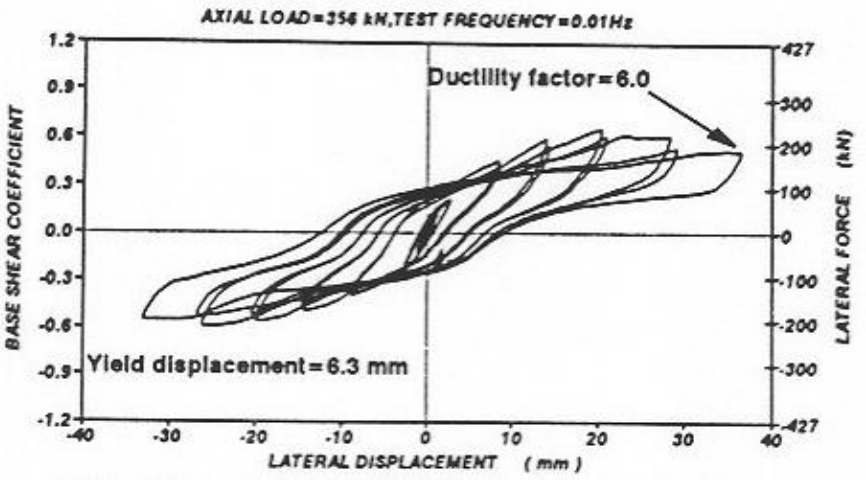

Figure 2.11 Longitudinal test results for the high type fixed bearings on a concrete pedestal (Mander et al. 1996)

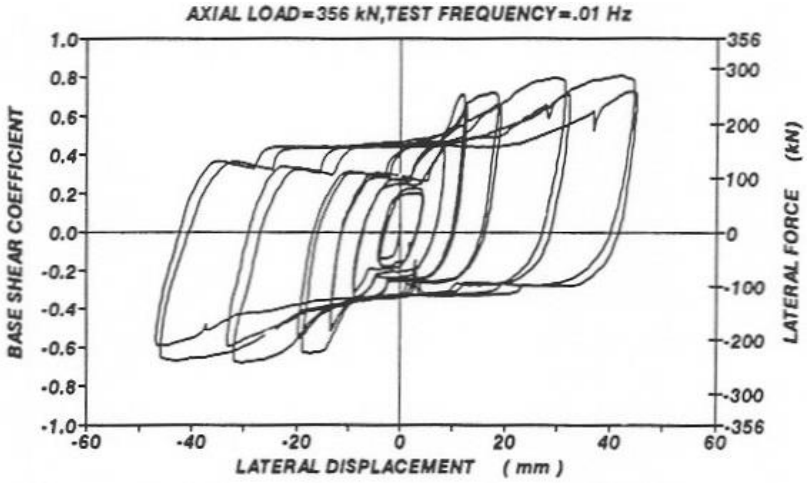

Figure 2.12 Transverse test results for the high type fixed bearings on a concrete pedestal (Mander et al. 1996)

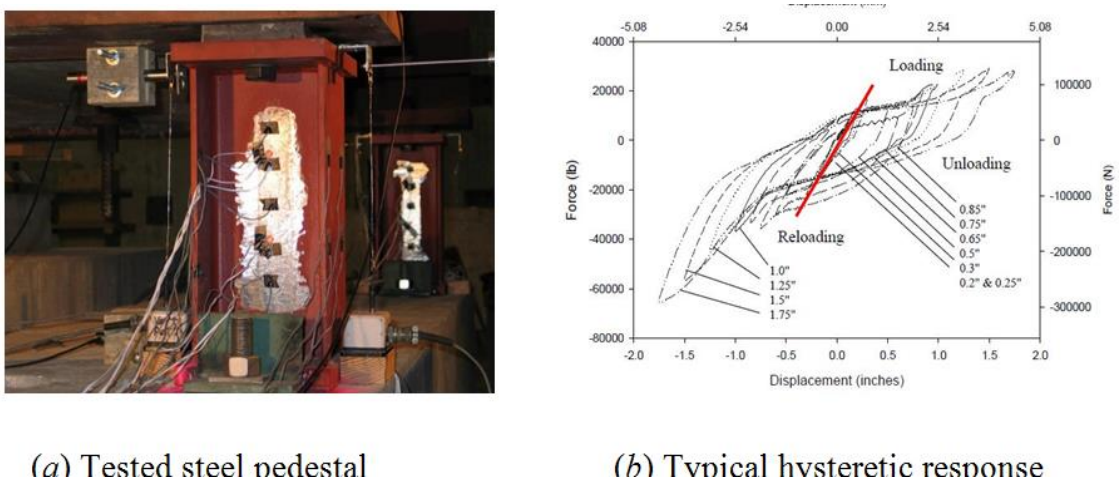

(a) Tested steel pedestal (b) Typical hysteretic response

Figure 2.13 Steel pedestal specimen studied by Hite (2007) and the typical response of the steel pedestal-concrete base assembly

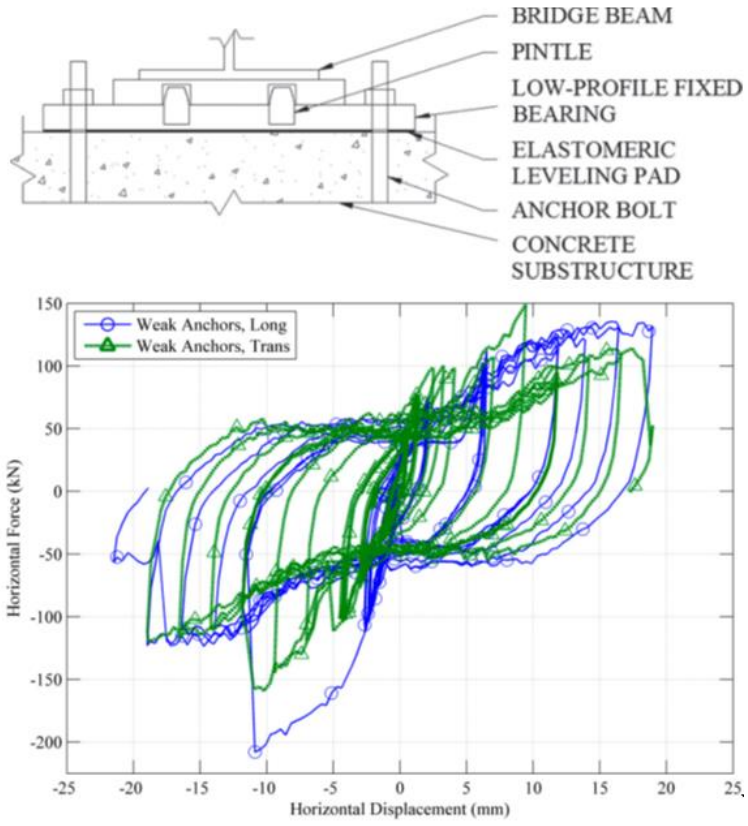

Figure 2.14 Low-type steel bearing and its cyclic behavior under both longitudinal and transverse loading (Steelman et al. 2014)

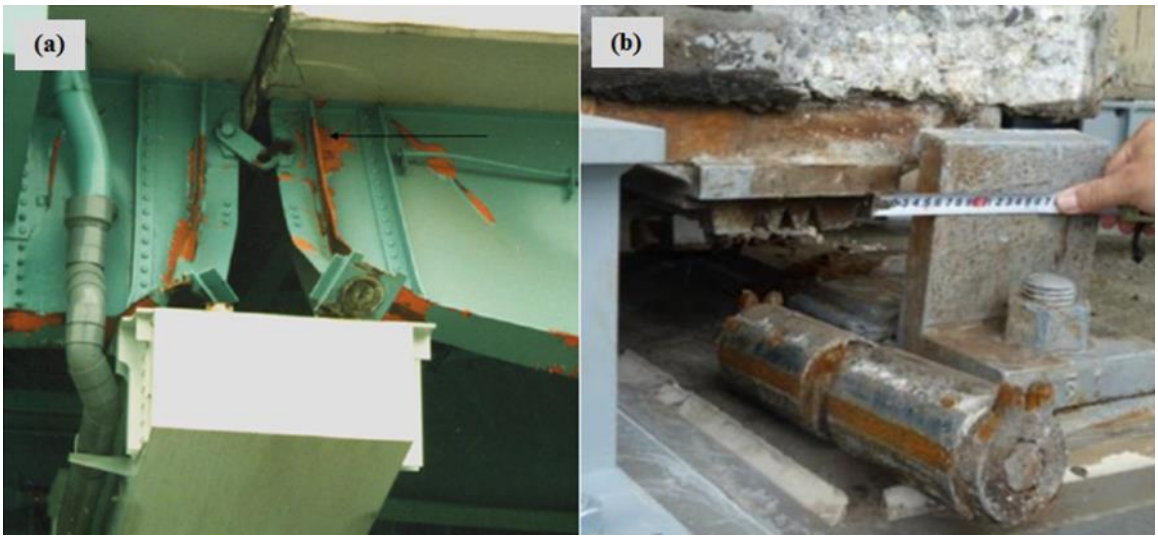

Figure 2.15 Steel bearing failures observed during the: (a) 1995 Kobe earthquake and (b) 2011 Tohoku earthquake

CHAPTER 3 THEORETICAL ANALYSIS OF STEEL BRIDGE BEARINGS

3.1 Introduction

A theoretical analysis of the studied steel bearings is performed to provide a better understanding of the stiffness, stability, and strength of steel rocker and bolster bearings. The longitudinal stiffness and transverse stability of a steel rocker bearing are investigated using rigid body kinematics. Two major failure modes are identified for a steel bolster bearing considering pure shear fracture of the anchor bolts and fracture of the anchor bolts under combined shear and tension due to prying of the bolster bearing body on top of the pedestal. An upper bound analysis is performed to estimate the ultimate lateral strength of the bolster bearing under longitudinal and transverse monotonic loading. The methodologies used in this chapter can be applied to further analyze steel bearings that have other dimensions and configurations. The results obtained from this theoretical study help to validate the finite element models developed in Chapter 4 and further guide the design of the experimental setup (Chapter 6). Findings of this chapter are also presented in Fan and McCormick (2014).

3.2 Rigid Body Kinematics of Steel Rocker Bearings

3.2.1 Longitudinal behavior

The longitudinal behavior of the studied rocker bearings can be determined using rigid body kinematics. The rocker bearing shown in Figure 1.1(b) has two identical top and bottom cylindrical surfaces. To ensure stability, the two cylindrical surfaces do not form a concentric circle, but rather two overlapping circles of radius r. Figure 3.1 provides a free body diagram illustrating the rocker bearing given a small rotation of the rocker body, θ, induced by a longitudinal displacement of the sole plate, u, at the top of the bearing

body. Point C in Figure 3.1 represents the center point of the circle created by the top cylindrical surface while point A is located at the top of this circle where the vertical load is applied in the displaced configuration assuming small displacements. Point E, O, and F represent the top, mid-height, and bottom of the bearing body in its undeformed configuration. As a result, segment AC and CE have lengths equal to the radius, *r*.

Based on equilibrium and the free body diagram shown in Figure 3.1, the following equations are derived:

$$W = N \qquad \text{Equation 3-1}$$

$$H_L = V \qquad \text{Equation 3-2}$$

$$H_L h = Wd \qquad \text{Equation 3-3}$$

where W is the gravity load from the superstructure, N is the total normal reaction at the bottom bearing surface, H_L is the applied horizontal load, V is the resultant horizontal resistance generated at the rocker body-masonry plate interface, d is the horizontal distance between the gravity load and normal reaction due to longitudinal displacement, and h is the distance between the horizontal forces acting at the top and bottom of the bearing.

Considering the displaced geometry of the rocker bearing system, the following relationships are also derived.

For ΔAOC,

$$\sin\alpha/OC = \sin\beta/AC \quad \text{or} \quad \sin\alpha/(r - h_0/2) = \sin\beta/r \qquad \text{Equation 3-4}$$

$$\alpha + \beta + \theta = \pi \qquad \text{Equation 3-5}$$

For ΔAGB,

$$d = h\tan\alpha \qquad \text{Equation 3-6}$$

Assuming small rotations,

$$\sin\alpha \approx \alpha, \text{ and } \sin\beta = \sin(\alpha + \theta) \approx \alpha + \theta \qquad \text{Equation 3-7}$$

Substituting Equation 3-7 into Equation 3-4 gives,

$$\alpha = (2r/h_0 - 1)\theta \qquad \text{Equation 3-8}$$

Then the load-rotation relationship for a longitudinally displaced rocker bearing can be determined by substituting Equation 3-6 and 3-8 into Equation 3-3.

$$H_L = W(2r/h_0 - 1)\theta \qquad \text{Equation 3-9}$$

where h_0 is the height of the rocker body (distance between the vertices at the top and bottom of the bearing body, i.e. line segment EF). Equation 3-9 can be rewritten in terms of the displacement of the sole plate, *u*, considering *u* is a product of θ and h_0 given small rotations.

$$H_L = uW(2r - h_0)/h_0^2 \qquad \text{Equation 3-10}$$

For this derivation, the rocker bearing body is assumed to be rigid. In reality, the rocker bearing body may undergo small changes in geometry due to elastic and inelastic deformation during loading. However, considering the normal contact pressure level under service loads, effects of this geometry change will be small and can be ignored.

Equation 3-10 suggests that the longitudinal stiffness of the rocker bearing is a function of the vertical load, *W*, the radius of the top and bottom contact surfaces, *r*, and the height of the rocker bearing body, h_0. This finding suggests that the longitudinal stiffness should be accounted for to accurately assess the behavior of rocker bearings under seismic loads and that corrosion, which can alter the contact surface, may also influence the longitudinal behavior. However, traditionally the behavior of rocker bearings under longitudinal loading has been modeled as an ideal pin. When studying the seismic response of existing bridges, Hindi and Dicleli (2006) used a 3-D beam pinned on both ends to simplify the longitudinal behavior of a rocker bearing ignoring its longitudinal stiffness as derived herein. It also should be noted that the longitudinal displacement

capacity of the rocker bearing is conditioned upon the arc length of the top and bottom cylindrical surfaces of the rocker body.

3.2.2 Transverse behavior

The transverse kinematics of the rocker bearing under lateral load consists of two phases. The first phase is rigid sliding between the sole plate and the rocker body with Coulomb friction under smaller lateral loads. The second phase begins when the pintle hole clearance is exhausted as a result of sliding and the pintles on both the top and bottom of the rocker body engage and resist the applied lateral load. At this point, the rocker body still maintains its upright position without tipping. However, as the lateral load, $H_{T,}$ increases, the overturning moment created by the lateral load also increases. Since the gravity load, W, remains constant during lateral loading, the vertical reaction force, N, will shift toward opposite ends of the rocker body to increase the moment arm between these two forces and balance the overturning moment. Figure 3.2 shows the general case of a transversely displaced rocker bearing with the angle, α, disproportionately exaggerated. The lateral load can be expressed by Equation 3-11 based on equilibrium.

$$H_T = W(w_0 - h_0\alpha)/(h_0 + w_0\alpha) \qquad \text{Equation 3-11}$$

From Equation 3-11, the critical state for instability can be found when α is zero, which yields the maximum transverse resistance. The transverse load capacity is then given by Equation 3-12.

$$H_{Tcritical} = W(w_0/h_0) \qquad \text{Equation 3-12}$$

Equation 3-12 shows that the maximum applied transverse lateral load is a function of the vertical load, W; width, w_0; and height, h_0, of the rocker bearing body.

Another possible failure mode for a transversely loaded rocker bearing is failure of the anchor bolts or pintles under shear provided that the shear force required does not exceed the load capacity obtained from Equation 3-12. Based on the definition of this alternative failure mode, the following equation is established to find the maximum lateral shear capacity of the rocker bearing.

$$H_{shear} = \min\{n_p V_p,\ \ n_b V_b\} + \mu_1 W \qquad \text{Equation 3-13}$$

where, H_{shear} is the shear capacity of a rocker bearing determined by the smaller value between the pintle shear capacity and the anchor bolt shear capacity; V_p and V_b are the shear capacity of a pintle and an anchor bolt, respectively; μ_1 is the friction coefficient at either the pintle or the anchor bolt shear interface; and n_p and n_b are the total number of pintles or anchor bolts (both values are 2 for the studied rocker bearing).

The transverse load capacity of the rocker bearing is finally determined by the smaller value between the results from Equation 3-12 and 3-13.

3.3 Upper Bound Plastic Analysis of Steel Bolster Bearings

The strength of the studied bolster bearings under lateral loading in the two orthogonal directions, longitudinal and transverse, can be inferred by considering potential failure modes based on the load path through the bolster bearing assembly. In this study, two similar failure modes are identified for the bolster bearing in either loading direction. The first failure mode is dictated by rocking and prying of the bolster bearing body together with the masonry plate on top of the pedestal, for which a plastic mechanism analysis method, consistent with that proposed by Mander et al. (1996), is adopted for deriving the corresponding maximum strength at the failure state. The second failure mode is governed by shear failure at either the sole plate-bolster bearing body contact interface, where the shear capacity comes from friction and the shear resistance of the pintles, or the masonry plate and concrete pedestal interface, where the shear resistance derives from the anchor bolts and sliding friction.

3.3.1 Longitudinal behavior

Considering longitudinal loading, the free body diagram of a bolster bearing when rocking and prying occur is provided in Figure 3.3, where the ultimate state is defined as when the anchor bolt reaches its maximum strength under combined tension and shear and a yield stress block develops on the compression side of the masonry plate.

Equilibrium of the bolster bearing based on the state shown in Figure 3.3 gives Equation 3-14, 3-15, and 3-16. The definition of the ultimate state also produces Equation 3-17 assuming the amplitude of the stress block acting on the masonry plate is determined by the yield stress (i.e. σ_y) of the masonry plate or compression strength (i.e. $0.85f_c'$) of the concrete pedestal. It should be noted that when a steel bolster bearing is mounted on top of a steel pedestal with a higher yield stress, the yield stress of the masonry plate (σ_y) governs the stress block amplitude. However, when a steel bolster bearing is anchored to a reinforced concrete pedestal, the concrete compression strength ($0.85f_c'$) dictates the stress block amplitude.

$$H = 2V_b + \mu C \qquad \text{Equation 3-14}$$

$$C = W + 2T_b \qquad \text{Equation 3-15}$$

$$Hh_b = C(w_m - a)/2 \qquad \text{Equation 3-16}$$

$$C = \sigma_y a l_m \text{ or } 0.85f_c' a l_m \qquad \text{Equation 3-17}$$

In the above equations, H is the applied longitudinal load; W is the superstructure gravity load; C is the resultant force from the masonry plate bearing on the pedestal; μ is the friction coefficient between the masonry plate and concrete pedestal; T_b and V_b are the tensile and shear forces acting on the bolt; h_b is the height of the bolster; a is the width of the stress block; and w_m and l_m are the width and length of the masonry plate, respectively.

To consider the combined shear and tension acting on the anchor bolts, the finding by Kulak et al. (2001) is adopted, which gives the following elliptical relationship for the interaction between the tensile stress and shear stress in a bolt:

$$(f_t/F_u)^2 + (f_v/(0.62F_u))^2 = 1 \qquad \text{Equation 3-18}$$

where f_t is the tensile stress, f_v is the shear stress at the shear plane, and F_u is the tensile strength of the bolt. Equations 3-14 through 3-18 can be used to solve for the maximum strength of the limit state associated with rocking and prying of a bolster bearing under longitudinal loading.

3.3.2 Transverse behavior

Considering transverse loading, the ultimate state of the first failure mode is defined as when the anchor bolt on the tension side fails under combined tension and shear and a stress block forms in the masonry plate at the compression side. It is assumed that the shear force at the base of the bolster assembly is resisted completely by the anchor bolts and friction between the masonry plate and pedestal. Equations 3-19, 3-20, and 3-21 are derived based on equilibrium of the free body diagram shown in Figure 3.4. Similar to the longitudinal loading scenario, Equation 3-22 is derived considering the governing resultant force of the stress block:

$$C = W + T_b \qquad \text{Equation 3-19}$$

$$H = 2V_b + \mu C \qquad \text{Equation 3-20}$$

$$Hh_b + Wl_1 = C(l_1 + (l_m - a)/2) \qquad \text{Equation 3-21}$$

$$C = \sigma_y a w_m \; or \; 0.85 f_c' a w_m \qquad \text{Equation 3-22}$$

where l_1 is the distance between the center lines of the anchor bolt and the bolster bearing body. For the combined tension and shear acting on the anchor bolt, Equation 3-18 remains applicable. Based on the governing Equations 3-18 to 3-22, the maximum strength of the bolster bearing under transverse loading can be determined for the limit state of rocking and prying.

For loading in both the longitudinal and transverse directions, the maximum strength corresponding to rocking and prying needs to be compared to the maximum shear resistance obtained from considering shear failure at either the sole plate-bolster bearing body interface or the masonry plate-concrete pedestal interface, whichever is smaller. This failure mode yields an identical shear capacity regardless of the loading direction due to the fact that in either loading direction the shear resistance at the interface comes from either the two pintles or the two anchor bolts in addition to friction. Moreover, this shear failure mode of the bolster bearing is consistent with that of the rocker bearing when loaded transversely and can be determined by the same equation, i.e. Equation 3-13.

In the above calculations, a perfect bond is assumed between the anchor bolts and the concrete pedestal. Although this may not be the case, the above equations were derived to consider the behavior of the steel bearings and not anchorage failure under large cyclic loads. It is assumed proper installation and design would minimize anchorage pullout.

3.4 Case Study

The bearings considered as part of this study are from the Meridian Road bridge (Figure 1.2) along the Rockford Bypass in Illinois that was approved for construction in 1964. It is a steel girder bridge consisting of three wall piers and two abutments. The rocker and bolster bearings to be considered are shown in Figure 3.5 and Figure 3.6, respectively, along with their detailed dimension information. The capacity of these bearings will first be considered based on the previously discussed analyses. The gravity load acting on the bearings is assumed to be 205 kN based on the configuration of the studied bridge. For illustration purposes, the friction coefficient is set at 0.2 for all of the contact interfaces associated with the bearings given the findings of McCormick et al. (2009) and Steelman et al. (2014). Considering the variability of the diameter of in-situ anchor bolt, two cases are calculated where the anchor bolt diameter is taken as 25.4 mm and 38.1 mm, respectively. More information regarding the rocker and bolster bearings considered in this case study is provided in Table 3.1 and 3.2, respectively.

For the rocker bearing, the longitudinal response can be determined using Equation 3-10. The results provide a linear relationship between the horizontal capacity and displacement where the longitudinal stiffness is 0.84 kN/mm. Likewise, the load at which the rocker bearing becomes unstable in the transverse direction can be calculated based on Equation 3-12 while Equation 3-13 estimates the transverse capacity associated with the shear resistance of the top and bottom sliding interfaces. Considering the width and height of the bearing and the 205 kN gravity load, the theoretical transverse load at which the bearing undergoes rocking and becomes unstable is 231 kN. This value is much smaller compared to the capacity determined by Equation 3-13 considering the shear resistance of the pintles and bolts.

Table 3.1 Rocker bearing parameters used for the case study

Rocker bearing				Bolt		Pintle		Load
w_0 (mm)	h_0 (mm)	r (mm)	μ_1	d_{bolt} (mm)	σ_u (MPa)	d_{pintle} (mm)	σ_u (MPa)	W (kN)
318	283	305	0.2	25.4 38.1	413	31.8	413	205

Table 3.2 Bolster bearing parameters used for case study

Bolster bearing				Bolt		Pintle		Load
w_m (mm)	l_m (mm)	h_b (mm)	l_1 (mm)	d_{bolt} (mm)	σ_u (MPa)	d_{pintle} (mm)	σ_u (MPa)	W (kN)
229	483	343	197	25.4 38.1	413	31.8	413	205

For the bolster bearing, the limit state of combined rocking and prying can be determined from Equations 3-14 to 3-18 and Equations 3-18 to 3-22 for the longitudinal and transverse directions, respectively. Substituting in the parameters (Table 3.2) gives lateral load capacities of 351 kN and 442 kN for longitudinal and transverse loading. The limit state of shear at the sole plate-bearing body interface can also be calculated based on Equation 3-13 resulting in a capacity of 447 kN for both longitudinal and transverse loading. The results suggest that rocking and prying dictate the failure of the bolster bearing, rather than shearing of the pintles at the top of the bearing. It should be noted that a diameter of 38 mm is used for the anchor bolts in the above calculations. The diameter of the anchor bolts used will directly affect the result of Equation 3-13 since the bolt diameter needs to be compared with that of the pintles. Table 3.3 provides further results considering the bolt diameter as a variable.

Table 3.3 Strength and failure mode of the bolster bearing

Bolster bearing analysis		Combined shear and tension failure mode		Shear failure mode	
		Longitudinal	*Transverse*	*Pintle*	*Bolt*
d_{bolt}	25.4 mm	192 kN	226 kN	447 kN	301 kN
	38.1 mm	351 kN	442 kN	447 kN	626 kN

3.5 Summary

Analytical studies are performed for both the steel rocker and bolster bearings to provide a means of estimating the mechanical strength of the bearings and identifying potential failure modes. In determining the behavior of the steel rocker bearing, rigid body kinematics is applied to derive equations that can calculate the longitudinal stiffness and transverse bearing capacity. Toppling due to excessive lateral displacement is identified as the main failure mode for the steel rocker bearing in both loading directions. On the other hand, upper bound plastic analyses are conducted for the bolster bearing to establish a set of equations that can approximate the strength of the bearing in either loading direction considering the failure mode as prying of the bearing body and failure of the anchor bolt under combined tension and shear. The shear failure of either pintles or anchor bolts is recognized as a second potential failure mode for the bolster bearing under larger lateral loads. The equations proposed in this chapter are versatile in estimating the lateral capacity of the steel bearings in that they allow the user to define a variety of variables regarding loading direction, bearing dimensions, material properties, bolt size, and the substructure type supporting the bearings of interest.

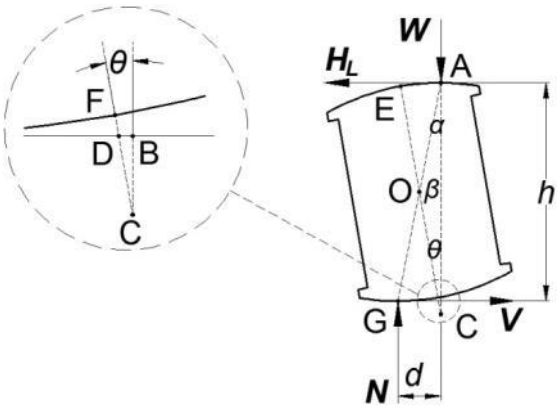

Figure 3.1 Free body diagram of a longitudinally displaced rocker bearing

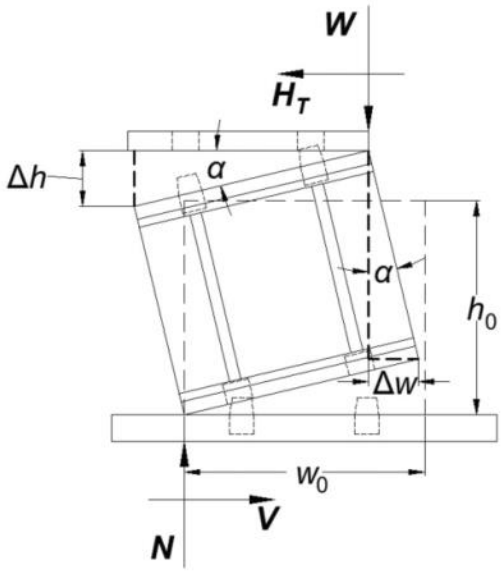

Figure 3.2 Free body diagram for determining the critical applied load for a rocker bearing displaced in the transverse direction

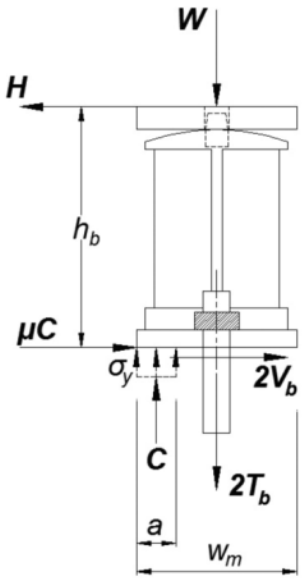

Figure 3.3 Free body diagram of a bolster bearing at its ultimate state under longitudinal loading

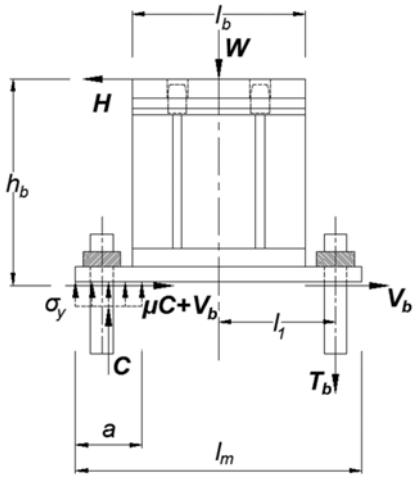

Figure 3.4 Free body diagram of a bolster bearing at its ultimate state under transverse loading

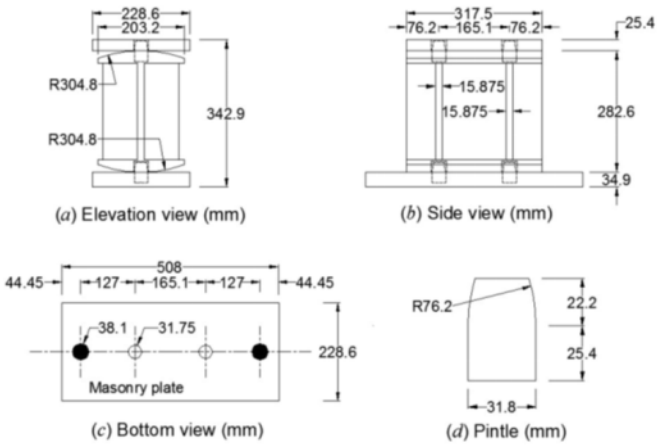

Figure 3.5 Dimensions of the studied rocker bearing and its components

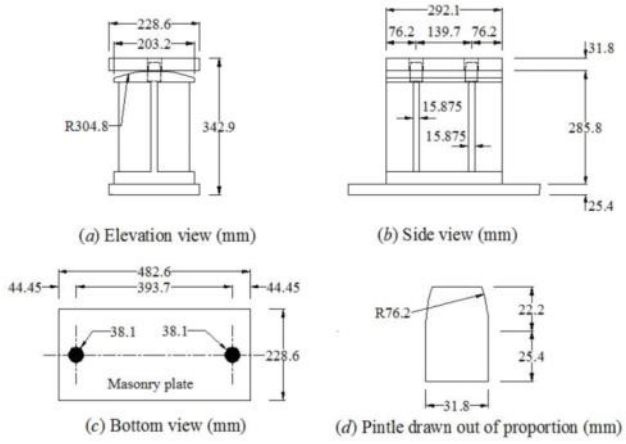

Figure 3.6 Dimensions of the studied bolster bearing and its components

CHAPTER 4 FINITE ELEMENT MODELING OF STEEL BRIDGE BEARINGS

4.1 Introduction

Past studies of bridges have considered a variety of bearing types including elastomeric bearings (Ghobarah and Ali 1988, Makris and Zhang 2004), sliding bearings (Su et al. 1989, Park et al. 2002), friction pendulum bearings (Dicleli et al. 2003, Mosqueda et al. 2004), and steel bearings (Choi et al. 2004). Existing models of steel bearings were achieved mainly through phenomenological models that match experimental data, while almost no studies have used finite element modeling for predicting the behavior of steel bearings. Prior to the experimental work of Mander et al. (1996), researchers focused on analytical models for the behavior of the bearings considering only the stiffness of the bearing assemblages. Dicleli and Bruneau (1995a and 1995b) adopted springs connected in series to model the fixed and expansion bearings in their numerical models of single-span simply supported and continuous bridges as well as multi-span simply supported bridges. A stiffness analysis of an idealized bearing is used to calculate the stiffness used for the springs in the model. Rashidi and Saadeghvaziri (1997) proposed a combination of truss elements to model steel bearings for the seismic evaluation of bridges in New Jersey. Instead of a stiffness analysis, they numerically derived the stiffness of a bearing assemblage by developing 2-dimensional finite element models in ADINA for each subcomponent of the bearing. However, due to the susceptibility of the predicted behavior of bridge models to the bearing model, the accuracy and effect of this simplification in obtaining the bearing stiffness is questionable. Use of truss or spring elements in modeling bridge steel bearings can also be found in Saadeghvaziri and Rashidi (1998), Choi et al. (2004), DesRoches et al. (2004), Nielson and DesRoches (2006), and Pan et al. (2010). However, only Saadeghvaziri and Rashidi (1998) used a theoretical analysis to derive the stiffness. The rest of these studies obtained parameters for the models based on experimental data obtained by Mander et al. (1996). A recent

study conducted using both experiments and numerical modeling by Filipov et al. (2013a and 2013b) and Steelman et al. (2014) led to a set of macro models based on experimental results from cyclic testing of low-type steel fixed bearings that have been implemented in the OpenSees platform (McKenna et al. 2000). However, there is still a lack of accurate models and means of capturing the behavior of other bearing configurations.

Because a large number of steel bearings exist in today's bridge inventory and the behavior of these bearings is susceptible to changes in the friction coefficients and surface loss due to aging and configuration variations, an experimental approach alone is not economically feasible for evaluating the seismic performance of the whole bridge inventory. As a result, there is a need for more accurate finite element steel bearing models as an alternative to evaluate steel bearing and bridge behavior. To address this, the commercial finite element software package ABAQUS (DS-Simulia 2008) is used to model and analyze the nonlinear behavior of steel bearings under longitudinal and transverse cyclic loads. All subcomponents of the modeled bearings (sole plate, pintles, bearing body, masonry plate, anchor bolts, and concrete pedestal) are considered in the finite element model (Figure 4.1). A loading beam with an identical cross-section to that of an actual bridge girder is modeled to apply the horizontal cyclic loading. The modeled bearings are based on those used for the case study performed in Chapter 3 as shown in Figure 3.5 and Figure 3.6. The finite element models account for nonlinearities due to yielding, contact, and friction. Validation of the finite element models of the steel rocker and bolster bearings is achieved through comparison with the previous theoretical analyses described in Chapter 3. The results provide a further understanding of the bearing behavior and are instrumental in guiding the experimental study that follows. Findings presented in this chapter can also be found in Fan and McCormick (2014).

4.2 Modeling Procedure

4.2.1 Material model

The studied steel bearings (Figure 3.5 and Figure 3.6) were manufactured with ASTM A36 steel that has a minimum required yield strength of 248 MPa and a Young's modulus of 200 GPa. A bilinear constitutive material relationship considering elastic-plastic behavior with strain hardening is adopted for the entire bearing assemblage including the sole plate, pintles, bearing body, bolts, and masonry plate (Figure 4.2). The post-yielding stiffness of this bilinear material model is 1112 MPa. The concrete pedestal is modeled as elastic in order to focus on the load-displacement behavior of the bearings rather than potential failure patterns associated with the concrete pedestal (i.e. corner concrete breakout or bolt pull-out). An elastic stiffness of 15 GPa is used for the concrete material model, considering the concrete compression strength of 10 MPa specified in the original bridge design. The loading beam is modeled as a rigid beam considering that the rigidity of the bridge superstructure is significantly larger than that of the studied bearings.

4.2.2 Model description

The mechanisms that allow rotation and translation of a rocker bearing and rotation about a bolster bearing result from the contact interfaces between components of the bearing assembly. The contact interfaces in a bolster and rocker bearing assembly include the: (1) pintle-sole plate interface; (2) sole plate-bearing body interface; (3) bearing body-masonry plate interface (rocker bearing only); (4) masonry plate-pedestal interface; (5) anchor bolt-pedestal interface; and (6) anchor bolt-masonry plate interface (Figure 2.5). These contact interfaces consist of either steel-steel interfaces or steel-concrete interfaces. Figure 4.3 illustrates one steel-steel interface that exists in between the masonry plate and bottom surface of the rocker bearing body.

Previous studies modeling bolted connections have shown the effectiveness and accuracy of using finite element models with reduced integration elements to capture the contact behavior between solid bodies (Van de Vegte and Makino 2004, Sarraj et al. 2007, and

Garlock and Selamet 2010). Contact pairs are adopted for modeling the steel bearing assemblages allowing contact interaction to be established between a pair of contact surfaces on two individual bodies. Two types of behavior are defined at the contact interface in the normal direction and tangential direction. The normal behavior dictates how pressure is transferred between the two bodies in contact and after separation, while the tangential behavior determines the magnitude of the relative slip as well as whether friction is developed between the two surfaces in contact. In the normal direction, "hard contact" is assumed, which prevents penetration of the bodies in contact. Contact constraints are removed once the contact compression force becomes zero or negative indicating a separation of the contact surface pair. A classic isotropic Coulomb friction model is assumed for the tangential behavior, which permits slip when the equivalent friction stress surpasses the critical stress determined by the product of the friction coefficient and the contact pressure. Since the steel bearings can undergo large cyclic displacements under seismic loads, a finite sliding algorithm is adopted in the models for tracking contact. The finite sliding formulation allows for arbitrary sliding, rotation, and separation of the contacting surfaces, while updating the connectivity of the active contact regions based on the feedback from the relative tangential motion of the surfaces in contact (DS-Simulia 2008).

Solid elements are chosen to model the bearings, loading beam, and pedestal. Element type selection plays a key role in obtaining an accurate and converging solution when considering nonlinear contact mechanics between the rocking and sliding interfaces as well as between other contact surfaces (i.e. pintles and anchor bolts) (Bursi and Jaspart 1998). First-order continuum hexahedral brick elements with incompatible modes (C3D8I) are chosen to model all interfaces involving contact and friction. Compared with the fully-integrated brick element C3D8, the C3D8I element has thirteen additional degrees of freedom relating to the incompatible modes, which help to improve bending behavior by eliminating the parasitic shear stresses pertaining to first-order elements. This type of element uses full integration and thus has no hourglass phenomena (DS-Simulia 2008). However, the C3D8I element requires more computation time than the full-integration eight-node brick element, C3D8, and the reduced-integration element, C3D8R, due to the additional degrees of freedom. Thus, C3D8R elements are adopted for

modeling the loading beam and the main bearing body since modeling contact is not necessary for these components and stress concentrations are not expected to occur at these locations.

4.2.3 Loading and boundary conditions

Gravity loads acting on the rocker and bolster bearings at different pier locations of the Meridian bridge are calculated based on tributary area. Given the Meridian bridge configuration (see Section 1.2), the calculated gravity loads range from 47 kN at the exterior girder at the abutment to 205 kN for an interior bearing on a pier. Table 4.1 provides the calculations for all dead loads of any bearing of the bridge. The superstructure consisting of steel girders and a concrete slab is assumed to be rigid so that the same displacements are transferred to each bearing as the superstructure displaces laterally. Given the rigidity of the superstructure, it is also assumed to remain horizontal during loading. As a result, the loading beam is restrained in all of the rotational degrees of freedom and the sole plate is rigidly attached to the underside of the girder to ensure accurate loading of the bearings. In the model, the concrete pedestal is assumed fully fixed at its base to focus on the behavior of the bearing rather than the substructure. The cyclic longitudinal or transverse loading is applied as equal loading cycles or incrementally increasing cycles to gain an understanding of the expected behavior of the bearings under seismic loads.

Table 4.1 Dead loads acting on the Meridian bridge bearings based on location

Long. Pos. / Trans. Pos.	Left Abutment		Left Pier	Middle Pier	Right Pier	Right Abutment	
Span length (m)	--	14.0	17.8	17.8	14.0	--	
Exterior span (kN)	47		107	119	107	47	
Interior span (kN)	81		183	205	183	81	

4.2.4 Other modeling details

In modeling the steel bolster and rocker bearings, six contact interfaces are considered. However, a typical rocker bearing can have as many as thirteen independent contact

interfaces while a bolster bearing can have ten pairs of contact surfaces. A single anchor bolt has three independent contact interfaces (Figure 4.4): one with the masonry plate, one with the interior of the bolt hole in the masonry plate, and one due to embedment in the concrete pedestal. Past research has shown that more contact interfaces in a FE model leads to difficulties in achieving a converged solution due to the increase in displacement boundary nonlinearities induced in the model (Bursi and Jaspart 1998, Wheeler et al. 2000, Citipitioglu et al. 2002, and Swanson et al. 2002). Moreover, the FE models in this study utilize 3-dimensional, 8-node continuum brick elements that require a significant amount of computation time and storage. Thus, it is necessary to consider simplified modeling details to reduce the number of contact interfaces.

To reduce computation time and ensure a converged solution while also minimizing impacts on the accuracy of the model, some modeling assumptions are made. Contact interfaces involving the anchor bolts are assumed to be rigidly tied to their counterparts on the masonry plate. Even though slip of the anchor bolts is restrained, this assumption is deemed acceptable since the focus is on the behavior of the bearing and not the anchorage. Considering longitudinal loading of a rocker bearing, the effect of the pedestal and anchor bolts on the overall behavior of the rocker is negligible since no rocking or prying of the masonry plate is expected to be induced given the lack of a moment connection at the bottom of the bearing body. As a result, the pedestal and anchor bolts are neglected in the rocker bearing model to accelerate the solution process under longitudinal loading.

4.3 Steel Rocker Bearing Behavior

4.3.1 Longitudinal response of the rocker bearing

To consider the general cyclic behavior of steel rocker bearings, a constant gravity load of 205 kN is applied as an evenly distributed vertical load acting on the sole plate simulating the dead load acting on a typical interior bearing (Table 4.1). The friction coefficient is taken as 0.2 at all steel-steel interfaces, consistent with findings by Mander et al. (1996) and Steelman et al. (2014). Two cyclic loading patterns are applied in

displacement control to consider the behavior under both equal and increasing displacement magnitudes.

Figure 4.5(a) presents the behavior of the rocker bearing under five loading cycles to a magnitude of 50.8 mm. A linear relationship is observed between the horizontal resistance and longitudinal displacement with minor deviations during loading. Overall, the response of the rocker bearing is symmetric reaching a maximum absolute horizontal load of 44 kN at a displacement of 50.8 mm in both the positive and negative directions. The cyclic behavior of the rocker bearing exhibits a steady and identical response under all five loading cycles. The linear load-displacement relationship also indicates that the rocker bearing has a constant longitudinal stiffness, 0.88 kN/mm, which is contrary to the way rocker bearings are often modeled in bridge systems. A similar behavior is observed when considering the response of the rocker bearing under increasing displacement cycles of 10.2 mm, 20.3 mm, 30.5 mm, 40.6 mm, and 50.8 mm as shown in Figure 4.5(b). No degradation in stiffness is observed under both loading patterns. These observations suggest that the cyclic behavior of the rocker bearing can be modeled as elastic for simplicity, while still maintaining accuracy. Further, the finite element results suggest a displacement capacity equal to or greater than 50.8 mm. This value is a significant longitudinal displacement for highway bridges found in the Central and Eastern United States.

Equation 3-10 establishes a linear relationship between the applied longitudinal load and the longitudinal displacement for the rocker bearing, showing the stiffness as only a function of the vertical load level and the geometry of the rocker bearing. Similar observations are made from the finite element results. Figure 4.5(a) presents a comparison between the theoretical prediction and numerical results. As discussed previously, the rocker bearing under a gravity load of 205 kN has a theoretical stiffness of 0.84 kN/mm and a load capacity of 43 kN when the lateral displacement magnitude is 50.8 mm. Good agreement is found between the stiffness and load capacity predictions from the finite element model and theoretical analysis. This agreement further validates the accuracy of the finite element model in simulating the longitudinal cyclic behavior of the steel rocker bearings.

A pair of parametric studies is conducted to consider the effects of the friction coefficient and gravity load on the longitudinal behavior of rocker bearings to gain an understanding of how corrosion and bridge type may change their seismic performance. One displacement cycle to 50.8 mm is used to study the friction coefficient and gravity load effects. As shown in Figure 4.6(a), the friction coefficient at the steel-steel contact interfaces has little influence on the longitudinal behavior of the rocker bearing. For the considered friction coefficients, 0.2, 0.3, and 0.4, the cyclic response of the rocker bearing remains the same with nearly identical longitudinal stiffness values of 0.88 kN/mm, 0.88 kN/mm, and 0.89 kN/mm. This observation results from the fact that the longitudinal displacement of the rocker bearing is governed by rolling of the rocker body about its two cylindrical surfaces. Figure 4.6(b), which provides the load-displacement behavior under different gravity loads, further confirms the fact that rolling dictates the behavior as the longitudinal cyclic response of the rocker bearing is linearly proportional to the vertical load level. The maximum load levels reached for each gravity load level (102 kN, 154 kN, and 205 kN) are 22 kN, 33 kN, and 44 kN, respectively. As a result, larger stiffness values are observed for larger vertical loads, 0.44 kN/mm for a gravity load of 102 kN versus 0.88 kN/mm for a gravity load of 205 kN. Figure 4.6 demonstrates that the longitudinal stiffness is not influenced by the friction coefficient, but is linearly proportional to the gravity load level. The findings suggest that aging in terms of influencing the friction coefficient will have little effect on the seismic performance of rocker bearings. However, debris buildup or locking due to corrosion could significantly alter the initial cycles and section loss at the contact interface could affect the overall rolling behavior.

4.3.2 Transverse response of the rocker bearing

The transverse behavior of the rocker bearing also is considered using the finite element model under constant and increasing magnitude cycles. A constant vertical load of 205 kN and a friction coefficient of 0.2 for all steel-steel interfaces are adopted for both loading scenarios to gain an understanding of the seismic performance of the rocker bearing under transverse loading.

Figure 4.7(a) shows the cyclic behavior of the rocker bearing for four displacement cycles to a magnitude of 3.18 mm. This displacement is chosen because it is greater than the gap around the top and bottom pintles. Figure 4.7(a) shows that rigid sliding dominates the cyclic response of the rocker bearing, allowing the gap around the pintles to be exhausted during loading and the pintles to engage. In general, the cyclic behavior is symmetric showing a consistent maximum resistance with each cycle. The resistances in the positive and negative directions are 97 kN and 98 kN, respectively, at the maximum displacement level of 3.18 mm. The sudden increase in resistance when the displacement reaches roughly 2.5 mm occurs when the pintles engage in resisting lateral load through shear. The only difference between cycles occurs after the first loading cycle when the rocker bearing first engages the pintles at an earlier displacement. The subsequent cyclic response following the first cycle shows a slightly longer sliding plateau, approximately 0.5 mm in each direction, which is due to the plastic deformation of the pintles during the initial loading cycle.

Figure 4.7(b) presents the results of the rocker bearing under four loading cycles to displacement magnitudes of 1.59 mm, 3.18 mm, 3.81 mm, and 5.08 mm. It should be noted that the rocker bearing can only accommodate transverse displacements due to thermal expansion and contraction up to 3.18 mm and are not designed to undergo large transverse displacements. Thus, a transverse displacement of 5.08 mm is large for the rocker bearings as reflected in Figure 4.7(b) by the rocker bearing reaching an unstable state due to loss of stiffness at this displacement level. In addition to exhibiting symmetric behavior, the cyclic response of the rocker bearing under progressively increasing displacement cycles shows sliding within a displacement range of 3.0 mm. The increasing length of the sliding plateau is attributed to accumulation of plastic deformation of the pintles. After this displacement is reached, a rapid increase in resistance is observed due to the shear resistance of the pintles. For each cycle, the maximum transverse load reached is 44 kN, 95 kN, 180 kN, and 207 kN. As the displacement increases further, the stiffness of the rocker bearing gradually decreases to nearly zero owing to overturning. The findings suggest that a similar behavior will be obtained from equal and unequal loading cycles.

Based on Equation 3-12, the transverse resistance of the rocker bearing is only a function of the applied gravity load and the geometry of the bearing. Considering this formulation, the theoretical ultimate capacity can be compared to the finite element analysis results for the case where the friction coefficient is 0.2 and gravity load is 205 kN. Both the theoretical findings and numerical maximum resistance are similar, 231 kN and 225 kN, respectively. The small difference in these values can be associated with the rigid body assumption made in the theoretical derivation and the results suggest that the finite element model can be used for further consideration of the bearing behavior.

The effect of the friction coefficient (0.2, 0.3, and 0.4) and gravity load (102 kN, 154 kN, and 205 kN) on the transverse behavior of the rocker bearing are again considered based on the response to a single 3.18 mm magnitude cycle. Figure 4.8(a) shows that the transverse resistance of the rocker bearing is directly proportional to the friction coefficient for a constant gravity load. This result suggests that sliding dominates the behavior until overturning initiates. In addition, the sliding resistance corresponding to each of the plateaus between displacements of 0.5 mm and 2.5 mm is equal to the product of the gravity load and friction coefficient, which are 44 kN, 66 kN, and 88 kN, respectively. The initial transverse stiffness of the rocker bearing is much larger than the longitudinal stiffness and varied between 289 kN/mm and 427 kN/mm for the different friction coefficient values. This variation can be attributed to how the friction model is implemented in the finite element analysis program. The responses shown in Figure 4.8(b) indicate that under a constant friction coefficient, the sliding resistance is linearly proportional to the gravity load level. The sliding resistance increases from 22 kN to 33 kN to 44 kN with an increase in gravity load. Moreover, it is found that the initial stiffness of the rocker bearing varied between 173 kN/mm to 289 kN/mm for the different gravity load levels. The findings of the study of the transverse rocker bearing behavior suggests at small displacements the behavior is dominated by sliding, which means changes in the friction coefficient induced by corrosion can have a significant impact on the transverse response of a rocker bearing during an earthquake.

4.4 Steel Bolster Bearing Behavior

4.4.1 Longitudinal response of the bolster bearing

Similar to the rocker bearing analysis, a constant gravity load of 205 kN and a friction coefficient of 0.2 are adopted for studying the longitudinal behavior of the bolster bearing. Two types of loading scenarios including equal and increasing displacement magnitude cycles are considered for better understanding the cyclic behavior of the bolster bearing.

Figure 4.9(a) shows the longitudinal response of a steel bolster bearing under four equal magnitude loading cycles to 10.2 mm. The general response is symmetric with loading plateaus within the hysteretic loops. The longitudinal force at these plateaus can be attributed to sliding friction and equals 40 kN. This value is the product of the gravity load and friction coefficient. The length of the plateau increases with each cycle due to the accumulation of plastic deformation in the pintles at the top of the bearing body, where as much as 3 mm of shear deformation is observed. The increase in stiffness at larger displacements is due to the pintles contacting the sole plate leading to further lateral load resistance and overall rocking of the bearing and prying on the anchor bolts. As a result of the rocking and prying, the anchor bolts become involved in the lateral resistance of the bearing assembly. It is found that the maximum resistance in each half loading cycle occurs at the largest displacement magnitude of 10.2 mm. The first loading cycle in the positive direction yields a maximum resistance of 306 kN. This resistance is lower than those for subsequent cycles where the maximum resistance is approximately constant at 345 kN. Strain hardening and not fully yielding the pintles during the initial cycle leads to the lower first cycle maximum load. The secant stiffness for each half cycle response remains nearly constant at 33 kN/mm with slight variations indicating little degradation in the load capacity of the bolster bearing under repeated lateral loading. The findings show that cycling effects mainly influence the length of the sliding plateau due to permanent deformation of the pintle provided the cycles are large enough to engage the pintle. Little effect is seen on the capacity of the bearing.

Figure 4.9(b) presents the cyclic response of the bolster bearing under displacement cycles with progressively increasing magnitudes of 1.6 mm, 3.2 mm, 6.4 mm, 9.5 mm, and 12.7 mm. A symmetric response again is observed. As with the equal loading cycles, plateaus occur in both the positive and negative loading directions. The resistance at the plateau is again found to be 40 kN due to sliding friction at the sole plate-bolster body interface. Further, this plateau gradually elongates with increasing displacement levels owing to plastic deformation of the pintles. The absolute maximum resistance attained in each loading cycle also increases from 56 kN to 166 kN to 289 kN to 333 kN to 353 kN as the displacement level increases. In addition, a slight degradation in the secant stiffness of the force-displacement response is observed during both the positive and negative portion of the cycles. The secant stiffness values associated with the positive cycles to 6.4 mm, 9.5 mm, and 12.7 mm are 42 kN/mm, 33 kN/mm, and 27 kN/mm while those with the negative cycles are 45 kN/mm, 35 kN/mm, and 27 kN/mm. The findings suggest that the displacement level has a significant effect on the longitudinal behavior of the bolster bearing in terms of secant stiffness and load capacity, particularly when transitioning from smaller cycles to larger cycles.

Considering a gravity load of 205 kN and friction coefficient of 0.2, Equations 3-14 through 3-18 are applied to solve for the maximum bolster bearing load capacity under longitudinal loading. The calculated load capacity is 351 kN. The last loading cycle in the negative direction shown in Figure 4.9(b) reaches a maximum force level of 353 kN at a displacement of -9.3 mm during the 12.7 mm cycle. The theoretical and numerical load capacities (i.e. 351 kN and 353 kN) show good agreement validating the accuracy of the bolster bearing finite element model.

As with the rocker bearings, the effect of both the friction coefficient and gravity load on the response of the bolster bearing is considered. Figure 4.10 shows that the largest effect of these parameters is on the sliding resistance prior to the pintles engaging. Figure 4.10(a) shows that for a constant gravity load of 205 kN, the sliding resistance increases from 40 kN to 60 kN to 81 kN when the friction coefficients are assumed 0.2, 0.3, and 0.4, respectively. Meanwhile when keeping the friction coefficient constant at 0.2 (Figure 4.10(b)), the sliding resistance increases from 20 kN to 30 kN to 40 kN for gravity loads

of 102 kN, 154 kN, and 205 kN. The sliding resistance is linearly proportional to the gravity load and friction coefficient, which is typical of Coulomb friction. The length of the sliding plateau remains approximately the same at 5.5 mm in the positive loading direction and 4 mm in the negative for all considered responses. The initial stiffness varied between 137 kN/mm and 211 kN/mm for the different gravity load and friction coefficient levels as was similarly seen in the transverse response of the rocker bearing. Moreover, the maximum resistance of the bolster bearing increases from 306 kN to 310 kN to 312 kN in the positive loading direction and from 332 kN to 336 kN to 340 kN in the negative loading direction as the friction coefficient increases from 0.2 to 0.3 to 0.4 when the gravity load is constant. This trend also occurs for increasing gravity loads where the maximum resistances are 295 kN, 301 kN, and 306 kN for positive loading and 319 kN, 326 kN, and 332 kN for negative loading when the gravity loads are 102 kN, 154 kN, and 205 kN, respectively. The small discrepancy between the maximum positive and negative resistance is due to more plastic strain being developed in the pintles in the negative half loading cycle. Overall, both the friction coefficient and gravity load can affect the cyclic response of the bolster bearing under longitudinal loading in terms of the sliding resistance and maximum resistance. As a result, aging can have a significant influence on the performance of the bolster bearing.

4.4.2 Transverse response of the bolster bearing

The transverse behavior of the bolster bearing is similar to its longitudinal behavior in the sense that in both loading directions, the bolster bearing relies on the pintles and friction at the sole plate-bearing body interface to transfer shear from the girders to the bolster bearing body. The moment created by the shear force at the masonry plate-pedestal interface is resisted by the anchor bolts in tension and bearing of the masonry plate on the pedestal in compression. Similar to the longitudinal study, a constant gravity load of 205 kN and friction coefficient of 0.2 is considered for two loading scenarios consisting of equal and increasing magnitude cycles to investigate the transverse behavior of the bolster bearing.

Figure 4.11(a) presents the cyclic response of the bolster bearing under four cycles of equal magnitude loading to 3.2 mm. As with the longitudinal response, a symmetric response with sliding plateaus is observed. The corresponding sliding resistance at the plateaus is again 40 kN, equal to the product of the gravity load and friction coefficient. The length of the plateau increases as the loading cycle repeats due to accumulation of plastic deformation in the pintles. At the end of the loading, the amount of permanent deformation sustained by the pintle reaches nearly 1.0 mm. As the displacement level increases, the sole plate bears against the pintles preventing further sliding and leading to a sudden increase in stiffness in the force-displacement response. For the first cycle, the maximum resistance is 258 kN at 3.2 mm of displacement, which is less than the maximum resistance for subsequent cycles, approximately 296 kN. This behavior is similar to the longitudinal loading case and results from strain hardening and progressive accumulation of plastic shear strain in the pintles, while the initial cycle does not fully yield the pintle. The secant stiffness remains approximately the same at 95 kN/mm for all loading cycles, indicating cycling has little influence on the load capacity of the bolster bearing when loaded transversely to 3.2 mm.

Figure 4.11(b) shows that the cyclic response of the bolster bearing is symmetric under four loading cycles with increasing magnitudes of 1.6 mm, 3.2 mm, 4.8 mm, and 6.4 mm. Similar to the equal magnitude loading cycles, sliding at the sole plate-bearing body interface occurs with a lateral force of 40 kN. The initial stiffness remained constant throughout loading at 299 kN/mm, which is the same as the equal cycles loading case. For displacement cycles to 3.2 mm, 4.8 mm, and 6.4 mm, the maximum resistance is found to be 258 kN, 335 kN, and 352 kN for positive loading, respectively, and 291 kN, 350 kN, and 354 kN for negative loading, respectively. It is also found that the maximum resistance is achieved prior to reaching the maximum displacement for the last two negative half loading cycles, indicating that 354 kN is the transverse capacity of the bolster bearing. The secant stiffness for the last three loading cycles also decreases from 81 kN/mm to 55 kN/mm for positive loading and from 91 kN/mm to 55 kN/mm for negative loading. This decrease shows that cycling to large displacement levels can result in a gradual degradation in the secant stiffness of the bolster bearing. The findings are similar to those found under longitudinal loading where increasing displacement levels

significantly affect the sliding at the sole plate-bearing body interface, secant stiffness, and maximum resistance of the bolster bearing.

It was found in the previous theoretical calculation that the bolster bearing has a load capacity of 442 kN when the gravity load is held at 205 kN and the friction coefficient is 0.2. This number is larger than the load capacity (354 kN) obtained from the finite element analysis, indicating a potentially more complex behavior than what was analyzed theoretically occurs in reaching the maximum capacity of the bolster bearing under transverse loading.

Gravity load and friction coefficient effects on the transverse response are also examined considering 5 mm displacement cycles (Figure 4.12). As the assumed friction coefficient increases from 0.2 to 0.4, the friction plateau force and overall maximum resistance increase, while the general shape of the responses remains the same. The increase in the resistance at the plateau is directly associated with friction due to sliding. The maximum resistance also increased slightly from 349 kN to 386 kN in the negative direction due to the contributions of sliding as well. A similar trend is observed for increasing gravity loads due to the role that the normal force plays in the sliding resistance due to friction. The maximum resistance increases from 328 kN to 349 kN when the gravity load is increased from 102 kN to 205 kN. These findings are similar to those observed for the bolster bearing under longitudinal loading and suggest that the friction coefficient and gravity load affect the cyclic transverse response with respect to secant stiffness, sliding friction, and maximum resistance.

4.5 Bearing Capacity

To further consider the effect of the friction coefficient and vertical load on the maximum resistance of the rocker bearing (transverse) and bolster bearing (longitudinal and transverse), pushover analyses are conducted and compared to the theoretical findings. The friction coefficient is varied with a constant gravity load of 205 kN and the gravity load is varied with a constant friction coefficient of 0.2. The results from the finite element pushover analyses and theoretical calculations are provided in Table 4.2.

For the rocker bearing, a good agreement is found between the finite element results and theoretical prediction. It is found that the finite element model generally under-predicts the theoretical calculation. This can be attributed to the use of rigid body kinematics in deriving Equation 3-12 while the rocker bearing assembly is actually deformable under gravity loads and thus undergoes changes in geometry in the finite element model leading to the observed minor discrepancy. The finite element model gives the same result for different friction coefficients, consistent with the theoretical prediction that the transverse load capacity of a rocker bearing is only a function of its dimensions and the gravity load.

Table 4.2 Comparison of the maximum resistance obtained from the finite element pushover analysis and theoretical prediction for the steel bearing under monotonic loading (kN)

Bearing type/Loading direction	Analysis	Friction coefficient			Vertical load (kN)		
		0.2	*0.3*	*0.4*	*102*	*154*	*205*
Rocker/Transverse	FEM	225	224	224	117	173	225
	Theoretical	231	231	231	116	174	231
Bolster/Longitudinal	FEM	334	334	334	315	325	334
	Theoretical	351	366	360	322	337	351
Bolster/Transverse	FEM	340	359	379	320	330	338
	Theoretical	442	470*	490*	411	427	442

*These values are determined by the shear failure mode controlled by pintle shear failures

For the bolster bearing, the finite element results satisfactorily match the theoretical prediction under longitudinal loading with an average 5% difference. This result further confirms the accuracy of the bolster bearing finite element model in the longitudinal direction. Larger differences are observed in the transverse direction where the finite element model predicts values below the theoretical analysis. This difference is largely associated with the difficultly in capturing the complexity of the transverse behavior with the theoretical equations. For longitudinal loading, the finite element model and the theoretical prediction suggest that the friction coefficient has an insignificant influence on the load capacity. However, changes in the gravity load between 102 kN and 205 kN have a larger impact on the capacity. An approximately linear relationship between

gravity load level and capacity is observed for longitudinal loading. Meanwhile, for transverse loading, both the friction coefficient and gravity load have a noticeable effect on the bearings horizontal capacity. For friction coefficients from 0.2 to 0.4, an increase of 0.1 leads to an approximately 20 kN increase in capacity. A similar increase of 10 kN is observed when the gravity load is increased by 52 kN. Overall, the finite element model tends to yield lower results compared to the theoretical prediction in all scenarios. This observation can be attributed to the fact that an upper-bound plastic analysis solution is used to derive the theoretical equations for the bolster bearing, which overestimates the capacity if the wrong failure mode is considered.

4.6 Summary

This study provides a better understanding of the cyclic behavior of steel bridge bearings under both the longitudinal and transverse loadings, which is integral in assessing the seismic performance of older highway bridges that are equipped with steel bearings subject to low-to-moderate seismic loads and aging effects. Detailed finite element models of the considered rocker and bolster bearings are developed and run in displacement control under constant loading cycles and increasing loading cycles to preliminarily investigate the cyclic behavior of the bearings. Two sets of parametric studies are conducted considering friction coefficient level, representing the effects of corrosion and aging, and gravity load level, representing varying bridge configuration influences. A final set of pushover analyses is performed to examine the maximum load resistance of the bearings under monotonic loading and to compare the results with the theoretical formulations.

The findings led to a better understanding of the general cyclic behavior of steel bearings and the potential influence of aging and different bridge configurations on their performance:

- Theoretical values were able to be reproduced using finite element models that account for contact and sliding suggesting that such models are appropriate for studying the cyclic behavior of steel rocker and bolster bearings.

- The rocker bearing has a roughly linear response under longitudinal cyclic loading owing to the rolling behavior as predicted by the finite element model and rigid body kinematics. The friction coefficient does not influence the behavior while the overall slope (or stiffness) of the response is a function of the gravity load level.
- The rocker bearing exhibits a more limited displacement capacity and significantly larger load resistance in the transverse direction. The critical load capacity for transverse displacement of a rocker bearing is again a function of the gravity load level and the dimensions of the bearing. If corrosion were to influence the overall dimensions of the rocker bearings, then transverse capacity may be affected by aging.
- It is found that the bolster bearing demonstrates similar hysteretic behavior for both longitudinal and transverse loading as a result of combined sliding, rocking, and prying action. Both the friction coefficient and gravity load influence the cyclic response of the bolster bearing in either loading direction in terms of sliding resistance, secant stiffness, and maximum load resistance.
- Under large displacements where the pintles are engaged for transverse loading of rocker bearings or longitudinal and transverse loading of bolster bearings, deformations as large as 3 mm may be observed leading to increases in sliding plateau lengths and stiffness.
- Overall, changes in the friction coefficient resulting from aging and corrosion will have a minor influence on the behavior of steel bearings in older bridge systems like those found in the Central and Eastern United States. However, the friction coefficient is not the only concern in regards to aging effects and the distribution of corrosion may not be uniform leading to further influences on the vulnerability of steel bridges that require consideration.
- The maximum bearing resistance and displacement data obtained from the FE models are instrumental in designing the experimental setup and tests discussed in Chapter 6.

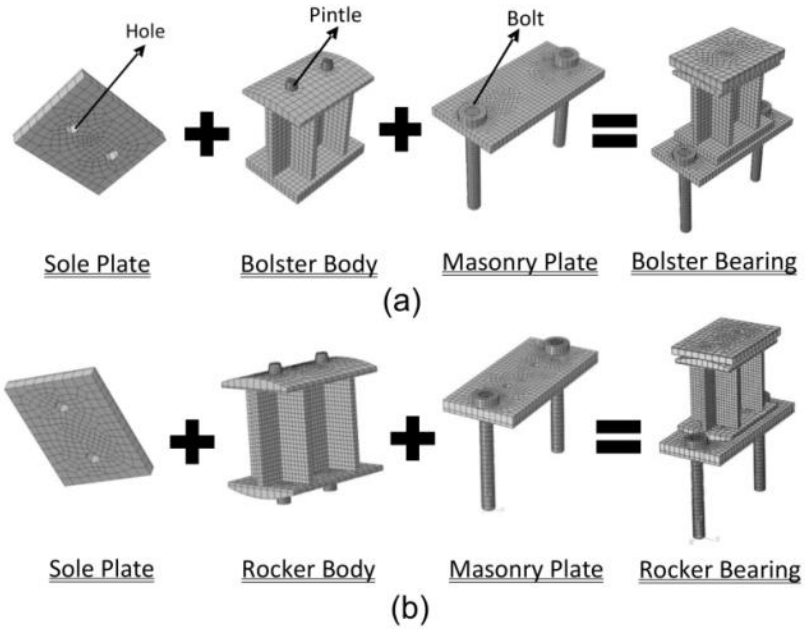

Figure 4.1 Illustrations and mesh of the 3-D finite element models of the (a) bolster and (b) rocker bearing

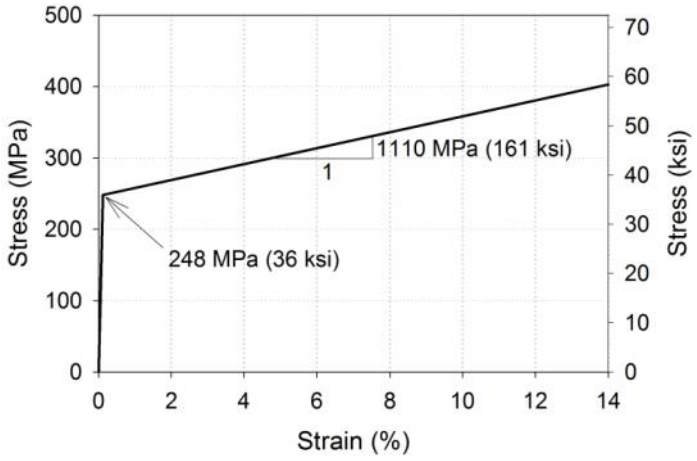

Figure 4.2 Steel material model used for all steel components of the bearings

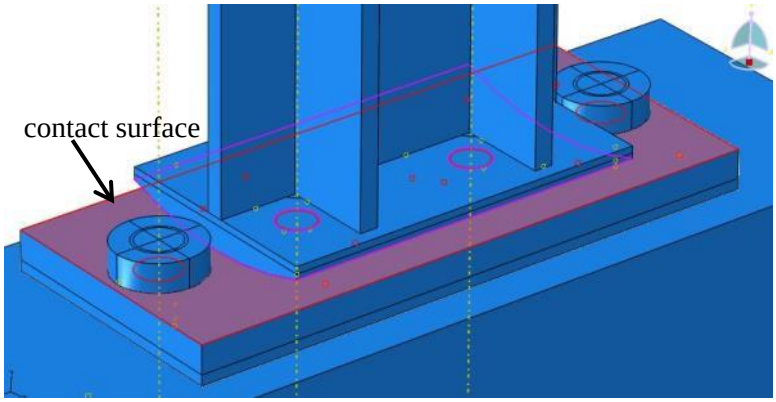

Figure 4.3 Illustration of the contact interface between the rocker body and masonry plate in the finite element model

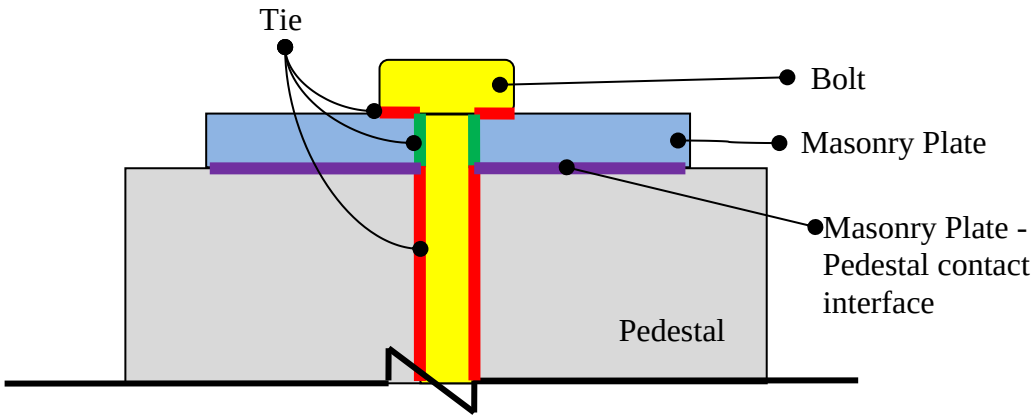

Figure 4.4 Interaction definition for the anchor bolt and its contact interfaces

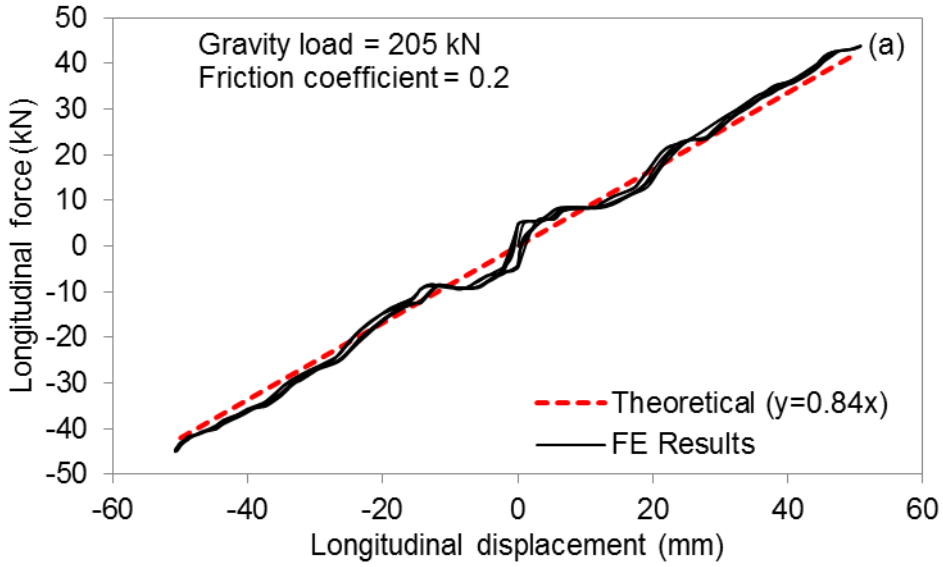

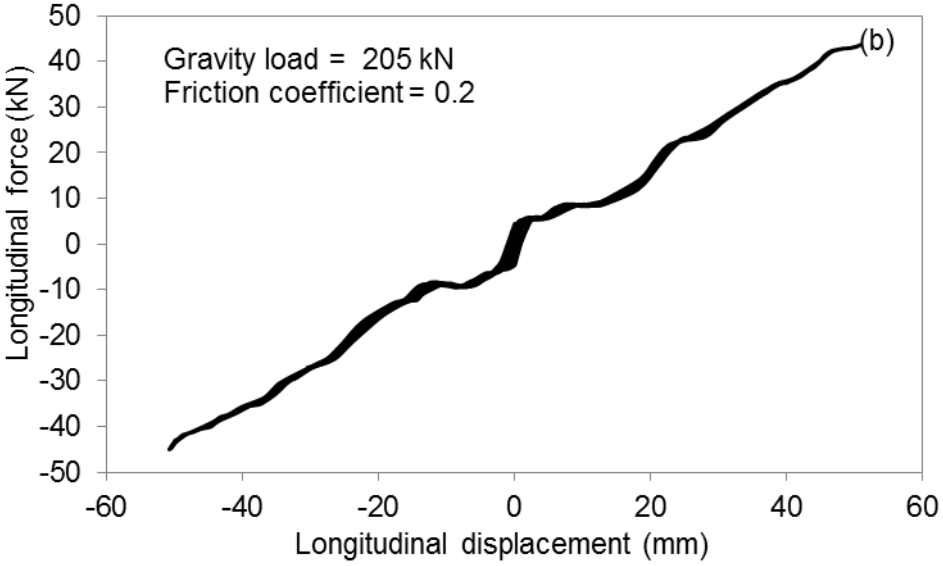

Figure 4.5 Longitudinal response of the steel rocker bearing under (a) reversed loading cycles with equal displacement magnitude and (b) increasing displacement magnitudes

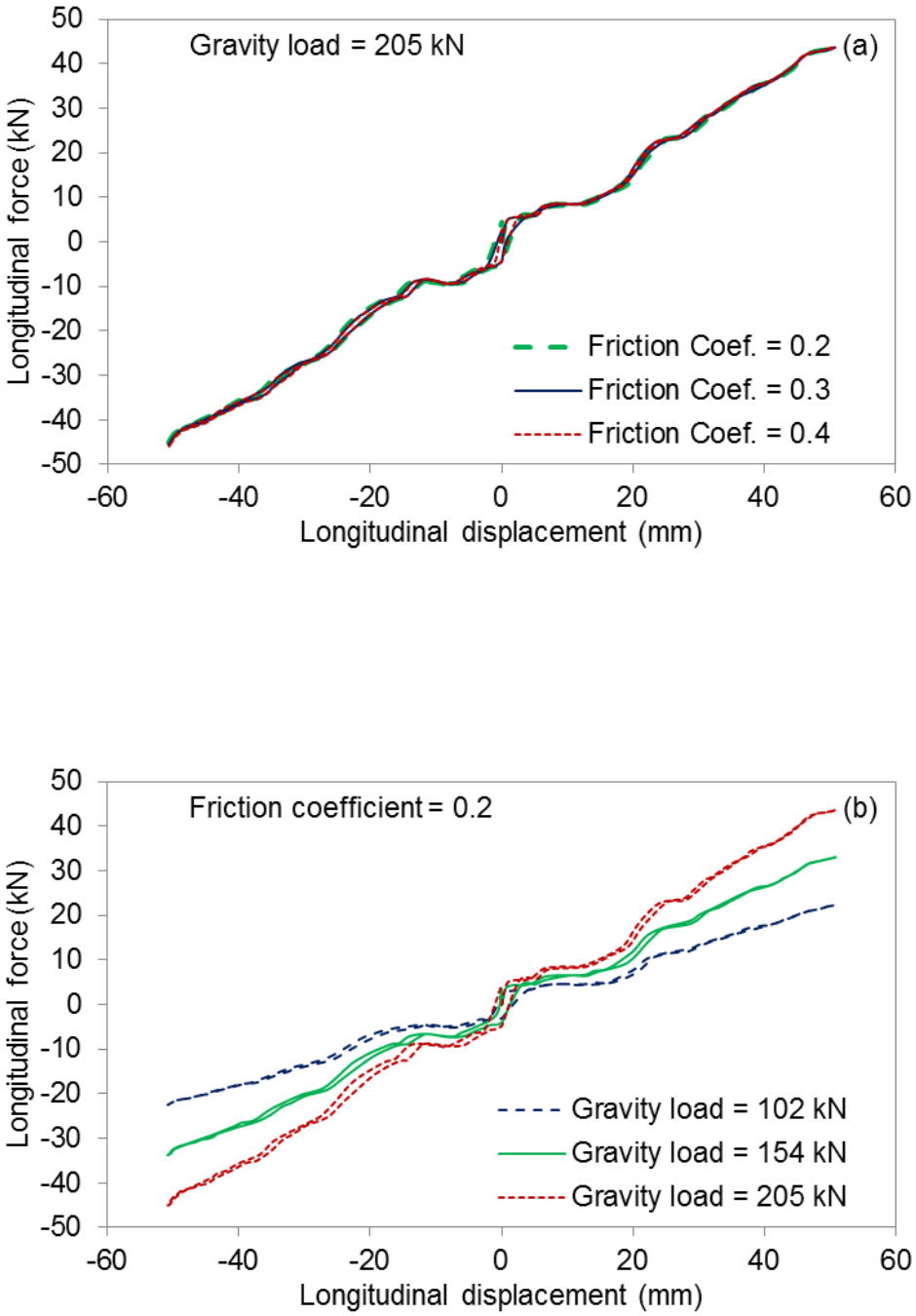

Figure 4.6 Longitudinal response of the steel rocker bearing under a single loading cycle considering the effect of the (a) friction coefficient and (b) gravity load

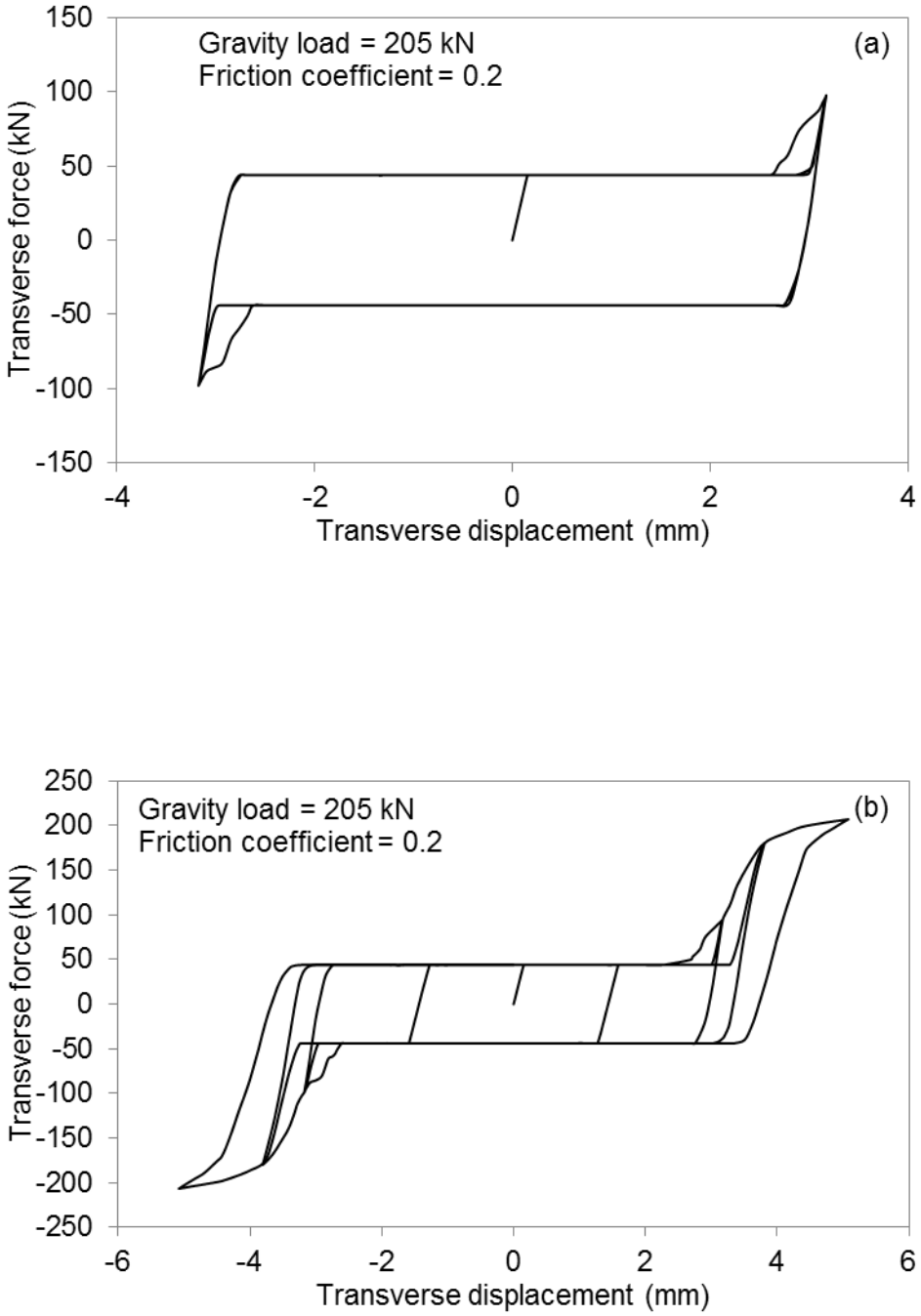

Figure 4.7 Transverse response of the steel rocker bearing under (a) reversed loading cycles with equal displacement magnitude and (b) increasing displacement magnitudes

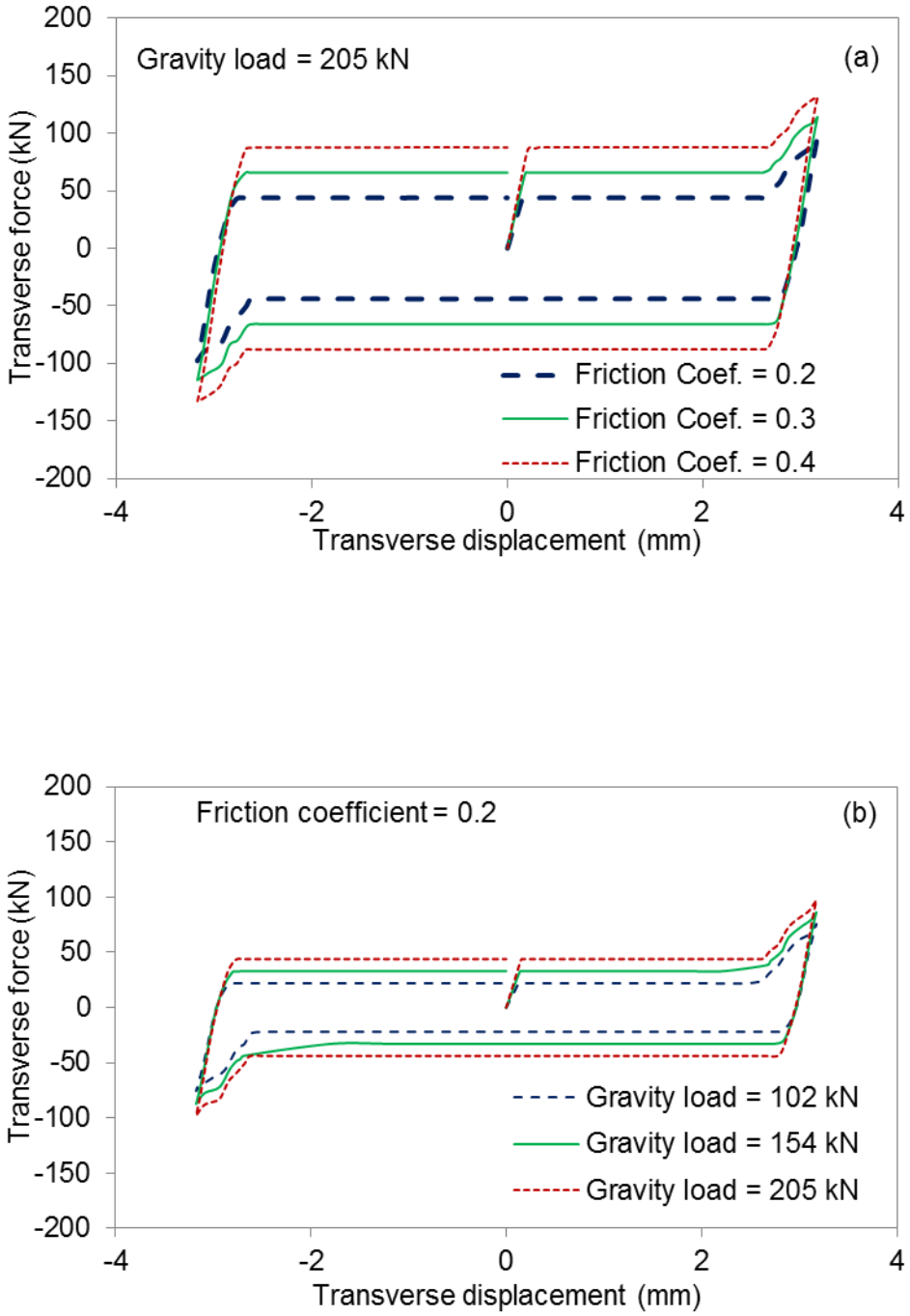

Figure 4.8 Transverse response of the steel rocker bearing under a single loading cycle considering the effect of the (a) friction coefficient and (b) gravity load

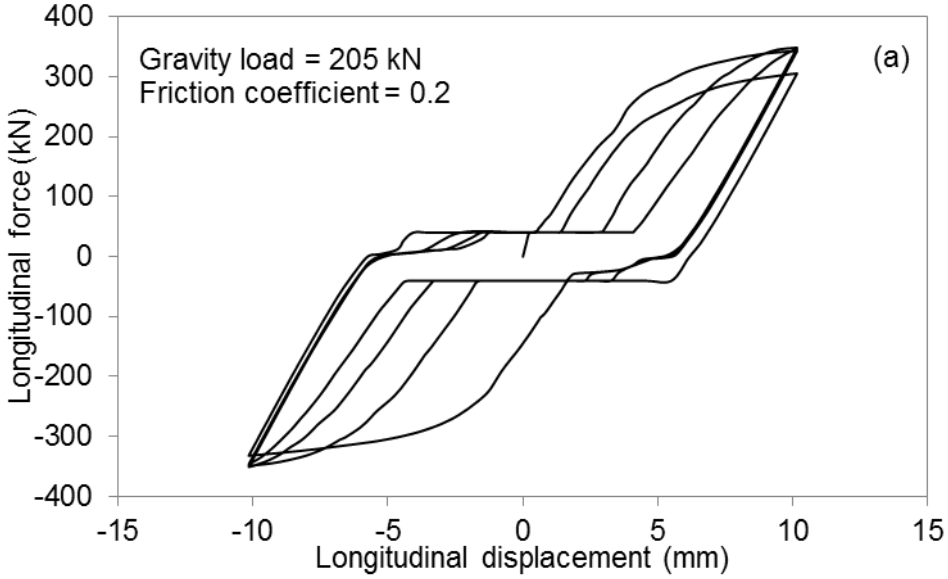

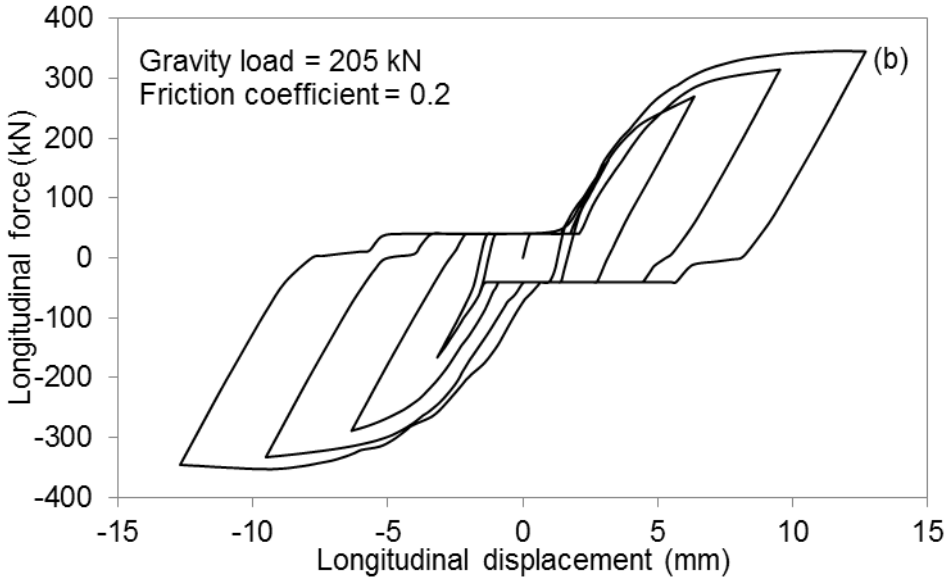

Figure 4.9 Longitudinal response of the steel bolster bearing under (a) reversed loading cycles with equal displacement magnitude and (b) increasing displacement magnitudes

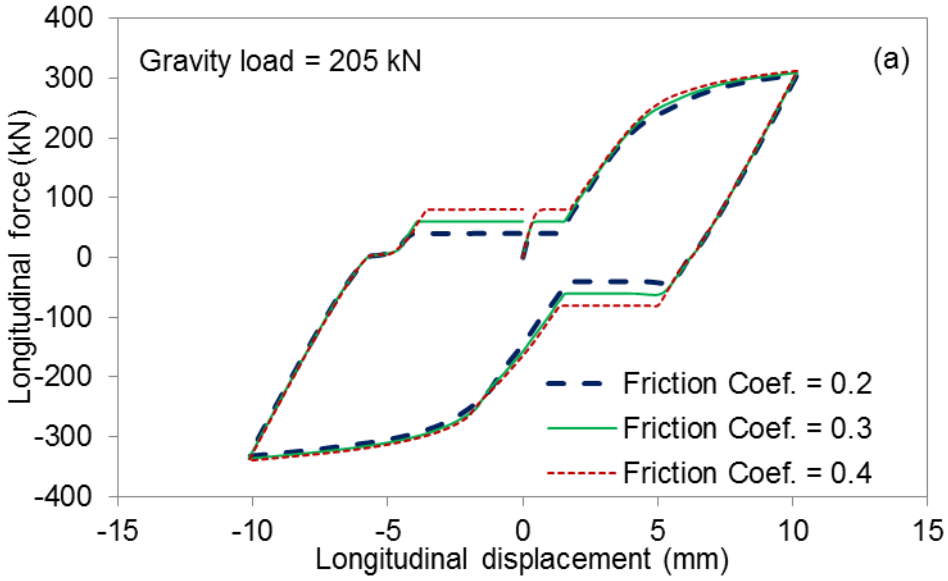

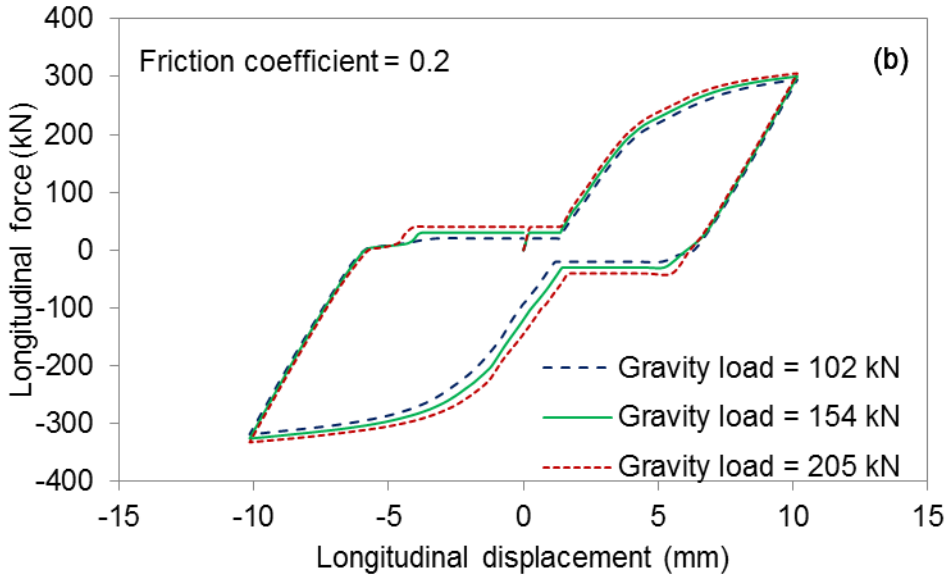

Figure 4.10 Longitudinal response of the steel bolster bearing under a single loading cycle considering the effect of the (a) friction coefficient and (b) gravity load

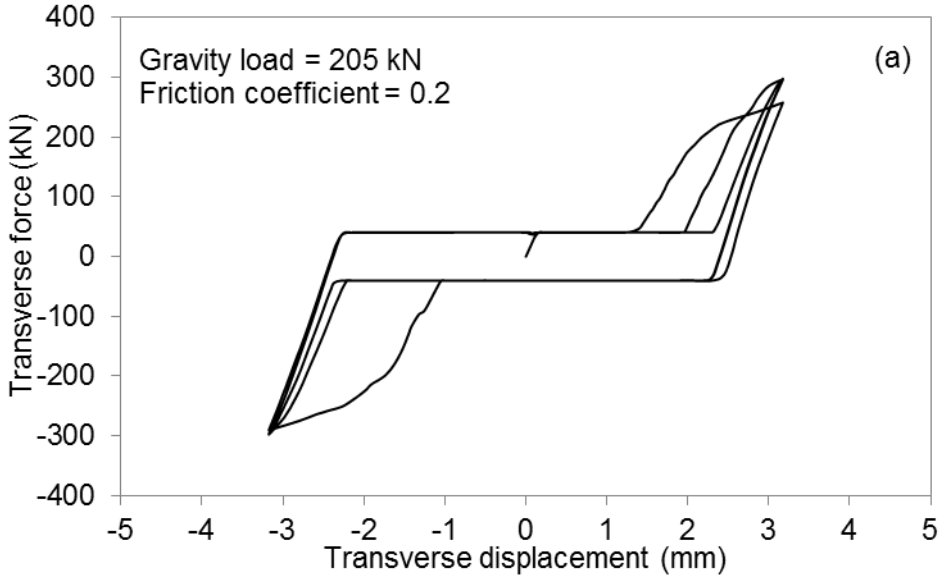

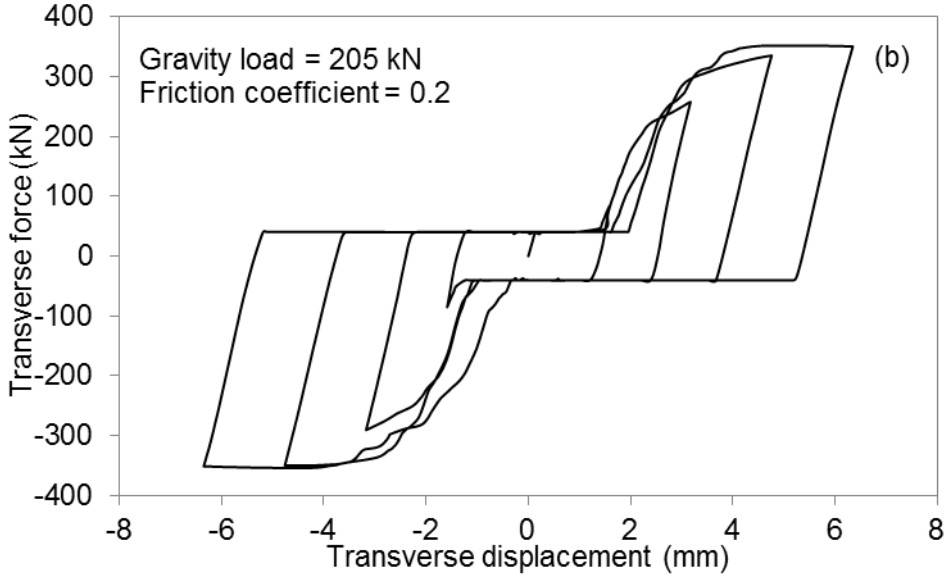

Figure 4.11 Transverse response of the steel bolster bearing under (a) reversed loading cycles with equal displacement magnitude and (b) increasing displacement magnitudes

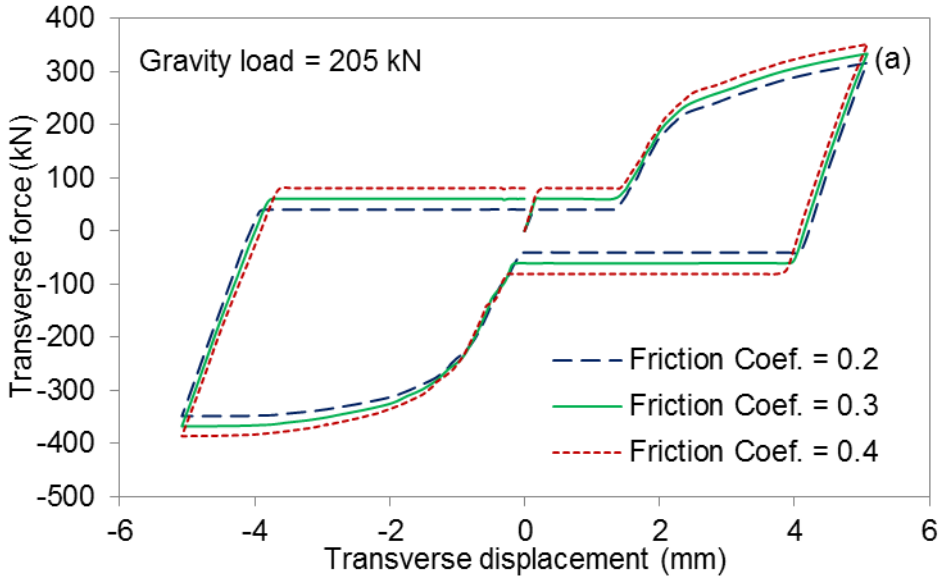

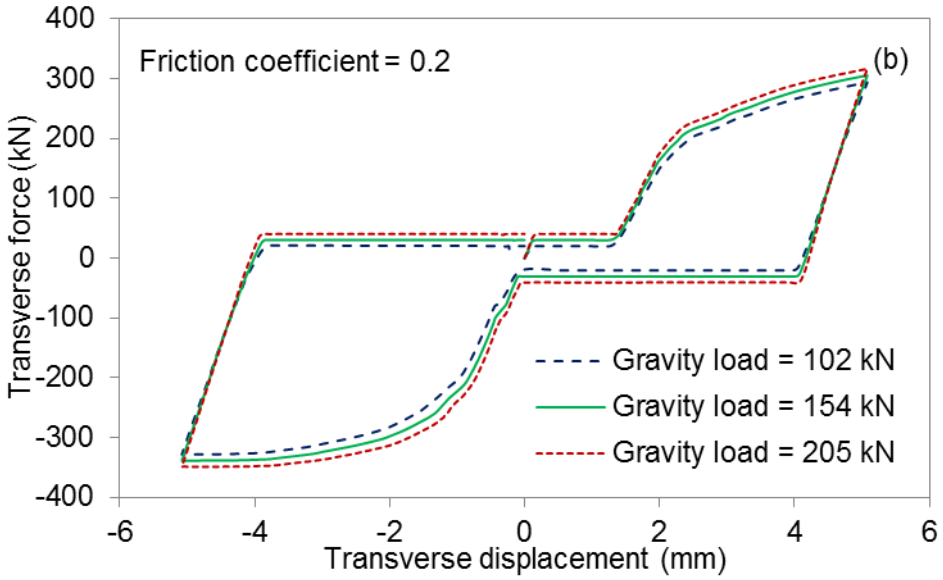

Figure 4.12 Transverse response of the steel bolster bearing under a single loading cycle considering the effect of the (a) friction coefficient and (b) gravity load

CHAPTER 5 CORROSION CHARACTERIZATION OF SALVAGED STEEL BEARINGS

5.1 Introduction

Past studies (Kayser 1988, Park 1999, and Czarnecki 2006) have shown that for steel highway bridges, the most prevalent corrosion pattern is general or uniform corrosion. The effect of general corrosion on steel highway bridges is section loss resulting in possible degradation in stiffness, strength, and functionality of a component and change in the friction coefficient between contact materials. Prediction of the rate of corrosion of steel is difficult due to the stochastic nature of corrosion, the lack of quantifiable statistical data, and the effect of local conditions which has led to the use of empirical formulas to predict corrosion rates of steel bridges (Czarnecki and Nowak 2008). Section loss of steel members or components can be accounted for by considering corrosion penetration depth across the steel section. Proposed by Townsend and Zoccola (1982) based on the data from an extensive test program on corrosion of weathering steel, Equation 5-1 characterizes corrosion loss for steel, where C represents the average corrosion penetration (μm) after t years of exposure, A is the corrosion penetration (μm) after one year of exposure, B is a coefficient determined from regression analysis of experimental data, and t is the number of years of exposure. More information regarding this equation and its constants is available in Komp (1987).

$$C = A \cdot t^B \qquad \text{Equation 5-1}$$

The values of the coefficients in Equation 5-1 depend on the bridge location as specified by the National Cooperative Highway Research Program (NCHRP) (Albrecht and Naeemi 1984). Table 5.1 lists average values for these coefficients considering different types of steel and different bridge locations. However, the prediction of corrosion loss

given by Equation 5-1 assumes that corrosion initiates right after the erection of a bridge without considering the protection provided by paint and lubrication. Although the 25 steel bearings being considered have been salvaged from the same bridge, they each exhibit various levels of corrosion bringing into question the assumption associated with Equation 5-1. According to Park and Nowak (1997), the effective protection time offered by paint and lubrication varies between 10 to 20 years depending on the environment, which further complicates an accurate estimate of corrosion progression rate.

The scope of this chapter focuses on providing a complete account of the effects that corrosion has on in-situ highway bridge steel bearings by quantifying material and section loss for the salvaged steel bearings considered in this study.

Table 5.1 Coefficient values for Equation 5-1 (Albrecht and Naeemi 1994)

Environment	Carbon Steel		Weathering Steel	
	A	B	A	B
Rural	34.0	0.65	33.3	0.50
Urban	80.2	0.59	50.7	0.57
Marine	70.6	0.79	40.2	0.56

5.2 Corrosion of Steel Bearings

5.2.1 General observations and location effect

In general, corrosion can result in a reduction of the net area of steel bearings leading to a potential decrease in its capacity under both dead and seismic loads or a change in its functionality due to changes in geometry. Buildup of debris and corrosion byproducts at locations, such as the pintle holes, anchor bolt holes, and contact interfaces, can restrain free movement of a rocker or bolster bearing leading to unanticipated lateral forces imparted to the superstructure and the substructure, unexpected behavior, and potential toppling of the rocker bearing. Lindquist-Hoeke et al. (2009) found that excessive corrosion buildup around the anchor bolts and inside the anchor bolt holes of the masonry plate often leads to loss of expansion clearances and a complete bond between the bolts and masonry plate. Table 5.2 provides a list of corrosion phenomena observed in typical

in-situ steel bearings and their potential impact on the bearing performance. As discussed in Section 2.2, the steel bearings rely on their pintles to restrain excessive lateral movements of the superstructure. However, this constraint capability of the pintles can be severely undermined by corrosion-induced volume loss of the pintles. The top and bottom cylindrical surfaces share the same diameter while the bearing height is designed to be shorter than this diameter in order to achieve a stable bearing configuration at the rest position. This design nuance can be compromised provided that enough section loss occurs to the top and bottom flanges causing variations in their cylindrical surface diameter or the bearing height. Additionally, the anchor bolt holes in the masonry plate offer a clearance of 6.4 mm on either side of the anchor bolts assuming the anchor bolts are centered in the hole, which provides a favorable environment for corrosion to develop and accumulate. This corrosion can lead to a decrease in the gap clearance around the bolts or severely corroded anchor bolts. These phenomena can result in a lateral strength reduction of the bearing.

Figure 5.1 further illustrates the listed corrosion phenomena in Table 5.2 seen on an actual salvaged steel rocker bearing. Clearly shown in this figure is the severity of how much corrosion can develop on in-situ steel bearings over four decades. Significant material loss due to the formation of pack rust is observed at the top and bottom contact cylindrical surfaces, on the web and stiffeners, and at the masonry plate. The top pintles have experienced substantial volume reduction while the bottom pintles suffered nearly complete volume loss. Additionally, the bottom pintle holes located in the bottom cylindrical surface have been entirely filled with corrosion byproducts. The whole rocker bearing assembly, when left unsupported, is no longer able to maintain an upright position due to the uneven corrosion developed at the contact surfaces.

A thorough examination of the salvaged steel bearings reveals that the corrosion severity varies significantly between bearings located on the abutments and those mounted on the piers. Figure 1.2 shows a plan view of the bridge from which the bearings were salvaged. The ten steel rocker bearings that were installed on the two abutments sustained severe corrosion similar to what is shown in Figure 5.1 while the five bolster bearings and ten other rocker bearings that were located on the piers experienced only minor corrosion, if

any. In part, this is due to the fact that the abutment provides a location for the accumulation of debris that can accelerate corrosion. In contrast, the location of the bearings on the piers was open on all sides and under continuous spans leading to less chance of debris buildup and standing liquid, which indicates that the local environment of the pier bearings is drier and less susceptible to corrosion initiation and progression.

Table 5.2 Qualitative account of corrosion location, observations, and effect on the behavior of steel rocker and bolster bearings

Location	Corrosion effect	Effect on rocker bearing	Effect on bolster bearing
Top pintles	Reduced volume	Lateral constraint loss	
Top cylindrical surface	Flattened, roughened	Rolling behavior change	Sliding behavior change
Web	Thinned	Vertical strength loss	
Stiffeners	Thinned	Vertical strength loss	
Bottom cylindrical surface	Flattened, roughened	Rolling behavior change	N/A
Bottom pintles	Reduced volume	Lateral constraint loss	N/A
Masonry plate	Thinned, roughened	Sliding behavior change	
Anchor bolt holes	Excessive buildup	Expansion gap loss	
Anchor bolts	Reduced section	Lateral constraint loss, strength reduction	

5.2.2 Corrosion distribution and measurements

Visual observation of the steel rocker bearings shows that they have suffered the most severe corrosion in terms of both material loss and geometry changes. A close examination of the abutment rocker bearings indicates that corrosion distribution is highly nonhomogeneous. It is quite common to see that one side of the contact surface has lost more than half of its original depth while the other side only has experienced negligible section reduction. This is significant since it will also lead to a very asymmetric response under seismic loads. Section loss also varies significantly among different bearing components, i.e., pintles, contact surfaces, web and stiffeners, and masonry plate.

Geometry information for the uncorroded steel bearings is obtained from the original design drawings of the bearings, which were contributed by the Illinois Department of Transportation. These bearing dimensions are used to estimate the volume and mass of each bearing component, from which the original mass of the bearing is then calculated by summing all the component masses. The salvaged steel bearings are each weighed three times in the laboratory using a scale with a tolerance of 0.09 kg (0.2 lbs) and the average measurement is taken as the current bearing mass. The mass loss of a bearing is estimated by subtracting its current mass from the original bearing mass. This difference is further divided by the original mass to calculate the mass loss percentage for the bearing. Dimension measurements of the bearing components are also taken three times at each location to find an average measurement. The average dimension measurements are used to calculate the current thickness or volume of the bearing components, which are then compared with the original thickness or volume to determine section or volume loss percentages.

Results of mass and section loss measurements for the abutment steel rocker bearings are provided in Table 5.3 and analyzed using box plots as shown in Figure 5.2 considering eight representative loss categories including mass loss, top and bottom pintle volume reduction, top and bottom contact surface section loss, web section loss, stiffener section loss, and masonry plate section loss. The top and bottom of the box represent the 3rd and 1st quartiles of loss percentage, respectively, with the 2nd quartile or median given by the band inside the box. Whiskers are extended to data that are within 1.5 interquartile range (IQR) of either the lower or upper quartile. Data outside the range between the whiskers is considered as outliers, but no outlier is found in any loss category.

As shown in Figure 5.2 the mass loss box plot indicates an insignificant dispersion for the considered eight abutment rocker bearings. The average mass loss for the eight abutment rocker bearings is 11% with a standard deviation of 3.1% while the maximum mass loss reaches as much as 16% and the minimum is only 6%. However, the allocation of the mass loss among different components for a bearing varies significantly in regards to dispersion and median and the maximum and minimum losses. The statistical information provided in Table 5.3 further confirms this observation.

The effect of mass loss is largest on the volume reduction of the bottom pintles that on average lose nearly three quarters of their volume. This loss severely limits the functionality of the pintles to prevent lateral translation. In contrast, the top pintles lose 40% less volume on average compared to that of the bottom pintles. Both the top and bottom pintles have a similar dispersion in volume reduction. The masonry plate experiences the least corrosion loss with the smallest mean (10%) and standard deviation (2.4%). The bottom contact surface compared with the top contact surface has sustained 9% more section reduction in terms of flange thickness due to easier corrosion buildup at the bottom contact interface of a rocker bearing. The web thickness also has more prominent loss reaching a mean loss of 24% and larger spread of roughly 11% than the stiffener thickness that shows a mean loss of 15% and a standard deviation of 7%.

The above discussion clearly shows that corrosion is nonhomogeneous not only among different steel bearings retrieved from the same abutment, but also among various components of a specific bearing. The bottom pintles out of all bearing components suffer the most corrosion-induced material loss with the top pintles experiencing the second most corrosion loss. The pintles are 3.2 mm shorter in diameter than the pintle holes, which creates a perfect environment to trap moisture and thus highly conducive to corrosion progression while being difficult for maintenance. The bottom contact interface of an abutment rocker bearing is also susceptible to significant corrosion as debris and water can more easily accumulate at this location than at the top contact interface. This fact is proven by the section loss data for the bottom pintles and bottom contact surfaces that all exhibit much larger values than those of the top pintles and top contact surfaces.

The primary function of the abutment rocker bearings to accommodate longitudinal movements and transverse rotations relies on mechanisms such as rolling and rocking. However, the top and bottom contact surfaces experience substantial changes in their geometric characteristics (i.e. radius and height), which significantly undermines the bearing rolling and rocking ability as discussed previously. In addition, pack rust formed on many in-situ bridges from corrosion adheres firmly to steel bearings and is commonly found at the contact interfaces as seen in Figure 5.1. This occurrence can lock the rocker bearings from rolling or rocking provided enough accumulation of corrosion byproducts

occurs. This locking mechanism can restrain the bridge superstructure from moving freely under thermal or vehicle braking actions leading to lateral forces developed between the superstructure and the substructure. This lateral force sometimes can be large enough to break the locking mechanism and further topple the rocker bearing resulting in unseating of the superstructure as mentioned in Chapter 1. This poor lateral performance of corroded steel bearings brings into question their performance during a seismic event.

Table 5.3 Mass and section loss statistics for eight abutment steel rocker bearings

Loss (%)	Left abutment rocker bearings				Right abutment rocker bearings				Statistical data*	
	1	2	3	4	5	6	7	8	μ	σ
Mass	16	9	14	6	11	12	10	13	11	3
Top pintle volume	50	44	25	18	40	19	44	22	33	13
Bot pintle volume	81	79	65	85	77	85	52	62	73	12
Top contact surface section	30	8	16	8	18	12	9	18	15	7
Bot contact surface section	30	22	21	14	30	20	27	26	24	6
Web section	43	18	24	14	19	14	19	37	24	11
Stiffener section	21	3	13	9	13	17	25	16	15	7
Masonry plate section	13	11	15	9	9	8	9	9	10	2

*μ=mean and σ=standard deviation.

5.3 Summary

This chapter provides a concise review on corrosion of steel highway structures, a quantitative analysis of corrosion-induced mass loss, and geometric variations observed in steel rocker bearings that are retrieved from bridge abutments. The nonhomogeneity of corrosion spatial distribution is exemplified through the observed location effect between pier bearings and abutment bearings and the uneven distribution among various bearing components. The bottom contact interface in an abutment rocker bearing is identified as the most vulnerable to corrosion. The bottom pintles are particularly prone to lose significant material as a result of their enclosed environment that traps in water and foreign particles such as chlorides and thus facilitates corrosion progression. Potential for locking as a result of corrosion and debris buildup and subsequent unseating of the superstructure is also discussed. These observations all lead to a question of how

corrosion affects the lateral cyclic performance of these bearings and the overall bridge. To consider this question, an experimental and numerical approach to characterizing the corroded bearing cyclic behavior and its influence on the seismic performance of typical highway bridges is undertaken and described in the following chapters.

Figure 5.1 Illustration of various corrosion locations and effects on a steel rocker bearing salvaged from an abutment

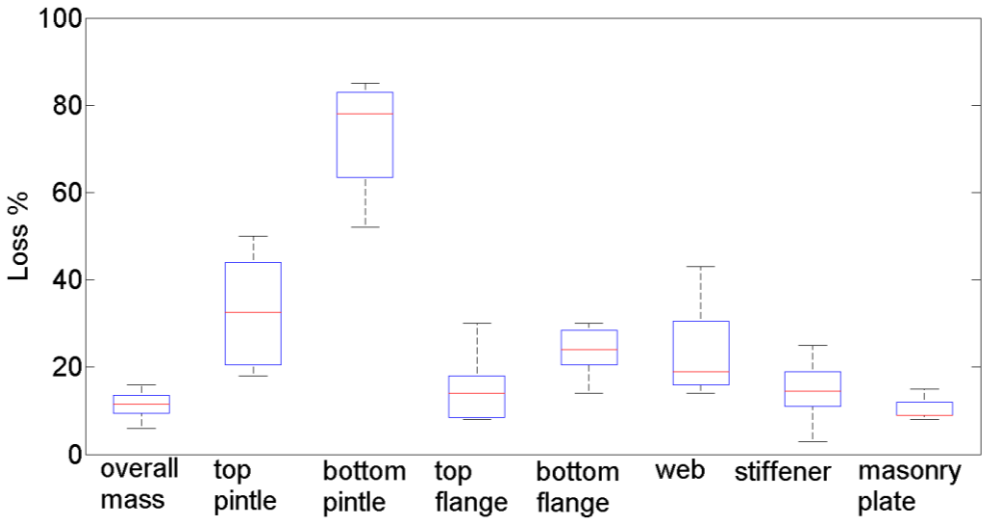

Figure 5.2 Box plots of mass and section loss distributions for eight abutment steel rocker bearings

CHAPTER 6 EXPERIMENTAL STUDY OF SALVAGED STEEL BEARINGS

6.1 Introduction

The experimental evaluation of the salvaged steel bridge bearings, whose corrosion levels have been quantified in Chapter 5, is considered in two parts. The first part focuses on the behavior of the bearing alone by mounting the bearings on a steel pedestal and evaluating their monotonic and cyclic behavior. The use of a steel pedestal mitigates anchorage failure modes associated with the pier, such as concrete breakout or anchor bolt pullout, when the bearings undergo significant lateral displacements. By focusing on the bearing itself, its behavior and the effect of corrosion can be directly assessed. The steel bearings with minor and severe corrosion as well as bearings that have been cleaned of pack rust are subjected to an increasing monotonic lateral displacement or an increasing cyclic displacement loading. Specifically, this first part of the experimental work aims to: 1) quantify the secant stiffness and ultimate strength of the studied steel bearings considering three condition categories, i.e. minor/good, severe, and cleaned; 2) identify the governing failure modes of the steel bearings under lateral loading; 3) characterize the steel bearing behavior under longitudinal and transverse loading; and 4) establish a correlation between corrosion level and the cyclic behavior of the steel bearings.

The second part of the large-scale experimental study uses a reinforced concrete pedestal instead of a steel pedestal as a base for the bearings. This pedestal is designed based on the original cap beam design of the bridge from which the bearings were salvaged. Only the steel bolster bearings will be considered because of their ability to transfer moment to the pedestal. It is important to also consider the anchorage failure modes as they have been observed during some past seismic events. The aim of this portion of the experimental study is to characterize the cyclic behavior and governing failure modes of

the combined steel bolster bearing and concrete pedestal assembly. In addition, sliding and post-bolt fracture behavior is compared to the steel base tests.

6.2 Experimental Program Overview

6.2.1 Test setup

The test setup, shown in Figure 6.1 and Figure 6.2, is used to load the bearings either longitudinally or transversely by rotating the initial position of the bearing. An actuator, with a capacity of 445 kN and a stroke of ±127 mm, provides the horizontal loading to the bearings in displacement control. The left end of the actuator is anchored to an existing reaction wall while its right end is connected to the loading beam. The loading beam is chosen such that the flange has the same width as the girders of the bridge in which the bearings were salvaged. Four identical hydraulic jacks are mounted on top of the loading beam and apply a vertical load to simulate the gravity load acting on the bearings from the superstructure. The vertical load is applied through pretension cables connected to the jacks and anchored using chucks to the steel base beam that is fixed to the strong floor. Two pinned columns are outfitted with load cells to record axial load variations in the columns. These columns ensure that the loading beam remains horizontal and enhance the stability of the setup. The top pin connection on the west column has an enlarged pin hole to minimize the axial load transferred into the column. A load cell fixture, shown in Figure 6.3, is placed between the bearing and the loading beam to transfer the horizontal and vertical loads to the bearing specimen. The fixture is designed so that only axial load is transferred through the load cell and all lateral loads are transferred through the fixture. The bottom segment of the load cell fixture is bolted to the sole plate of the bearing assembly, while the top segment is bolted to the loading beam. The load cell sits between these segments and records the axial load applied to the bearing specimen allowing the hydraulic pressure in the jacks to be adjusted in order to maintain a quasi-constant axial load level. The masonry plate at the base of the bearing assembly is anchored to either a steel pedestal (Figure 6.2(a)) or a concrete pedestal (Figure 6.2(b)).

6.2.2 Instrumentation

The main goal of this experimental work is to characterize the monotonic and cyclic behavior (load-deformation relationship) of salvaged steel bearings under longitudinal and transverse loading. Thus, the primary instrumentation is used to obtain the applied horizontal load, monitor the vertical load, and record the displacement history of the bearing. A displacement profile for the whole bearing assemblage and test setup is obtained through a variety of instruments capable of measuring both absolute and relative displacements at various locations. Figure 6.4 shows an array of optical markers distributed over the bearing and test setup. These markers work with an optical tracking system to record the displacement histories of these locations throughout the entire loading duration. In addition, a number of potentiometers are installed to provide backup measurements should a marker dislodge. The load cells in the actuator, two side columns, and middle load cell fixture measure and record the horizontal and vertical load histories incurred during testing.

6.2.3 Loading protocol

All loading protocols are applied in displacement control. Considering the multi-directional nature of ground excitations, the behavior of bridges and their components under longitudinal and transverse loading is important. As such, the loading protocols are applied in either the longitudinal or transverse loading direction. The monotonic loading protocol is applied in displacement increments of 1.6 mm or 3.2 mm until the bearing fails or the test setup capacity is reached. Table 6.1 summarizes the cyclic loading protocols used in past tests of steel bearings and pedestals. Mander et al. (1996) found that the loading rate effect on the response of steel bearings is negligible. Thus, the loading rate is maintained at a quasi-static rate throughout the cyclic tests. Both the longitudinal and transverse cyclic loading protocols consist of two equal magnitude cycles followed by two more cycles with an increase in magnitude of 1.6 mm or 3.2 mm. This loading increment is continued until the bearing fails or the limits of the test setup are reached. The 1.6 mm increment is used for loading the rocker bearings in the transverse direction. For the bolster bearings loaded in either direction and the rocker

bearings loaded in the longitudinal direction, 3.2 mm is used as the increment. Figure 6.5 shows the general pattern of the cyclic loading protocol adopted in this work. In addition, a vertical load of 102 kN provided by the four loading jacks is used for all the bearing tests. This gravity load level is typical for the considered steel bearings based on a static dead load analysis of the Meridian bridge (see Table 4.1), from which the bearing specimens were salvaged. Due to the constraints of the test setup, variations of the vertical load acting on the bearings are observed. To maintain a relatively constant vertical load level on the bearings, the hydraulic pressure in the jacks is adjusted at a 1.6 mm displacement increment such that the vertical load variation is confined within ±13 kN.

Table 6.1 Past loading patterns for tests of steel bearings and pedestals

Bearing type	Pattern	Mander et al. (1996)	Barker and Hartnagel (1998)	Hite (2007)
Steel Expansion	Longitudinal constant	40 mm, 50 mm	44 mm (80 cycles)	-
	Transverse constant	25 mm, 50 mm	-	-
Steel Fixed	Longitudinal increasing	2 mm, 6 mm, 10 mm, 14 mm	-	-
	Longitudinal constant	6 mm	-	-
	Transverse constant	25 mm, 50 mm	-	-
Steel Pedestal	Longitudinal increasing	-	-	89 mm (10 cycles)
	Transverse increasing	-	-	51 mm (9 cycles)

6.2.4 Concrete pedestal

The lateral resistance of the steel bolster bearings can depend on the strength of the anchor bolts depending on the size of the pintles. For the steel bearings considered in this study, the anchor bolts are 25.4 mm in diameter while the anchor bolt holes in the masonry plate are enlarged to 38.1 mm. This anchor bolt diameter is less than the pintle diameter of 31.8 mm meaning the failure mode of the steel bearings under large lateral loads is dictated by failures associated with the anchor bolts such as bolt fracture or bolt pullout provided that the bolts and pintles are made of the same steel material. While the bolt fracture mode is best evaluated via using a steel pedestal, it is also necessary to examine their performance under cyclic loads when embedded in concrete. Additionally,

the use of anchor bolts with larger diameters (e.g. 34.9 mm), still less than the anchor hole size, has the potential to shift the controlling bearing failure mode from bolt fracture to pintle fracture provided that the concrete substructure can provide enough anchorage to the bolts, which may result in a better overall bridge performance (Steelman et al. 2014). However, this idea has not been considered for high type bolster bearings such as those being tested in this study. In this work, two concrete pedestals are fabricated, one with embedded anchor bolts having a diameter of 25.4 mm and the other with embedded anchor bolts with a diameter of 34.9 mm. These pedestals are used to cyclically test the steel bolster bearings and investigate the effect of concrete anchorage and bolt diameter on their performance and ultimate failure mode.

Figure 6.6 shows the reinforcement layout for the concrete pedestals, which is consistent with that of the concrete bent beams of the Meridian bridge. The top layer of the longitudinal reinforcement consists of 5 #11 bars that are spaced at 140 mm at the edge and 156 mm toward the center. Two layers of 5 #5 bars 171 mm apart are positioned at the bottom of the reinforcement cage with a spacing of 143 mm at the edge and 159 mm toward the center. Fourteen steel tie pairs are spaced at 152 mm apart along the length of the pedestal. Each pair consists of one 686 mm x 552 mm tie around the perimeter of the reinforcement cage and one 686 mm x 235 mm tie around the two bottom layers of longitudinal bars. Overall, the concrete pedestal is 2388 mm long, 629 mm tall and 762 mm wide and provides a 38.1 mm concrete cover. Figure 6.7 shows photographs of the formwork with the reinforcement cage placed inside and the poured concrete pedestal. Although concrete with a specified strength of 21 MPa was ordered, the actual strength of the concrete is much higher with a 28-day strength of 29 MPa. Concrete cylinder tests conducted on the test days show a slightly higher strength value of 30 MPa.

Each pedestal is used for two bearing tests, one longitudinal and one transverse. To achieve this, four anchor bolts, either 25.4 mm or 34.9 mm in diameter, are installed in each pedestal in a diamond pattern as shown in Figure 6.8. The longitudinal test precedes the transverse test, after which any damage to the concrete is repaired with high strength non-shrink grout.

It should be noted that the reinforced concrete pedestal used in this study are newly fabricated without explicitly considering degradation of the reinforced concrete pedestal due to aging. Further changes in the behavior may result from loss of concrete cover, corrosion induced cracking, and rebar and anchorage corrosion which is not considered in this study.

6.2.5 Steel bearing specimens and test matrix

As discussed in Chapter 5, the studied salvaged steel bearings have sustained varying levels of corrosion due to their spatial location on the bridge. Table 6.2 provides a detailed inventory of the bearings and their level of corrosion. The bearings are numerally numbered in an ascending manner based on their location from the left abutment to the right abutment. The corrosion level is divided into three categories, i.e. severe, minor, and cleaned, according to the mass loss study performed in Chapter 5. All 10 abutment rocker bearings are classified as having sustained severe corrosion while all pier bearings (both rocker and bolster) are labeled with minor corrosion.

The test parameters considered in this experimental study consist of bearing type (i.e. rocker or bolster), bolt diameter (i.e. 25.4 or 34.9 mm), corrosion level (i.e. severe, cleaned or minor), loading direction (i.e. longitudinal or transverse), and loading protocol (i.e. monotonic or cyclic). The test matrix shown in Table 6.3 is used to fully study the bearing behavior considering these parameters. In the table, AR, PR, and PB are abbreviated for abutment rocker bearing, pier rocker bearing, and pier bolster bearing, respectively. Additionally, L stands for longitudinal and T for transverse, while C is short for cyclic and M for monotonic. The bearing ID is derived based on the information in the first column of Table 6.2, for example, PB11 corresponds to the eleventh bearing that is a bolster bearing located on the middle pier. Two bearing conditions, as-received and cleaned, are considered as well. The cleaned condition corresponds to the condition where the rust layers are completely removed from the bearing surface prior to testing. The abutment rocker bearings are first tested in the as-received condition and then again in the cleaned condition, while all the pier rocker and bolster bearings are tested only in their as-received condition.

6.2.6 Steel anchor bolts

Steel anchor bolts used for this experimental study are made of plain low carbon steel material with a minimum yield strength of 248 MPa, which is consistent with the anchor bolts installed originally in the bridge. However, corrosion of the anchor bolts and potential decrease in capacity is not addressed in this study. A detailed account of steel anchor bolt corrosion and potential changes in capacity can be found in Lindquist (2008). Tensile test results for the 25.4 mm and the 34.9 mm anchor bolts used for experimental testing are provided in Figure 6.9. Test results show that the actual tensile capacities are 226 kN and 225 kN for two 25.4 mm diameter anchor bolts that were tested. These values are all greater than the nominal capacity of 203 kN for the 25.4 mm diameter bolts. Moreover, the actual tensile capacity of the 34.9 mm diameter bolt is 812 kN, much greater than the nominal value of 383 kN.

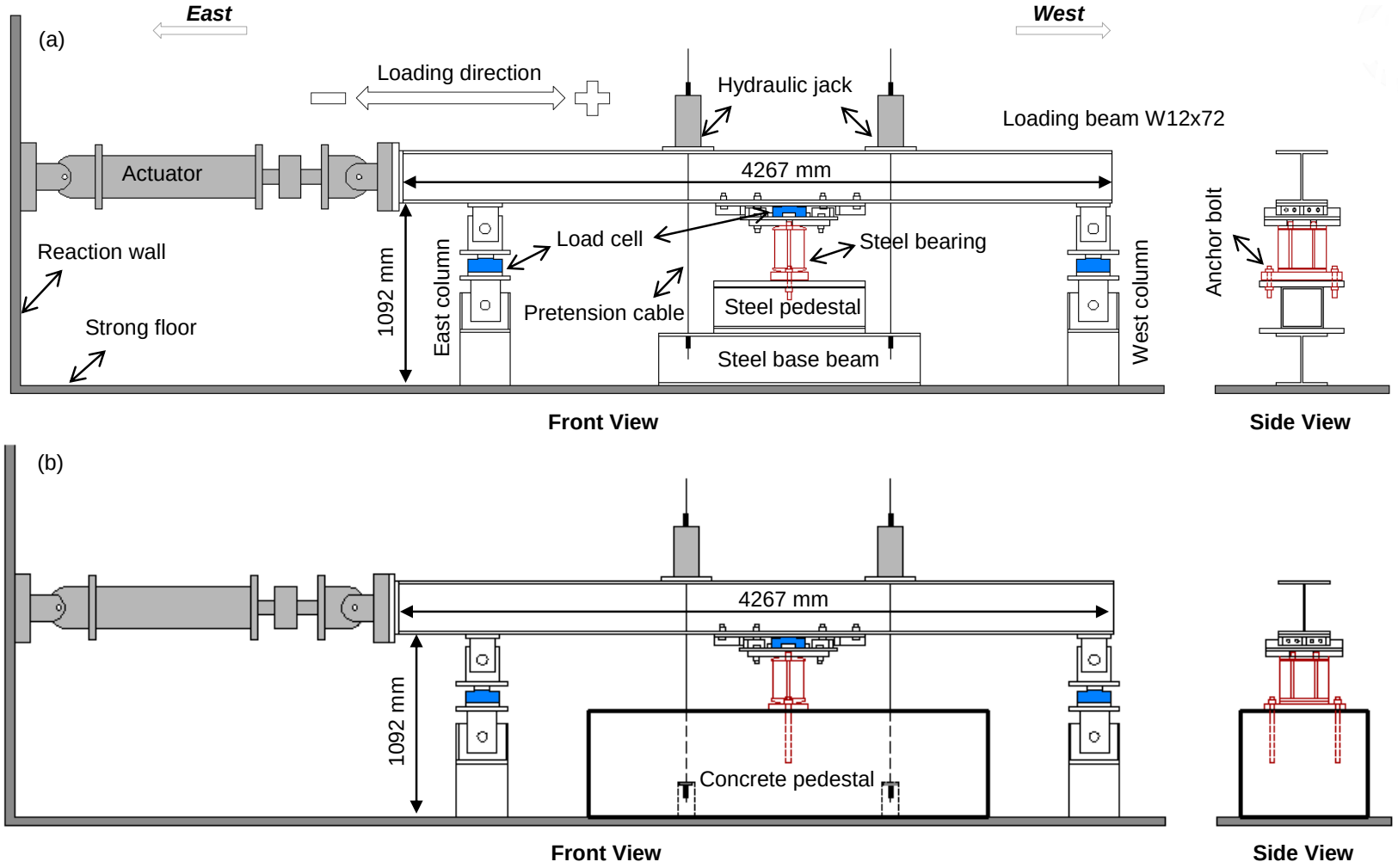

Figure 6.1 Experimental test setup with (a) a steel pedestal and (b) a concrete pedestal

Figure 6.2 Photograph of the bearing test setup

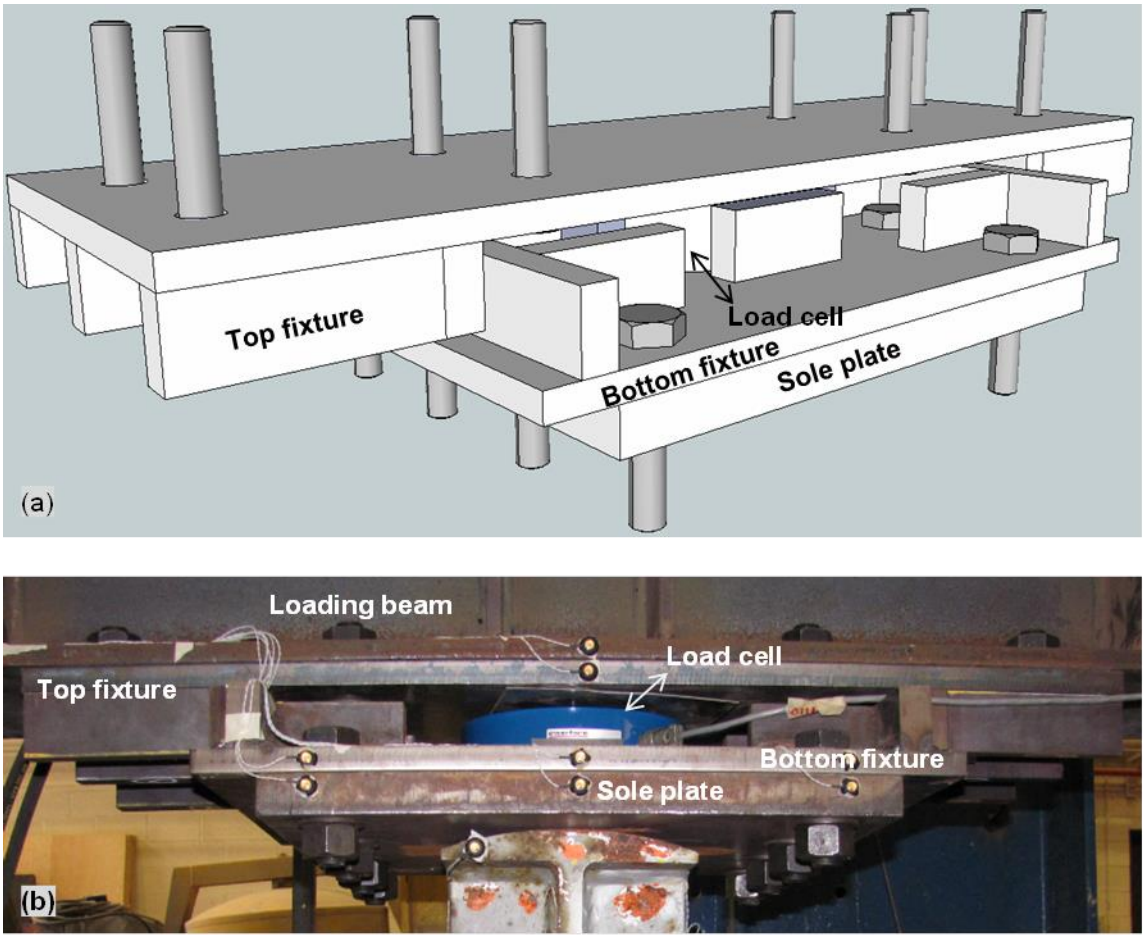

Figure 6.3 Load cell fixture illustrations: (a) 3-D diagram and (b) photograph

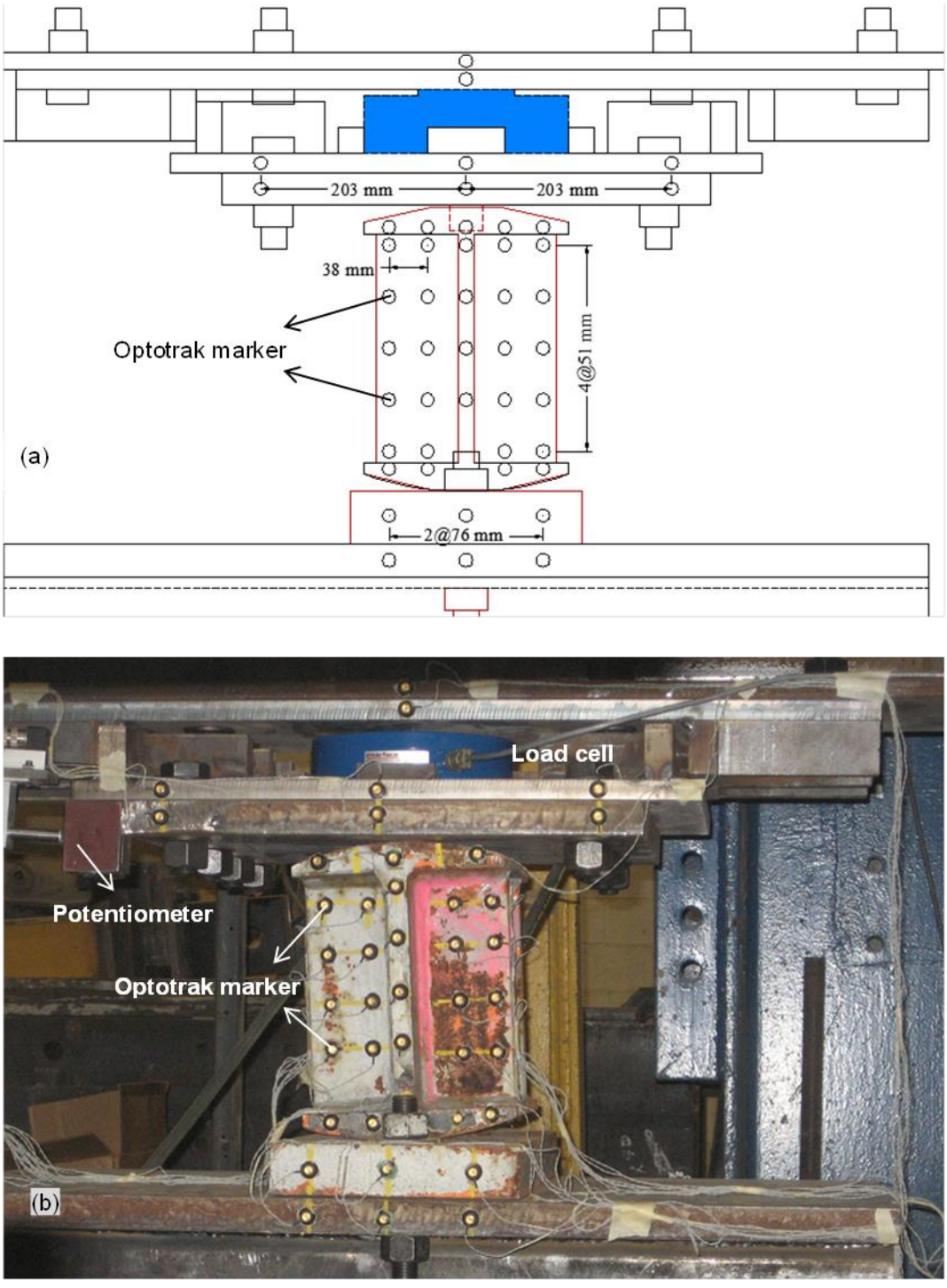

Figure 6.4 Optotrak marker layout on a steel bearing specimen: (a) diagram and (b) photograph

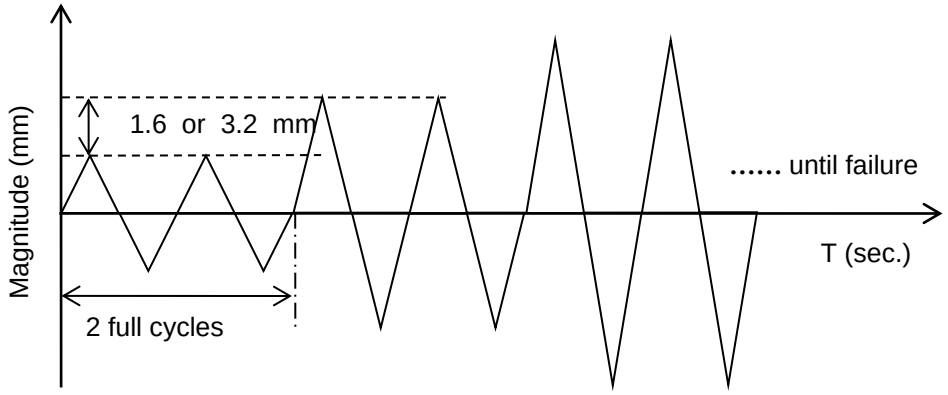

Figure 6.5 Loading protocol used for the experimental testing of the salvaged bearings

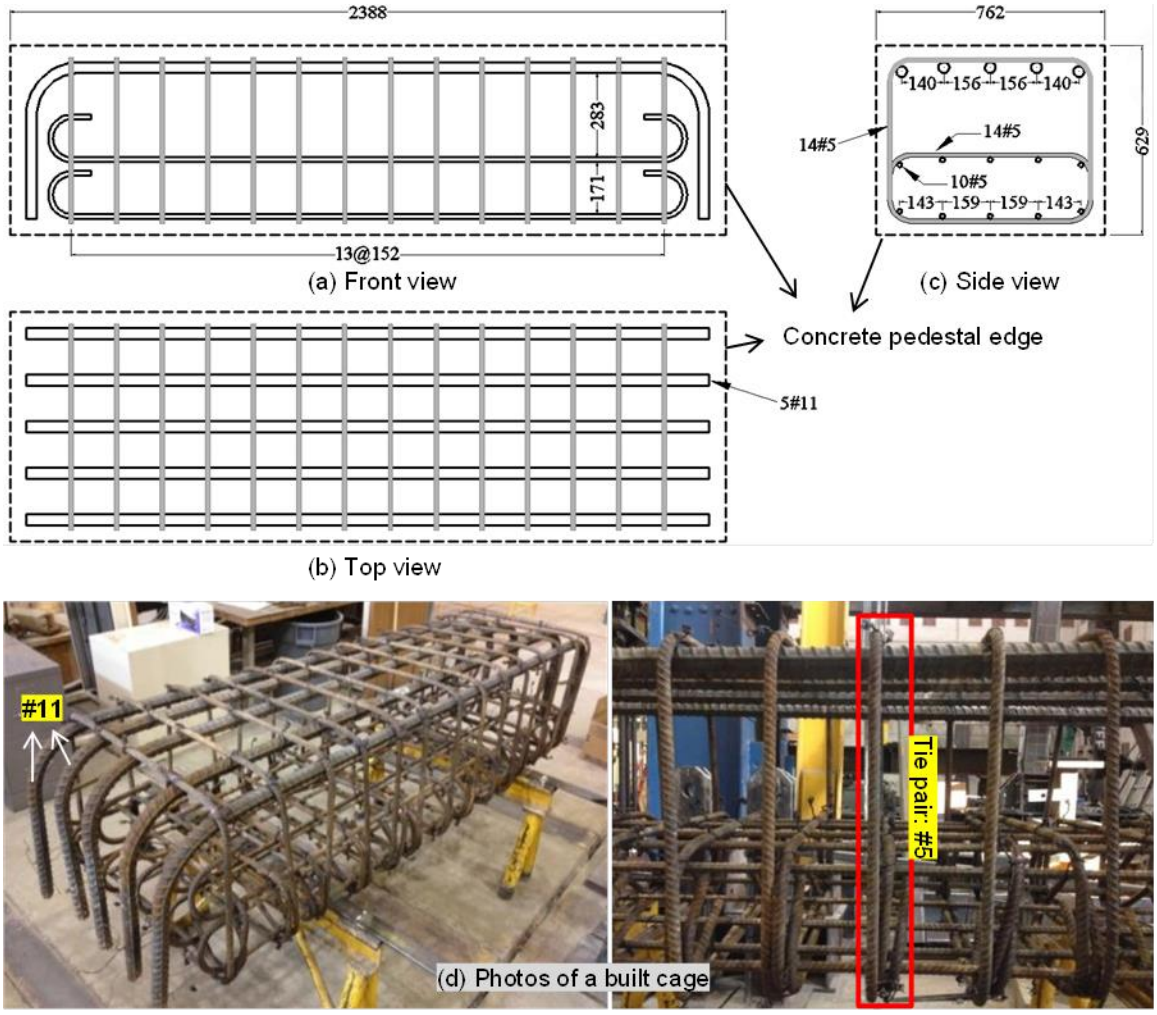

Figure 6.6 Design of the reinforcement cage of the concrete pedestals (unit of dimensions: mm)

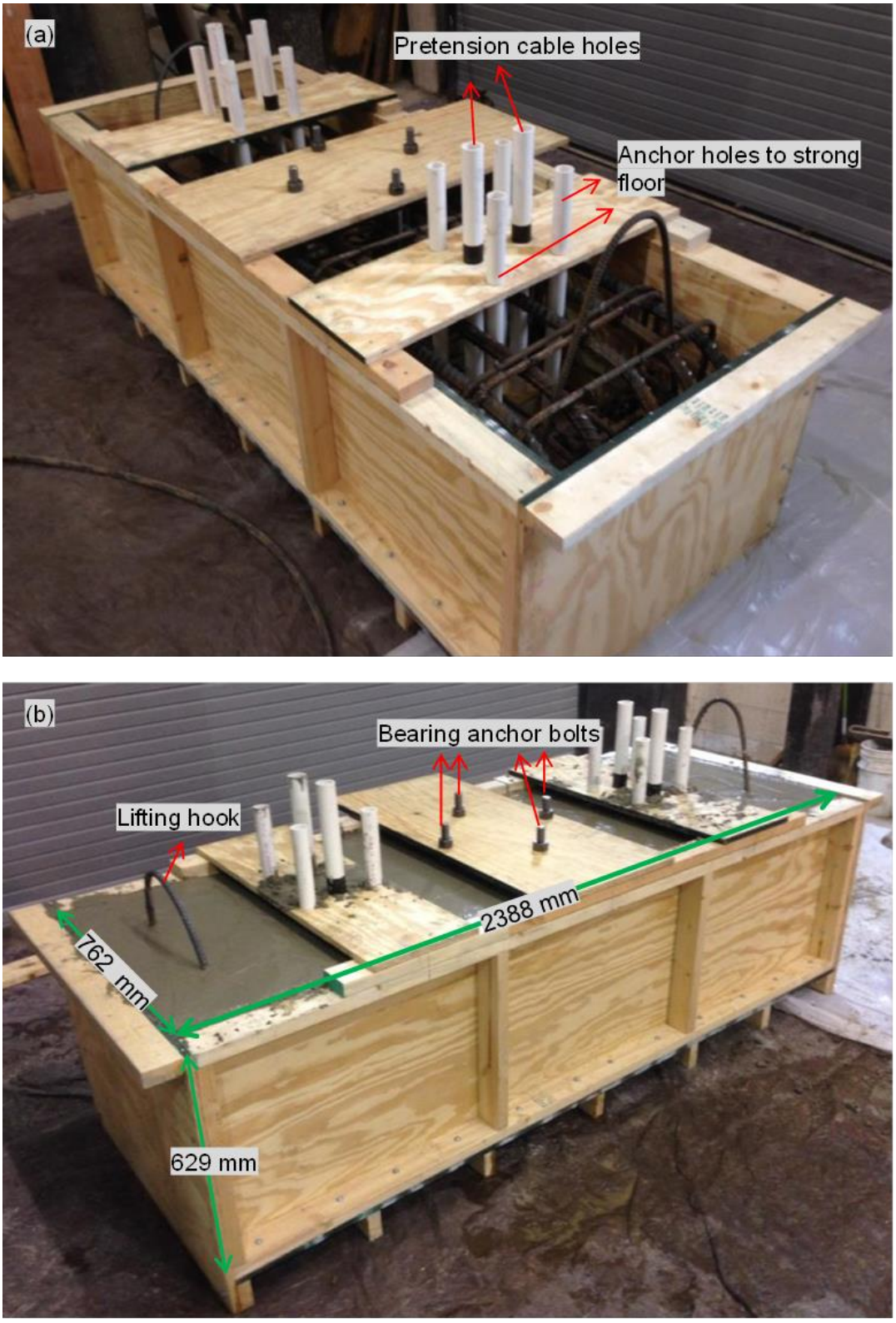

Figure 6.7 Photographs of one reinforced concrete pedestal: (a) reinforcement cage inside the form work and (b) poured concrete pedestal

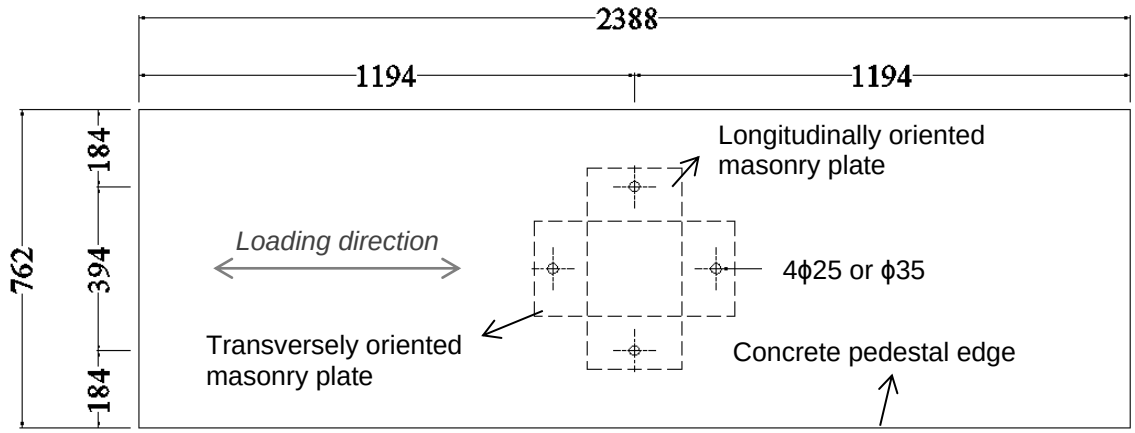

Figure 6.8 Layout of anchor bolts in the concrete pedestal (units are in mm)

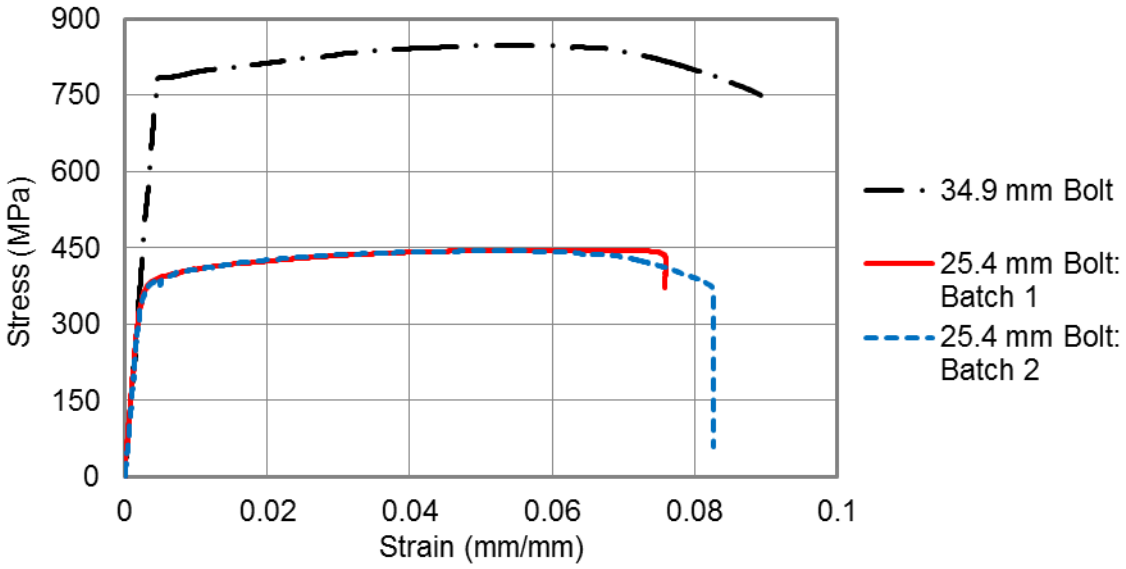

Figure 6.9 Tensile test results of the anchor bolts

Table 6.2 Inventory of the salvaged steel bearings

Bearing ID		Corrosion level	Bearing body weight (kg)				Masonry plate weight (kg)				Total weight (kg)			
			Initial	*As-received*	*Cleaned*	*Loss (%)*	*Initial*	*As-received*	*Cleaned*	*Loss (%)*	*Initial*	*As-received*	*Cleaned*	*Loss (%)*
left abutment	1	Severe	45.1	40.1	37.0	17.8	30.9	27.0	26.9	13.1	76.0	67.1	63.9	15.9
	2	Severe	45.1	44.6	42.4	5.9	30.9	27.9	26.7	13.6	76.0	72.4	69.2	9.0
	3	Severe	45.1	41.0	38.7	14.2	30.9	27.1	26.3	14.8	76.0	68.1	65.0	14.4
	4	Severe	45.1	46.0	43.2	4.3	30.9	28.9	28.2	8.8	76.0	74.9	71.4	6.1
	5	Severe	45.1	43.9	40.6	10.0	30.9	27.4	27.0	12.6	76.0	71.3	67.6	11.1
left pier	6	Minor	42.4	42.7	N/A	0	40.1	41.5	N/A	0	82.5	84.1	N/A	0
	7	Minor	42.4	42.6	N/A	0	40.1	41.4	N/A	0	82.5	84.0	N/A	0
	8	Minor	42.4	43.0	N/A	0	40.1	42.0	N/A	0	82.5	85.0	N/A	0
	9	Minor	42.4	42.5	N/A	0	40.1	41.6	N/A	0	82.5	84.1	N/A	0
	10	Minor	42.4	42.4	N/A	0	40.1	41.8	N/A	0	82.5	84.2	N/A	0
middle pier	11	Minor	47.2	N/A	N/A	N/A	21.6	N/A	N/A	N/A	68.7	69.1	N/A	0
	12	Minor	47.2	N/A	N/A	N/A	21.6	N/A	N/A	N/A	68.7	68.9	N/A	0
	13	Minor	47.2	N/A	N/A	N/A	21.6	N/A	N/A	N/A	68.7	69.1	N/A	0
	14	Minor	47.2	N/A	N/A	N/A	21.6	N/A	N/A	N/A	68.7	69.0	N/A	0
	15	Minor	47.2	N/A	N/A	N/A	21.6	N/A	N/A	N/A	68.7	68.4	N/A	0.5
right pier	16	Minor	42.4	42.0	N/A	0.9	40.1	41.7	N/A	0	82.5	83.7	N/A	0
	17	Minor	42.4	42.2	N/A	0.4	40.1	41.2	N/A	0	82.5	83.4	N/A	0
	18	Minor	42.4	42.5	N/A	0	40.1	42.3	N/A	0	82.5	84.9	N/A	0
	19	Minor	42.4	44.4	N/A	0	40.1	41.5	N/A	0	82.5	85.9	N/A	0
	20	Minor	42.4	44.3	N/A	0	40.1	41.0	N/A	0	82.5	85.4	N/A	0
right abutment	21	Severe	45.1	42.9	40.4	10.4	30.9	28.2	26.8	13.3	76.0	71.2	67.2	11.6
	22	Severe	45.1	42.3	N/A	N/A	30.9	27.7	N/A	N/A	76.0	70.0	N/A	N/A
	23	Severe	45.1	43.6	40.2	10.8	30.9	28.5	28.1	9.1	76.0	72.1	68.3	10.1
	24	Severe	45.1	43.7	N/A	N/A	30.9	27.6	N/A	N/A	76.0	71.3	N/A	N/A
	25	Severe	45.1	41.5	39.2	13.1	30.9	27.3	27.1	12.4	76.0	68.8	66.3	12.8

Table 6.3 Experimental test matrix of the steel bearings

Test sequence	Bearing ID	Corrosion level	Vertical load (kN)	Bolt diameter (mm)	Loading direction	Loading protocol	Condition
1	AR 5	Severe	102	25.4	L	M	As-received
2	AR 5	Severe	102	25.4	L	M	Cleaned
3	AR 25	Severe	102	25.4	T	M	As-received
4	AR 25	Severe	102	25.4	T	M	Cleaned
5	PR 18	Minor	102	25.4	L	M	As-received
6	PR 19	Minor	102	25.4	T	M	As-received
7	PB 12	Minor	102	25.4	L	M	As-received
8	PB 14	Minor	102	25.4	T	M	As-received
9	AR 21	Severe	102	25.4	L	C	As-received
10	AR 21	Severe	102	25.4	L	C	Cleaned
11	AR 23	Severe	102	25.4	T	C	As-received
12	AR 23	Severe	102	25.4	T	C	Cleaned
13	PR 8	Minor	102	25.4	L	C	As-received
14	PR 19	Minor	102	25.4	T	C	As-received
15	PB 14	Minor	102	25.4	L	C	As-received
16	PB 13	Minor	102	25.4	T	C	As-received
17	PB 15	Minor	102	25.4	L	C	As-received
18	PB 11	Minor	102	25.4	T	C	As-received
19	PB 11	Minor	102	34.9	L	C	As-received
20	PB 15	Minor	102	34.9	T	C	As-received

Note: AR=abutment rocker, PR=pier rocker, PB=pier bolster; L=longitudinal, T=transverse; C=cyclic, M=monotonic

6.3 Monotonic Behavior of Steel Bearings

The monotonic tests conducted on the steel bearings provide an understanding of the deformation and failure mode of the abutment rocker bearings with severe corrosion, the pier rocker bearings with minor corrosion, and the pier bolster bearings with minor corrosion. They also provide a base line for considering the effects of cyclic loading. For the longitudinal monotonic tests of the steel rocker bearings, the bearings are first pushed in one direction (positive) to its displacement capacity (or the capacity of the test setup). After unloading, they are then loaded in the opposite direction (negative). This procedure is followed to consider how the uneven corrosion at the contact surface triggers a different rolling response in each direction. All other tests are only performed under

negative loading displacements since the uneven corroded contact surfaces have less directional influence on the transverse behavior of the steel rocker bearings and either the longitudinal or transverse behavior of the steel bolster bearings. The anchor bolts used in all the monotonic tests have a diameter of 25.4 mm with a minimum yield stress of 248 MPa.

6.3.1 Longitudinal response of abutment rocker bearings

The longitudinal monotonic test is conducted on abutment rocker bearing #5 (AR5) as shown in Figure 6.10. This bearing has an overall mass loss of 11% due to corrosion. The as-received conditions of the rolling interfaces of AR5 are illustrated in Figure 6.11 and Figure 6.12 where thick pack rust can be seen on the cylindrical rolling surfaces. Corrosion byproducts are also found covering the pintles and inside the pintle and anchor bolt holes. The top and bottom pintles of AR5 have sustained volume losses of 40% and 77%, respectively, which are evident in Figure 6.13 and Figure 6.14. The top and bottom cylindrical flanges on average have experienced thickness losses of 18% and 30%, respectively. Additionally, the bearing web on average has sustained a 19% reduction in thickness, while the stiffeners sustained a 13% reduction. The asymmetry of the corrosion distribution on the cylindrical surface is also obvious in these figures.

The first monotonic test of AR5 consists of increasing positive displacements at increments of 1.6 mm. The bearing is pushed toward the west (see definition in Figure 6.1) reaching a maximum displacement of 70 mm shown in Figure 6.15(a). The optotrak markers are deployed in the pattern shown in Figure 6.15. The resulting load deformation curve under positive displacement is shown in Figure 6.16. The load-displacement behavior consists of two noticeable modes of deformation, rolling and rocking. The initial stiffness of the bearing under positive displacement loading is 2 kN/mm. After reaching a positive load of 1.88 kN at 0.9 mm, the bearing resistance gradually decreases to -3.9 kN as the displacement level increases to 42 mm, resulting in a negative rolling stiffness of -0.14 kN/mm. This negative stiffness is due to the uneven section loss of the top and bottom cylindrical surfaces induced by corrosion. The bearing resistance shows a rapid increase from -3.9 kN at 42 mm to 39 kN at 70 mm. The secant stiffness of the bearing

measured at the maximum positive displacement reaches 0.56 kN/mm, which exhibits a 33% reduction from the theoretical secant stiffness of 0.84 kN/mm obtained for uncorroded rocker bearings in Chapter 3.

After repositioning AR5 to its rest position, a second monotonic test is performed on the bearing toward the east (see Figure 6.1) with negative loading displacements. The displacement increment used is -1.6 mm. The bearing is taken to a maximum displacement of -70 mm. The resultant response is shown in the negative displacement range of the plot given in Figure 6.16. Three different deformation modes are seen in the response, which consist of rolling, rocking, and sliding. The initial stiffness is 1 kN/mm which is 50% less than that of the positive loading response. Having a small negative stiffness of -0.3 kN/mm, the rolling response starts with a load level of -0.3 kN at -0.3 mm and ends at -32.4 mm with a resistance of 9.6 kN. The negative stiffness is again due to uneven section loss distribution on the cylindrical surfaces caused by corrosion. A rapid increase in resistance is seen from 9.6 kN to -25.6 kN at -59 mm due to rocking. Sliding of the bearing and the masonry plate together on top of the steel pedestal is observed during testing in the displacement range of -59 mm to -70 mm rendering a roughly constant bearing resistance of 26 kN. The secant stiffness of the bearing measured at the maximum negative longitudinal displacement is 0.37 kN/mm smaller than the secant stiffness obtained in the positive loading direction.

Post-test examination of the bearing shows that most of the pack rust on the contact surfaces becomes loose and detached during loading. After testing, the bearing is then cleaned with a metal scraper to remove all of the remaining rust layers on the bearing surface. The cleaned condition of AR5 is shown in Figure 6.13 and Figure 6.14 where the top and bottom contact surfaces and what remains of the pintles are shown without the pack rust. In order to understand the effect of corrosion byproducts on the lateral monotonic behavior of the bearing, AR5 is subjected to the same loading protocol as with the as-received tests. Test results from the positive and negative loading are combined into one curve and given in Figure 6.17.

The initial stiffness of the cleaned bearing under positive loading is 3 kN/mm, 1 kN/mm larger than that of the as-received bearing. The rolling response initiates at 0.4 mm with a resistance of 1.2 kN and stops at 35.5 mm with a resistance of -9.3 kN. The rocking response begins at 35.5 mm of displacement leading to a rapid increase in stiffness and resistance. A 62 kN resistance is achieved at 70 mm of displacement resulting in a secant stiffness of 0.89 kN/mm, which is close to the theoretical value.

The negative loading response of the bearing shows an initial stiffness of 5.3 kN/mm. The rolling plateau starts at -0.3 mm with a resistance of -1.4 kN and ends at -30.4 mm with a resistance of 4.8 kN showing a negative rolling stiffness of -0.21 kN/mm. The rocking response also shows a sudden increase in stiffness and resistance that reach 1.4 kN/mm and -36 kN, respectively. Significant sliding is observed during testing after the displacement level surpasses -59 mm. At the maximum displacement of -70 mm, the negative secant stiffness is 0.53 kN/mm smaller than that measured during positive loading.

The response of the cleaned bearing shows a larger initial stiffness, a shorter rolling plateau, and a larger secant stiffness compared to the as-received response of the bearing. For AR5, the cleaned rocker bearing body has a reduced height due to the removal of the thick rust layers from the contact surfaces meanwhile the effect of the rust removal on the radius of the cylindrical surfaces is minimal. Equation 3-11 indicates that if the height of the rocker body (h_0) decreases while the radius of the cylindrical surfaces (r) stays the same, a larger resistance and secant stiffness are expected. Even though Equation 3-11 is not applicable to the corroded abutment bearings, it still qualitatively explains why AR5 has larger secant stiffness and resistance after rust removal.

In addition, significant disparities exist between the positive and negative loading responses with respect to initial stiffness, rolling stiffness, rocking stiffness, and maximum resistance. The differences between various stiffness terms are due to uneven section loss on the cylindrical contact surfaces caused by corrosion. The disparity between the absolute maximum positive and negative resistances is 13 kN for the as-received bearing test and increases to 25 kN for the cleaned bearing test. This asymmetric

monotonic response owes directly to the nonhomogeneous development of corrosion on the rolling cylindrical surfaces, which needs to be properly accounted for when evaluating the lateral behavior of in-situ steel bearings and the bridges in which they are installed.

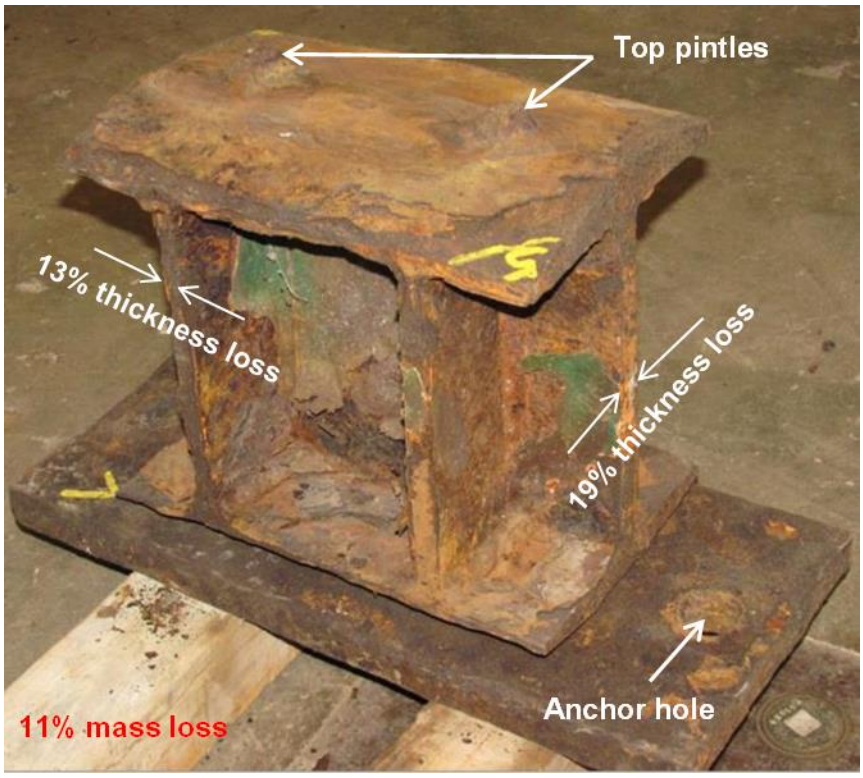

Figure 6.10 Abutment rocker bearing #5 (AR5) in its as-received condition

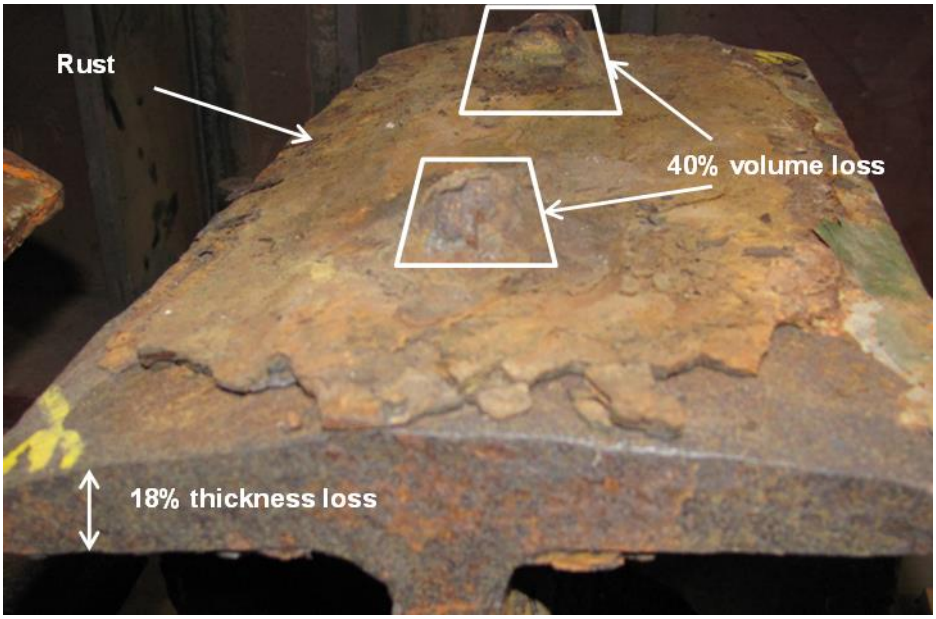

Figure 6.11 Top cylindrical rolling surface of AR5 before rust removal

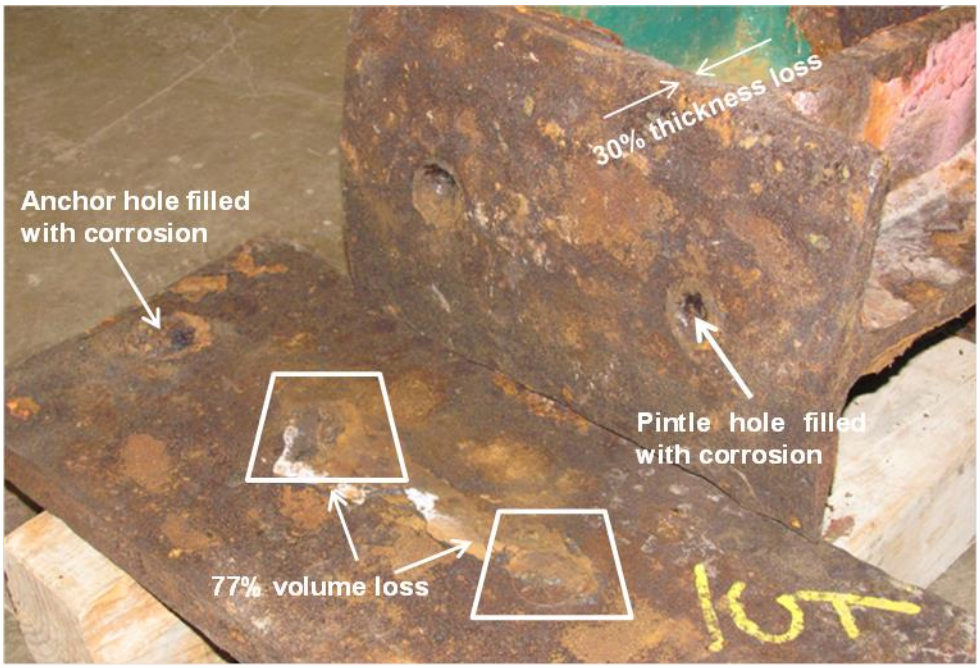

Figure 6.12 Bottom rolling interface of AR5 in the as-received condition

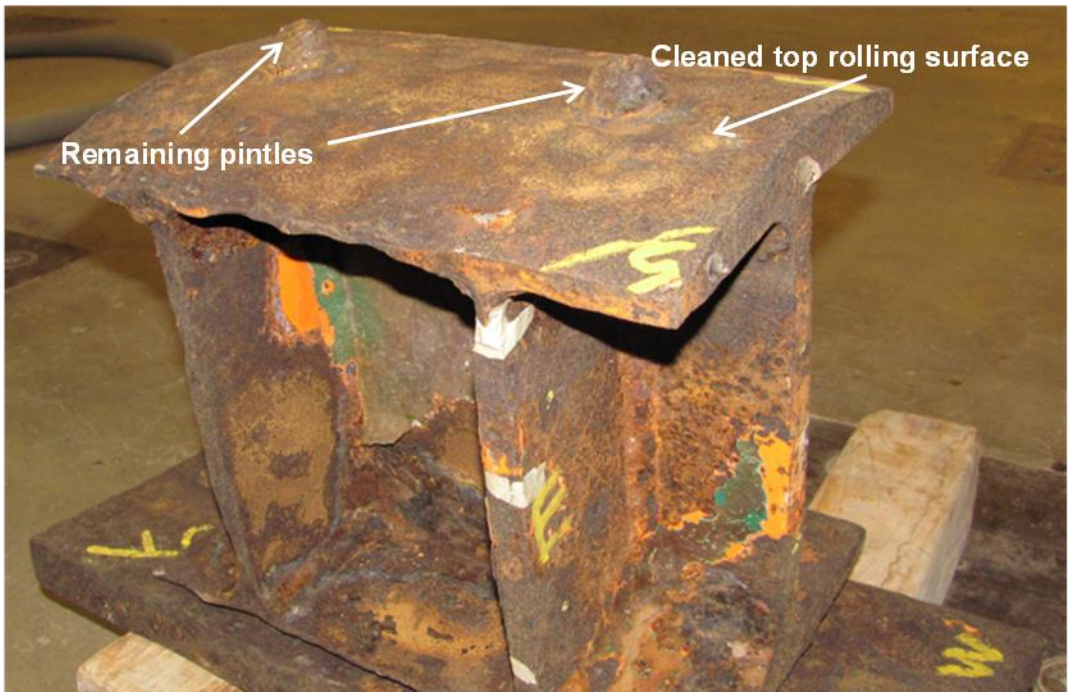

Figure 6.13 AR5 rocker bearing with surface rust removed after the first set of monotonic tests

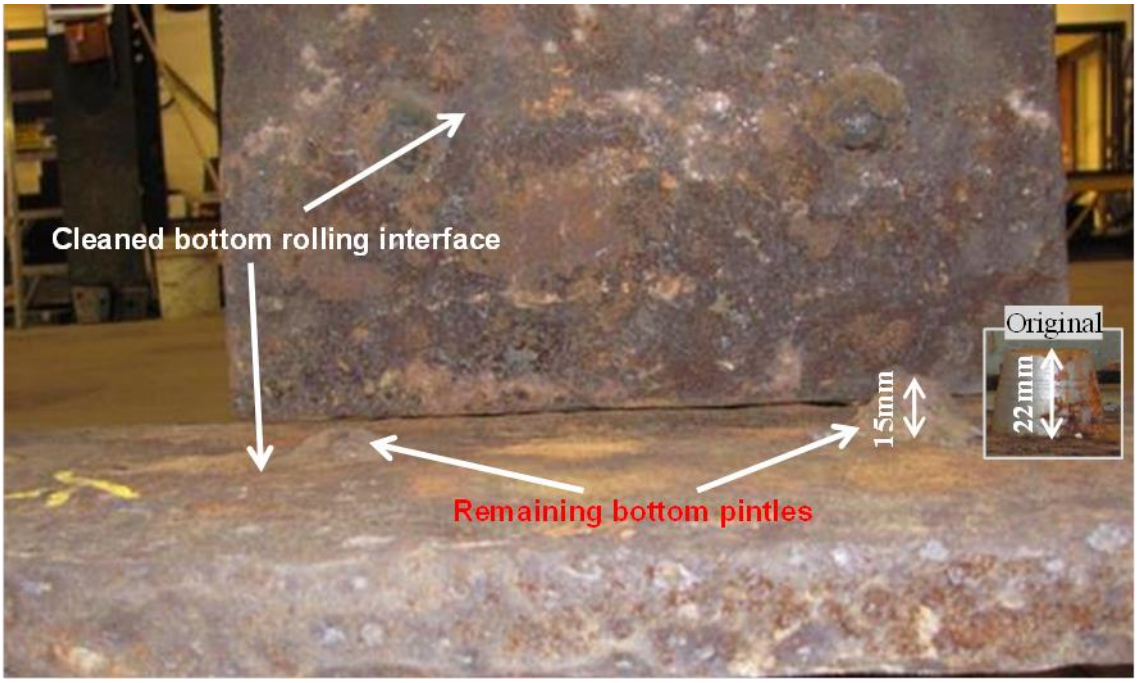

Figure 6.14 Cleaned bottom rolling interface of AR5

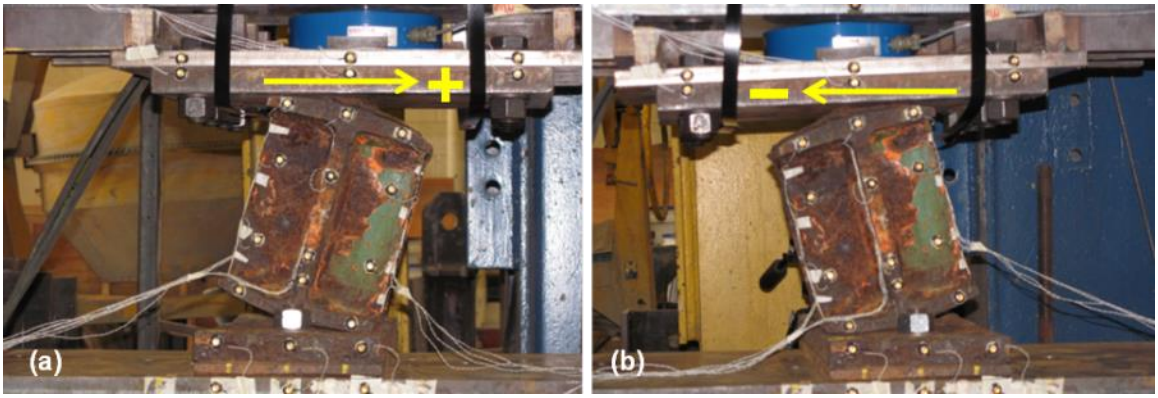

Figure 6.15 Photographs during testing of the as-received AR5 under (a) positive monotonic loading and (b) negative monotonic loading

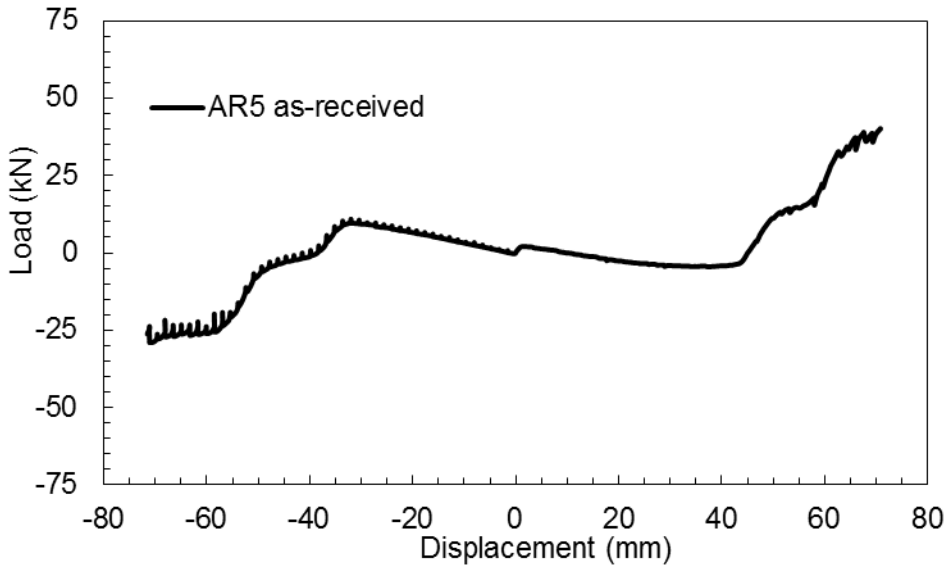

Figure 6.16 Full longitudinal response of the abutment rocker bearing (AR5) in the as-received condition under positive and negative monotonic loading

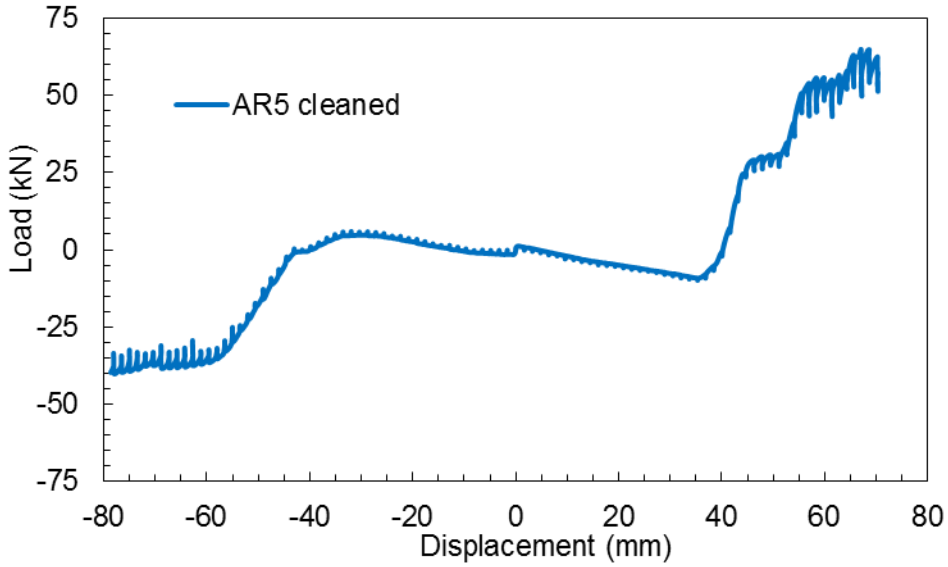

Figure 6.17 Full longitudinal response of the abutment rocker bearing (AR5) in the cleaned condition under positive and negative monotonic loading

6.3.2 Transverse response of abutment rocker bearings

The transverse monotonic test is conducted on abutment rocker bearing #25 (AR25) that has an overall mass loss of 13%. Figure 6.18 provides a photograph of this bearing in the as-received condition. Figure 6.19 and Figure 6.20 show in more detail the corroded condition at the top and bottom contact surfaces. Corrosion byproducts are found inside both the pintle and anchor bolt holes. As shown in Figure 6.21 and Figure 6.22, volume losses of the top and bottom pintles of AR25 reach 22% and 62%, respectively. Section losses of the top and bottom contact surfaces are 18% and 26%, respectively. The web has sustained a 37% section loss, while the stiffeners a 16% section loss. The masonry plate of AR25 has experienced a thickness reduction of 9%. The cleaned AR25 bearing can no longer rest in an upright position as shown in Figure 6.21, which provides further evidence that corrosion is unevenly distributed over the bearing and is capable of causing unanticipated lateral bearing behavior.

The transverse monotonic test is conducted only under negative monotonic loading. A maximum displacement of -50 mm is applied to the bearing. Figure 6.23 clearly shows significant tipping of the rocker bearing body at this displacement and how one of the bottom pintles disengages due to tipping. Sudden sliding of the masonry plate occurs during the test when the displacement level exceeds -30 mm resulting in a load drop of over 50 kN in magnitude (Figure 6.24). However, no continuous sliding is observed in the test results. The main deformation mode of the bearing is tipping of the rocker body. The initial stiffness of the bearing is 46 kN/mm. The maximum load reaches 241 kN at -50 mm resulting in a secant stiffness of 4.8 kN/mm. Based on Equation 3-13, the maximum shear capacity of the bearing can be estimated. Since the bolts used in the test have a diameter of 25.4 mm and are smaller than the pintle diameter, the shear capacity at the anchor bolt shear interface should govern. By substituting the anchor bolt fracture strength obtained from the tensile test in Section 6.2.6 into Equation 3-13, a shear capacity of 320 kN is obtained which is larger than that obtained during testing and provide a reason why anchor bolt failure did not occur.

All pack rust is removed from Bearing AR25 after the initial monotonic test. It is then reinstalled in the test setup to be tested in its cleaned condition. This test again examines whether cleaning can be used as a potential retrofit method and the variations it introduces in the bearing behavior under transverse monotonic loading. It is obvious that the masonry plate slides twice during testing at -22 mm and -32 mm, respectively, which leads to an abrupt drop in the load of over 60 kN at these displacements (see Figure 6.25). Each time the masonry plate slides, the rocker bearing body experiences a backward rocking that brings the rocker body back to its upright position. The predominant deformation mode of the rocker bearing is still tipping without continuous sliding, which is identical to what is observed in the test of the as-received bearing. The maximum applied displacement is -57 mm. At the maximum applied displacement, the bottom west pintle again is seen completely disengaged from the pintle hole in the rocker bearing body. The initial stiffness of the cleaned bearing is 21 kN/mm. The maximum measured load is -319 kN at -57 mm giving a secant stiffness of 5.6 kN/mm that is slightly larger than that of the as-received bearing. The cleaned rocker bearing also reaches a load of -280 kN at -50 mm which is roughly 40 kN larger in magnitude than the load of the as-received bearing at the same displacement. These differences are largely associated with the section variation along the top and bottom cylindrical surfaces due to rust removal.

In general, the test results of AR25 in the as-received and cleaned conditions are similar with respect to the load-deformation behavior. Both specimens experience sudden sliding of the masonry plate and consequent load drops at similar displacement levels. The cleaned specimen response provides a larger secant stiffness than the as-received specimen. Overall, tipping is the predominant deformation mode of the bearing under monotonic transverse loading whether as-received or cleaned. Sliding of the rocker body is minimal, potentially due to the rough contact surfaces shown in Figure 6.22.

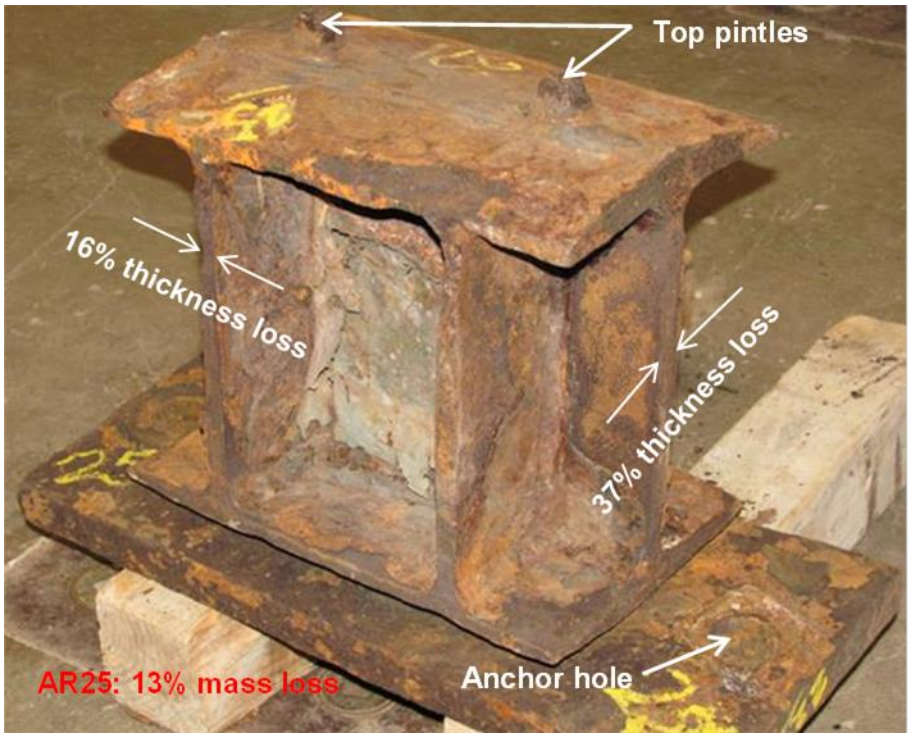

Figure 6.18 Abutment rocker bearing #25 (AR25) in its as-received condition

Figure 6.19 Top cylindrical contact surface of AR25 before rust removal

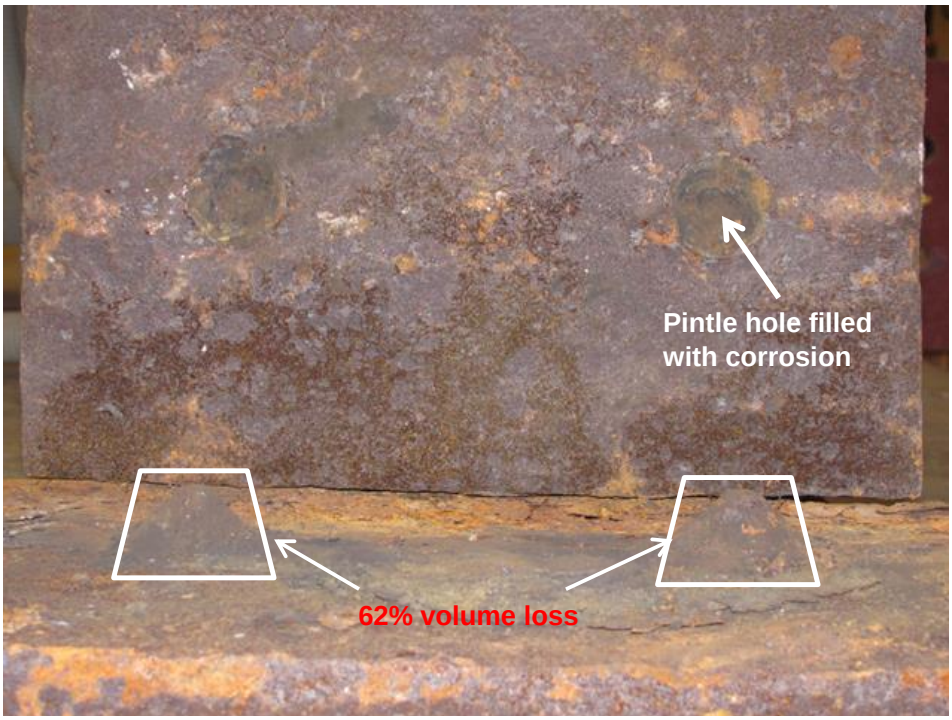

Figure 6.20 Bottom contact interface of the AR25 bearing in the as-received condition

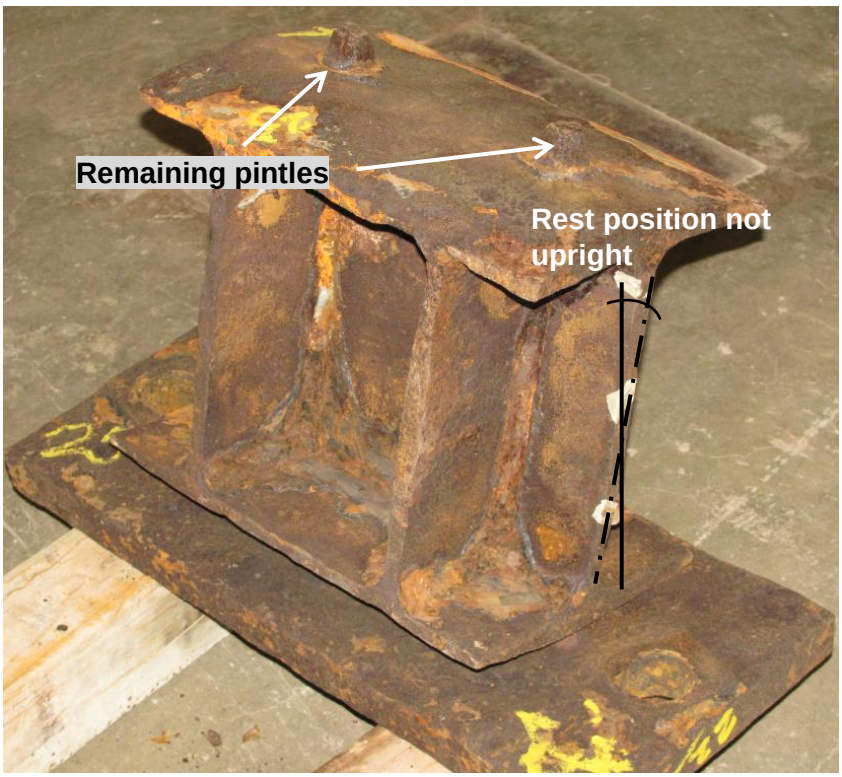

Figure 6.21 Bearing AR25 with rust removed after the initial monotonic tests

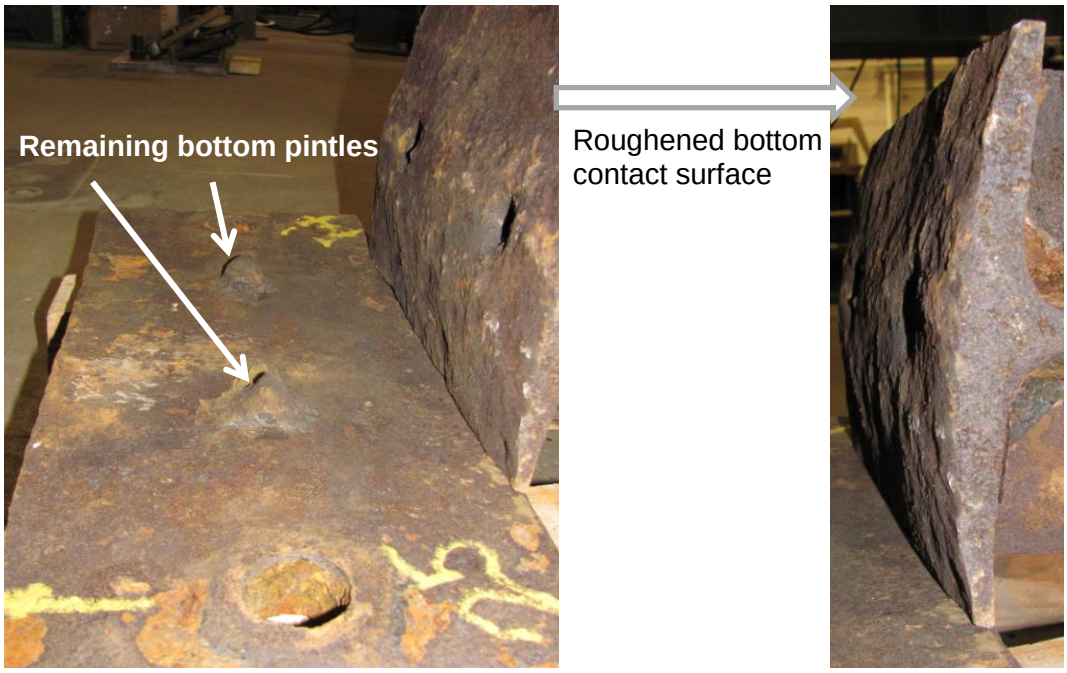

Figure 6.22 Cleaned bottom contact interface of bearing AR25

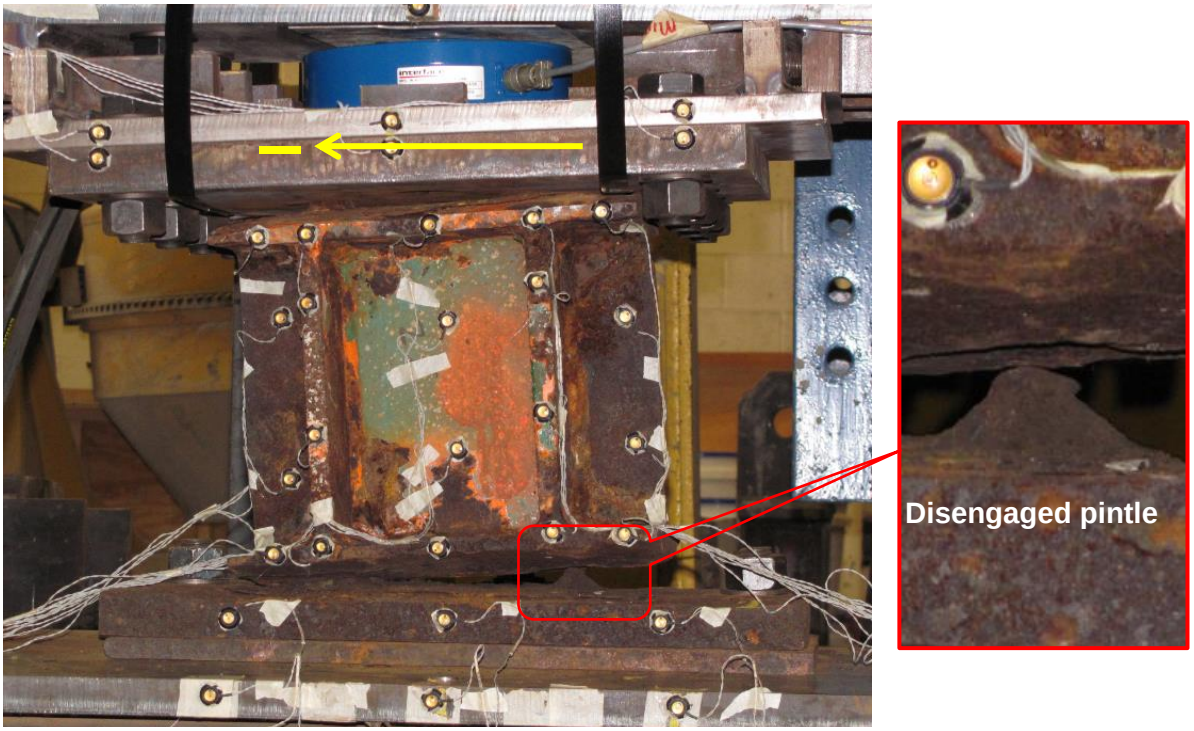

Figure 6.23 Test photographs of the as-received AR25 bearing under negative monotonic loading

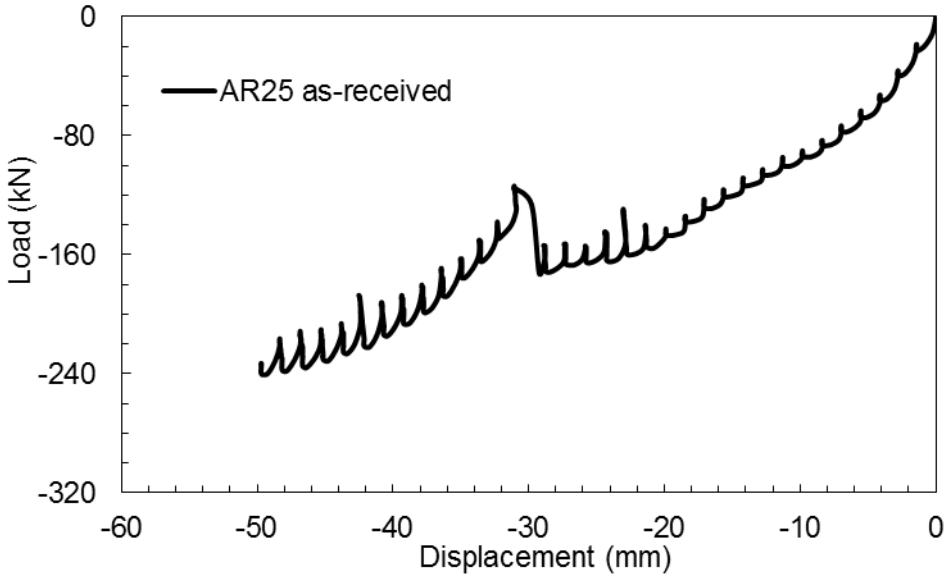

Figure 6.24 Transverse response of the AR25 bearing in the as-received condition under negative monotonic loading

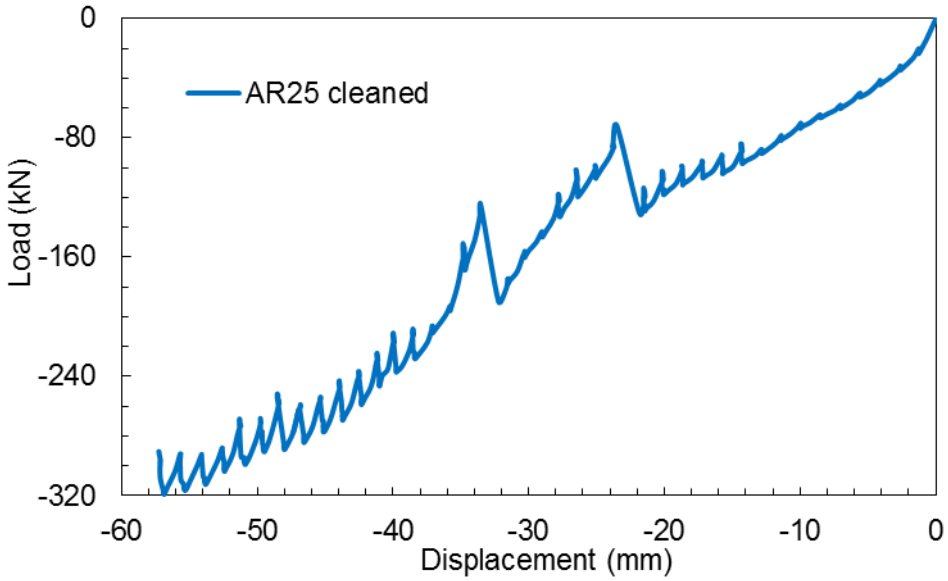

Figure 6.25 Transverse response of the AR25 bearing in the cleaned condition under negative monotonic loading

6.3.3 Longitudinal response of pier rocker bearings

The monotonic test of the longitudinal behavior of the pier rocker bearings is conducted on pier rocker bearing #18 (PR18). As shown in Figure 6.26, PR18 is in a well-maintained condition with negligible corrosion. The top pintles are intact with minimal corrosion. Only minor corrosion is seen on the top surface at the contact region (Figure 6.27). The bottom cylindrical surface also has sustained minor corrosion at the contact region (Figure 6.28). At the bottom contact interface, the pintles are still in good condition while the pintle holes also have negligible corrosion as seen in Figure 6.28. The masonry plate for all of the pier rocker bearings has a larger thickness of 47.6 mm, by design, compared to the masonry plate for the abutment bearings. Figure 6.28 also shows that the masonry plate is in a satisfactory condition with only minor corrosion and some loose paint at the contact region. Similar to the longitudinal tests of the abutment rocker bearings, bearing PR18 is also monotonically tested in both the positive and negative direction. Figure 6.29 shows the optotrak marker layout and provides two photographs taken during testing.

The positive monotonic response of the bearing is shown in Figure 6.30. The initial stiffness of the bearing is 2.9 kN/mm. A prominent rolling response, shown between 2 mm and 25 mm, governs the behavior. The rolling resistance is approximately 5 kN. Once the displacement exceeds 25 mm, the bearing response steadily increases for both the secant stiffness and resistance reaching 0.49 kN/mm and 30 kN at 77 mm of displacement. During this portion of the loading, the masonry plate begins to slightly slide. A secant stiffness of 0.39 kN/mm is achieved at the 77 mm displacement level.

The negative monotonic response of the bearing is also shown in Figure 6.30. The initial stiffness is 5 kN/mm. A dominant rolling behavior again is seen in the response between displacements of -2 mm and -25 mm with a rolling resistance of -10 kN. The resistance then gradually starts to increase after the displacement surpasses -25 mm, which reaches -57 kN at the maximum displacement of -74 mm. A secant stiffness of 0.77 kN/mm is achieved at this displacement level. Slight masonry plate sliding is observed after the displacement exceeds -25 mm and as the load level increases.

6.3.4 Transverse response of pier rocker bearings

Pier rocker bearing #19 (PR19) is tested monotonically under transverse loading to investigate the transverse behavior of rocker bearings that are in good condition. Figure 6.31 shows that bearing PR19 has experienced very minor corrosion to its top pintles, top contact surface, webs and stiffeners. The top contact surface shown in Figure 6.32 has minor corrosion at the contact region while most of the cylindrical surface is still protected by paint. Similar observations are found for the bottom contact interface consisting of the bottom cylindrical surface and the masonry plate. In Figure 6.33, minor corrosion can be seen at the contact regions of the cylindrical surface and the top surface of the masonry plate while the pintles and pintle holes show no visual corrosion effects and still have the protective paint on them. Only minor corrosion is found inside the anchor bolt holes without any significant rust buildup. The optotrak markers are distributed as shown in Figure 6.34.

A displacement increment of -1.6 mm is used for the monotonic transverse test. The initial deformation mode of Bearing PR19 is sliding of the rocker body together with the masonry plate on top of the steel pedestal. Tipping of the rocker body dominates the deformation mode after the bolt hole clearance is exhausted and the bolts start to bear on the masonry plate. The west pintle is exposed at larger displacement levels as seen in Figure 6.34. The overall load-deformation relationship is given in Figure 6.35. The initial stiffness of the bearing is 60 kN/mm. The bearing has a resistance of -348 kN at its largest applied displacement of -43 mm. This leads to a secant stiffness of 8.1 kN/mm measured at a -43 mm displacement.

6.3.5 Corrosion effect on steel rocker bearing monotonic behavior

The longitudinal and transverse behavior of the steel rocker bearings with minor corrosion, severe corrosion, and in a cleaned condition has been studied under monotonic loading. The responses obtained from these bearing tests are discussed in the preceding sections. This section focuses on comparing the responses of the abutment rocker bearing and the pier rocker bearing to demonstrate the effect of corrosion on the lateral behavior

of steel rocker bearings. Values obtained for the key parameters of the bearing behavior from these test are compiled in Table 6.4 and Table 6.5.

The longitudinal bearing results for the rocker bearings from the positive and negative loading tests are averaged in Table 6.4 to simplify the discussion. For the longitudinal behavior, the pier rocker bearing and the abutment rocker bearing show similar deformation modes consisting of rolling and rocking (i.e. tipping). However, significant differences exist in the values of the key parameters indicating the effect corrosion has on their response (Table 6.4). The initial stiffness sees a major decrease from 4 kN/mm for the pier rocker bearing to 1.5 kN/mm for the abutment rocker bearing. The pier rocker bearing shows a zero rolling stiffness with a constant rolling resistance of 10 kN, while the abutment rocker bearing has a negative rolling stiffness of -0.2 kN/mm indicating instability of the bearing body caused by uneven corrosion distribution at the contact surfaces. The maximum longitudinal resistance decreases from 43.5 kN for the pier rocker bearing to 32.5 kN for the abutment rocker bearing. However, both bearings are capable of accommodating significant longitudinal displacements up to 70 mm. These results suggest that corrosion has caused significant degradation in the longitudinal load-deformation relationship of the steel rocker bearing with respect to initial stiffness, rolling stiffness, secant stiffness, and maximum load capacity, but the longitudinal displacement capacity has not sustained any major decrease.

The cleaned abutment rocker bearing exhibits an improved behavior compared to the as-received bearing in that major increases in the initial stiffness and the overall secant stiffness are achieved. Both the initial stiffness (4.2 kN/mm) and the secant stiffness (0.7 kN/mm) of the cleaned abutment rocker bearing are comparable to those of the pier rocker bearing. An increase in the maximum resistance to 49 kN is also observed for the cleaned bearing test. The maximum applied displacement for the cleaned abutment rocker is on a par with that for the pier rocker bearing reaching 70 mm as well.

The transverse behavior of the steel rocker bearings shows major disparities regarding deformation mode, stiffness, and displacement capacity between the pier rocker bearing and the abutment rocker bearing (Table 6.5). The pier rocker bearing undergoes steady

masonry plate sliding while the abutment rocker bearing experiences sudden slipping of the masonry plate that induces abrupt load drops during rocking. The transverse resistance of the pier rocker bearing undergoes a larger increase when the displacement increases from -5 mm to -20 mm than the abutment rocker bearing over this displacement range. At a -20 mm displacement, the pier rocker bearing has a resistance of -250 kN, roughly 100 kN larger in magnitude than that of the abutment rocker bearing. Both bearings then undergo a relatively slow increase in resistance as the displacement increases to -30 mm. Another steady increase in resistance is seen in both bearing responses when the displacement is further increased.

The pier rocker bearing achieves a maximum resistance of -348 kN at a displacement of -43 mm while the abutment rocker bearing reaches a maximum resistance of -241 kN at -50 mm. The initial stiffness of the pier rocker bearing (60 kN/mm) is larger than that of the abutment rocker bearing (46 kN/mm). The secant stiffness of the abutment rocker bearing also is 3.3 kN/mm below that of the pier rocker bearing. These findings show that corrosion significantly affects the transverse behavior of the steel rocker bearings.

The cleaned abutment rocker bearing shows a large decrease in the initial stiffness and a slight increase in the overall secant stiffness compared with the as-received abutment bearing. The maximum resistance of the cleaned bearing (319 kN) is comparable to the 348 kN achieved by the pier bearing. These observations suggest that cleaning of the corrosion byproducts can have varying influence and improvement on the bearing behavior.

In general, corrosion of the steel rocker bearings has a significant influence on their lateral (longitudinal and transverse) load-deformation relationships causing reductions in stiffness and resistance. While corrosion has an impact on the deformation modes of the rocker bearing, it causes negligible impact to its displacement capacities. Cleaning of the abutment rocker bearings generally leads to an improved performance in terms of stiffness and resistance.

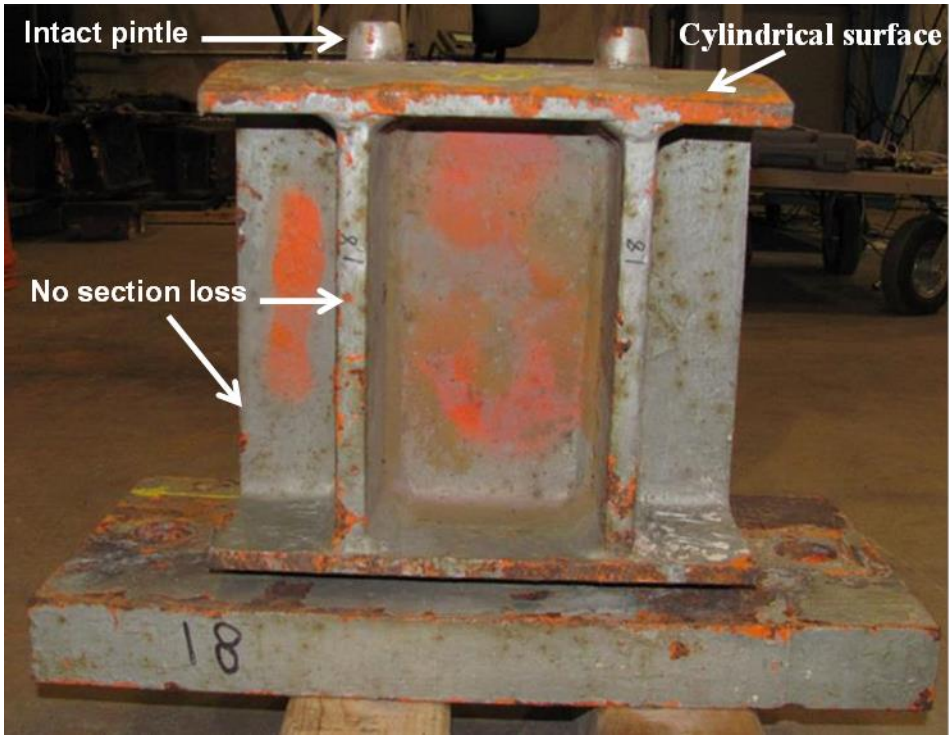

Figure 6.26 Pier rocker bearing #18 (PR18) in the as-received condition

Figure 6.27 Top cylindrical contact surface of Bearing PR18

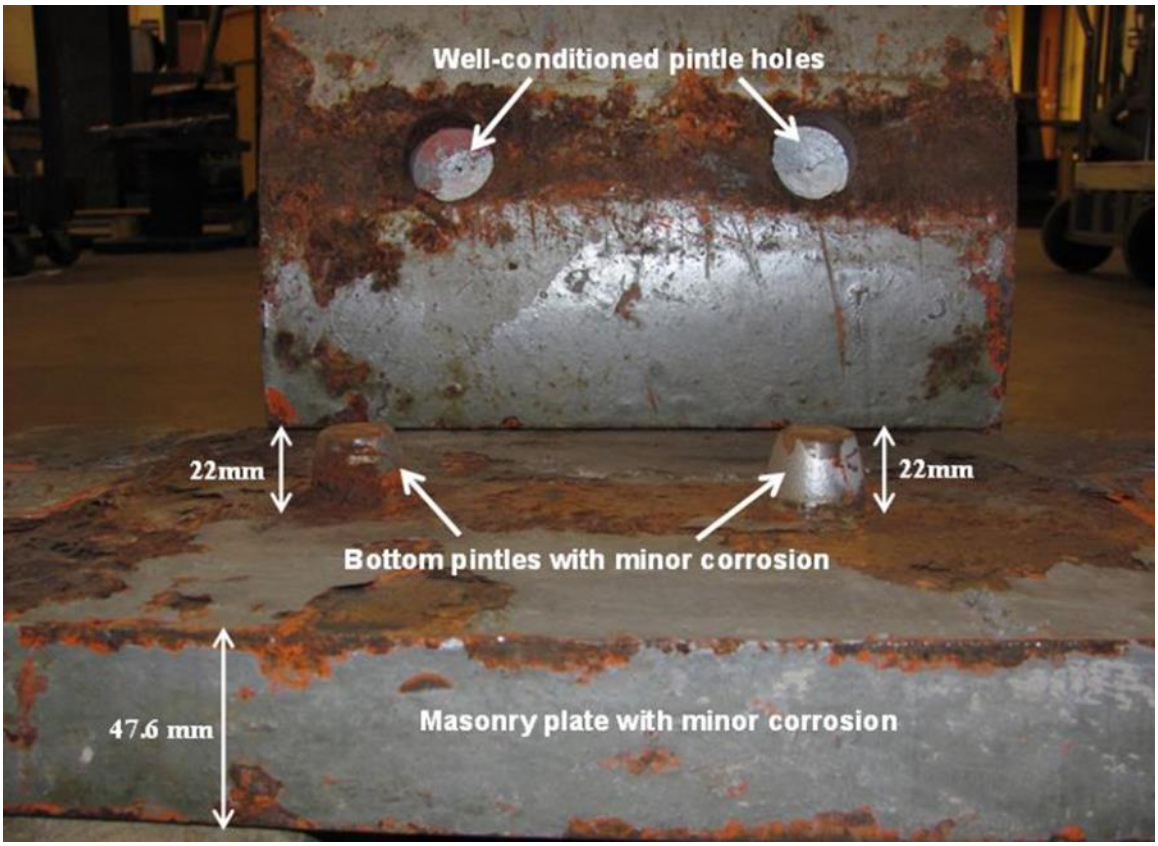

Figure 6.28 Bottom contact interface of Bearing PR18 in the as-received condition

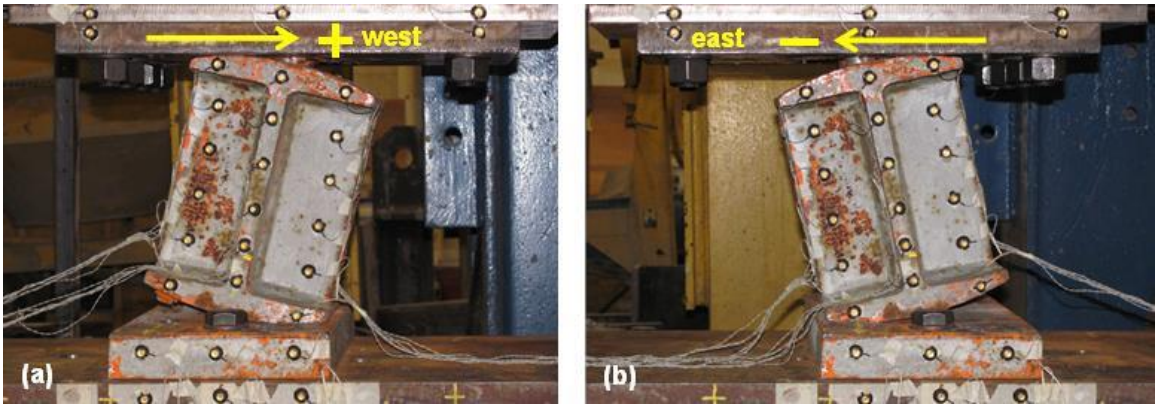

Figure 6.29 Test photographs for Bearing PR18 under (a) positive monotonic loading and (b) negative monotonic loading

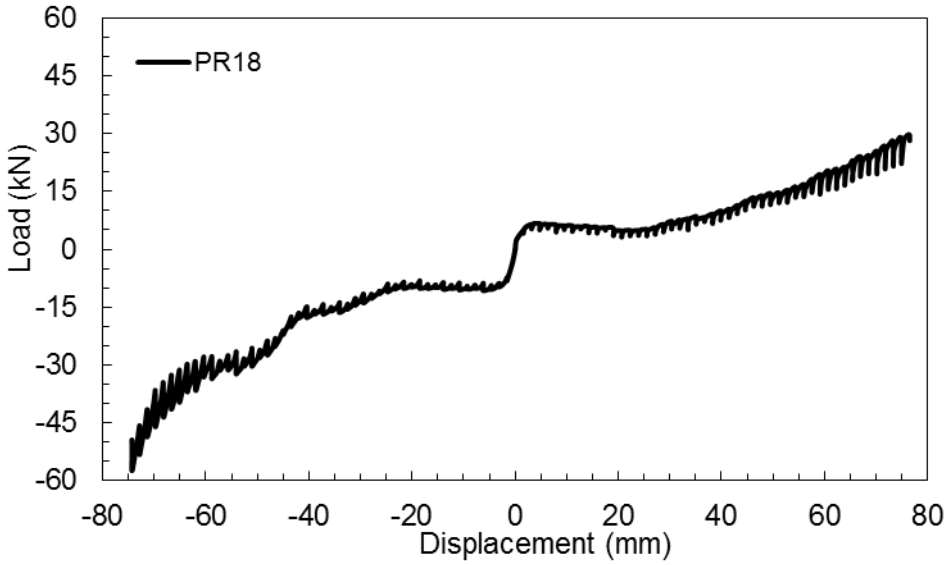

Figure 6.30 The full longitudinal response of Bearing PR18 in the as-received condition under positive and negative monotonic loading

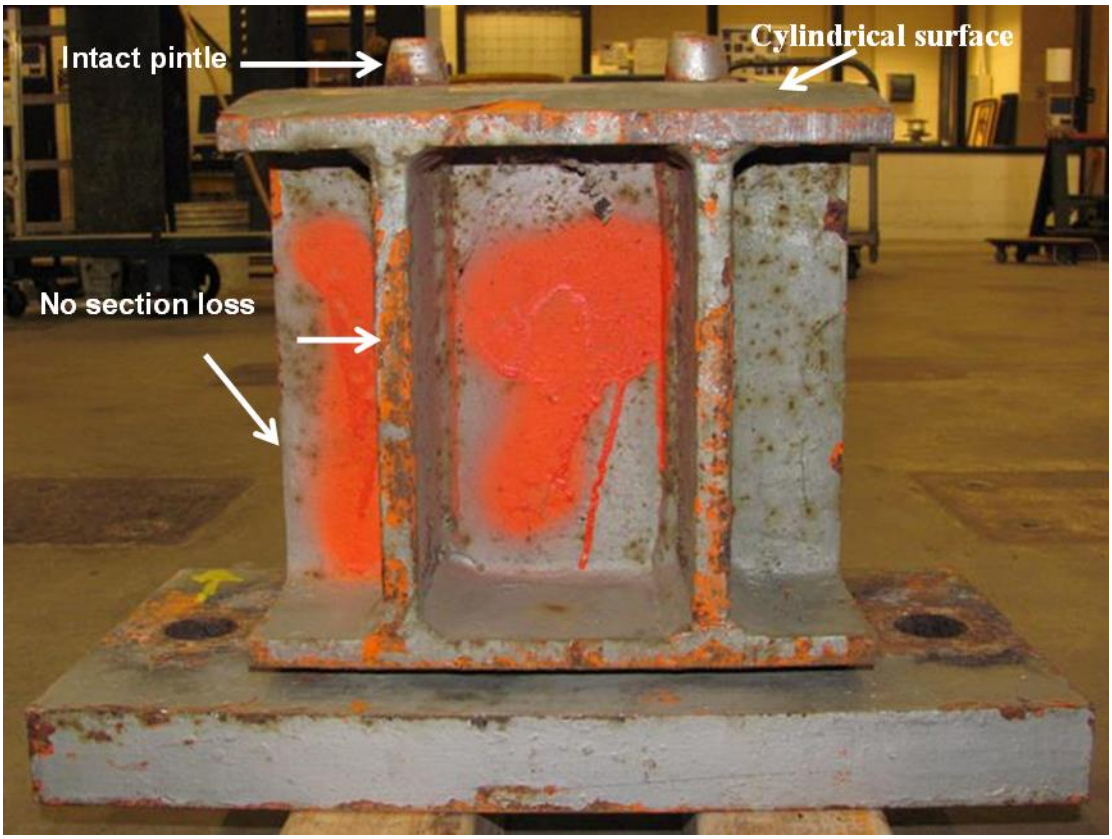

Figure 6.31 Pier rocker bearing #19 (PR19) in the as-received condition

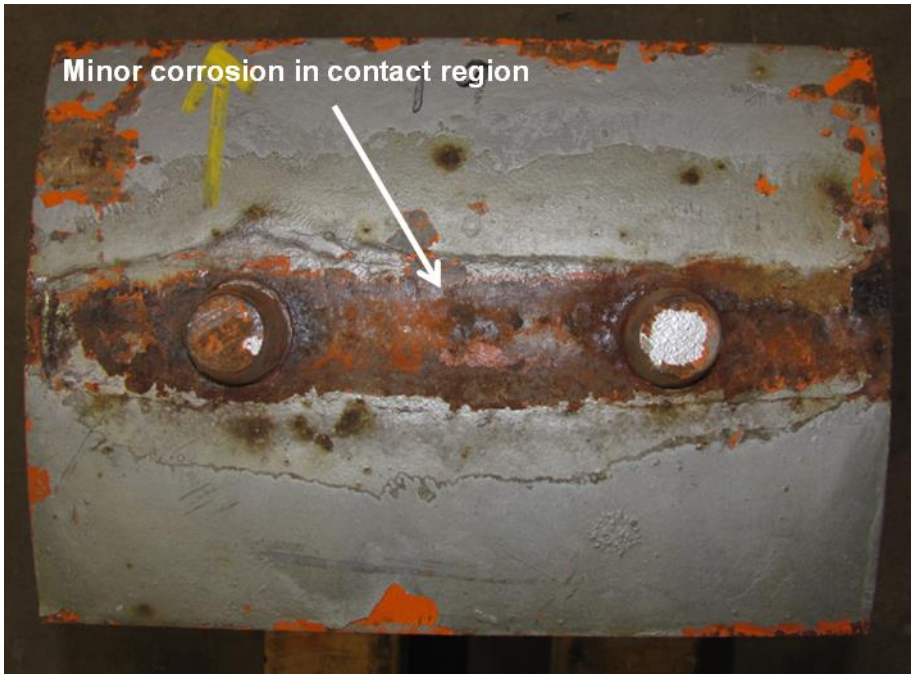

Figure 6.32 Top cylindrical contact surface of Bearing PR19

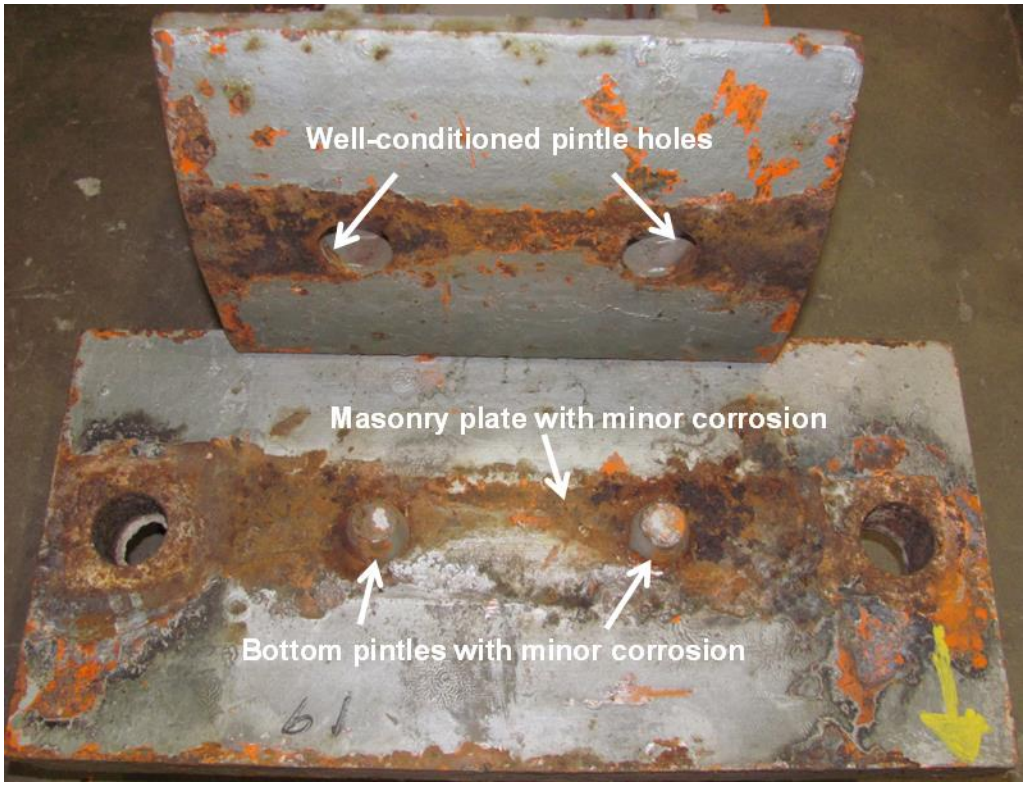

Figure 6.33 Bottom contact interface of Bearing PR19

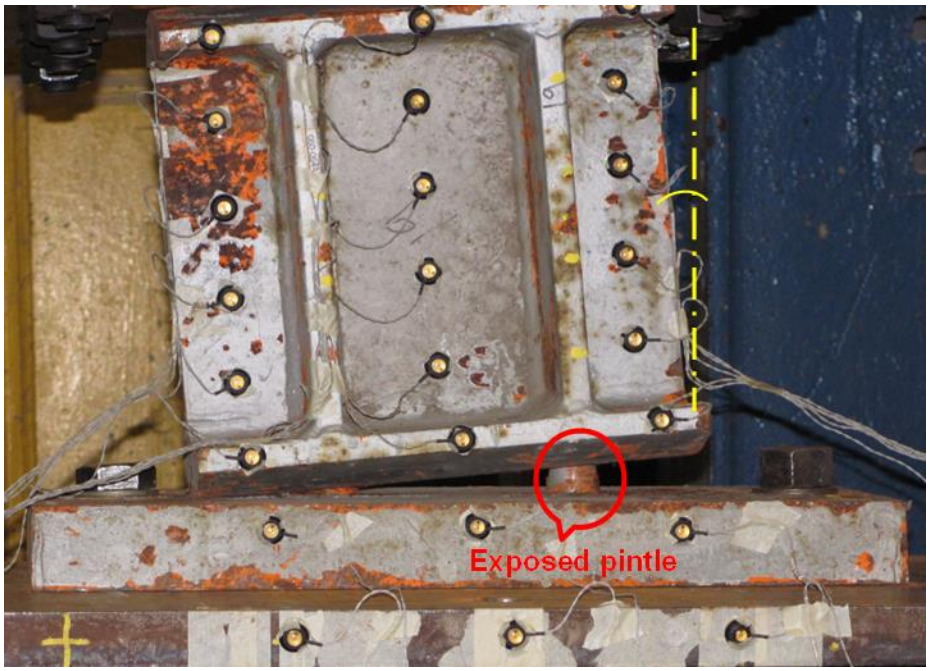

Figure 6.34 Photographs during testing of Bearing PR19 under transverse monotonic loading

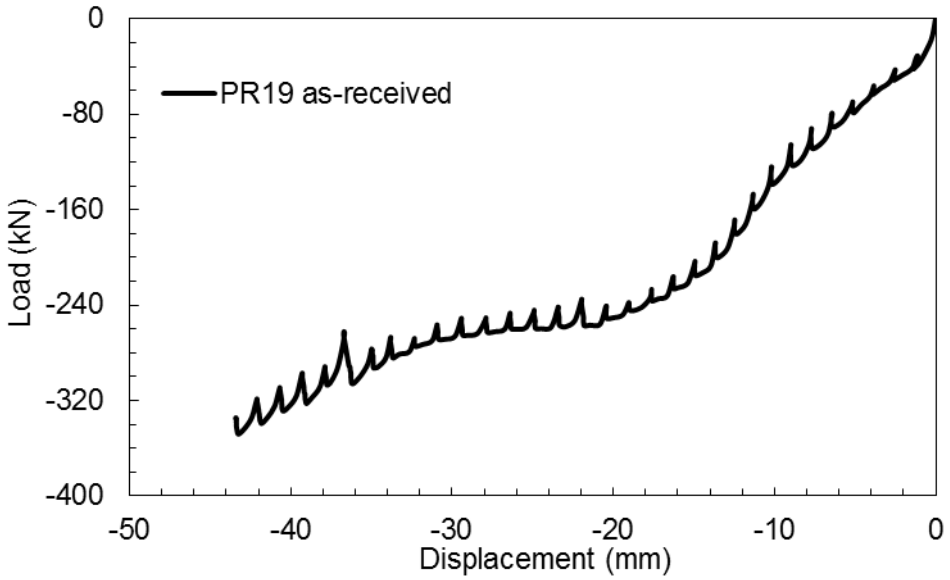

Figure 6.35 The transverse response of Bearing PR19 in the as-received condition under negative monotonic loading

Table 6.4 Summary of the monotonic test results for the steel rocker bearings under longitudinal displacements

Bearing ID	Initial stiffness (kN/mm)	Rolling stiffness (kN/mm)	Maximum load (kN)	Maximum displacement (mm)	Secant stiffness measured at maximum displacement (kN/mm)
PR18 as-received	4.0	0	43.5	75.5	0.6
AR5 as-received	1.5	-0.2	32.5	70	0.5
AR5 cleaned	4.2	-0.3	49	70	0.7

Table 6.5 Summary of the monotonic test results for the steel rocker bearings under transverse displacements

Bearing ID	Initial stiffness (kN/mm)	Maximum load (kN)	Maximum displacement (mm)	Secant stiffness measure at maximum displacement (kN/mm)
PR19 as-received	60	348	43	8.1
AR25 as-received	46	241	50	4.8
AR25 cleaned	21	319	57	5.6

6.3.6 Longitudinal response of steel bolster bearings

The longitudinal monotonic test of the steel bolster bearings is carried out on pier bolster bearing #12 (PB12). Bearing PB12 shown in Figure 6.36 has only minor corrosion present at the bearing surface. Minimal corrosion effects are seen on the pintles as well. Only minor corrosion of the contact region at the top surface is observed (Figure 6.37). The bolster bearing body, including the web, stiffeners, and the masonry plate, has sustained only minimal corrosion and remains covered by protective paint. Photographs taken during testing are provided in Figure 6.38.

The initial deformation mode of the bolster bearing is sliding of the sole plate on top of the bearing body; however, this deformation quickly transitions to mixed sliding and rocking leading to increasing secant stiffness and resistance. As the clearance in the pintle holes is exhausted, the pintles are engaged in resisting the applied load and the deformation mode immediately transitions to prying of the bolster bearing body on top of the steel pedestal. Consequently, the anchor bolts are subject to combined tension and shear forces causing the bolts to yield and eventually fracture. After both bolts fracture, severe overturning of the bolster bearing body is observed before unloading. An initial stiffness of 25 kN/mm is achieved. A maximum bearing resistance of -232 kN is achieved at a displacement of -28 mm. The first bolt fracture occurs at a displacement of -42 mm when the bearing resistance decreases to 209 kN. A sudden load loss of roughly 150 kN results from this bolt fracturing as can be seen in Figure 6.39. After the first anchor bolt fractures, the lateral resistance of the bolster bearing undergoes a slight increase reaching the second load peak of -114 kN at -53 mm. As the loading further increases to -58 mm, the second bolt fractures at a load level of -101 kN, after which the bearing resistance decreases suddenly to -25 kN. The fractured bolts are shown in Figure 6.38. Post-test examination shows that the pintles are still intact without any noticeable damage due to testing. The bearing strength of 232 kN obtained in this test is 40 kN larger than the theoretical value of 192 kN derived in Chapter 3. This discrepancy is due to the fact that the bolt strength used in the theoretical study is smaller than the true strength of the anchor bolts used in the test (Figure 6.9).

6.3.7 Transverse response of steel bolster bearings

Pier bolster bearing #14 (PB14) is selected for the transverse monotonic loading study. As shown in Figure 6.40, PB14 has minor corrosion along the contact region at the top surface of the bearing and around the anchor bolt holes of the masonry plate. Both pintles show very little corrosion. Figure 6.41 provides photographs taken during and after the bearing test. The optotrak marker layout also can be seen in Figure 6.41.

The initial deformation mode of the bolster bearing under transverse loading consists of a mix of rocking and sliding of the bolster bearing on top of the steel pedestal when the displacements are less than -10 mm. Once the clearance around the pintles and anchor bolts is exhausted, the bolster bearing shows a rapid increase in its lateral load resistance because the dominant deformation mode switches to rocking and prying on the anchor bolts. The anchor bolts are engaged in resisting both tension and shear force and the pintles also resist shear. The initial stiffness of the bearing is 67 kN/mm. A lateral resistance of -360 kN is achieved at -29 mm, after which a slight strength degradation is seen before the bolts fracture. Both bolts fracture simultaneously at -38 mm at a lateral load of -343 kN. Bolt fracture causes a complete loss of the bearing's lateral load capacity as reflected by the sudden change in the load deformation curve in Figure 6.42. The ultimate strength (360 kN) obtained experimentally is significantly larger than the theoretical estimates (226 kN from a combined tension and shear failure and 301 kN from bolt shear failure). This discrepancy is again due to the difference between the nominal and true anchor bolt strengths.

6.3.8 Summary of steel bolster bearing monotonic tests

All five of the salvaged steel bolster bearings show negligible corrosion effects. Thus, the effect of corrosion on the lateral behavior of the steel bolster bearings is not addressed. Monotonic test results of the bolster bearings with minor corrosion indicate that the bearing lateral behavior is determined by the anchor bolts given that the anchor bolts have a smaller fracture strength than the pintles. Both the longitudinal and transverse bearing tests provide higher maximum lateral resistance than the theoretical prediction as

a result of the bolts used in the tests having fracture strength larger than the nominal value used in the analytical study.

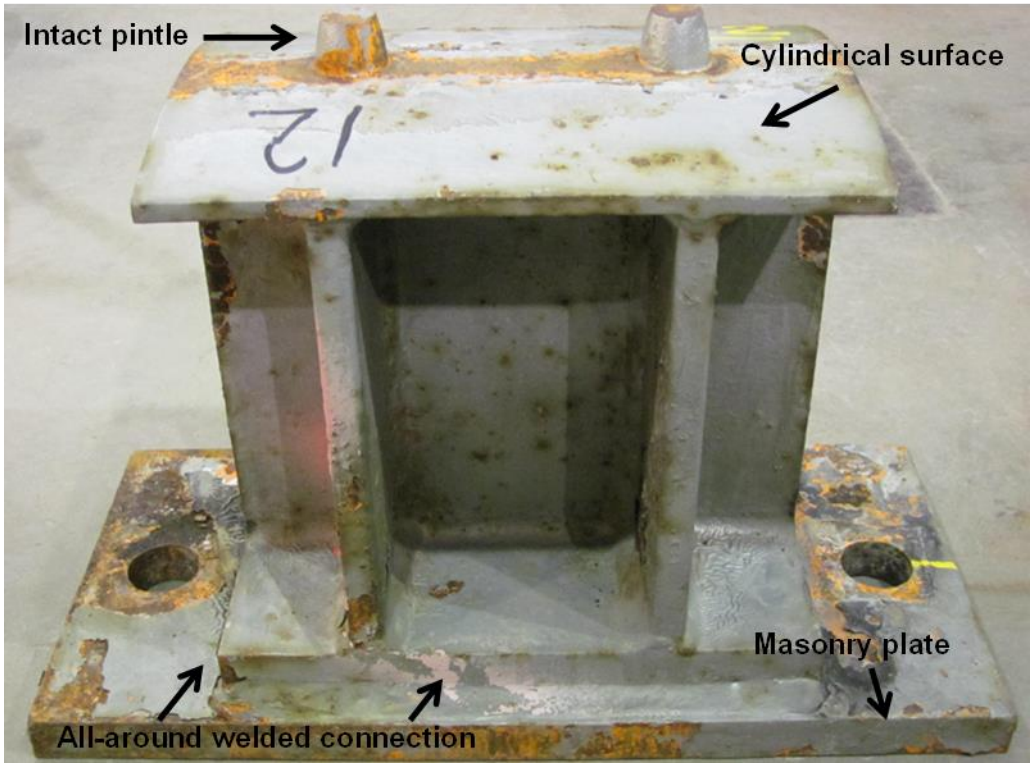

Figure 6.36 Pier bolster bearing #12 (PB12) in the as-received condition

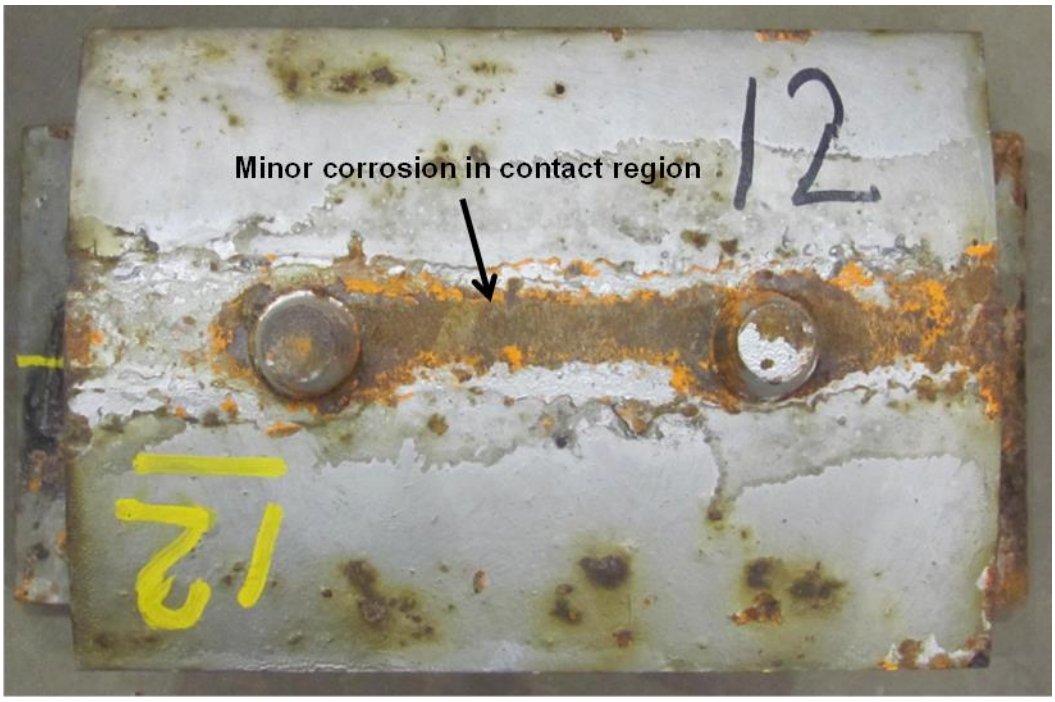

Figure 6.37 Top contact surface of Bearing PB12 in the as-received condition

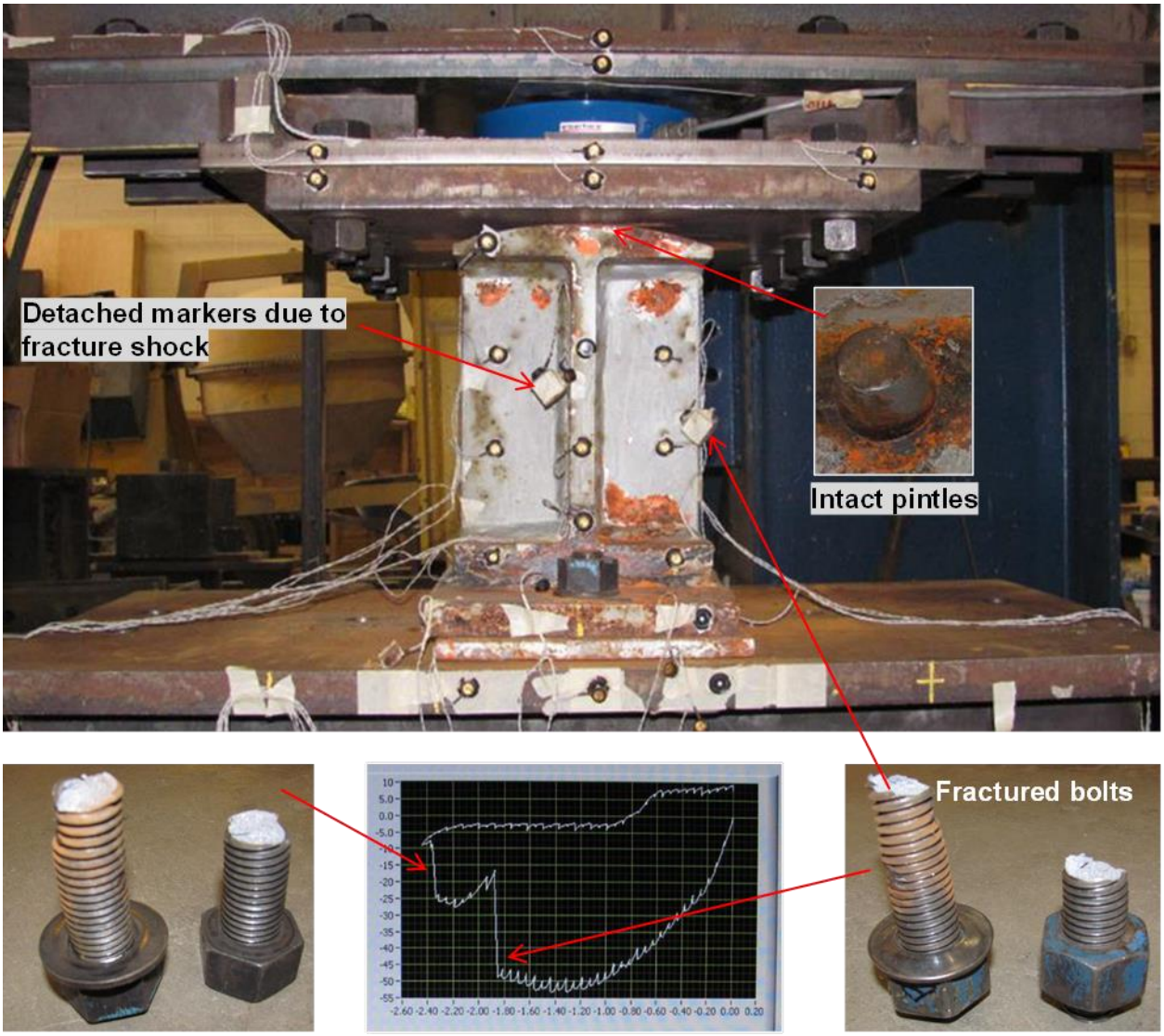

Figure 6.38 Photographs of Bearing PB12 under longitudinal monotonic loading

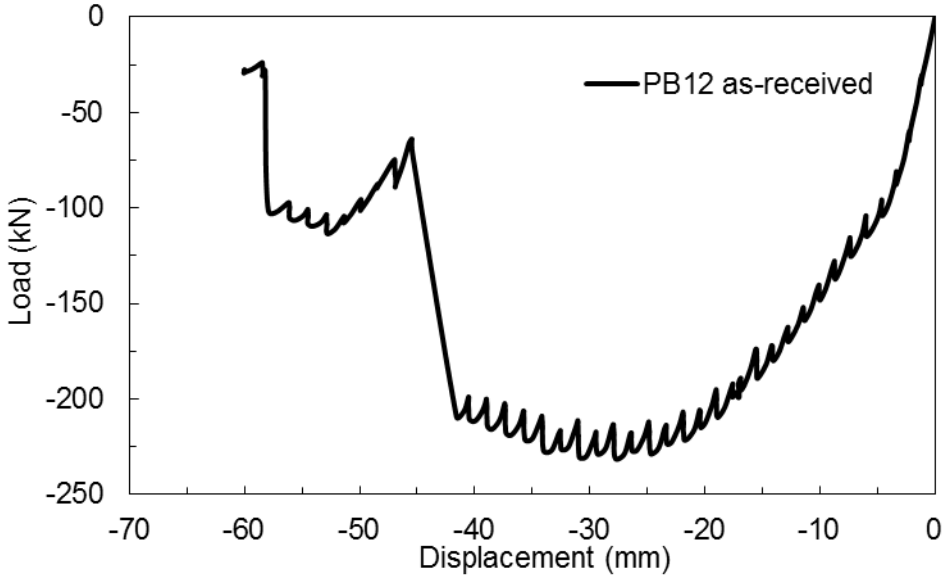

Figure 6.39 Longitudinal response of Bearing PB12 in the as-received condition under negative monotonic loading

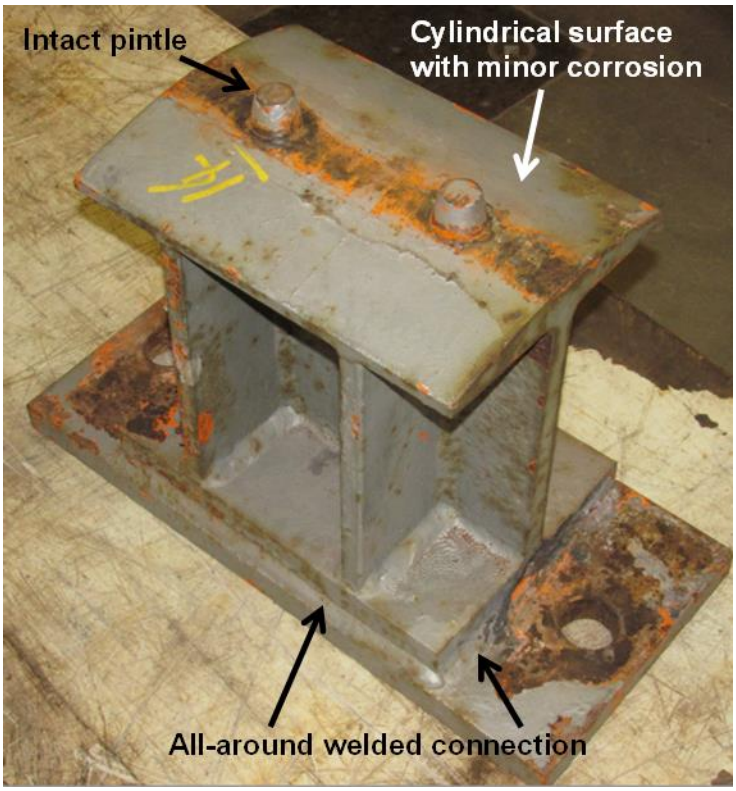

Figure 6.40 Pier bolster bearing #14 (PB14) in the as-received condition

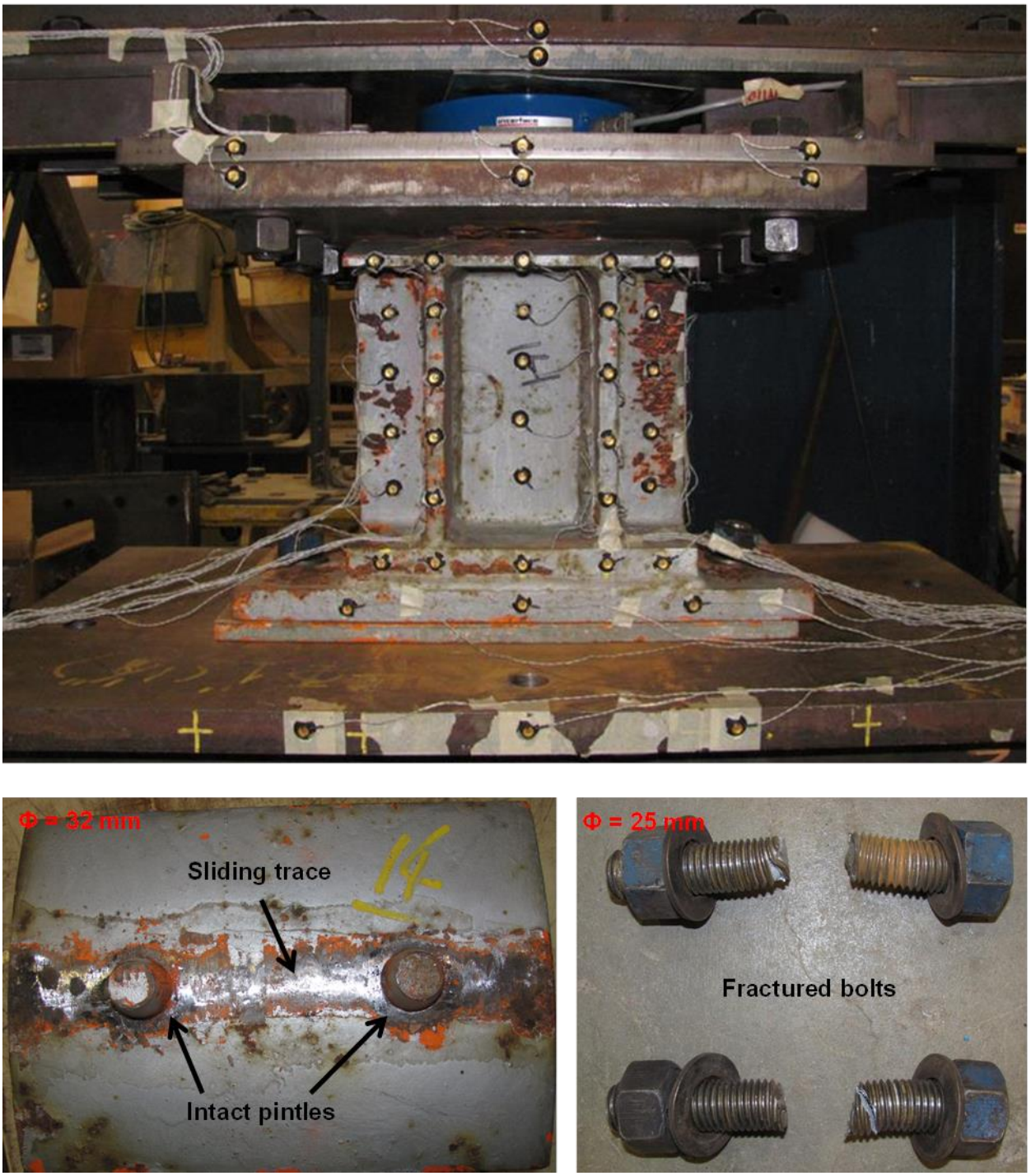

Figure 6.41 Photographs of Bearing PB14 under transverse monotonic loading

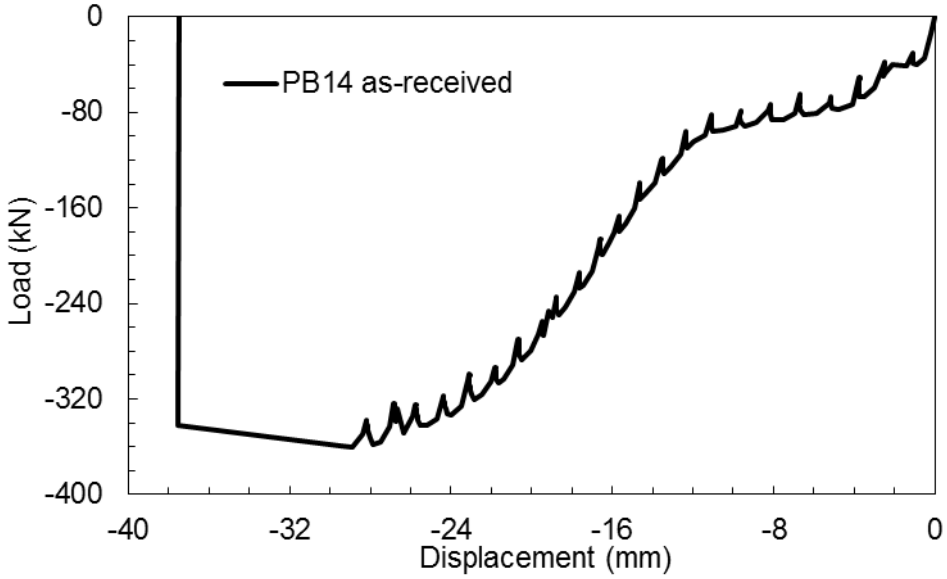

Figure 6.42 Transverse response of Bearing PB14 in the as-received condition under negative monotonic loading

6.4 Cyclic Behavior of Steel Bearings on a Steel Pedestal

In this section, cyclic test results of the steel rocker and bolster bearings are presented. These tests help to better define the hysteretic behavior of the steel bearings and predict their responses under earthquake loads. No previous studies have focused on evaluating the cyclic behavior of corroded steel rocker bearings and correlating this behavior with corrosion level. The findings of this study are used in the development of numerical models of steel bearings with varying levels of corrosion. As shown in Table 6.3, the scope of this cyclic study encompasses corroded and cleaned abutment rocker bearings, pier rocker bearings with minor corrosion, and pier bolster bearings with minor corrosion. The longitudinal and the transverse behavior is investigated for each of these categories of bearings. The applied vertical load is maintained at 102 kN for all cyclic tests.

6.4.1 Longitudinal cyclic response of abutment rocker bearings

Abutment rocker bearing #21 (AR21) is considered under longitudinal cyclic loading (Figure 6.43). This bearing has sustained a mass loss of 12%. The distribution of the measured mass loss on different bearing components is very uneven as discussed in Chapter 5. At the top contact interface shown in Figure 6.44, the pintles maintain over 80% of their volume while the cylindrical surface is covered by rust and has lost 12% of its thickness. The bearing web and stiffeners have sustained section losses of 14% and 17%, respectively. The bottom contact interface (Figure 6.45) has sustained the worst corrosion losses. While the top pintles maintain most of their volume (Figure 6.46), the bottom pintles have lost over 85% of their volume. Pack rust is present on the top surface of the masonry plate and on the bottom pintles. With a 20% section loss, the bottom cylindrical surface is rough due to corrosion-induced pitting and its pintle holes have been filled with corrosion byproducts (Figure 6.47).

The instrumentation used in testing Bearing AR21 is shown in Figure 6.48. A displacement increment of 3.2 mm is used with the same loading protocol shown in Figure 6.5. The actual loading history is provided in Figure 6.49, which shows a symmetric loading displacement history to a maximum displacement of 60 mm.

The initial stiffness of Bearing AR21 is 3.1 kN/mm. The overall hysteretic response shows a dominant rolling behavior in the displacement range of ± 20 mm (Figure 6.50) with a constant resistance of 5 kN. Rocking is the predominant deformation mode for displacement levels that are beyond 20 mm and leads to a steady increase in the bearing resistance with increasing displacements. However, the secant stiffness of the bearing shows a faster decrease in the positive response than in the negative response, which is mostly attributed to uneven corrosion distribution on the contact surfaces. Pack rust at the bottom contact interface is crushed and pushed off the masonry plate during testing. The maximum bearing resistance reaches 41 kN at 57 mm and -54 kN at -56 mm for the positive and negative responses, respectively. As a result, the bearing positive response has a secant stiffness of 0.72 kN/mm, while the negative response has a secant stiffness of 0.96 kN/mm, both of which are measured at the corresponding maximum displacements. Further examination of the test results indicates no degradation in strength and secant stiffness between loading cycles to the same displacement level. The total hysteretic energy dissipated during cyclic loading is calculated to be 1311 Joules.

Bearing AR21 was removed from the setup after testing in the as-received condition, cleaned with a metal scraper to remove the rust layers, and then replaced in the setup for a second cyclic test in a cleaned condition. Figure 6.51 shows the actual loading history of the second test that exhibits a symmetric displacement loading protocol with a maximum displacement level near 60 mm.

The initial stiffness of the cleaned bearing is 1 kN/mm less than that of the as-received bearing. As shown in Figure 6.52, the cleaned bearing has a more pronounced rolling response within the displacement range of ± 35 mm. This is a larger displacement range for rolling than that observed in the first test due to the removal of the pack rust from the contact surfaces. However, the rolling resistance (2.5 kN) is found to be half of that observed for the as-received bearing suggesting a decrease in the friction coefficient. Rocking of the bearing becomes predominant at displacement levels larger than 35 mm. Similar to the as-received bearing response, the negative rocking exhibits a larger stiffness than that of the positive rocking. As a result, the maximum negative bearing resistance reaches -54 kN at -54 mm while the maximum positive bearing resistance

achieves only 31 kN at 57 mm, resulting in secant stiffnesses of 1 kN/mm and 0.54 kN/mm for the negative and positive responses, respectively. The hysteretic energy dissipation for the cleaned bearing test is 1066 Joules.

Figure 6.50 and Figure 6.52 show that both bearing tests yield similar overall responses with either rolling or rocking of the bearing body governing its behavior depending on the displacement magnitude. However, differences are found between the initial stiffness, the rolling displacement ranges, and the overall positive secant stiffness. The cleaned bearing has a reduced initial stiffness and positive secant stiffness, while undergoing a longer rolling displacement range compared to the as-received bearing. Additionally, the cleaned bearing has a slight decrease in hysteretic energy dissipation than the as-received bearing under identical loading protocols.

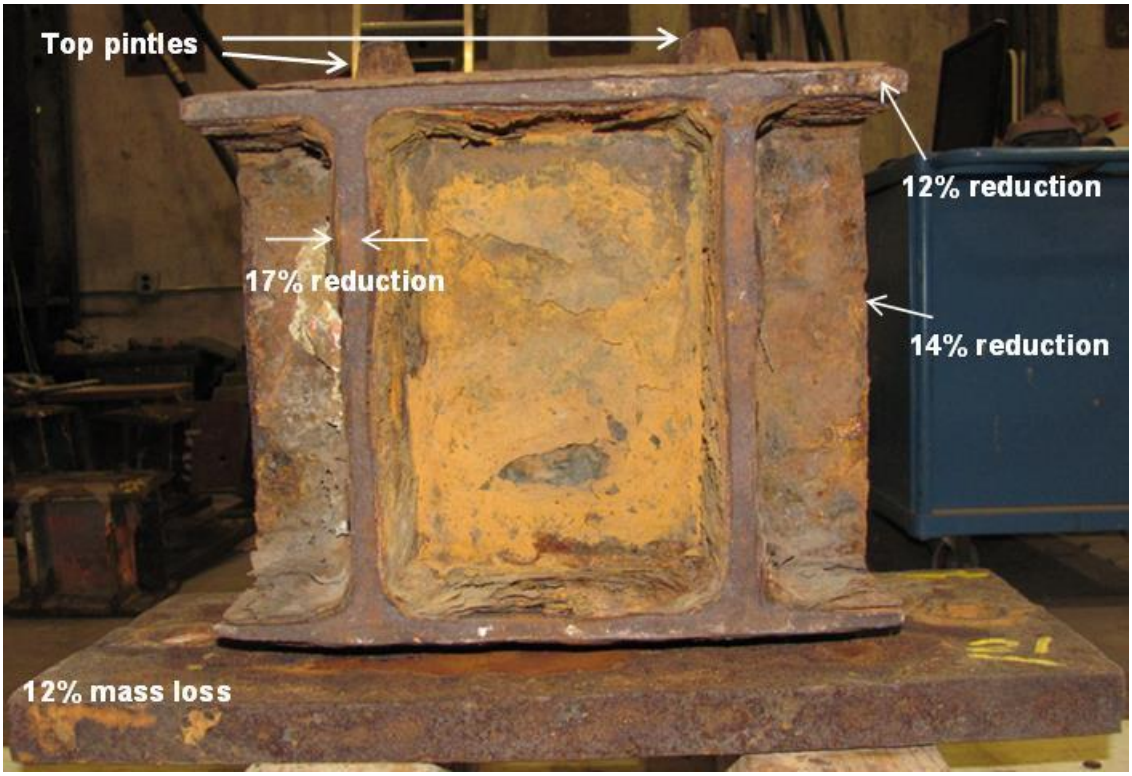

Figure 6.43 Abutment rocker bearing #21 (AR21) in the as-received condition

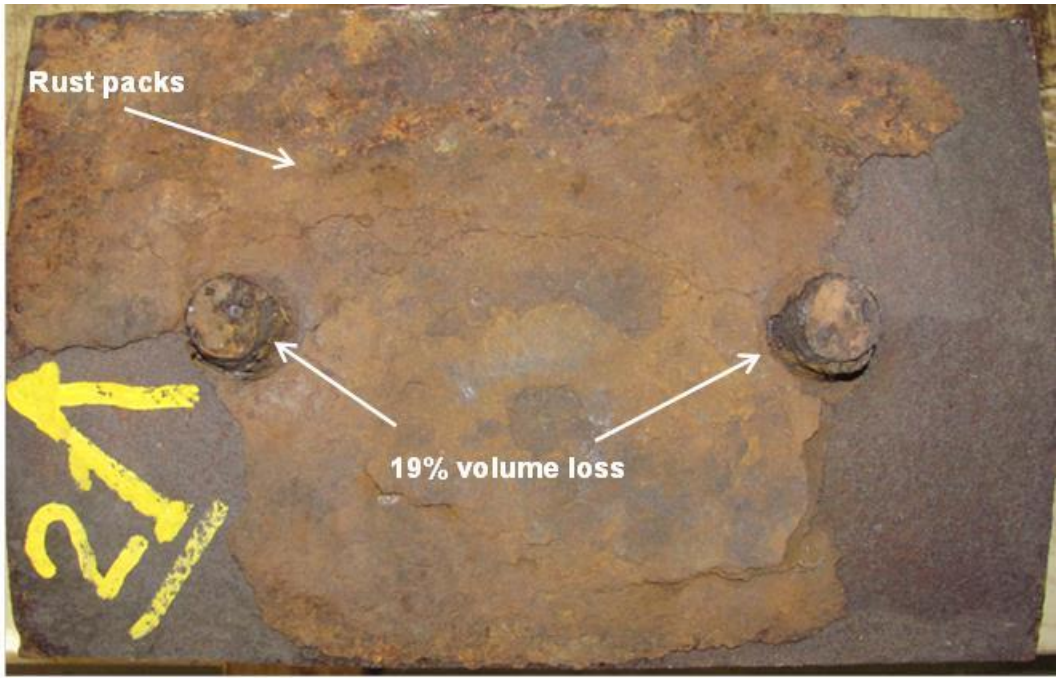

Figure 6.44 Top cylindrical contact surface of Bearing AR21 in the as-received condition

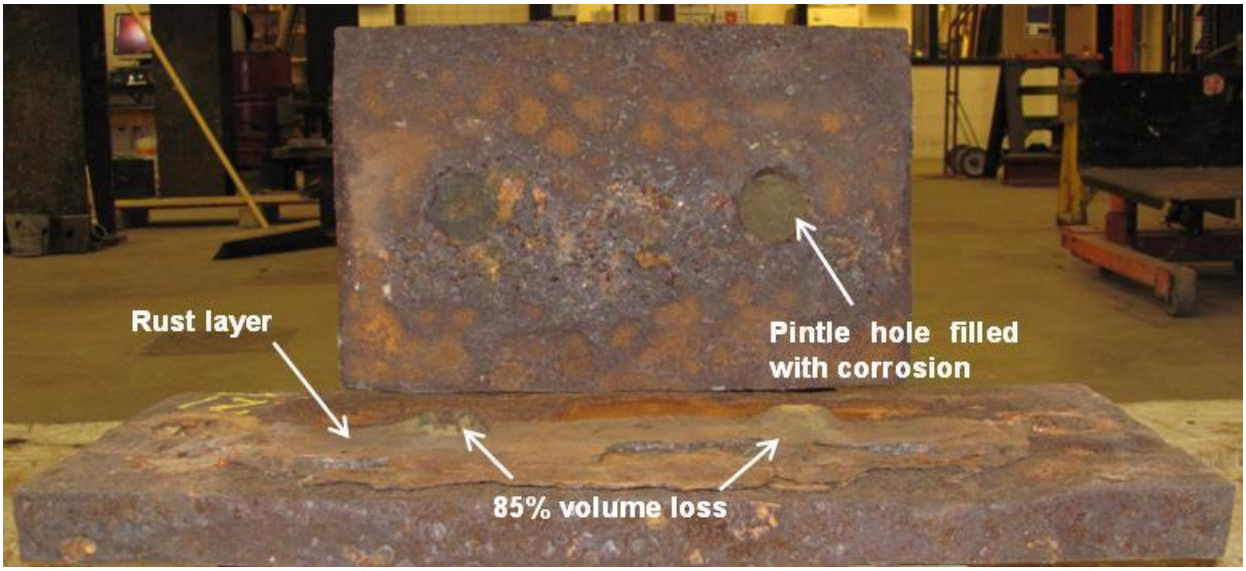

Figure 6.45 Bottom contact interface of Bearing AR21 in the as-received condition

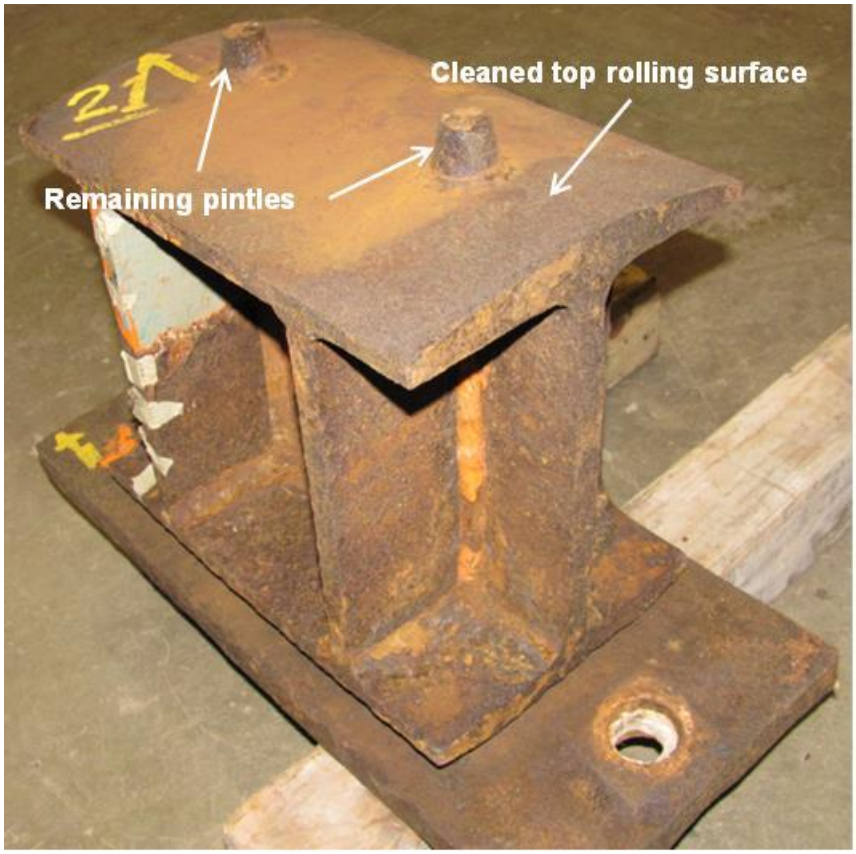

Figure 6.46 Bearing AR21 with surface rust removed

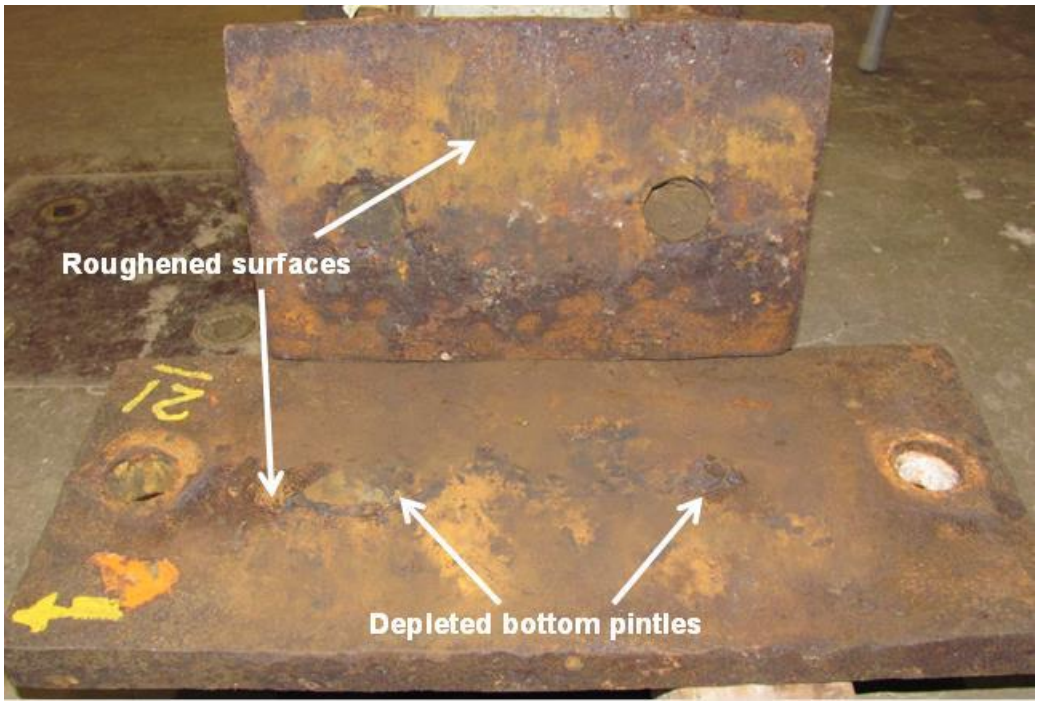

Figure 6.47 Cleaned bottom contact surfaces of Bearing AR21

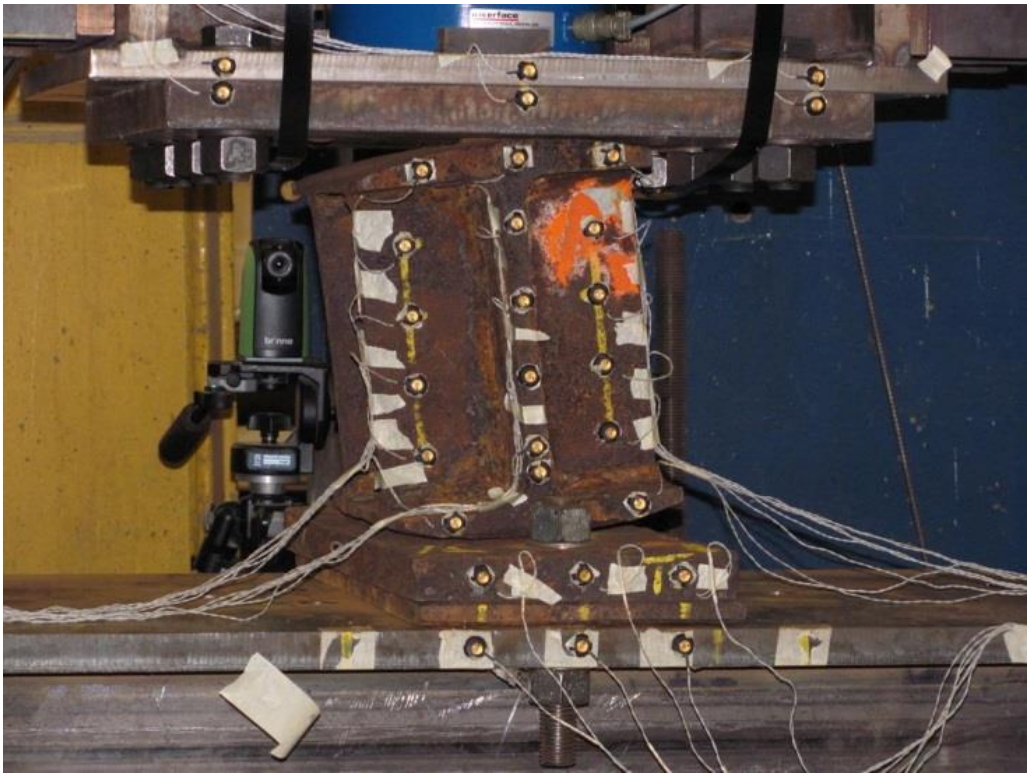

Figure 6.48 Photograph of the instrumentation used for testing Bearing AR21

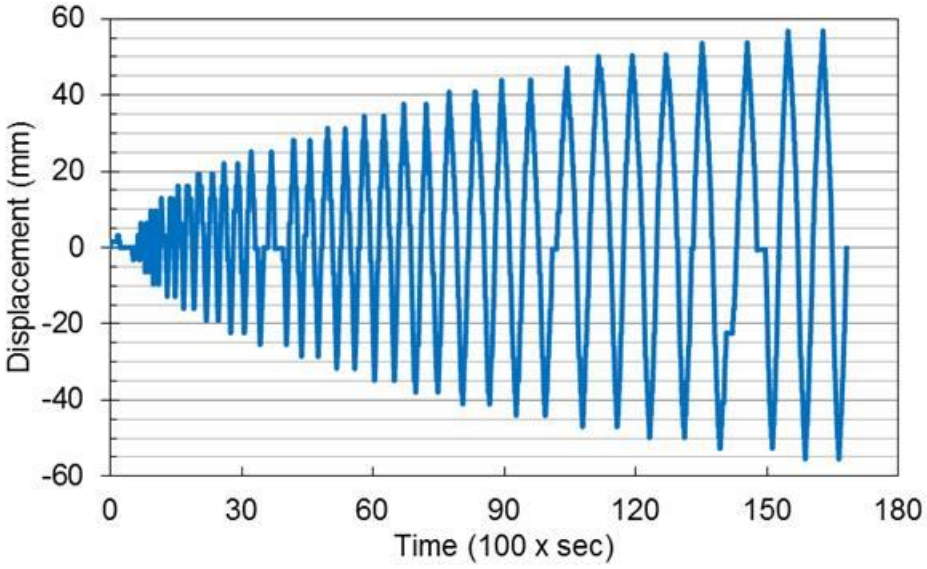

Figure 6.49 Actual loading protocol for the test of Bearing AR21 in the as-received condition

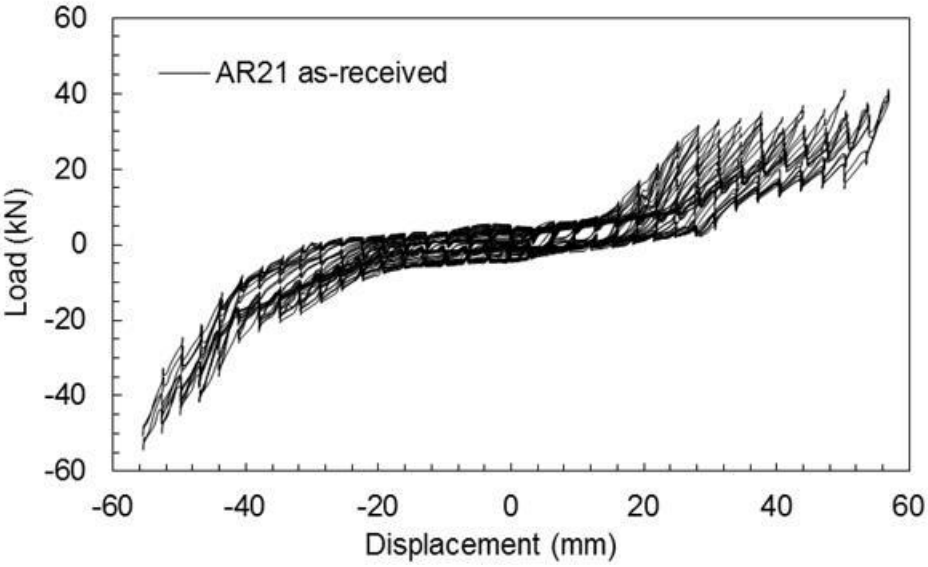

Figure 6.50 Longitudinal cyclic response of Bearing AR21 in the as-received condition

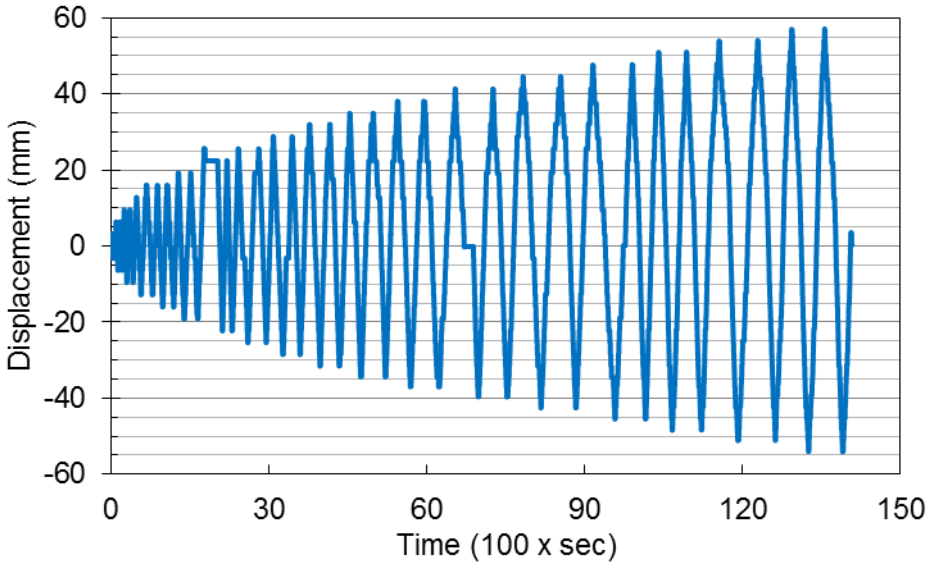

Figure 6.51 Actual loading protocol for the test of Bearing AR21 in the cleaned condition

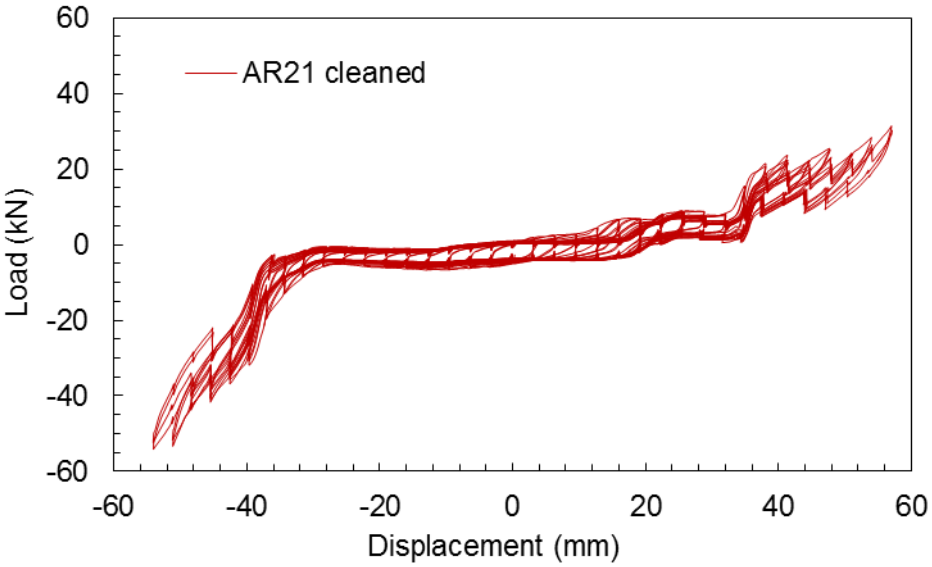

Figure 6.52 Longitudinal cyclic response of Bearing AR21 in the cleaned condition

6.4.2 Transverse cyclic response of abutment rocker bearings

Abutment rocker bearing #23 (AR23) is used to study the transverse cyclic behavior of abutment rocker bearings with severe corrosion. The as-received condition of Bearing AR23 shows a mass loss of 10% (Figure 6.53). Severe corrosion in the form of pack rust and surface pits is observed at the top and bottom contact interfaces shown in Figure 6.54 and Figure 6.55. The top pintles have sustained 44% volume loss (Figure 6.56), while the bottom pintles sustained 52% volume loss (Figure 6.57). Section loss is 9% for the top cylindrical surface and 27% for the bottom cylindrical surface. 19% and 25% section reductions are measured for the web and stiffeners, respectively. Corrosion byproducts also are observed inside of the bottom pintle holes and the anchor bolt holes.

Figure 6.58 provides a photograph of the optotrak marker layout on the bearing. Figure 6.59 shows the actual displacement loading history recorded during testing. A slight asymmetry is observed in the displacement history. Upon completion of the cyclic loading protocol, the bearing was loaded up to -41 mm in the negative direction to further observe the behavior. The experimental cyclic response of the bearing is shown in Figure 6.60.

The deformation mode of the bearing during its early loading cycles (< 5 mm) is rocking of the bearing body. The deformation mode quickly transitions to a mix of rocking and masonry plate sliding after displacement levels exceed 5 mm due to engagement of the pintles in resisting the applied load. Spalling of pack rust is extensive during this stage of loading due to the vibration created by the masonry plate suddenly sliding and stopping. The initial stiffness of the bearing is 23 kN/mm. A maximum positive lateral resistance of 221 kN is obtained at a displacement level of 17 mm during the 22 mm cycle. A maximum negative lateral resistance of -252 kN is recorded at the largest applied displacement during cyclic loading of -25 mm. The additional applied negative displacement yields the largest bearing resistance of -361 kN. The total hysteretic energy dissipated during the cyclic loading is 10891 Joules. The secant stiffness is 8.1 kN/mm for the positive response and 10.1 kN/mm for the negative response measured at the maximum applied displacements of 22 mm and -25 mm.

To further examine the effect of corrosion on the bearing cyclic behavior, Bearing AR23 is cleaned to remove the surface rust after the first test and retested using the same loading protocol and vertical load level. However, the actual loading history is asymmetric as shown in Figure 6.61 due to rigid sliding of the steel pedestal. During the retest, the bearing body both rocks and slides on top of the masonry plate at small displacements. At larger displacement levels, sliding of the masonry plate on top of the steel pedestal is also observed in the deformation mode. The initial stiffness is 35 kN/mm. The positive response shows a maximum resistance of 198 kN at 19 mm while the negative response has a maximum resistance of -195 kN at -26 mm (Figure 6.62). The secant stiffness of the bearing measured at maximum applied displacements is 10.4 kN/mm and 7.5 kN/mm for the positive and negative responses, respectively.

Comparing with the as-received bearing, the cleaned bearing shows a larger initial stiffness. The secant stiffness and the maximum resistance are larger for the as-received bearing than the cleaned bearing due to section loss caused by rust removal.

Figure 6.53 Abutment rocker bearing #23 (AR23) in the as-received condition

Figure 6.54 Top cylindrical surface of Bearing AR23 in the as-received condition

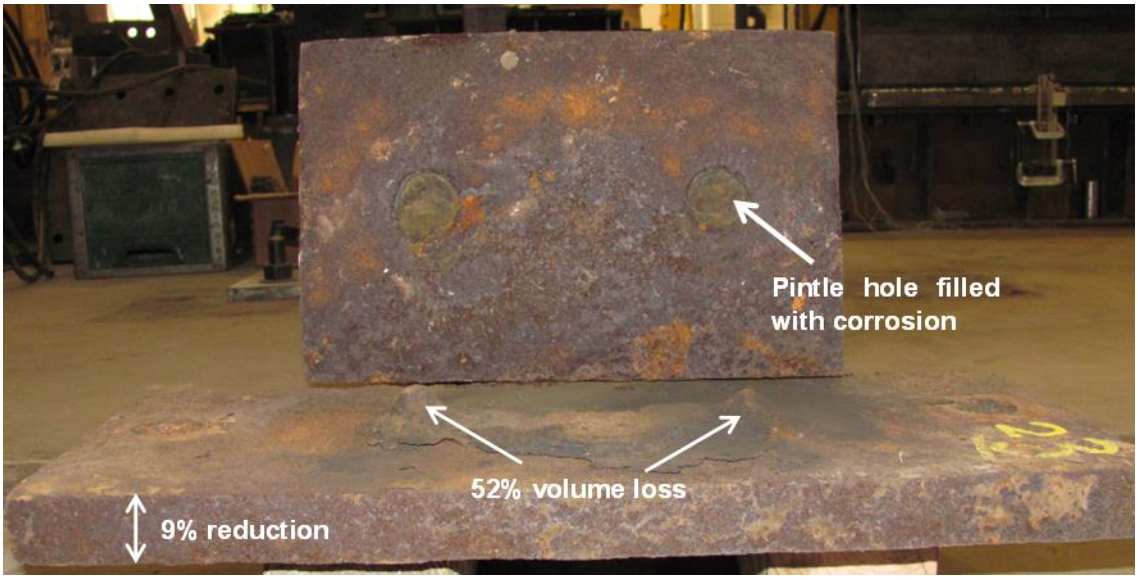

Figure 6.55 Bottom contact interface of Bearing AR23 in the as-received condition

Figure 6.56 Bearing AR23 in its cleaned condition with rust removed

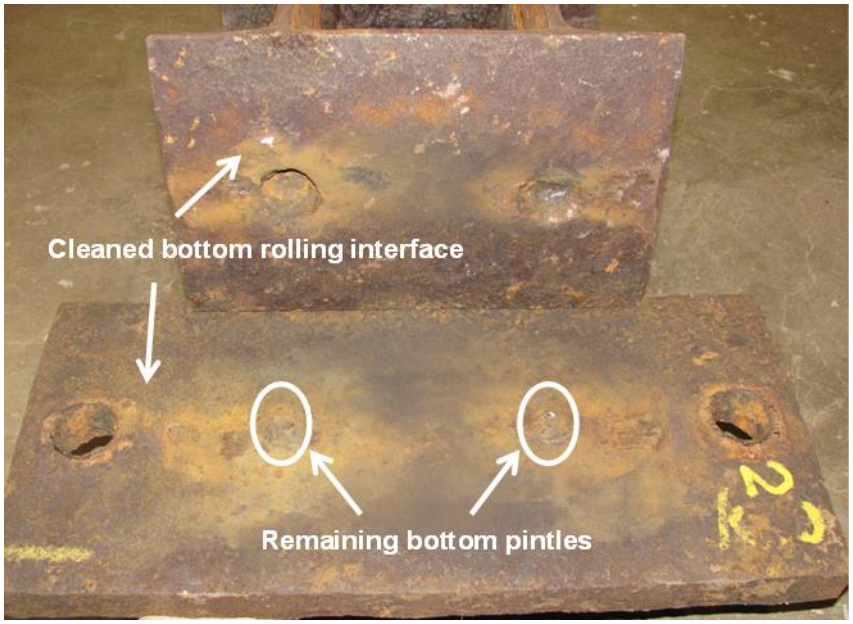

Figure 6.57 Cleaned bottom contact interface of Bearing AR23

Figure 6.58 Photographs of the marker layout for Bearing AR23

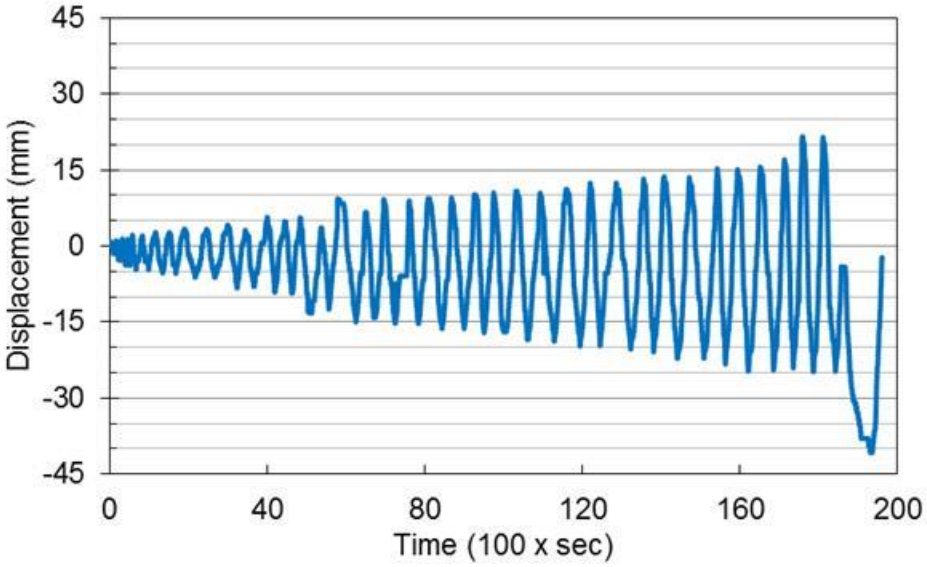

Figure 6.59 Actual loading protocol recorded for the as-received test of Bearing AR23

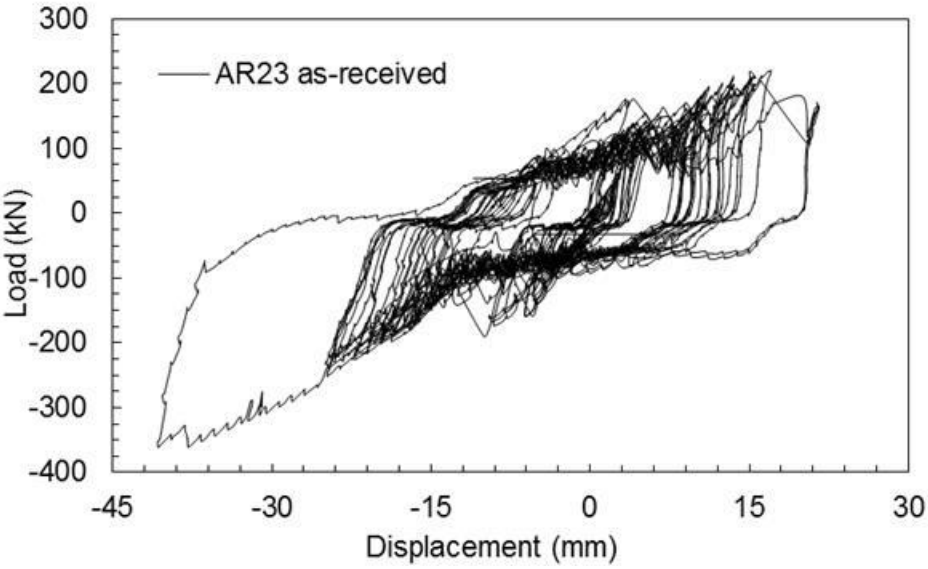

Figure 6.60 Transverse cyclic response of Bearing AR23 in the as-received condition

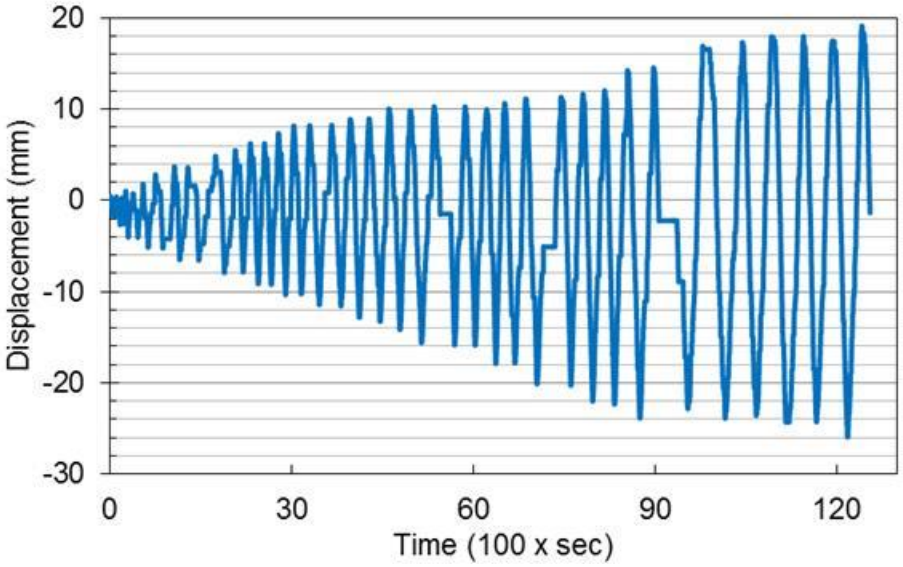

Figure 6.61 Actual loading protocol recorded for the cleaned test of Bearing AR23

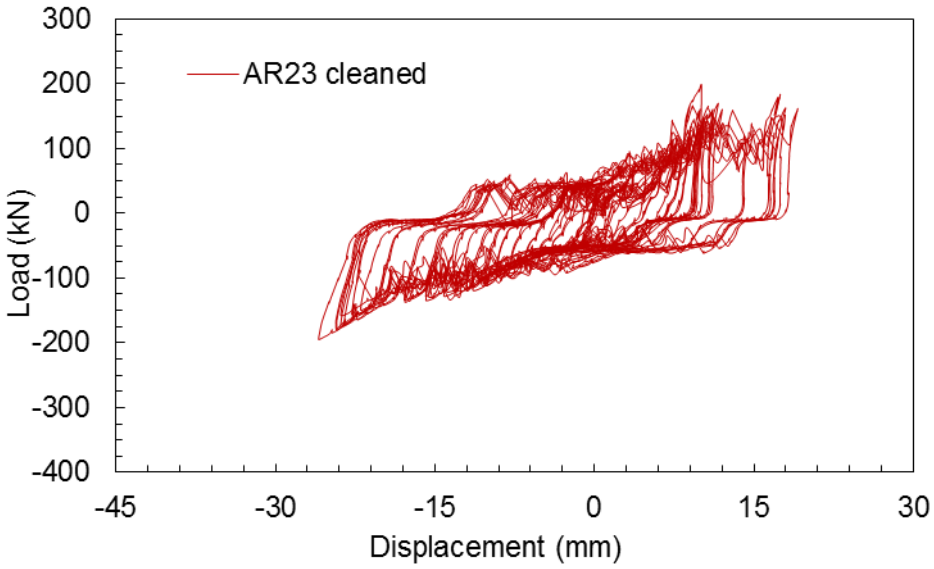

Figure 6.62 Transverse cyclic response of Bearing AR23 in the cleaned condition

6.4.3 Longitudinal cyclic response of pier rocker bearings

Pier rocker bearing #8 (PR8) is used to study the longitudinal behavior of the steel rocker bearings with minor corrosion under cyclic loading. As shown in Figure 6.63, Bearing PR8 only has minor corrosion on the bearing body and the masonry plate. Figure 6.64 shows that the contact region of the top cylindrical surface also only has minor corrosion with minimal effects on the pintles. The bottom contact interface, shown in Figure 6.65, has larger areas of corrosion on the bottom cylindrical surface and the masonry plate. However, an insignificant amount of corrosion is observed on the bottom pintles and within the pintle holes.

Figure 6.66 provides the layout of the optotrak markers on the bearing, while Figure 6.67 provides the actual displacement loading history recorded during testing that shows a maximum displacement level of approximately 60 mm.

The overall cyclic behavior of Bearing PR8, shown in Figure 6.68, is fairly symmetric. The observed predominant deformation mode is a mixture of rolling and rocking of the bearing body on the masonry plate. This is reflected by the hysteresis shown in Figure 6.68 that resembles a rotated rectangular response. The initial stiffness of the bearing is 8.5 kN/mm. The maximum positive bearing resistance of 43 kN is achieved at a displacement of 64 mm while, the maximum negative bearing resistance of -44 kN is reached at a displacement of -62 mm. At these displacements, a positive secant stiffness of 0.67 kN/mm and a negative secant stiffness of 0.71 kN/mm are measured. These values further confirm the symmetric cyclic behavior of the pier rocker bearings with minor corrosion. The bearing response shows no strength degradation in either loading direction with a consistent decrease in the secant stiffness. The cumulative hysteretic energy dissipation of the bearing during cyclic loading is 2226 Joules.

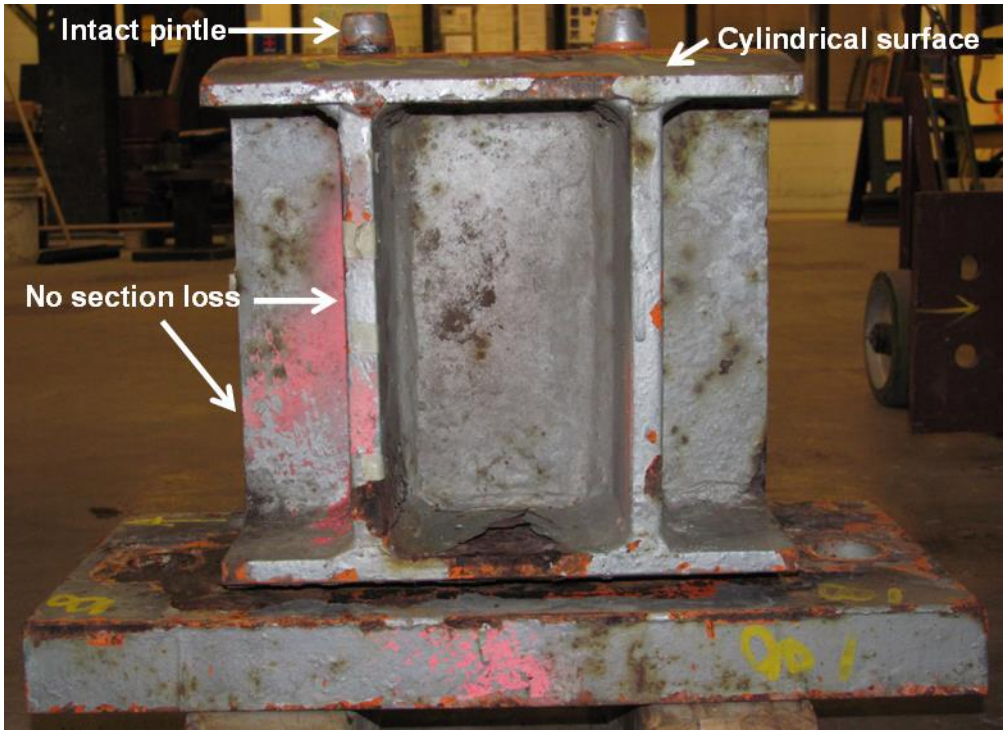

Figure 6.63 Pier rocker bearing #8 (PR8) in the as-received condition

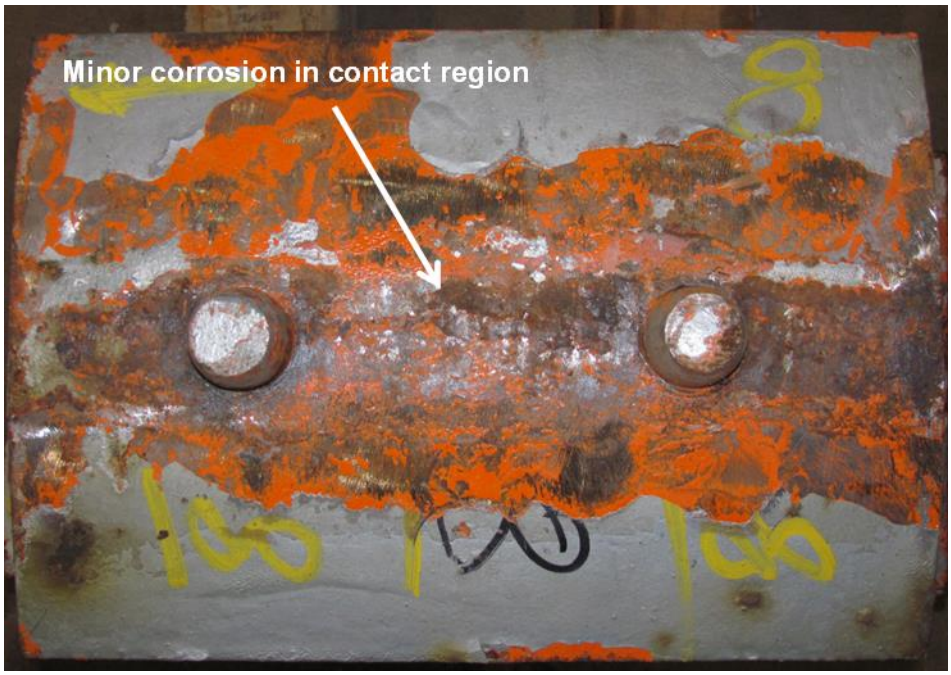

Figure 6.64 Top cylindrical surface of Bearing PR8 in the as-received condition

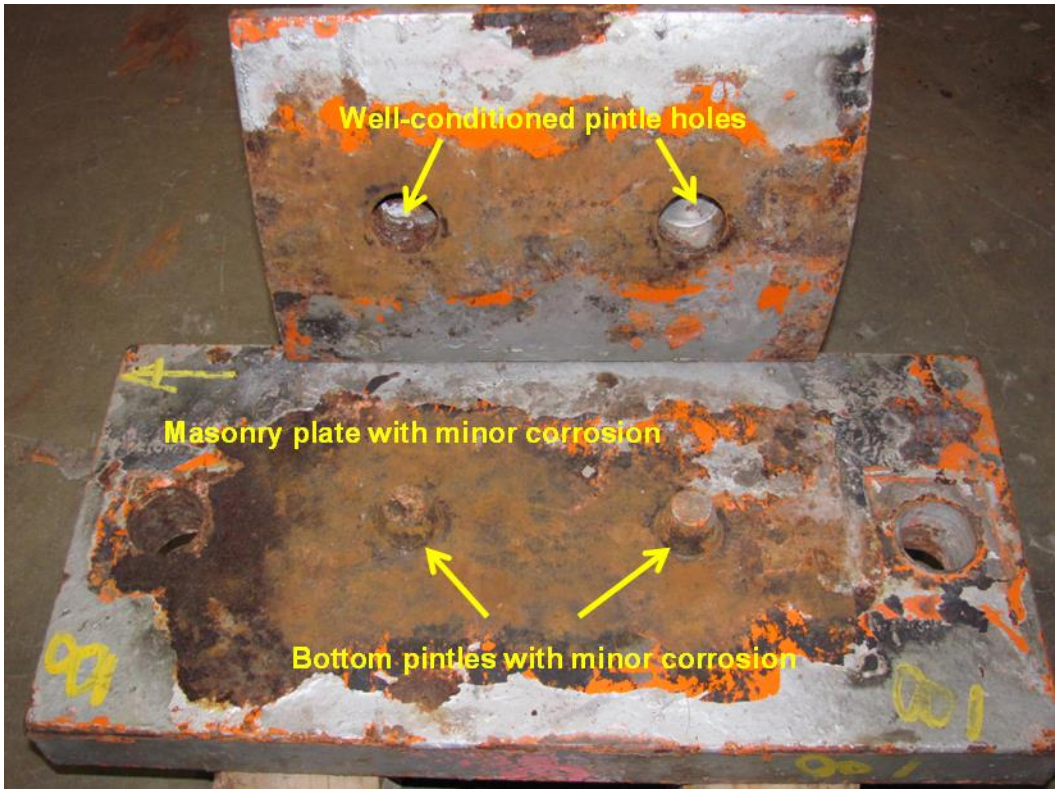

Figure 6.65 Bottom contact interface of Bearing PR8 in the as-received condition

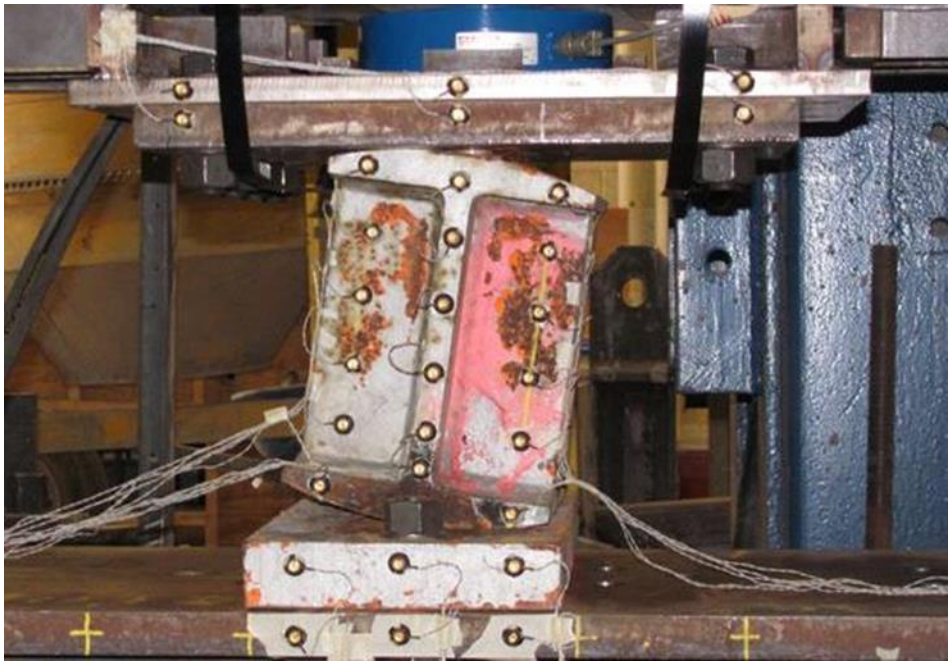

Figure 6.66 Photographs of Bearing PR8 under longitudinal loading

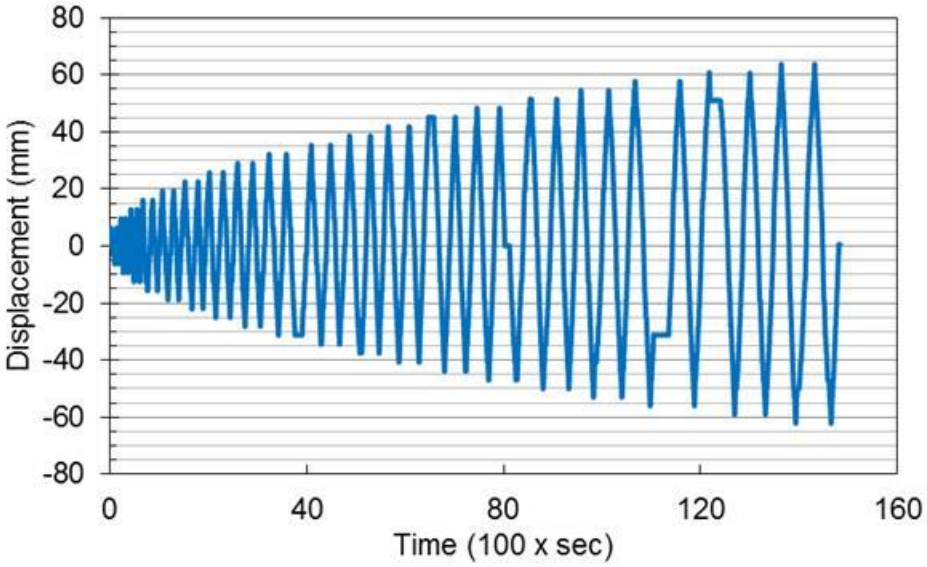

Figure 6.67 Actual loading history recorded during testing of Bearing PR8

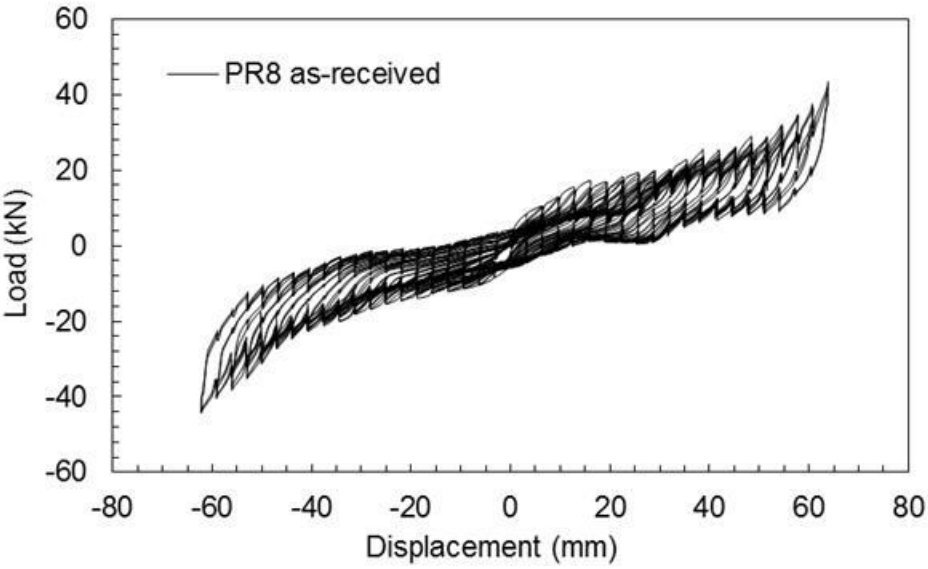

Figure 6.68 Longitudinal cyclic response of Bearing PR8 in the as-received condition

6.4.4 Transverse cyclic response of pier rocker bearings

Pier rocker bearing #19 (Figure 6.31) is cyclically tested under transverse loading to establish the cyclic behavior of the steel rocker bearings with minor corrosion. A detailed discussion of the bearing's condition is given in Section 6.3.4.

Figure 6.69 shows the actual loading history recorded during testing, which is not symmetric owing to rigid sliding of the steel pedestal. As a result of this asymmetric loading protocol, the hysteretic response of the bearing shown in Figure 6.70 is shifted by 5 mm toward the negative direction. The initial stiffness of the bearing is 85 kN/mm. A pronounced sliding plateau with a constant sliding resistance of 50 kN can be seen in the bearing response for displacements of ±5 mm. The primary deformation mode of the bearing under transverse cyclic loading is observed to be a combination of sliding and rocking of the bearing body and sliding of the masonry plate. Rocking of the bearing body becomes the main deformation mode when the masonry plate bears on the anchor bolts at displacements beyond ±10 mm. No strength degradation is seen in both the positive and negative responses. The bearing lateral resistance reaches 228 kN when the maximum positive displacement of 14 mm is applied while the bearing resistance is -250 kN at the maximum negative displacement of -23 mm. The secant stiffness of the bearing measured at the maximum applied displacements is 16.3 kN/mm for the positive response and 10.9 kN/mm for the negative response. The total hysteretic energy dissipated during the cyclic loading is estimated to be 6802 Joules.

6.4.5 Corrosion effect on steel rocker bearing cyclic behavior

The cyclic behavior of the steel rocker bearings with severe and minor corrosion has been considered under both longitudinal and transverse loading. Table 6.6 and Table 6.7 provide a summary of the results from the longitudinal and transverse bearing tests. In general, the steel rocker bearings with minor corrosion demonstrate a symmetric cyclic behavior under longitudinal and transverse loading, while the steel rocker bearings with severe corrosion do not show a symmetric cyclic response under the same loading protocol. From the experimental observations and data, corrosion is found to have a

significant influence on the initial stiffness, rolling or sliding resistance, maximum resistance, secant stiffness, and deformation modes of the steel rocker bearings.

Specifically, the longitudinal cyclic response of the severely corroded rocker bearing (i.e. abutment rocker bearing) has a much smaller secant stiffness and resistance than the pier rocker bearing with minor corrosion within the displacement range of ±20 mm. The abutment rocker bearing also shows a predominant rolling deformation mode in this displacement range, which quickly transitions to a governing rocking one as the displacement level surpasses 20 mm. In contrast, the pier rocker bearing has a predominant combined rocking and rolling deformation mode throughout the entire loading history. However, an identical rolling resistance of 5 kN is obtained for these two bearings. Removing the surface pack rust shows a significant impact on the rolling range of the severely corroded rocker bearing, which elongates the bearing rolling plateau roughly by 15 mm in each direction and reduces its rolling resistance by half to 2.5 kN.

The initial stiffness under longitudinal loading decreases significantly from 8.5 kN/mm for the steel rocker bearing with minor corrosion to 3.1 kN/mm for the steel rocker bearing with severe corrosion. The cleaned rocker bearing with severe corrosion shows a further decrease in the initial stiffness to 1 kN/mm, which is due to the corrosion-induced geometry changes of the bearing in terms of the radius of the cylindrical surface and the bearing height. The secant stiffness is larger for the corroded rocker bearing (0.72 and 0.96 kN/mm) than for the pier rocker bearing (0.67 and 0.71 kN/mm). Cleaning the abutment rocker bearing leads to a similar negative secant stiffness (1 kN/mm) and a smaller positive secant stiffness (0.54 kN/mm) compared with the test results in the as-received condition.

The transverse cyclic behavior of the steel rocker bearings differs during the initial displacement loading cycles between the pier rocker bearing with minor corrosion and the abutment rocker bearing with severe corrosion. The pier rocker bearing during early cycles mainly undergoes sliding of the bearing body on the masonry plate due to the pintle hole clearance in the sole plate, while the abutment rocker bearing immediately starts rocking due to that the presence of corrosion byproducts decreases the clearance

between the pintles and the pintle holes in the sole plate. The initial stiffness shows a significant decrease from 85 kN/mm for the pier rocker bearing to 23 kN/mm for the abutment rocker bearing. The deformation mode of the pier rocker bearing consists of a combination of sliding and rocking of the bearing body once the pintles are engaged in resisting the applied load. Under further deformation, combined bearing rocking and masonry plate sliding is observed with a sliding resistance of 50 kN. Finally, a predominant rocking mode is observed once the anchor bolts start bearing on the masonry plate leading to a rapid increase in the bearing resistance and secant stiffness. In contrast, the corroded abutment rocker bearing switches the deformation mode from bearing rocking to masonry plate sliding due to the relatively fast increase in the bearing resistance under rocking during early loading cycles. The masonry plate slides with a frictional force of approximately 60 kN, which causes the corrosion layers inside the anchor bolt holes and around the pintles to dislodge leading to an increase in clearance around the bolts and the pintles. Once the masonry plate starts bearing on the anchor bolts, the abutment rocker bearing also shifts to a predominant rocking mode resulting in a rapid increase in resistance and secant stiffness.

Table 6.7 shows that minor differences exist in the lateral resistances between the pier rocker bearing (228 kN and 250 kN) and the abutment rocker bearing (221 and 252 kN). The abutment rocker bearing has smaller secant stiffnesses of 8.1 kN/mm and 10.1 kN/mm for the positive and negative responses than those (16.3 kN/mm and 10.9 kN/mm) of the pier rocker bearing. The cleaned abutment rocker bearing shows identical deformation modes to the as-received abutment bearing. An increase to 35 kN/mm for the initial stiffness and a decrease to 50 kN for the sliding resistance are observed for the abutment bearing after cleaning. Cleaning further reduces the bearing resistance to 198 kN for the positive response and 195 kN for the negative response as a result of the geometry changes and changes in the friction coefficient caused by rust removal.

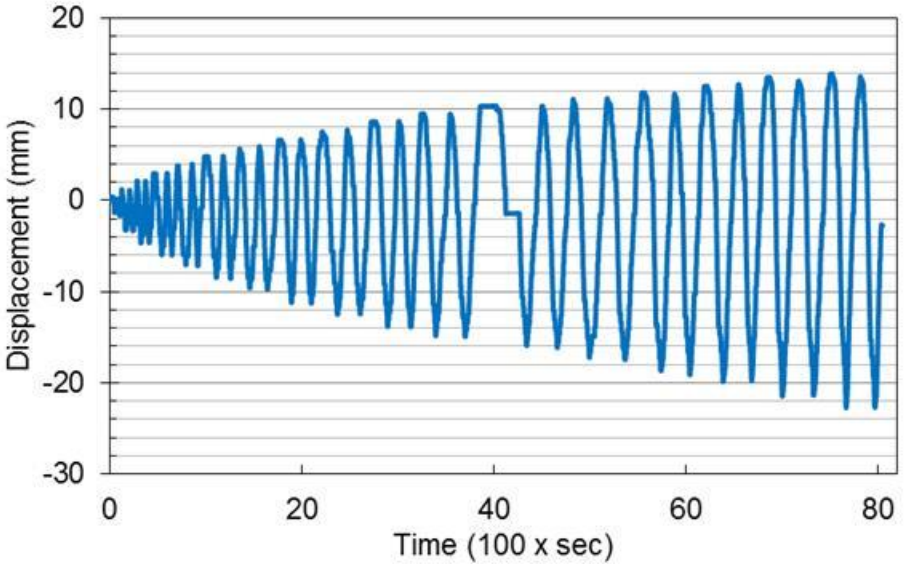

Figure 6.69 Actual loading protocol recorded during testing of Bearing PR19

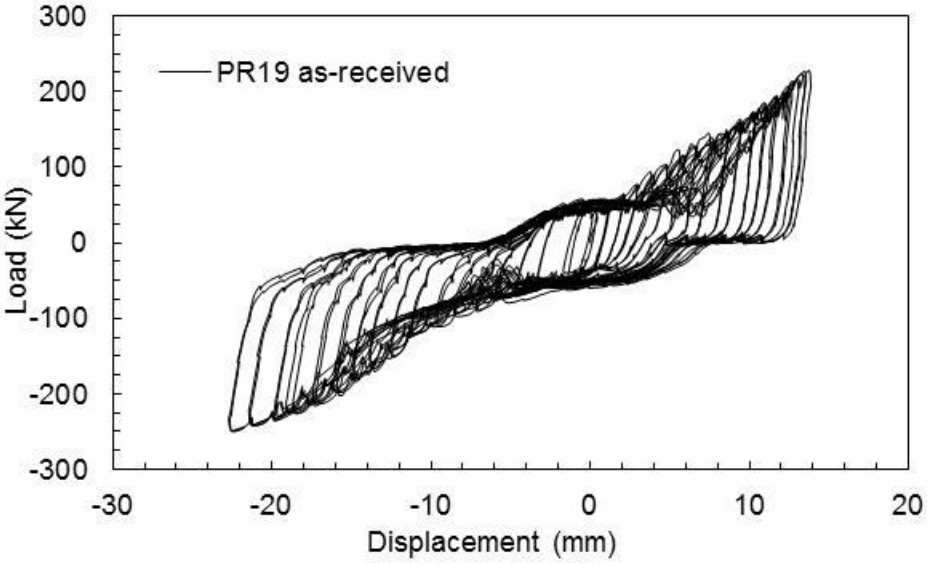

Figure 6.70 Transverse response of Bearing PR19 under cyclic loading in the as-received condition

Table 6.6 Summary of the longitudinal cyclic test results for steel rocker bearings with varying corrosion levels

Bearing ID	Initial stiffness (kN/mm)	Rolling resistance (kN)	Max positive response			Max negative response		
			Displacement (mm)	Resistance (kN)	Secant stiffness measured at maximum displacement (kN/mm)	Displacement (mm)	Resistance (kN)	Secant stiffness measured at maximum displacement (kN/mm)
PR8 minor	*8.5*	*5*	*64*	*43*	0.67	*62*	44	0.71
AR21 severe	3.1	5	57	41	*0.72*	56	*54*	0.96
AR21 cleaned	1.0	2.5	57	31	0.54	54	54	*1*

Table 6.7 Summary of the transverse cyclic test results for steel rocker bearings with varying corrosion levels

Bearing ID	Initial stiffness (kN/mm)	Sliding resistance (kN)	Max positive response			Max negative response		
			Displacement (mm)	Resistance (kN)	Secant stiffness measured at maximum displacement (kN/mm)	Displacement (mm)	Resistance (kN)	Secant stiffness measured at maximum displacement (kN/mm)
PR19 minor	*85*	50	14	*228*	*16.3*	23	250	*10.9*
AR23 severe	23	*60*	*22*	221	8.1	25	*252*	10.1
AR23 cleaned	35	50	19	198	10.4	*26*	195	7.5

6.4.6 Longitudinal cyclic response of steel bolster bearings

The pier bolster bearing #14 (PB14) is used in the study of the steel bolster bearing longitudinal behavior under cyclic loading. A detailed account of the corrosion condition of PB14 is provided in Section 6.3.7. Figure 6.40 shows that Bearing PB14 has negligible corrosion on the key bearing components such as the pintles, web, and stiffeners that all play a role in the bearing resistance against lateral loads.

The optotrak markers are distributed on the bearing in the pattern shown in Figure 6.71. Figure 6.72 shows the actual recorded loading history of the bearing test, which exhibits a symmetric displacement history with a maximum loading displacement of 45 mm.

The experimental cyclic behavior of the bolster bearing with minor corrosion is presented in Figure 6.73. The overall bearing behavior shows strength degradation at displacements beyond +16 mm and -26 mm. The initial deformation mode of the bolster bearing is governed by sliding with a resistance of roughly 40 kN as observed in the hysteretic curve. The sliding consists of two parts, sliding of the sole plate on the bolster bearing and sliding of the bolster bearing on the steel pedestal, due to the clearance around the pintles and the anchor bolts. When the displacement level exceeds 3 mm, the bearing deformation mode quickly becomes a mix of rocking and sliding leading to a rapid increase in resistance reaching over 100 kN at ±8 mm. As the displacement is further increased, the deformation mode shifts to combined rocking and prying, which engages the pintles in shear and the anchor bolts in combined tension and shear leading to a further increase in the lateral resistance. The maximum positive resistance of 180 kN occurs at a displacement level of 16.5 mm, while the maximum negative resistance of -179 kN occurs at a displacement of -25.6 mm. The combined tension and shear acting on the anchor bolts results in yielding and plastic deformation of the anchor bolts leading to the strength degradation observed in the bearing cyclic response. At this stage, rocking has become a more dominant deformation mode than prying because of the loss of bolt constraint since the bolts have sustained significant deformation as shown in Figure 6.72.

Continued cycling with increasingly higher displacement levels eventually leads to the first anchor bolt fracture at -38 mm during the second cycle to 41.3 mm. The load when

the first bolt fractures is -62 kN, significantly lower than the maximum value of -179 kN. The second bolt fractures at a displacement of 38 mm during the second cycle to 44.5 mm resulting in a sudden decrease in lateral resistance. As the displacement levels increase further to 44.5 mm, the resistance rapidly increases to 40 kN until unloading. The post-fracture response of the bolster bearing consists of two main deformation modes, sliding and rocking. A 40 kN resistance is found for this combined rocking and sliding deformation mode in the post-fracture bearing response. In the final negative half cycle response, the bolster bearing shows a tendency toward toppling as the bearing resistance starts to drop below -40 kN when the displacement approaches the target value of -44.5 mm. The total energy dissipation throughout this loading protocol is calculated to be 5253 Joules.

6.4.7 Transverse cyclic response of steel bolster bearings

Figure 6.74 shows the pier bolster bearing #13 (PB13) used in the transverse cyclic study of the steel bolster bearings with minor corrosion. As shown in Figure 6.74, Bearing PB13 only has minor corrosion on the bearing body (i.e. web, stiffeners) and the masonry plate. The top contact surface also has only minor corrosion and the pintles have sustained minimal if any section loss (Figure 6.75).

The instrumentation used for the bearing test is shown in Figure 6.76. The actual loading protocol recorded during the bearing test is given in Figure 6.77, which shows that the positive displacements are generally larger than the negative displacements in the same loading cycles. This inconsistency is due to the fact that the steel pedestal slips suddenly when large lateral loads are applied.

The overall bearing response under this transverse loading is shown in Figure 6.78. It shows a slight asymmetry due to the fact that the rest position of the bearing is not centered in the setup. Little strength degradation in the response is observed prior to anchor bolt fracture. When subjected to the early displacement cycles at small levels, the main observed deformation mode of the bearing is sliding. Similar to that of the longitudinal response, this sliding mode also consists of the sole plate sliding and the masonry plate sliding owing to clearance around the pintles and the anchor bolts.

As the level of the displacement cycles increases to larger values, the clearance is exhausted engaging the pintles and the anchor bolts in resisting the applied load by bearing on the sole plate and the masonry plate, respectively. As a result, a rapid increase in the bearing resistance is seen, while the deformation mode of the bearing shifts from sliding to a mix of rocking and prying that subjects the anchor bolts to combined tension and shear forces. The maximum resistance observed in the positive and the negative responses is 233 kN at 20 mm and -415 kN at -18 mm, respectively.

As opposed to the gradual anchor bolt deformation observed with the longitudinal test of the bolster bearing, the bolts fracture in an abrupt manner during the transverse loading of the bolster bearing. The first bolt fractures at a displacement of 17 mm during the second cycle to 31.8 mm, while the second bolt fractures at the negative displacement peak of this cycle. The lateral load at fracture is 165 kN and -270 kN for the first and second bolt, respectively. After bolt fracture, the bolster bearing is loaded for two more cycles to the next displacement level (34.9 mm), which shows a steady rigid sliding response (Figure 6.78). The sliding resistance is roughly 50 kN for both the positive and the negative loading directions. Considering the gravity load of 102 kN, the sliding friction coefficient for the bolster bearing under transverse loads is approximately 0.5. The cumulative hysteretic energy dissipated during loading of the bolster bearing reaches 10177 Joules.

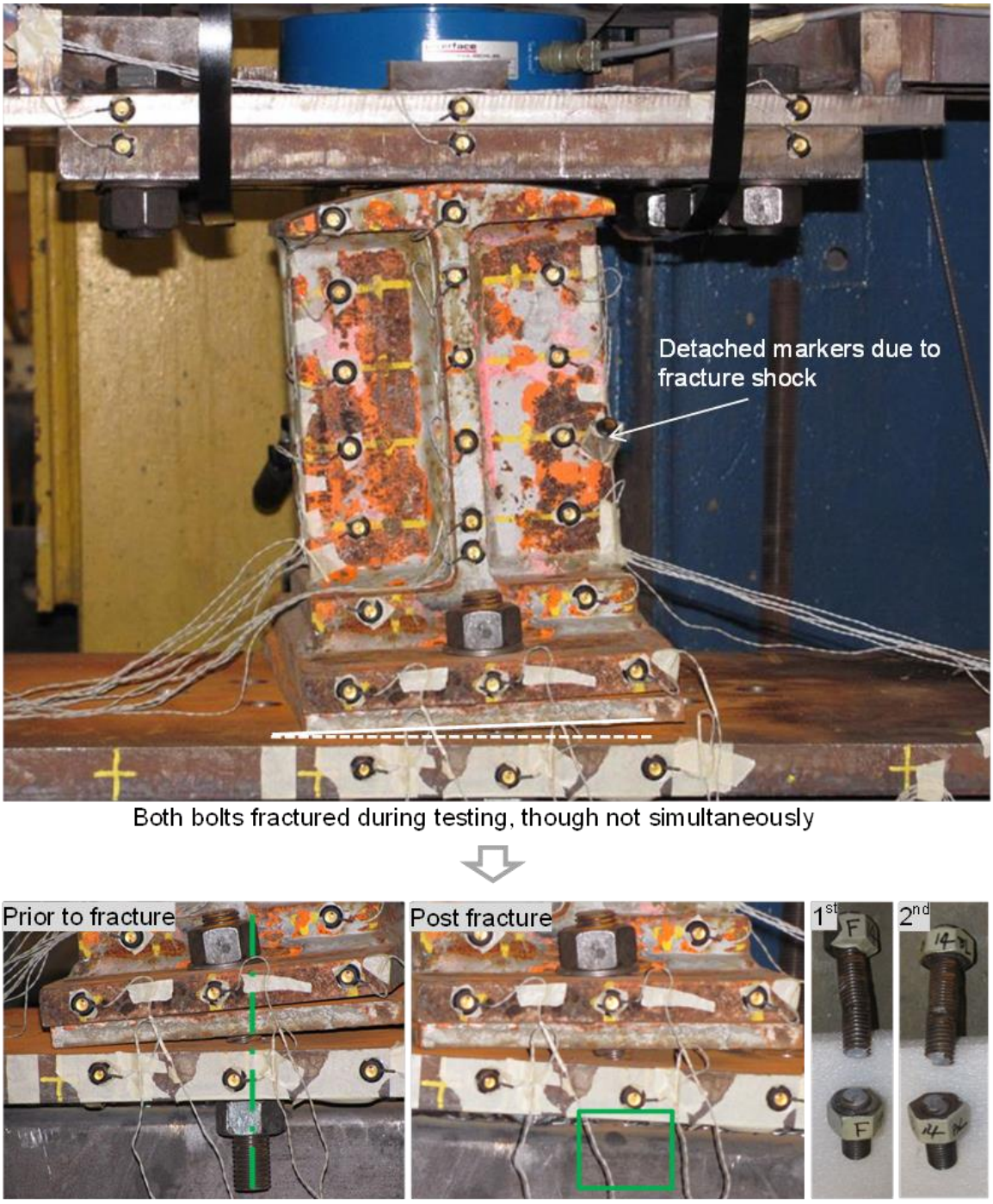

Figure 6.71 Photographs during testing of Bearing PB14 and after completion of loading

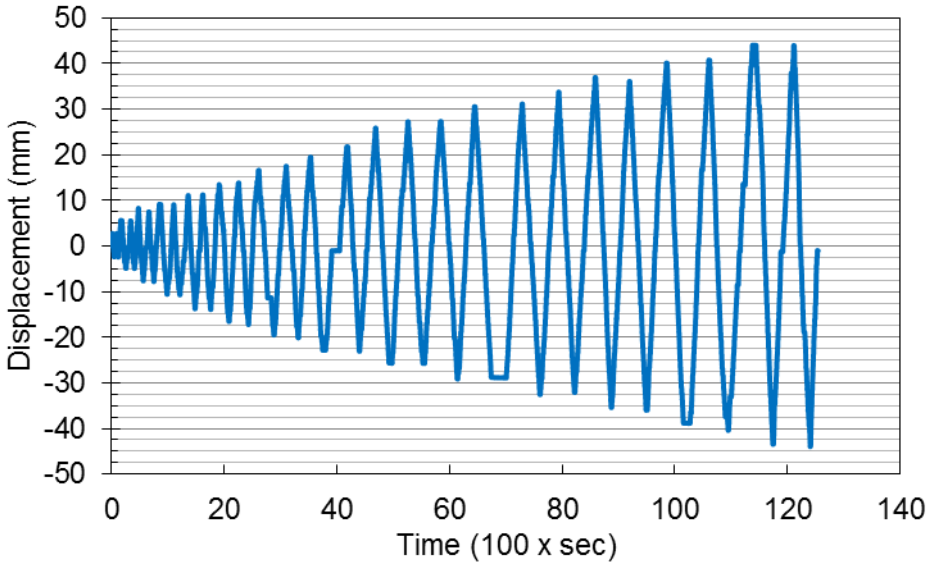

Figure 6.72 Actual loading protocol recorded during testing of Bearing PB14

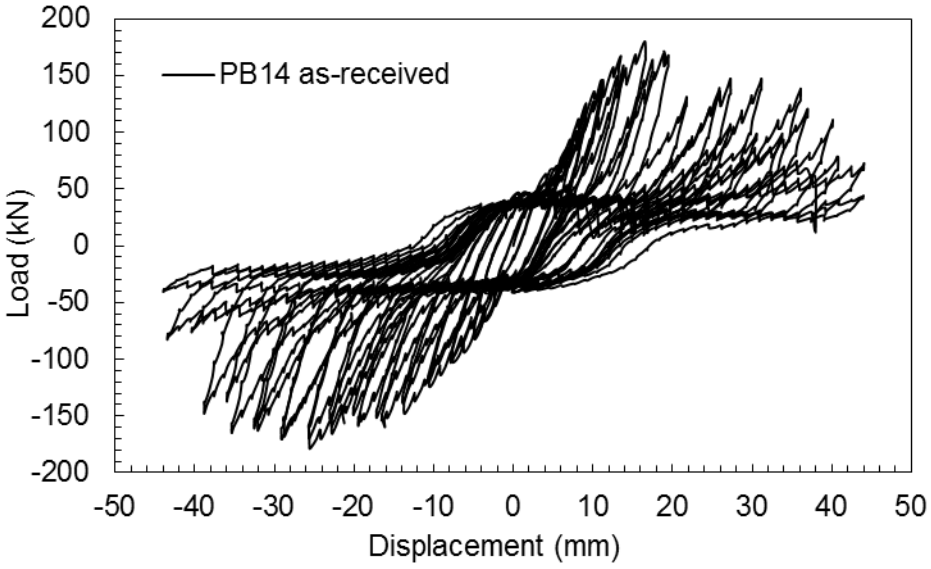

Figure 6.73 Longitudinal cyclic response of Bearing PB14 in the as-received condition

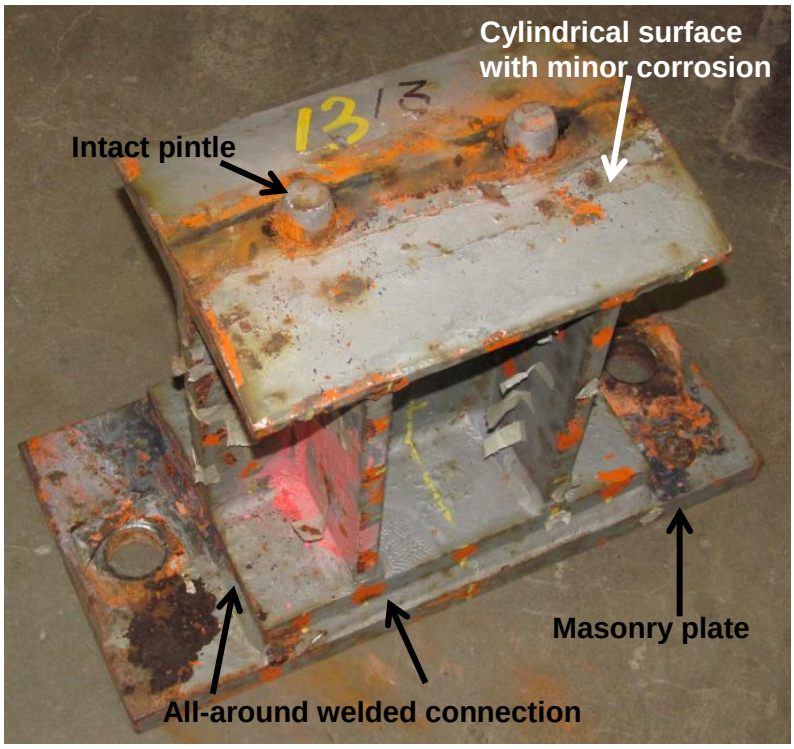

Figure 6.74 Pier bolster bearing #13 (PB13) in the as-received condition

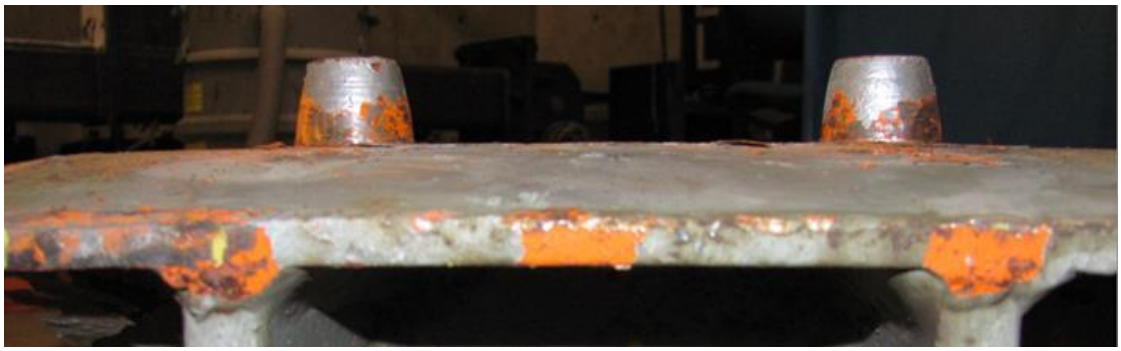

Figure 6.75 Top contact surface with pintles of Bearing PB13 in the as-received condition

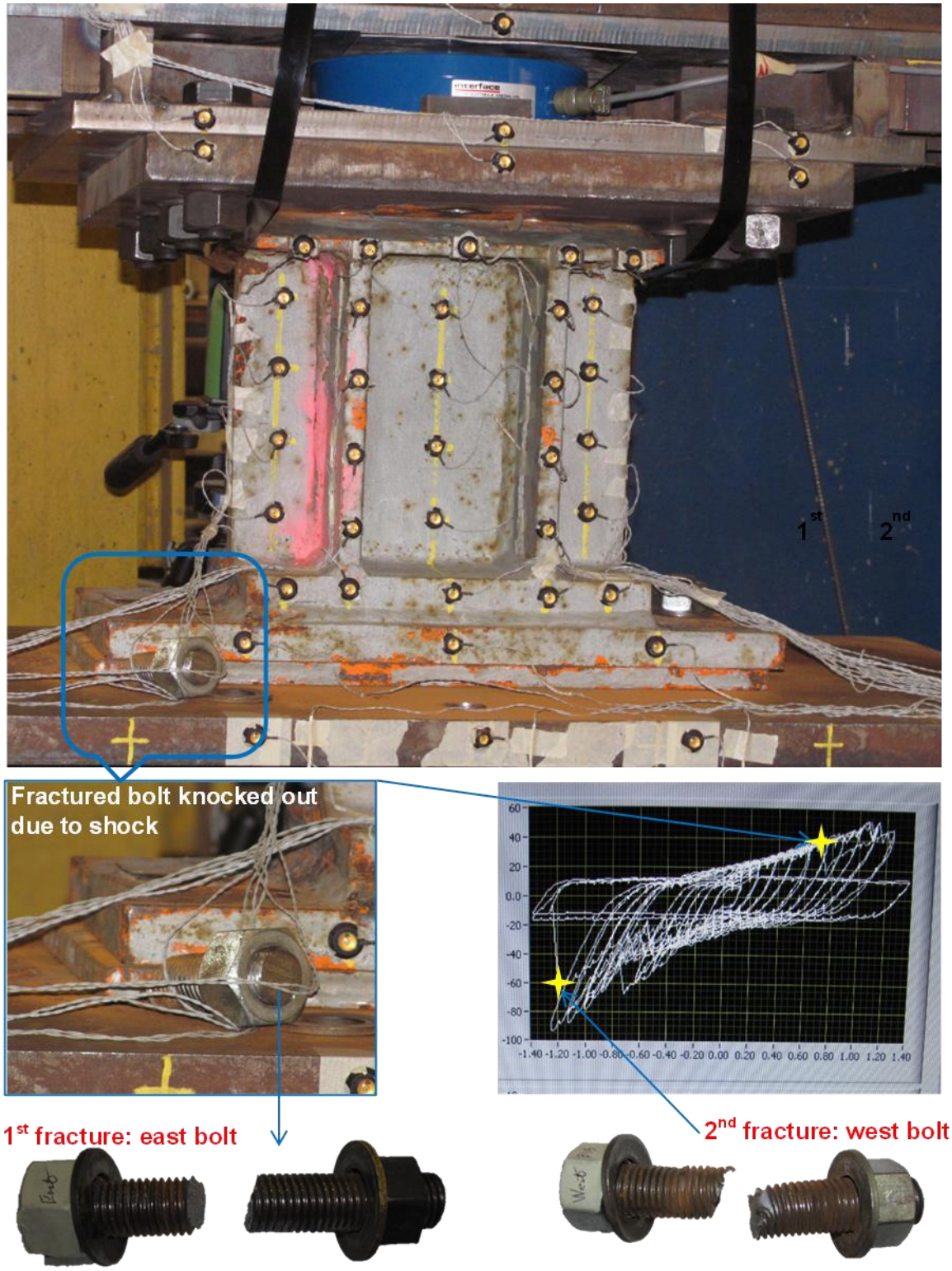

Figure 6.76 Photographs of Bearing PB13 taken during and after cyclic loading

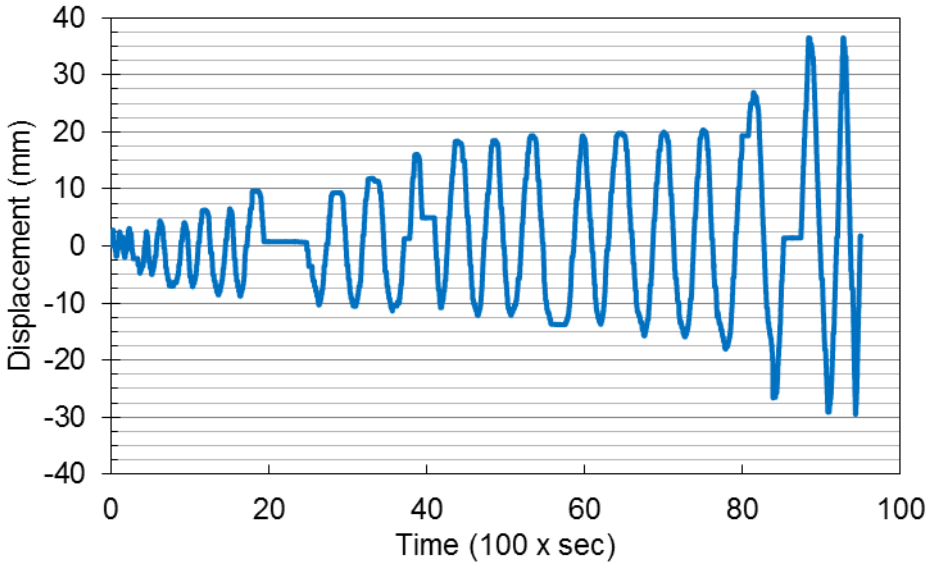

Figure 6.77 Actual loading protocol recorded during test of Bearing PB13

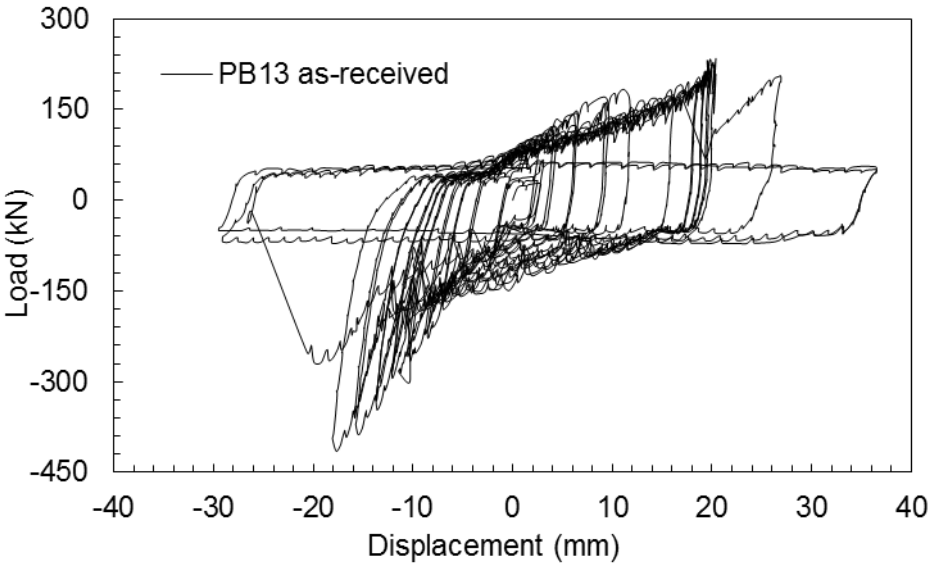

Figure 6.78 Transverse cyclic response of Bearing PB13 in the as-received condition

6.4.8 Summary of steel bolster bearing cyclic behavior

The salvaged steel bolster bearings have not sustained significant corrosion loss to any bearing component. Thus, only the cyclic behavior of bolster bearings with minor corrosion is investigated. Findings of these tests show that the bolster bearing behavior is determined by the clearance of bolt and pintle holes and the strength of the anchor bolts since the anchor bolts have a smaller diameter than the pintles. Table 6.8 provides a summary of the cyclic test results for the steel bolster bearings.

The bolster bearing shows a larger initial stiffness under transverse loading than under longitudinal loading. Sequential fracture of the anchor bolts is observed in both tests, but the anchor bolts fracture at much larger displacements in longitudinal bearing test. The transverse bearing response shows significantly larger bearing resistances and less strength degradation than the longitudinal response. Severe rocking is observed in the longitudinal response while the transverse response demonstrates a stable sliding behavior after the anchor bolts fracture.

Table 6.8 Summary of the cyclic behavior of the steel bolster bearings with minor corrosion

Bearing ID and loading direction		PB14: longitudinal	PB13: transverse
Initial stiffness (kN/mm)		25	60
First bolt fracture	Displacement (mm)	-38	17
	Load (kN)	-62	165
Second bolt fracture	Displacement (mm)	38	-20
	Load (kN)	61	-270
Max positive resistance	Displacement (mm)	16.5	20
	Load (kN)	180	233
Max negative resistance	Displacement (mm)	-25.6	-18
	Load (kN)	-179	-415
Post fracture response	Load (kN)	40	50
	Friction coefficient	-	0.5

6.5 Cyclic Behavior of Steel Bearings on a Concrete Pedestal

A common steel bearing failure pattern observed during past seismic events is associated with the anchorage of steel fixed bearings, such as pullout of the anchor bolts, extensive concrete cracking, or concrete breakout. To further investigate the cyclic performance of the steel bolster bearings, the bearing-concrete pedestal assembly behavior is considered experimentally. A total of two reinforced concrete pedestals are designed and fabricated (Section 6.2.4). These pedestals are designed to mimic the reinforcement layout of the actual bridge cap beams used for the Meridian bridge. The anchorage performance is investigated for two different bolt diameters, one with a 25.4 mm diameter and the other with a 34.9 mm diameter. The first bolt diameter is consistent with the bolt diameter used in the two preceding experimental studies, i.e. the monotonic and cyclic tests. The second bolt diameter is used to investigate whether different bearing deformation modes or failure patterns can be developed when the anchor bolt has a fracture strength larger than that of the pintles.

6.5.1 Longitudinal cyclic response of steel bolster bearings using 25.4 mm anchor bolts

The longitudinal cyclic test of the steel bolster bearing using anchor bolts with a 25.4 mm diameter is conducted on pier bolster bearing #15 (PB15) shown in Figure 6.79. Bearing PB15 has sustained very minor corrosion on the web and the masonry plate. The top cylindrical surface is in a good condition with minimal section loss experienced by the pintles. The observed minor corrosion at the contact region of the top surface is believed to have negligible influence on the overall bearing cyclic behavior and thus is considered only minor.

The loading protocol used in this test is identical to the one used in the steel-based bolster bearing test to better understand the influence of using a concrete pedestal. However, due to rigid sliding of the concrete pedestal, the actual loading history of the bolster bearing concrete pedestal test is not perfectly symmetric as shown in Figure 6.80. After finishing the two loading cycles to 38.1 mm of displacement, the bolster bearing was pushed to

-50.8 mm in an attempt to fracture the anchor bolts, which did not occur. These loading displacements are significantly large for a bolster bearing that was not designed to undergo these large deformations.

The cyclic response of the bolster bearing tested on a concrete pedestal is presented in Figure 6.81. Due to the asymmetry of the actual loading history, the experimental cyclic behavior is not symmetric. The initial deformation mode of the bolster bearing consists of rocking and prying, subjecting the anchor bolts to combined tension and shear. The initial stiffness is 18 kN/mm. As the tension force in the anchor bolts increases at larger displacements, the bond between the anchor bolt and the concrete pedestal is overcome and the anchor bolts start to pull out of the pedestal. This anchorage failure leads to a growing gap between the masonry plate and the bolt nuts (Figure 6.82), which permits more severe rocking of the bolster bearing before the masonry plate can engage the anchor bolts under combined tension and shear during subsequent cycles. As a result, larger displacements are required prior to seeing a significant increase in resistance. Once this gap is closed and the masonry plate starts bearing on the nuts, the bearing resistance then rapidly increases. The maximum positive resistance is 224 kN at the 42 mm displacement level. Since the actual negative loading displacement is smaller in magnitude than the positive loading displacement due to slip of the concrete pedestal, the bolster bearing cannot rock enough to close the gap between the bolt nuts and the masonry plate created during positive loading leading to lower resistances measured in the negative direction. This situation worsens as the displacement exceeds -15 mm. The negative monotonic push of the bolster bearing at the end of loading does show that once the loading displacement can cause enough rocking of the bolster bearing to engage the anchor bolts (Figure 6.83), the bearing resistance does rapidly increase to -202 kN at -50.8 mm, similar to that seen with the positive loading. This finding indicates that the anchor bolts have not sustained major damage yet and the perceived degradation is merely due to severe rocking and anchorage pullout as explained above. Post-test examination confirms that the anchor bolts have only been slightly bent due to bending as shown in Figure 6.84. However, the bolts pull out nearly 1 cm, resulting in minor radial cracking of the concrete around the bolts. These findings suggest that the bolster bearing

is capable of undergoing significant deformation when laterally loaded in the longitudinal direction.

6.5.2 Transverse cyclic response of steel bolster bearings using 25.4 mm anchor bolts

Figure 6.85 shows pier bolster bearing #11 (PB11) used in the transverse cyclic study of the steel bolster bearing-concrete pedestal assembly with 25.4 mm diameter anchor bolts. The overall condition of Bearing PB11 is good with only minor corrosion observed on the surfaces of the web, stiffeners, and masonry plate. However, the observed corrosion is not significant enough to induce strength reduction of the bearing. The top cylindrical flange is also in a good condition with minimal section loss for both of the pintles.

The loading protocol used in this test is identical to the one used in the transverse bolster test conducted on a steel pedestal. Figure 6.86 shows the actual recorded loading protocol which exhibits good symmetry.

Figure 6.87 shows the experimental cyclic behavior of the steel bolster bearing on a concrete pedestal. A symmetric response is obtained with minor force differences observed between the positive and negative maximum resistances. A predominant initial sliding response is observed with the sliding resistance varying at around 50 kN. This sliding response exists at two contact interfaces, i.e. the sole plate-bearing top flange interface and the masonry plate-shim plate interface. The initial stiffness is roughly 50 kN/mm. Once the pintles and the anchor bolts are engaged in resisting the applied load at larger displacements, a rapid increase in the bearing resistance is seen in the response. The deformation mode switches to combined rocking and prying (Figure 6.88) subjecting the anchor bolts to combined tension and shear. The maximum resistances observed in the positive and the negative responses are 207 kN at 15 mm of displacement and -309 kN at -31 mm of displacement, respectively. This disparity is due to the initial off-centered rest position of the bearing specimen in the setup, which causes the anchor bolts at relatively small negative displacements to engage leading to an accelerated increase in the negative resistance. A load drop of over 100 kN is seen in the negative response after reaching the peak resistance due to the fracture of the anchor bolts (Figure 6.89). The

bolster bearing is further loaded multiple cycles with the maximum displacement level approaching 50 mm. Post-fracture response of the bolster bearing is predominantly governed by rigid sliding at two interfaces, i.e. the masonry plate-shim plate interface and the shim plate-concrete pedestal interface, with a sliding resistance between 70 kN and 100 kN. The large variation observed in the sliding resistance is due to digging of the shim plate into the concrete surface as shown in Figure 6.90. Surface damage of the concrete pedestal is observed.

Post-test examination of the concrete pedestal and anchor bolts reveals two large craters that have formed in the pedestal around the anchor bolts as shown in Figure 6.91. The fracture in the anchor bolts is located roughly 25 mm beneath the concrete surface which matches the depth of the craters formed in the concrete. However, damage to the concrete pedestal is confined to these craters without any significant cracking of the adjacent concrete. Overall, the bolster bearing anchored to a concrete pedestal exhibits a significant deformation capacity and load carrying ability under transverse cyclic loading. The concrete pedestal also shows the ability to provide enough anchorage to permit anchor bolt fracture. A stable sliding behavior of the bolster bearing is also achieved post-fracture.

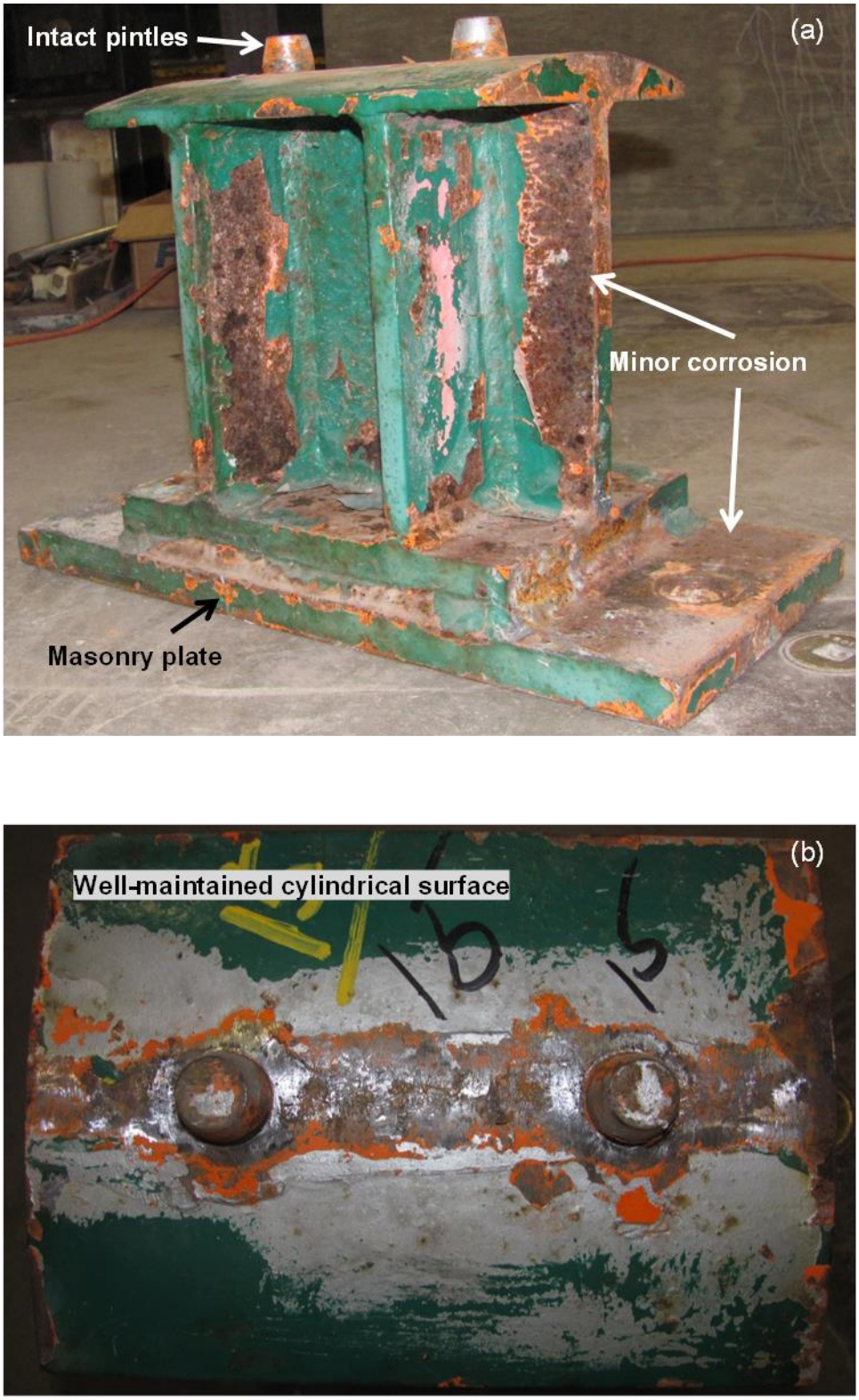

Figure 6.79 Pier bolster bearing #15 (PB15) in the as-received condition

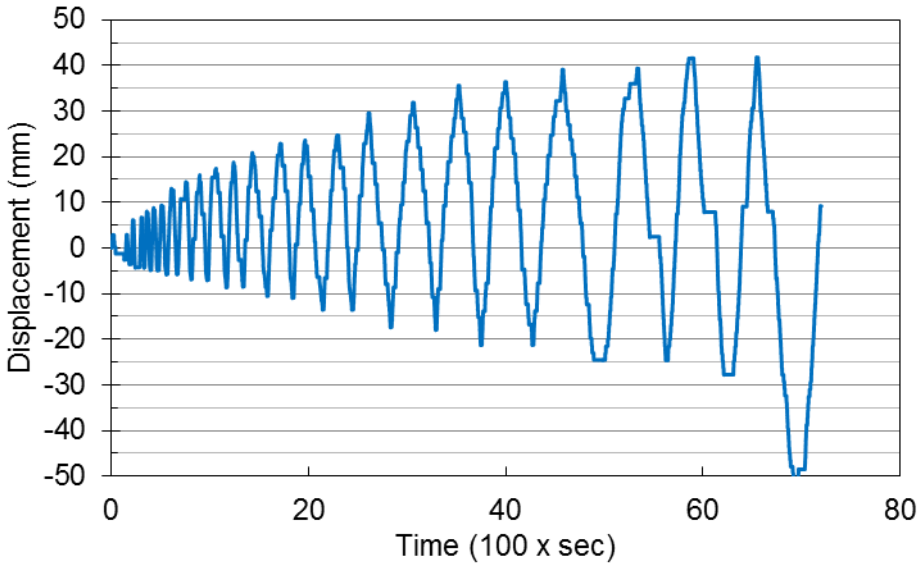

Figure 6.80 Actual loading protocol recorded during cyclic testing of Bearing PB15

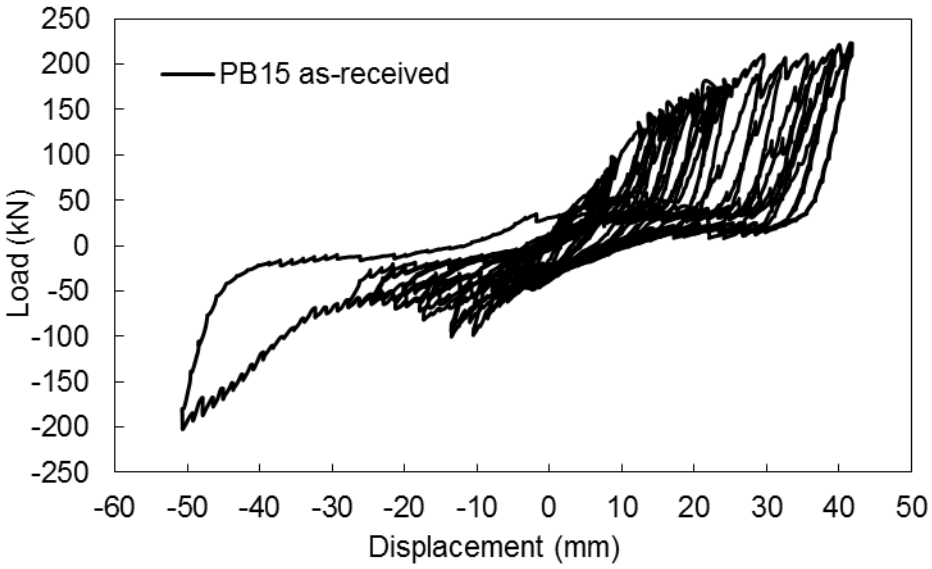

Figure 6.81 Longitudinal cyclic response of Bearing PB15 on a concrete pedestal and using anchor bolts with a 25.4 mm diameter

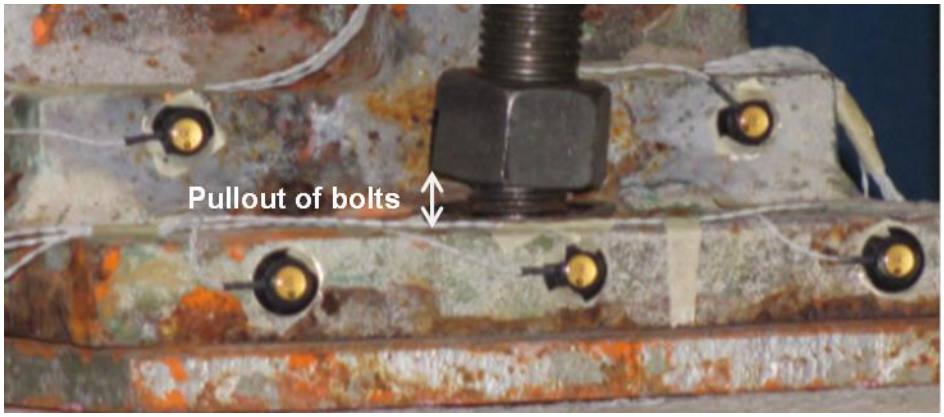

Figure 6.82 Photograph showing pullout of the anchor bolts under combined tension and shear due to bond failure between the bolts and the concrete

Figure 6.83 Photograph showing significant rocking of the bolster bearing due to anchor bolt pullout at larger displacements

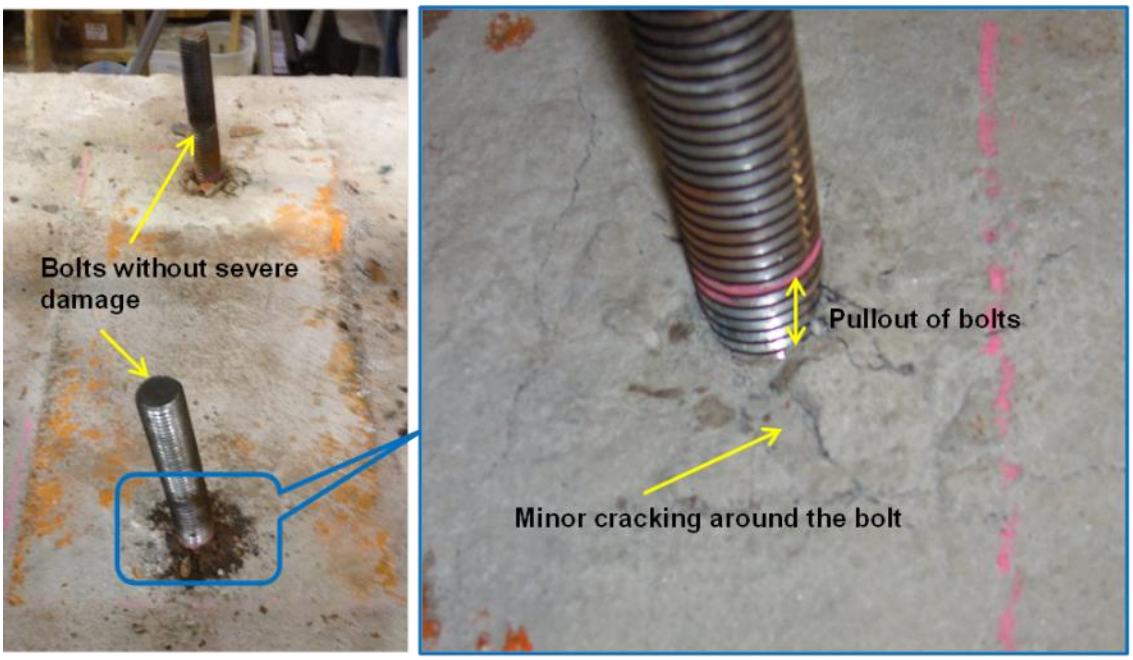

Figure 6.84 Photographs taken post test for the anchor bolts showing minor damage and minor cracking of the concrete pedestal around the bolts

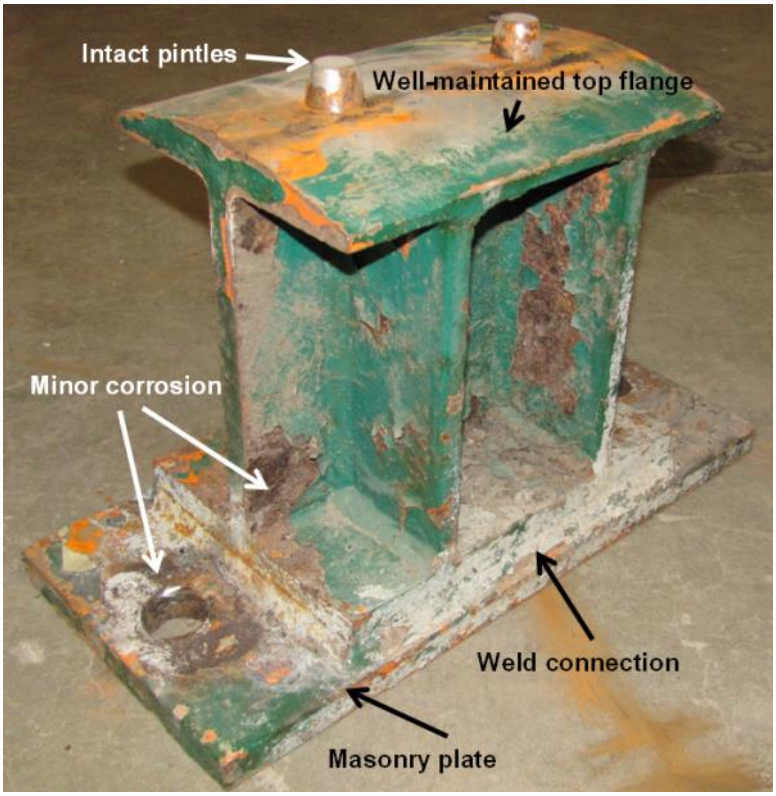

Figure 6.85 Pier bolster bearing #11 (PB11) in the as-received condition

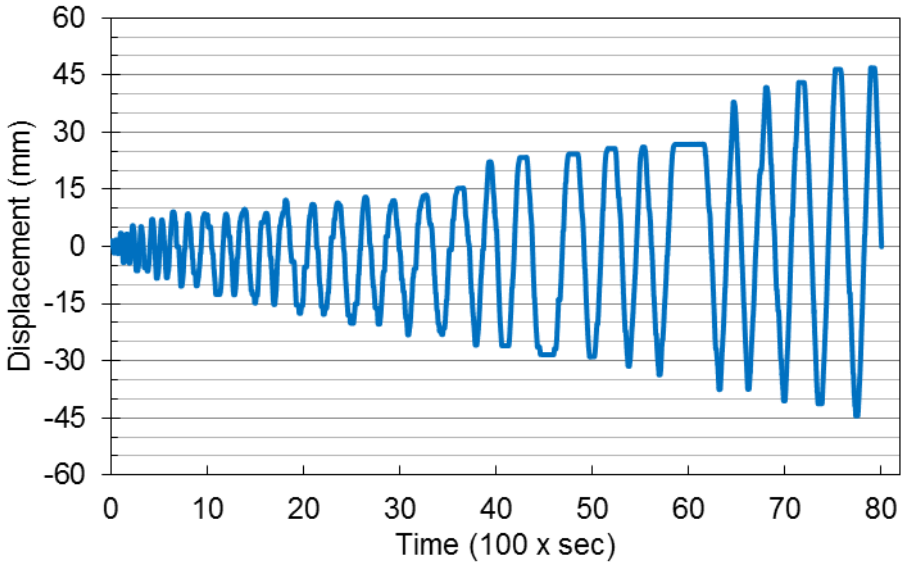

Figure 6.86 Actual loading history recorded during cyclic testing of Bearing PB11

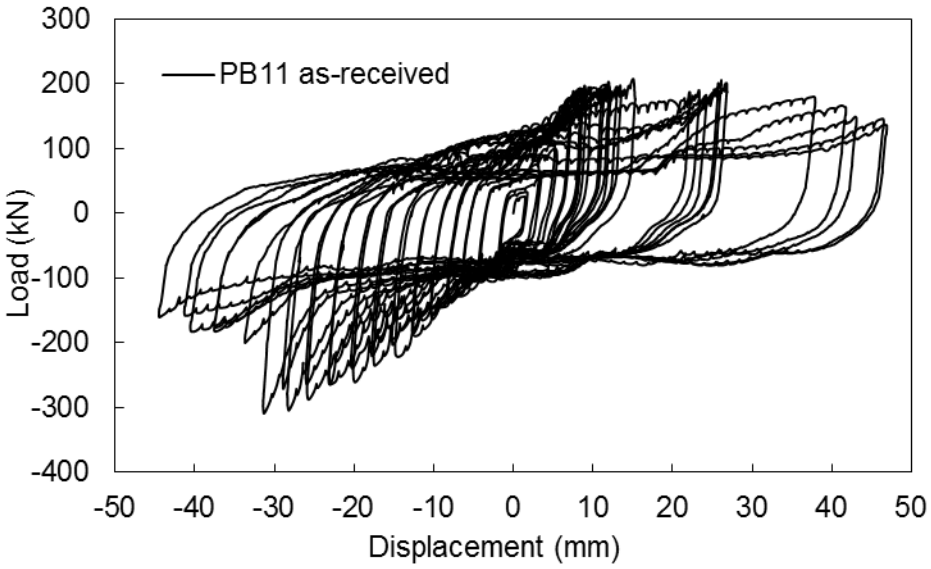

Figure 6.87 Transverse cyclic response of Bearing PB11 on a concrete pedestal and using anchor bolts with a 25.4 mm diameter

Figure 6.88 Photograph showing the rocking deformation mode of the bolster bearing

Figure 6.89 Photograph showing the severely deformed and fractured anchor bolt

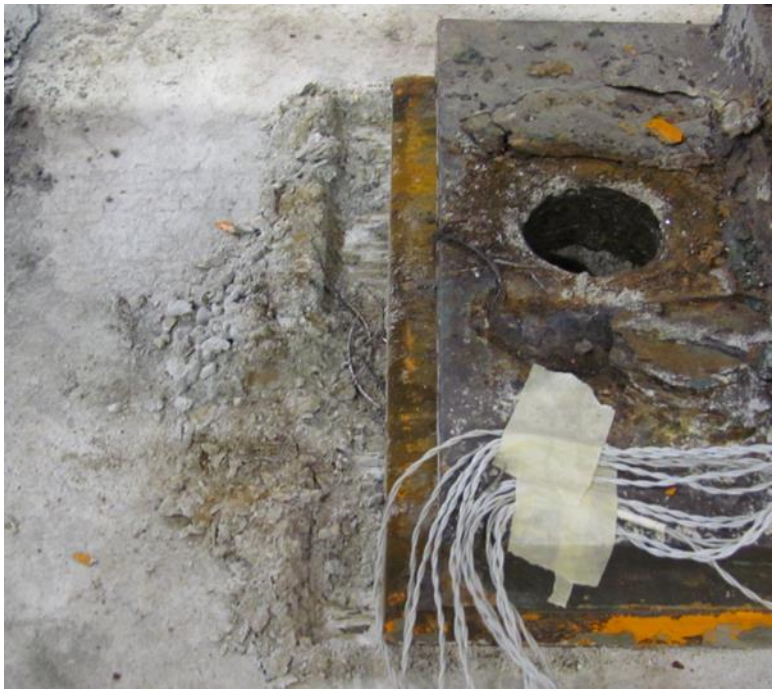

Figure 6.90 Photograph showing concrete pedestal surface damage due to digging of the shim plate

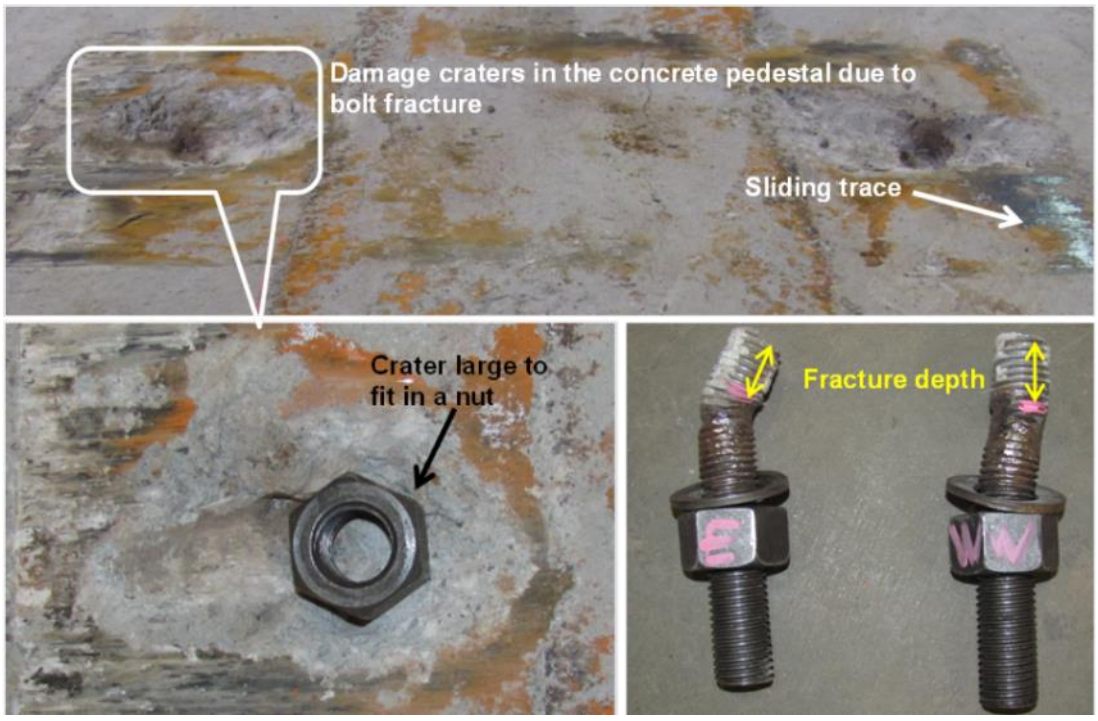

Figure 6.91 Photographs of the damaged concrete pedestal and anchor bolts due to bolt pullout and fracture

6.5.3 Longitudinal cyclic response of steel bolster bearings using 34.9 mm anchor bolts

The pier bolster bearing #11 (PB11) is used to consider the longitudinal cyclic response of the steel bolster bearing with 34.9 mm diameter anchor bolts. A detailed account of the corrosion condition of Bearing PB11 is provided in Section 6.5.2.

The loading protocol is identical to the one used in the bearing test presented in Section 6.5.1. The actual loading protocol recorded during the test is presented in Figure 6.92. After the two loading cycles to 44.5 mm are finished, the displacement increment is increased to 6.4 mm and the bearing was loaded two more cycles to 50.8 mm. After the bearing was loaded to -50.8 mm the second time, a monotonic push to 101.6 mm was carried out in an attempt to fracture the pintles and the test was subsequently discontinued upon returning to rest position.

The experimental cyclic response of the bolster bearing with 34.9 mm diameter anchor bolts is shown in Figure 6.93. Severe pinching is observed in the bearing response when the positive displacement is above 20 mm and the negative displacement is above -18 mm. The maximum positive bearing resistance is 227 kN at a displacement of 20.4 mm and the maximum negative bearing resistance is -249 kN at a displacement of -17.7 mm. The main deformation mode of the bolster bearing is combined rocking and prying, which leads to the anchor bolts being subjected to combined tension and shear. However, the anchorage provided by the concrete pedestal cannot withstand the tension forces being applied to the anchor bolts leading to pullout of the anchor bolts. The pullout of the anchor bolts increases the gap between the bolt nut and the masonry plate, which causes more severe rocking of the bearing before engaging the anchor bolts (Figure 6.94). This phenomenon is reflected in the strength degradation observed in the bearing response before applying the two loading cycles to 50.8 mm of displacement. A slight increase in resistance is seen in the bearing response when the first cycle to 50.8 mm of displacement is applied due to the fact that the bolts are engaged under both tension and shear at this larger applied displacement. However, this only leads to further pullout of the anchor bolts and again causes strength degradation as shown in the bearing response under the

second cycle to 50.8 mm. The final monotonic push to -101.6 mm yields a bearing resistance of -142 kN, showing an increase in the bearing resistance from that seen at -50.8 mm. Post-test examination shows that the anchor bolts undergo pullout of more than 25.4 mm (Figure 6.95) over the course of loading. However, the anchor bolts do not sustain any major deformation. Additionally, Figure 6.96 shows that the bolt pullout has caused severe radial cracking of the concrete around the bolts. Edge concrete breakout also can be observed in this figure. The bearing pintles have sustained minimal deformation as shown in Figure 6.97.

6.5.4 Transverse cyclic response of steel bolster bearings using 34.9 mm anchor bolts

Pier bolster bearing #15 (PB15) is used in the test of the steel bolster bearing with 34.9 mm diameter anchor bolts under transverse cyclic loading. A detailed account of the corrosion condition of Bearing PB15 is provided in Section 6.5.1.

The loading protocol used in this test is identical to the one used in the transverse bolster test using 25.4 mm diameter anchor bolts. Figure 6.98 shows the actual recorded loading protocol which exhibits good symmetry. However, due to an expected failure of the test setup, cyclic testing of Bearing PB15 was discontinued after finishing two cycles to 25.4 mm displacement. As a result of rigid sliding of the concrete pedestal, the actual maximum displacement applied to the specimens is approximately 13 mm.

Figure 6.99 shows the transverse cyclic response of the steel bolster bearing using 34.9 mm diameter anchor bolts. A predominant sliding behavior is observed for the bolster bearing during transverse cyclic testing. Sliding occurs at two interfaces, one at the sole plate-bearing top contact interface and one at the masonry plate-shim plate contact interface. The associated sliding resistance ranges between 30 kN and 35 kN. As the masonry plate sliding exhausts the clearance around the anchor bolts, it starts to bear on the anchor bolts leading to a rapid increase in both the lateral resistance and secant stiffness. Because of the early discontinuation of the testing, neither the bolts nor the pintles fracture during testing, leading to a hysteretic behavior without any strength degradation. A maximum lateral resistance of 372 kN is obtained at approximately 12

mm of displacement in the positive direction, while a maximum lateral resistance of -394 kN is obtained at -13 mm of displacement in the negative direction. Post-test examination shows that both the pintles and bolts are in good condition without any major deformation.

6.5.5 Summary of steel bearing-concrete pedestal assembly tests

To better understand the anchorage performance of steel bolster bearing-concrete pedestal assemblies, the results from four large-scale cyclic tests conducted on steel bolster bearings that are anchored to reinforced concrete pedestals are considered. These pedestals are designed and constructed based on the original concrete cap beam design to better represent the behavior of the in-situ concrete substructure. Anchor bolts with two different diameters of 25.4 mm and 34.9 mm are considered to investigate the effect of anchor bolt diameter on the cyclic performance of the steel bearing-concrete pedestal assembly in regards to deformation and failure modes. Results of these tests are presented in Table 6.9.

Table 6.9 Summary of the cyclic test results of the steel bolster bearing-concrete pedestal assemblies

Bearing test		Long. Cyclic 25.4 mm Bolt	Trans. Cyclic 25.4 mm Blot	Long. Cyclic 34.9 mm Bolt	Trans. Cyclic 34.9 mm Bolt
Max positive resistance	Displacement (mm)	42	15	20.4	12
	Load (kN)	224	207	227	372
Max negative resistance	Displacement (mm)	-50.8	-31	-17.7	-13
	Load (kN)	202	-309	-249	-394
Post fracture response	Load (kN)	NA	70 - 100	NA	NA
	Friction coefficient	NA	0.7 - 1.0	NA	NA

Significant anchor bolt pullout is observed in all tests except for the last one, which is discontinued early due to constraints with the test setup. Fracture of the anchor bolts is observed only during the transverse cyclic testing of the steel bearing-concrete pedestal

assembly using 25.4 mm diameter bolts. The anchor bolts remain in good condition without any substantial deformation for all other tests. For all tests, the bearing-concrete pedestal assembly is less stiff than the bearing-steel pedestal assembly. This loss of stiffness can largely be attributed to pullout of the anchor bolts and damge to the concrete pedestal with cycling. For the 34.9 mm diameter anchor bolt tests, the steel bearing is pushed to a displacement level over 100 mm without fracturing either the pintles or the bolts exhibiting a substantial deformation capacity, although the anchor bolts pullout is over 25 mm.

Table 6.9 shows that for the longitudinal response, using the 34.9 mm diameter bolts can lead to maximum lateral resistances occurring at much smaller displacement levels in both the positive and negative directions. A significant resistance increase is only observed in the negative response due to the use of a larger anchor bolt diameter. Pinching is observed at small displacements for the 25.4 mm diameter bolt tests, while degradation of the resistance is observed at small displacements for the 34.9 mm diameter bolt tests. Overall, the 34.9 mm diameter anchor bolt provides a much stiffer connection between the steel bearing and the concrete pedestal, thus permitting larger forces to be transferred to the pedestal at smaller deformation levels. Additionally, the 34.9 mm diameter bolt test results show a much stiffer response with a larger secant stiffness compared to the response for the 25.4 mm diameter bolt test results.

6.6 Summary

The lateral behavior of steel rocker bearings with both severe and minor corrosion and steel bolster bearing with only minor corrosion is investigated under both longitudinal and transverse loading. Two types of loading protocols, monotonic and cyclic, are considered to fully evaluate the deformation mode, failure pattern, and load-deformation relationship of steel bridge bearings. The steel rocker bearings with severe corrosion are also studied after rust removal to examine the effect of pack rust on the overall bearing performance. The steel bolster bearings are further tested to investigate potential anchorage failure modes associated with using reinforced concrete pedestals. These

studies show that for steel rocker bearings, corrosion can have a significant impact on the deformation modes, lateral stiffness, and resistance. Lower secant stiffnesses and resistances are observed for the corroded bearings compared to the bearings with minor corrosion. For steel bolster bearings anchored to a steel pedestal, sliding, rocking, and prying are found to be the dominant deformation modes prior to anchor bolt fracture. After anchor bolts fracture, rocking becomes the predominant deformation mode for the longitudinal behavior, while sliding governs the transverse behavior. Pinching and strength degradation are observed in the bolster bearing load-displacement behavior due to the inelastic behavior of the anchor bolts. For steel bolster bearings anchored to a concrete pedestal, lower stiffness is observed when using 25.4 mm diameter anchor bolts due to the pullout of the anchor bolts. As a result of the anchor bolt pullout, deformation modes for the longitudinal behavior experience slight changes from predominant prying to predominant rocking at larger displacement levels. This deformation mode variation leads to a bearing response with more severe pinching and less strength degradation, while the anchor bolts barely sustain any inelastic deformation. A prominent sliding response also develops for the transverse post-bolt fracture bearing behavior, but the friction resistance fluctuates due to digging and rocking on the masonry plate.

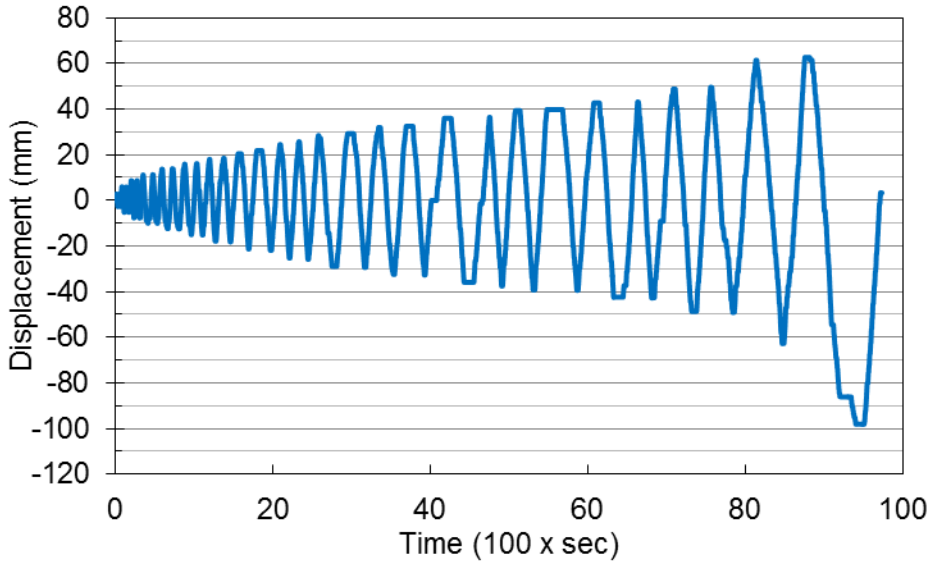

Figure 6.92 Actual loading protocol used in the test of Bearing PB11 on a concrete pedestal with 34.9 mm diameter anchor bolts

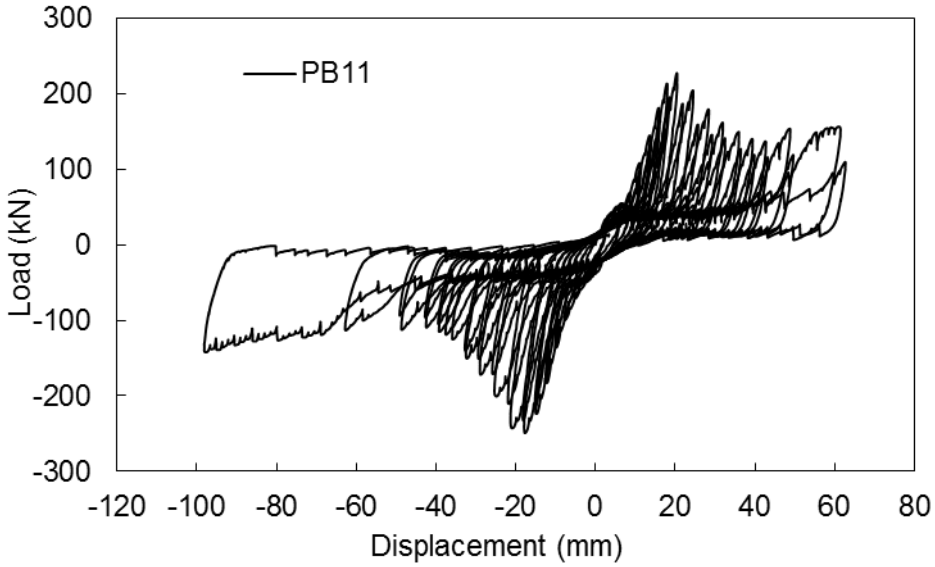

Figure 6.93 Longitudinal cyclic response of Bearing PB11 on a concrete pedestal with 34.9 mm diameter bolts

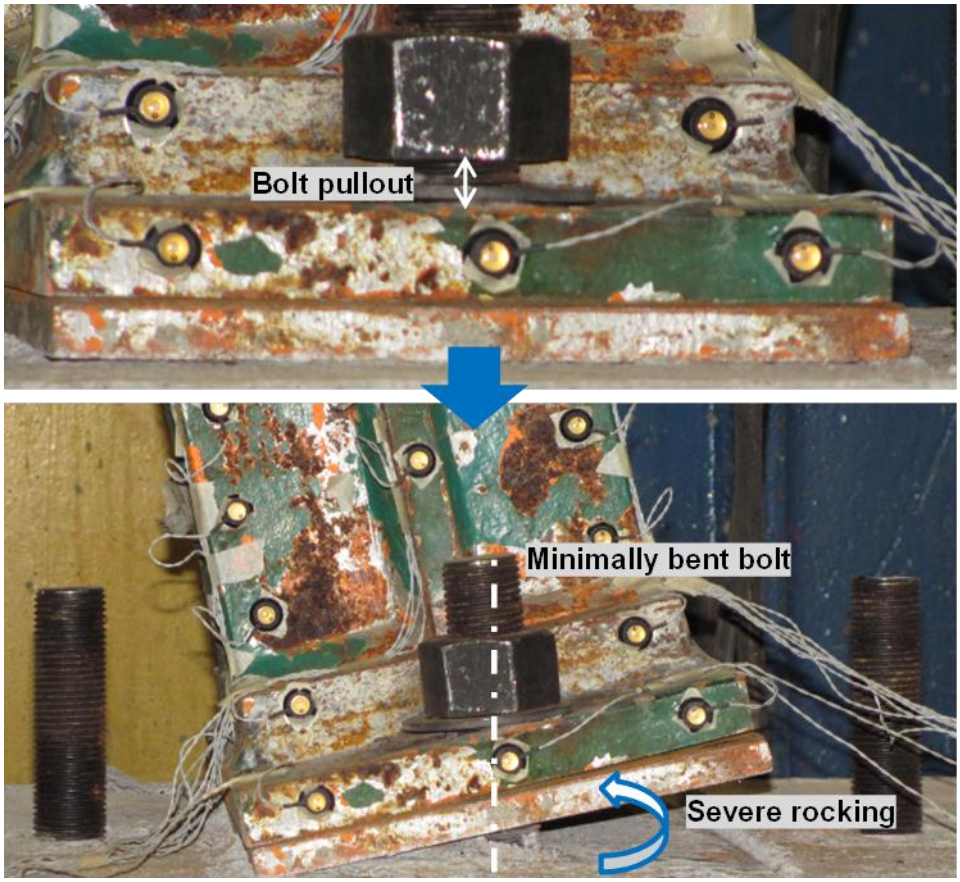

Figure 6.94 Photographs showing bolt pullout and bearing rocking behavior

Figure 6.95 Photograph taken post-test showing the extent of bolt pullout accumulated during cyclic testing

Figure 6.96 Photographs of the reinforced concrete pedestal taken after the cyclic test showing concrete cracking and bolt damage

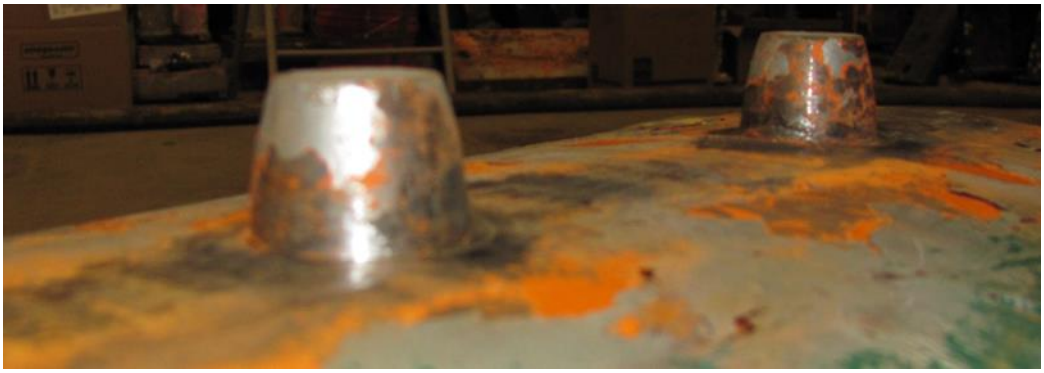

Figure 6.97 Photograph of the pintles taken after the cyclic test

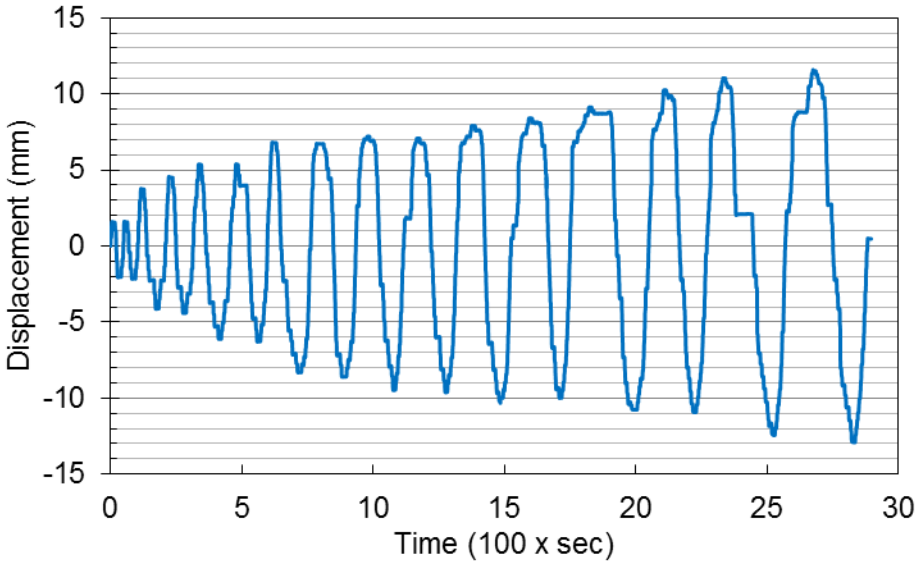

Figure 6.98 Actual loading history recorded during testing of Bearing PB15 on a concrete pedestal with 34.9 mm diameter anchor bolts

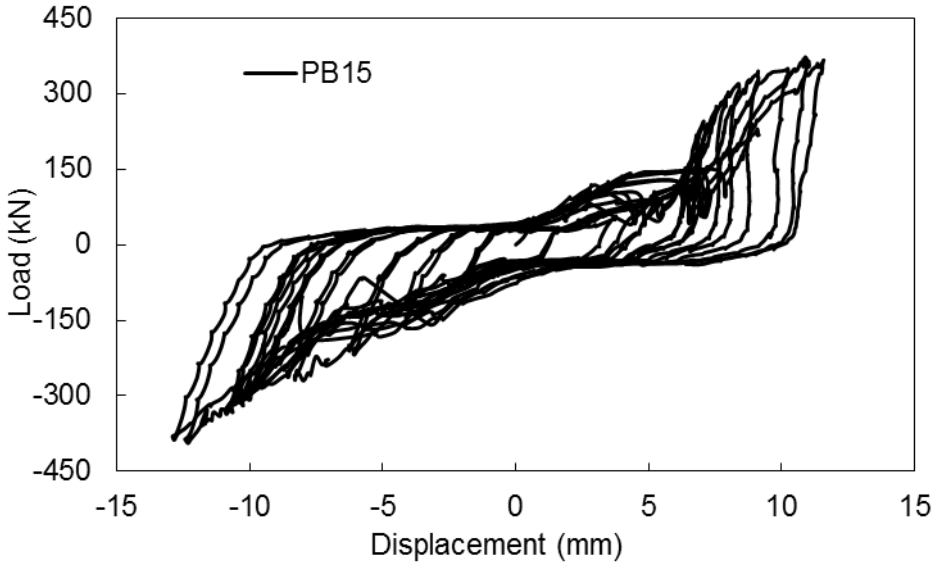

Figure 6.99 Transverse cyclic response of bearing PB15 on a concrete pedestal with 34.9 mm diameter anchor bolts

CHAPTER 7 EFFECT OF STEEL BEARING BEHAVIOR ON BRIDGE PERFORMANCE

7.1 Introduction

To further evaluate the seismic performance of steel bridge bearings and their influence on the overall bridge behavior, the experimentally obtained steel bearing load-displacement curves are first used to develop a suite of calibrated numerical bearing models that incorporate corrosion effects where necessary and are suitable for implementation in numerical simulations of steel bridge systems. Two bridge models then are created to perform system-level nonlinear time history analyses. These models include nonlinearities associated with the passive and active abutment-soil interactions, pounding between the superstructure and the abutments, the behavior of steel bearings with different corrosion levels, reinforced concrete wall pier models, and the behavior of pile group foundations. Latest research findings on the seismic behavior of various critical bridge components are adopted for these models and reflect the state of the art in seismic bridge simulation. Lastly, the seismic response of the bridge systems is investigated considering two suites of ground motions representing different levels of seismic hazard typical of the CEUS. These simulations lead to a further understanding of how steel bearing behavior affects the overall bridge system during seismic excitation, how corrosion of the steel bearings influences the overall bridge performance, and how various bridge components perform under different levels of seismic hazards.

7.2 Overview of the Prototype Bridge

The Meridian bridge (Chapter 1) is used as the prototype bridge considered in this study. The configuration of the Meridian bridge has been discussed partially in Chapter 1. In

this section, a more detailed account of the bridge with respect to the superstructure, substructure, bearings, abutments, and pile group foundations is provided. Figure 7.1 illustrates the configuration and components of the Meridian bridge.

With a total span length of 63.8 m, the Meridian bridge consists of two side spans with lengths of 10.4 m and two central spans with lengths of 17.8 m. The continuous composite superstructure is comprised of a reinforced concrete (RC) deck with a depth of 17.8 cm and five identical wide flange steel girders (W840×193 mm×kg/m). The girders supporting the deck are parallel and located 2.3 m apart. The width of the concrete deck is 10.9 m, which accommodates a 9.1 m wide roadway. The RC abutments at the ends of the bridge are typical seat-type abutments, as opposed to monolithic abutments that are integral with the superstructure. The abutment consists of wing walls, a back wall, and a bridge seat as shown in Figure 7.1. The RC substructure of the bridge consists of three sets of cap beams, wall piers, and footings. The load transfer mechanism between the superstructure and the substructure is provided by the steel bridge bearings that have been considered in this study. The steel rocker bearings are located at the two abutments and at the two side wall piers. The steel bolster bearings are mounted on the middle wall pier. A bearing is placed beneath each of the five steel girders at each abutment or pier leading to a total of 20 steel rocker bearings and 5 bolster bearings. The Meridian bridge uses a pile group foundation with a mix of vertical piles and battered piles. Vertical and battered piles support the two abutments and the middle wall pier, while the side wall piers are only supported by vertical piles. A total of 14 concrete piles with an average length of 8.2 m are embedded into each abutment footing. Eighteen concrete piles are embedded into each of the three footings of the wall piers with lengths of 5.5 m, 3.0 m, and 4.6 m for the footings shown in Figure 7.1 from left to right, respectively.

The global coordinate system used for the Meridian bridge model is shown in Figure 7.1. The global x-axis is parallel to the center line of the superstructure, i.e. the white center line shown in Figure 7.1, which is referred to as the longitudinal direction throughout this chapter. The global y-axis is perpendicular to the horizontal plane of the deck, which is referred to as the vertical direction throughout this chapter. Lastly, the global z-axis is determined using the right hand rule, which is denoted as the transverse direction. The

coordinate system defined above serves as the global coordinate system for all of the bridge subcomponents.

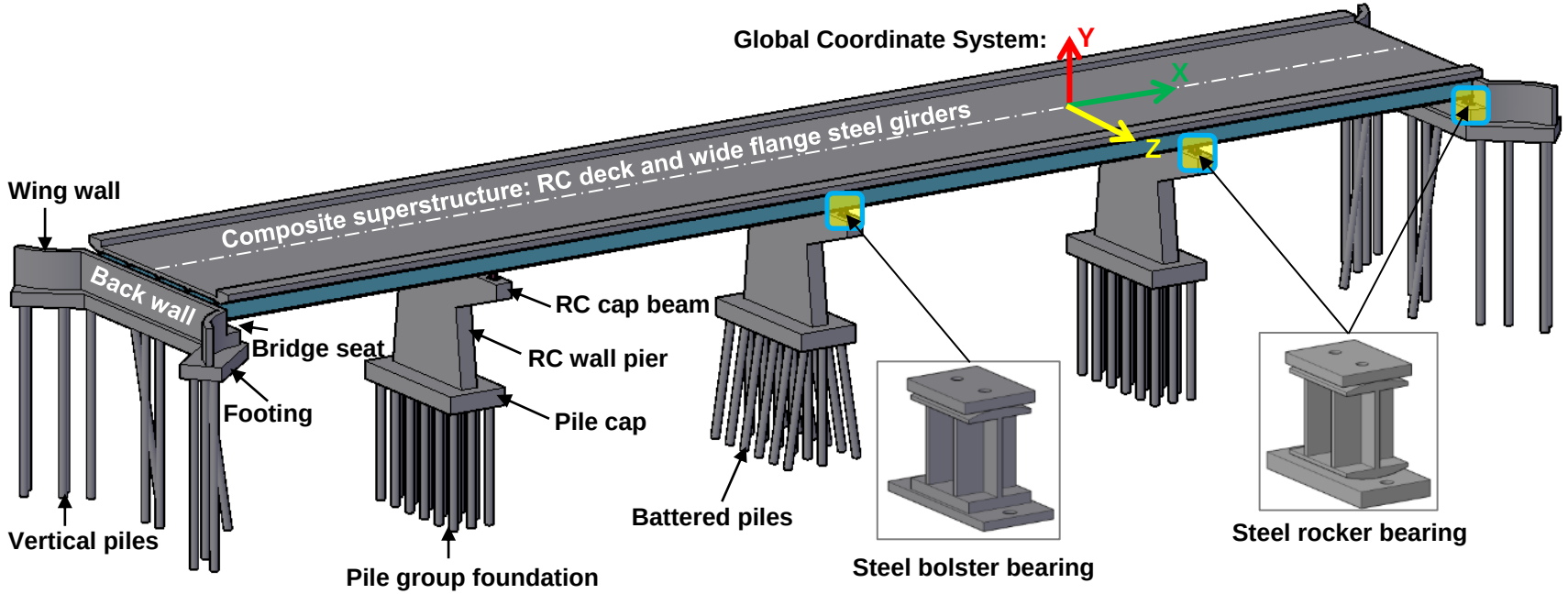

Figure 7.1 Plan and configuration of the Meridian bridge

7.3 Analytical Models of Steel Bearings

One of the first sets of analytical models for steel bearings was developed by Mander et al. (1996) based on their experimental findings on the cyclic behavior of salvaged steel bearings from New York. Macroscopic bearing models were developed by decomposing the overall bearing behavior into a combination of simple load-displacement relationships, such as friction, rocking, and hysteretic behavior, that can be readily simulated with existing analytical tools using a collection of spring elements placed in parallel or series. The versatility of such models lies in the fact that they can be implemented in different finite element packages. Unfortunately, the bearing models developed by Mander et al. (1996) only address one set of many steel bearing configurations and lack quantitative consideration of corrosion effects. Steel bearing models that incorporate corrosion effects are crucial to the seismic performance assessment of existing bridges with deteriorated steel bearings given their importance as the sole load transfer mechanism between the superstructure and substructure.

The analytical models of the steel bearings are created using the Open System for Earthquake Engineering Simulation (OpenSees) platform developed by the Pacific Earthquake Engineering Research Center (McKenna et al. 2000). These bearing models are validated and calibrated with the experimental results obtained from Chapter 6. Notably, the steel rocker bearing models explicitly incorporate the effects of corrosion-induced section loss on the bearing cyclic behavior, which has not been done in past studies. A variety of available constitutive models in OpenSees are implemented to accurately capture the behavior of the tested steel bearings with various levels of corrosion. Table 7.1 provides a list of constitutive models utilized in this study.

Based on findings from Chapter 5 and Chapter 6, three separate sets of steel rocker bearing constitutive models are established considering three corrosion condition categories, i.e. minor, severe, and cleaned. The steel rocker bearings with minor corrosion have sustained insignificant corrosion throughout their service life. Their behaviors in the longitudinal and transverse loading directions are essentially symmetric. The steel rocker bearings with severe corrosion have lost on average 11% of their mass and have

undergone significant geometry changes. Section losses on critical bearing components such as the top and bottom cylindrical flanges and pintles have led to a significant impact on the cyclic behavior of the steel rocker bearings as discussed in Chapter 6. The cleaned steel rocker bearings further demonstrate the effect that the rust layer formed on the bearing body surface has on the rocker bearing's cyclic behavior. Each bearing model for these corrosion conditions has two separate constitutive models to define, longitudinal and transverse, based on the findings of the experimental study. The steel bolster bearing models are created considering only the minor corrosion case since all of the salvaged steel bolster bearings show only minor corrosion. Separate constitutive models are also developed for the longitudinal and transverse cyclic behavior of the bolster bearing.

7.3.1 Steel rocker bearing models with minor corrosion

Longitudinal behavior

The backbone curve for the cyclic behavior of the steel rocker bearing with minor corrosion is provided in Figure 7.2(a). Given that the experimental response is symmetric, the backbone curve is also symmetric leading to identical positive and negative responses under cyclic loading. Based on the findings presented in Chapter 6, the backbone curve is decomposed into a combination of two constitutive models, i.e. *Steel01* and *ElasticMultiLinear* to capture the rolling and rocking behavior of the bearing, respectively. The two constitutive models, shown in Figure 7.2(b, c), are placed in parallel and the values used to define all parameters are provided in Table 7.2. A rolling resistance of 5 kN is used in the rolling model yielding a rolling friction coefficient of roughly 0.024 for a well-conditioned rocker bearing considering a gravity load of 205 kN. As presented in Table 7.2, seven sets of displacement and force coordinates are used to fully define the symmetric rocking behavior observed in the experimental study.

The simulated cyclic bearing behavior using the proposed model is presented and compared to the experimental response in Figure 7.2(d). The experimental loading protocol is applied to generate the simulated cyclic bearing behavior. The two load-displacement curves agree satisfactorily in regards to both the backbone curve and overall cyclic response. The initial stiffness of both responses is 8.5 kN/mm. The simulated

response results in a maximum positive force of 46 kN at a displacement of 64 mm and a maximum negative load of 43 kN at a displacement level of 61 mm, while the experimental results yield a maximum positive force of 43 kN and a negative force of 44 kN at displacements of 64 mm and -62 mm, respectively. The hysteretic energy dissipation for the simulated response is 2898 kN-mm showing some difference with that of the experiment (2226 kN-mm). This difference is largely associated with the linearization of the bearing rocking behavior in the numerical bearing model, which is inevitable given the complexity of exactly modeling nonlinear rocking. However, the steel rocker bearings, in general, have rather limited energy dissipation due to their inherent lack of moment resistance. As a result, it is more critical to accurately model the load and stiffness of the rocker bearings, which as discussed above has been achieved satisfactorily with the proposed bearing model.

Table 7.1 OpenSees constitutive models adopted in modeling the steel bearing behavior

OpenSees model	Function	Application in modeling steel bearing behavior
ElasticMultiLinear	Nonlinear elastic stress-strain relationship	Rocking
ElasticPPGap	Elastic perfectly-plastic stress-strain relationship with an initial gap	Clearance gap
Hysteretic	Uniaxial bi-/tri-linear hysteretic material model with pinching, damage, stiffness degradation for customization	Strength degradation, Fracture
Steel01	Uniaxial bilinear material model with kinematic hardening	Sliding, Rolling

Table 7.2 OpenSees models and parameters used in the rocker bearing longitudinal model with no corrosion

Rolling: *Steel01* Figure 7.2(b)		Rocking: *ElasticMultiLinear* Figure 7.2(c)	
Defining parameters	Value	Defining points	Coordinates (mm, kN)
k_0 (kN/mm)	4.25	*pt1*	-62, -39
F_y (kN)	5	*pt2*	-40, -18
b	0	*pt3*	-1.18, -5
		pt4	0, 0
		pt5	1.18, 5
		pt6	40, 18
		pt7	62, 39

Transverse behavior

Figure 7.3(a) shows the backbone curve for a steel rocking bearing with minor corrosion undergoing transverse loading. Contributions to the transverse backbone curve can be separated into three different constitutive models (Figure 7.3(b, c, d)) to account for the main behaviors observed during experimental testing. Sliding friction is modeled using the *Steel01* model with an elastic stiffness of 85 kN/mm and a sliding resistance of 50 kN. These values are obtained from the experimental results and have been discussed in Chapter 6. The bearing rocking behavior is again captured using the *ElasticMultiLinear* model with the displacement and load coordinates for this model provided in Table 7.3. Rocking is assumed to initiate at a displacement of 4 mm based on the experimental findings. For the bearing behavior at higher displacement levels, the *Hysteretic* model is applied to account for the observed softening in the bearing response. The hysteretic behavior is only initiated at displacement levels greater than 11 mm and assumes a tri-linear relationship between load and displacement. Pinching factors of 0.8 and 0.5 are found to best capture the pinching in the hysteresis curve developed during cycling. Other key parameters are also listed in Table 7.3.

Under the actual experimentally recorded loading protocol, the simulation and experimental results yield nearly identical hysteretic responses as shown in Figure 7.3(e). Both the experimental and the numerical responses have the same initial stiffness of 85 kN/mm and maximum negative force of -250 kN at -23 mm of displacement. However, an approximate 40 kN force difference exists between the two positive responses. This difference is due to the symmetry of the model, while the experimental response is not perfectly symmetric. The energy dissipated considering the simulation is 7652 kN-mm, 13% more than that found during experimental testing. Overall, the numerical bearing model captures all of the main deformation modes and the associated load-displacement relationships that are observed in the experimental response.

Table 7.3 OpenSees models and parameters used in the rocker bearing transverse model with no corrosion

Friction: *Steel01* (Figure 7.3(b))		Rocking: *ElasticMultiLinear* (Figure 7.3(c))		Softening: *Hysteretic* (Figure 7.3(d))	
Defining parameter	Value	Defining points	Coordinates (mm, kN)	Defining points	Coordinates (mm, kN)
k_0 (kN/mm)	85	*pt1*	-23, -70	*pt1*	-23, -130
F_y (kN)	50	*pt2*	-11, -70	*pt2*	-17, -100
b	0	*pt3*	-4, 0	*pt3*	-12, -40
		pt4	0, 0	*pt4*	-11, 0
		pt5	4, 0	*pt5*	0, 0
		pt6	11, 70	*pt6*	11, 0
		pt7	23, 70	*pt7*	12, 40
				pt8	17, 100
				pt9	23, 130

7.3.2 Steel rocker bearing models with severe corrosion

Longitudinal behavior

The experimental backbone curve for the severely corroded steel rocker bearing is shown in Figure 7.4(a). The behavior of the bearing consists of three major load-displacement relationships: rolling, rocking of the corroded rocker body, and crushing of loose pack rust at large displacement levels. The OpenSees constitutive models used to define these behaviors are the *Steel01* model, *ElasticPPGap* model, and *ElasticMultiLinear* model as shown in Figure 7.4(b, c, d). A 5 kN rolling resistance is assumed in the *Steel01* model. Eight sets of load displacement coordinates (Table 7.4), determined from the backbone curve, are defined to depict critical points that outline the rocking behavior using the *ElasticMultiLinear* model. The *ElasticPPGap* material model is applied to characterize the crushing of rust observed at larger positive displacement levels. The softening behavior associated with the crushing phenomenon is defined by a negative stiffness, k_n, of -0.74 kN/mm after reaching a yield force, F_m, of 17.7 kN. A gap of 15 mm is also applied based on the experimental observation of when the onset of rust crushing is observed.

Figure 7.4(e) illustrates a good agreement between the simulated and experimental behavior. The initial stiffness of the simulated response is 3 kN/mm, which is equal to that of the experimental response. The simulated response reaches a 44 kN maximum positive load that is 3 kN greater than that of the experimental results at the same displacement (57 mm). Meanwhile, the same maximum negative load of -54 kN as seen in the experimental results is achieved at a displacement of -55 mm. The total energy dissipation from the numerical simulation is 1453 kN-mm, which is roughly 11% larger than the experimental energy dissipation of 1311 kN-mm. The comparison between the simulated and experimental responses in Figure 7.4(e) shows that the numerical model satisfactorily captures the rolling, rocking, and rust crushing behavior observed during the experiment. Minor differences are found between the negative hysteretic response of the simulation and experiment between the displacement range of -20 mm and -40 mm. Over this range, the experimental response encompasses more hysteretic area than the simulated response. The overall performance of the bearing model is acceptable.

Transverse behavior

The transverse backbone curve of the severely corroded rocker bearing shown in Figure 7.5(a) depicts the main behaviors observed during experimental testing, sliding and rocking. The *Steel01* model is used to represent sliding friction with a friction resistance of 75 kN (Figure 7.5(b)). Because of the uneven corrosion distribution on the bearing, the experimental bearing behavior exhibits a strong asymmetry, which is incorporated into the numerical bearing model by utilizing two *ElasticPPGap* models with different parameter values (Figure 7.5(c, d)). The *ElasticPPGap* models are used to model the asymmetric positive and negative rocking behaviors, respectively. An 8 mm gap and a -12 mm gap are used to account for the fact that rocking is not observed until larger displacements are reached. These values are assigned to the *ElasticPPGap* models and define the gap lengths. Yield forces of 125 kN and -100 kN applied to the *ElasticPPGap* models are estimated based on experimental results. Further information regarding the parameter values associated with these models is provided in Table 7.5.

Figure 7.5(e) shows that the simulated and experimental responses are in good agreement. Both responses provide an initial stiffness value of 23 kN/mm. The simulated response yields a stable sliding plateau compared with the jagged one seen in the experimental response. The numerical model over predicts the maximum positive resistance by 8 kN at a 22 mm displacement because the bearing model does not account for the abrupt load drops caused by the steel pedestal slipping during experimental testing. The simulation and experimental results demonstrate similar behavior in their negative response in terms of the maximum load (-250 kN) and the overall secant stiffness (10 kN/mm). Additionally, the numerical bearing model also accurately captures the rocking behavior when displacements are beyond ±10 mm. The numerical bearing model over predicts the hysteretic energy dissipation by 10% achieving 11979 Joules compared with the experiment, 10891 Joules. This difference is considered acceptable. Noticeable differences exist between the two responses during early displacement cycles to displacement levels less than 10 mm. This difference is due to rust products limiting the sliding behavior of the experimental specimens, particularly rust that formed on the contact surfaces, pintles, and inside the anchor bolt holes. The presence of rust leads to the experimental bearing initially undergoing a combination of sliding, rocking, and crushing of the rust, which is too complex and localized to model numerically. As a compromise, the numerical bearing model simplifies the bearing behavior in the early loading stage to pure sliding, which maintains the average load resistance and ignores the spikes in the load observed in the experimental response.

Table 7.4 OpenSees models and parameters used in the rocker bearing longitudinal model with severe corrosion

Rolling: *Steel01* Figure 7.4(b)		Rocking: *ElasticMultiLinear* Figure 7.4(c)		Rust crushing: *ElasticPPGap* Figure 7.4(d)	
Defining parameters	Value	Defining points	Coordinates (mm, kN)	Defining parameters	Value
k_0 (kN/mm)	3	*pt1*	-55, -50	*gap* (mm)	15
F_y (kN)	5	*pt2*	-40, -20	k_p (kN/mm)	1.36
b	0	*pt3*	-15, 0	k_n (kN/mm)	-0.74
		pt4	-1.67, 0	F_m (kN)	17.67
		pt5	1.67, 0		
		pt6	15, 2.86		
		pt7	25, 5		
		pt8	52, 35		

Table 7.5 OpenSees models and parameters used in the rocker bearing transverse model with severe corrosion

Friction: *Steel01* Figure 7.5(b)		Positive rocking: *ElasticPPGap* Figure 7.5(c)		Negative rocking: *ElasticPPGap* Figure 7.5(d)	
Defining parameters	Value	Defining parameters	Value	Defining parameters	Value
k_0 (kN/mm)	23	gap_1 (mm)	8	gap_2 (mm)	-12
F_y (kN)	75	k_{e1} (kN/mm)	41.7	k_{e2} (kN/mm)	20
b	0	k_{h1} (kN/mm)	2.8	k_{h2} (kN/mm)	9.375
		F_{y1} (kN)	125	F_{y2} (kN)	-100

7.3.3 Steel rocker bearing model with corrosion cleaned

Longitudinal behavior

The backbone curve shown in Figure 7.6(a) for the longitudinal behavior of the cleaned steel rocker bearing is derived from the experimental findings. As a result of rust removal, the longitudinal behavior of the cleaned bearing consists of only rolling and rocking as illustrated in Figure 7.6(b, c), as opposed to rolling, rocking, and rust crushing seen with the corroded bearing. A 2.5 kN rolling resistance is assumed for the *Steel01* model based on experimental observation. The asymmetric rocking behavior induced by uneven corrosion distribution is captured using the *ElasticMultiLinear* model, of which the defining load displacement coordinates are provided in Table 7.6.

The comparison shown in Figure 7.6(d) between the simulated and experimental responses illustrates the capability of the numerical model to capture the critical behavior associated with the cleaned rocker bearing. Both responses yield an identical initial stiffness of 1 kN/mm and show a 2 kN difference between the maximum positive and negative resistances. The simulated response exhibits a dominant rolling response in the displacement range of ±40 mm, which is also observed in the experimental behavior. The asymmetric rocking behavior observed during testing is recreated in the numerical simulation as well and demonstrates a good match with that of the experimental response. For the positive bearing response, the mixed behavior of rocking and rolling between 20 mm and 40 mm of displacement is also reproduced in the simulated response. The overall secant stiffness of the simulated response is 0.57 kN/mm and 0.91 kN/mm for the positive and negative responses, respectively, which match well with 0.54 kN/mm and 1 kN/mm positive and negative secant stiffness observed during testing. With respect to the hysteretic energy dissipation, the simulation accumulates 1115 kN-mm while the experiment produces 1066 kN-mm, showing a negligible 5% difference. These results show the numerical bearing model's capability to capture the cleaned rocker bearing behavior under cyclic loading.

Transverse behavior

The backbone curve shown in Figure 7.7(a) for the transverse behavior of the cleaned bearing is achieved by placing a *Steel01* model, accounting for the friction behavior, in parallel with two *ElasticPPGap* models simulating the rocking behavior. A friction resistance of 50 kN, as observed during testing, is applied as the yield force parameter of the *Steel01* model shown in Figure 7.7(b). A 5 mm gap is assigned to both the positive and negative *ElasticPPGap* models that are given in Figure 7.7(c, d). However, these two models have different initial stiffnesses, yield forces, and post-yield stiffnesses as listed in Table 7.7 due to the asymmetric bearing rocking behavior observed during testing. The initial stiffness is 25 kN/mm for positive rocking with a yield force of 125 kN, while the negative rocking has an initial stiffness of 10.6 kN/mm and yields at -85 kN. The yield forces and stiffness discussed here are parameters used to define the *Steel01* and *ElasticPPGap* models and are not associated with actual material yielding of the steel bearing.

Figure 7.7(e) highlights the agreement between the numerical response and experimental results in regards to the major deformation modes and the backbone profile. However, the initial response of the cleaned bearing during testing consists of combined rocking and sliding that leads to a bearing response without a consistent load-deformation relationship during the early cycles. This phenomenon is simplified into a perfect sliding behavior to facilitate numerical modeling of the bearing behavior. A closer comparison shows that the numerical hysteresis envelops the experimental hysteretic response except within the displacement range of ±10 mm indicating that the numerical bearing model is able to reproduce the main deformation modes and the load-deformation relationships observed in the experimental testing. The simulation produces a total energy dissipation of 9905 Joules while the experiment shows an 8307 Joules hysteretic energy dissipation under the actual recorded loading protocol. The initial stiffness of both responses is found to be 35 kN/mm. The overall positive secant stiffness is 9.3 kN/mm for the simulation and 10.4 kN/mm for the experiment while the overall negative secant stiffness is 7.5 kN/mm for both responses. These energy dissipation and stiffness comparisons further indicate a good agreement between the numerical and experimental results.

The rocker bearing models described in the previous three sections include a total of 3 sets of cyclic constitutive models that are capable of simulating the lateral cyclic response of steel rocker bearings in their original (i.e. little to minor corrosion), severely corroded (i.e. accumulation of four decades of corrosion), and cleaned (i.e. corrosion removed) conditions. Each set consist of two orthogonal behaviors to better depict the bearing behavior subjected to arbitrary ground motions. The simulated responses discussed above prove the applicability of these rocker bearing models to accurately simulate the seismic response of older highway bridges with varying levels of corrosion and to account for potential retrofit strategies.

Table 7.6 OpenSees models and parameters used in the rocker bearing longitudinal model with corrosion cleaned

Rolling: *Steel01* Figure 7.6(b)		*Rocking: ElasticMultiLinear* Figure 7.6(c)	
Defining parameters	Value	Defining points	Coordinates (mm, kN)
k_0 (kN/mm)	1	*pt1*	-55, -47.5
F_y (kN)	2.5	*pt2*	-35, 0
b	0	*pt3*	15, 0
		pt4	25, 7.5
		pt5	35, 7.5
		pt6	38, 20
		pt7	57, 30

Table 7.7 OpenSees models and parameters used in the rocker bearing transverse model with corrosion cleaned

Friction: *Steel01* Figure 7.7(b)		Positive rocking: *ElasticPPGap* Figure 7.7(c)		Negative rocking: *ElasticPPGap* Figure 7.7(d)	
Defining parameters	Value	Defining parameters	Value	Defining parameters	Value
k_0 (kN/mm)	35	gap_1 (mm)	5	gap_2 (mm)	-5
F_y (kN)	50	k_{e1} (kN/mm)	25	k_{e2} (kN/mm)	10.63
b	0	k_{h1} (kN/mm)	1	k_{h2} (kN/mm)	4.62
		F_{y1} (kN)	125	F_{y2} (kN)	-85

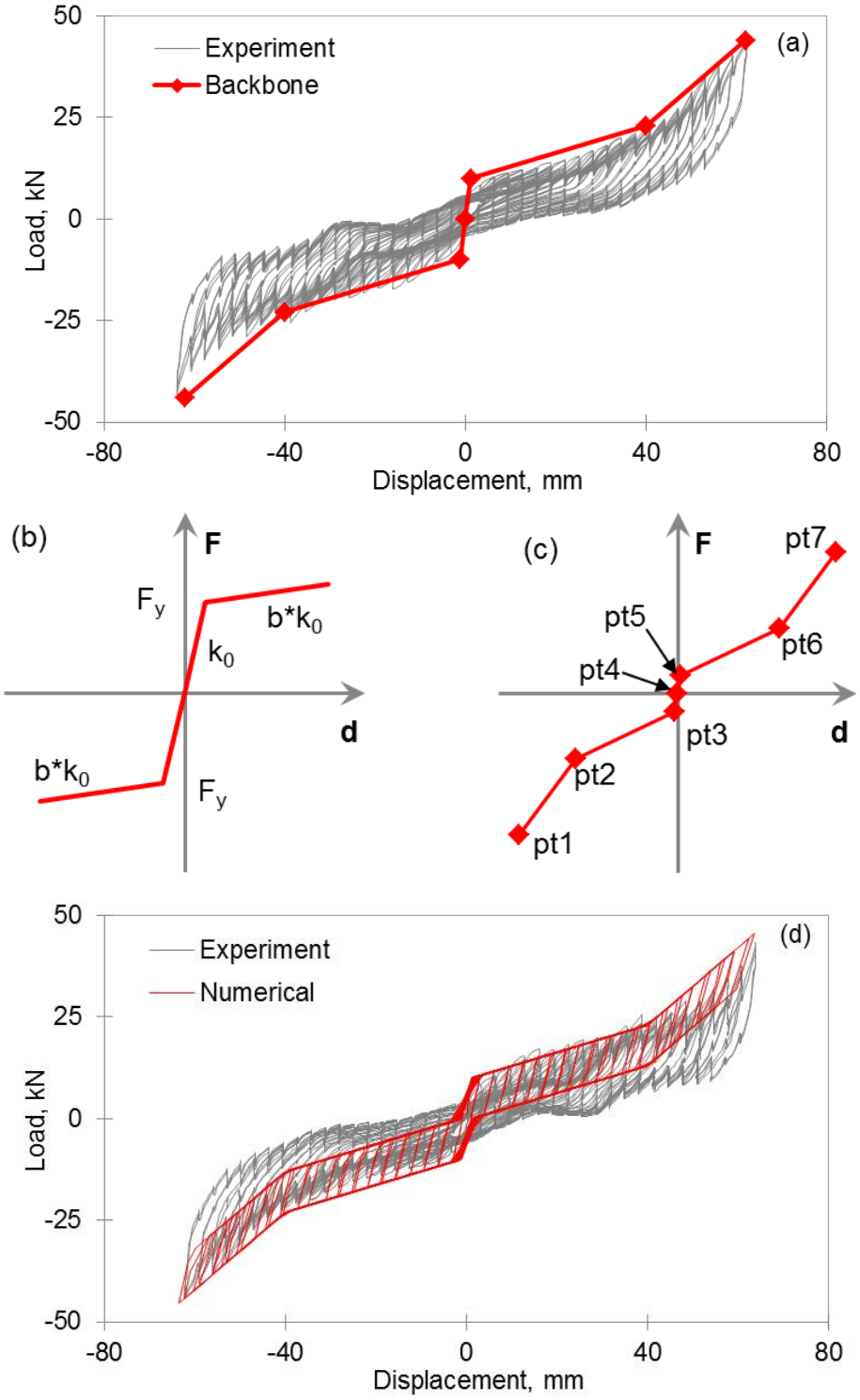

Figure 7.2 Steel rocker bearing longitudinal behavior model: (a) backbone curve, (b) *Steel01* model used to model rolling friction, (c) *ElasticMultiLinear* model used to capture rocking behavior, and (d) comparison between the simulated and experimental responses

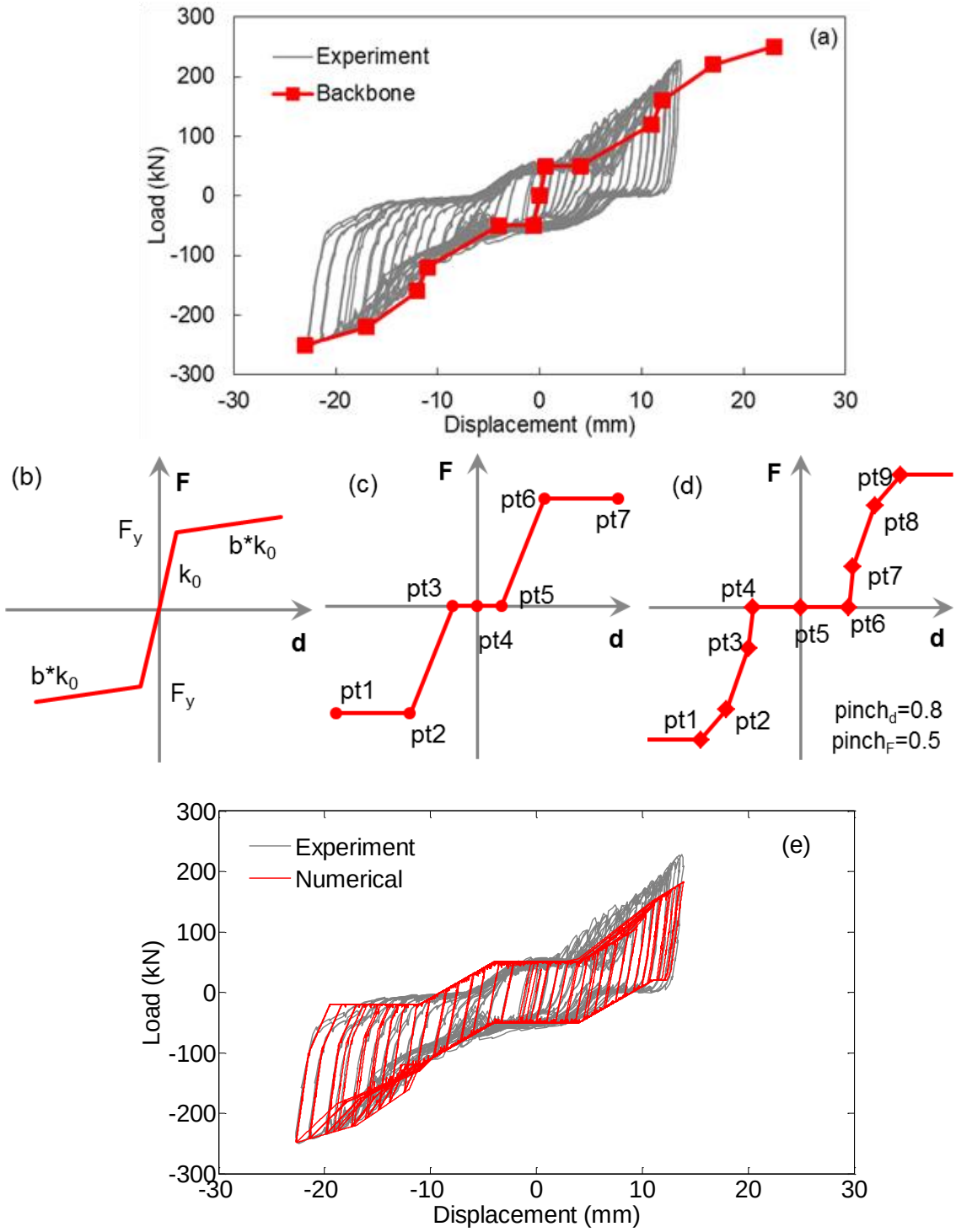

Figure 7.3 Steel rocker bearing transverse behavior model: (a) backbone curve, (b) *Steel01* model used to model friction, (c) *ElasticMultiLinear* model used to capture rocking behavior, (d) *Hysteretic* model used to capture softening, and (e) comparison between the simulated and experimental responses

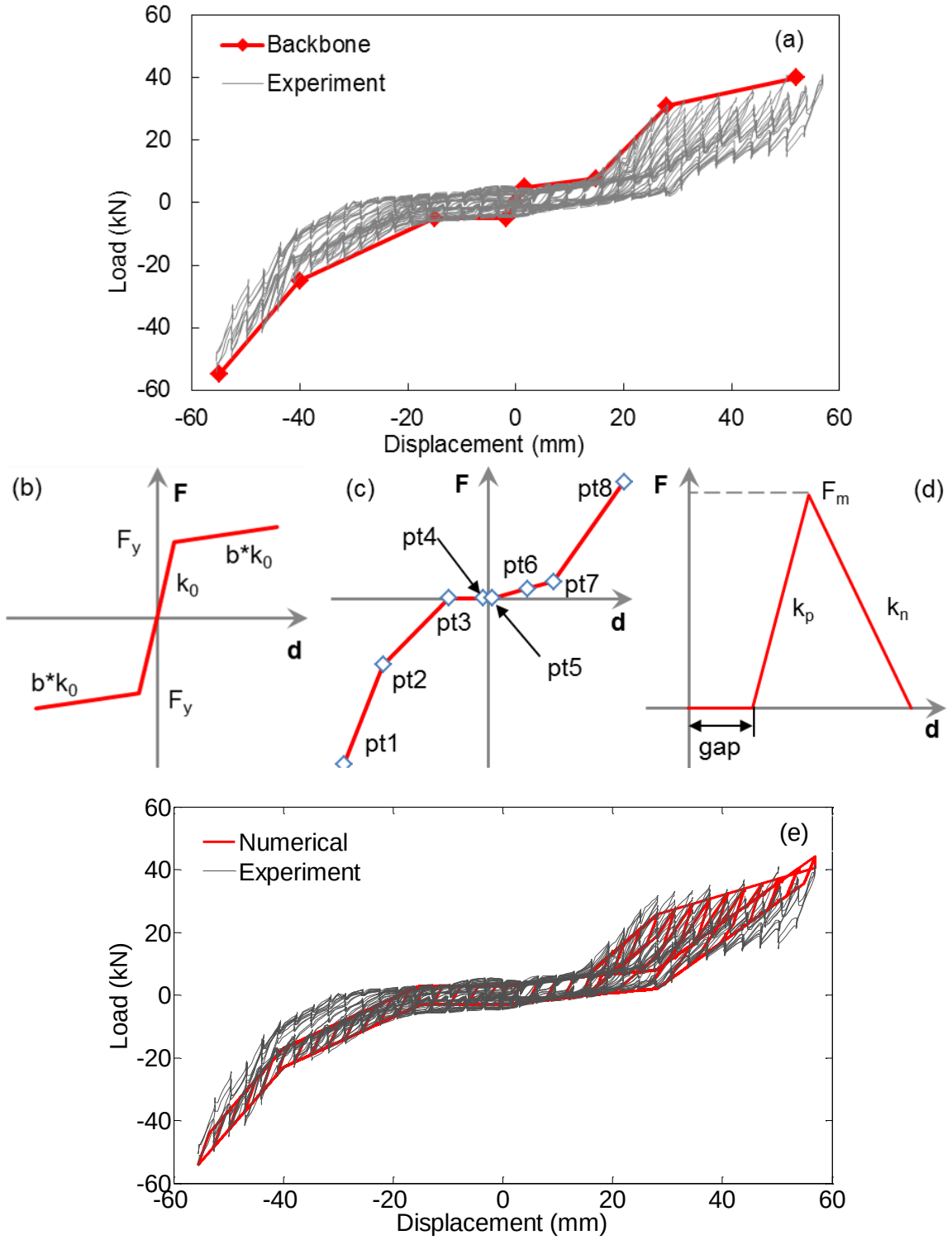

Figure 7.4 Steel rocker bearing with severe corrosion longitudinal behavior model: (a) backbone curve, (b) *Steel01* model used to model rolling, (c) *ElasticMultiLinear* model used to capture rocking, (d) *ElasticPPGap* model used to capture crushing of rust, and (e) comparison between the simulated and experimental responses

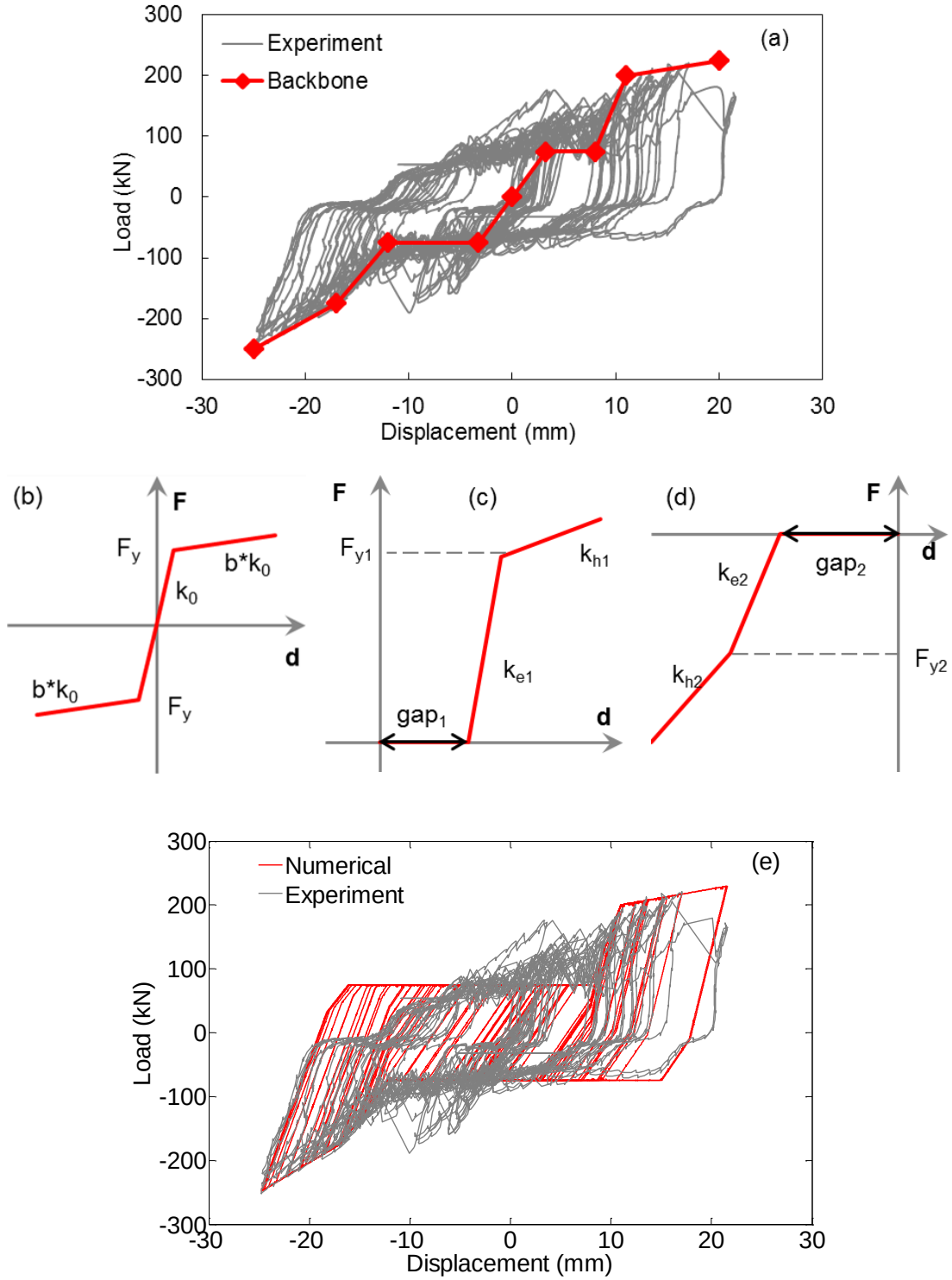

Figure 7.5 Steel rocker bearing with severe corrosion transverse behavior model: (a) backbone curve, (b) *Steel01* model used to model friction, (c) *ElasticPPGap* model used to capture positive rocking and yielding, (d) *ElasticPPGap* model for negative rocking and yielding, and (e) comparison between the simulated and experimental responses

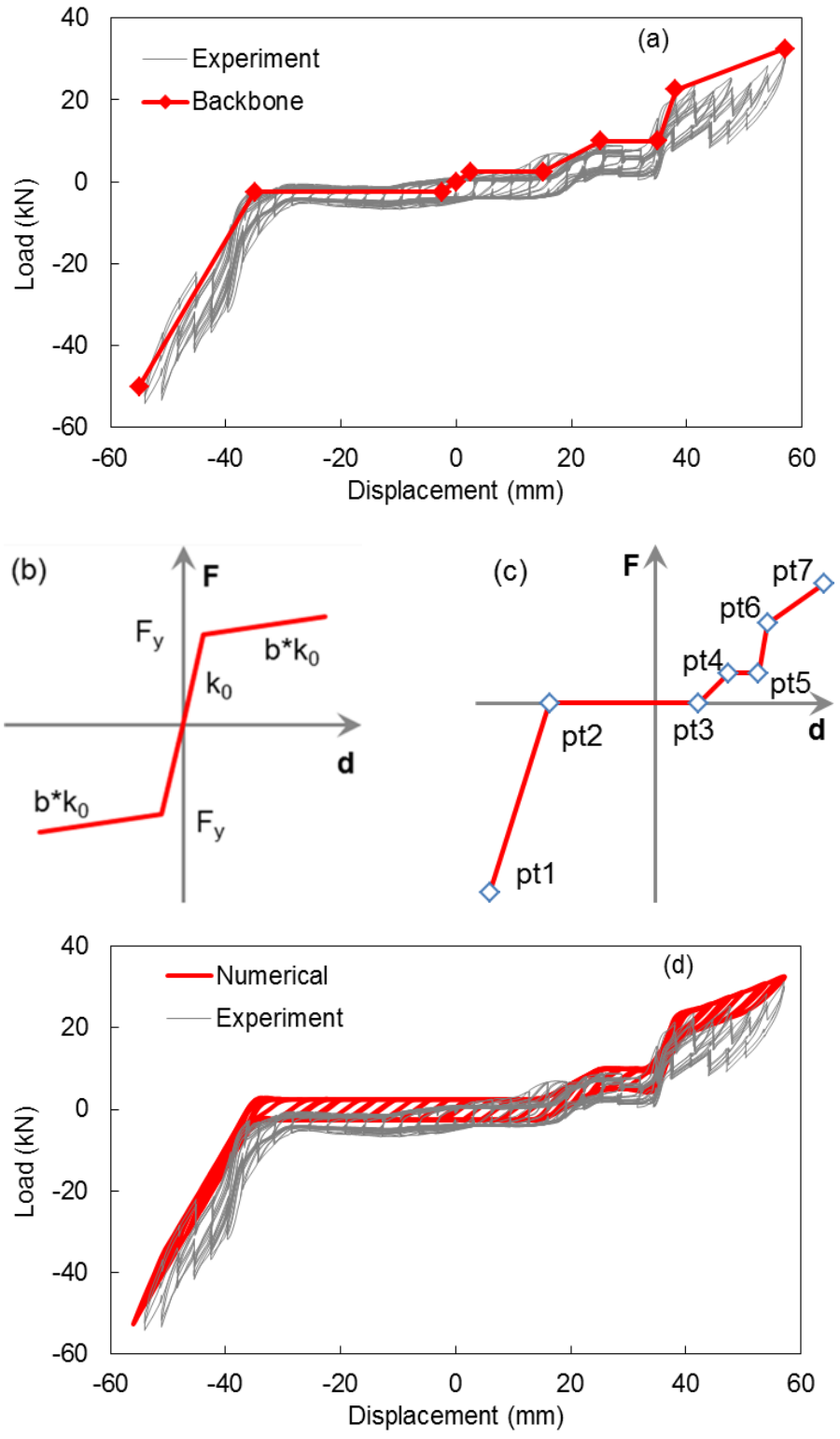

Figure 7.6 Steel rocker bearing with corrosion cleaned longitudinal behavior model: (a) backbone curve, (b) *Steel01* model used to model rolling, (c) *ElasticMultiLinear* model used to capture rocking, and (d) comparison between the simulated and experimental responses

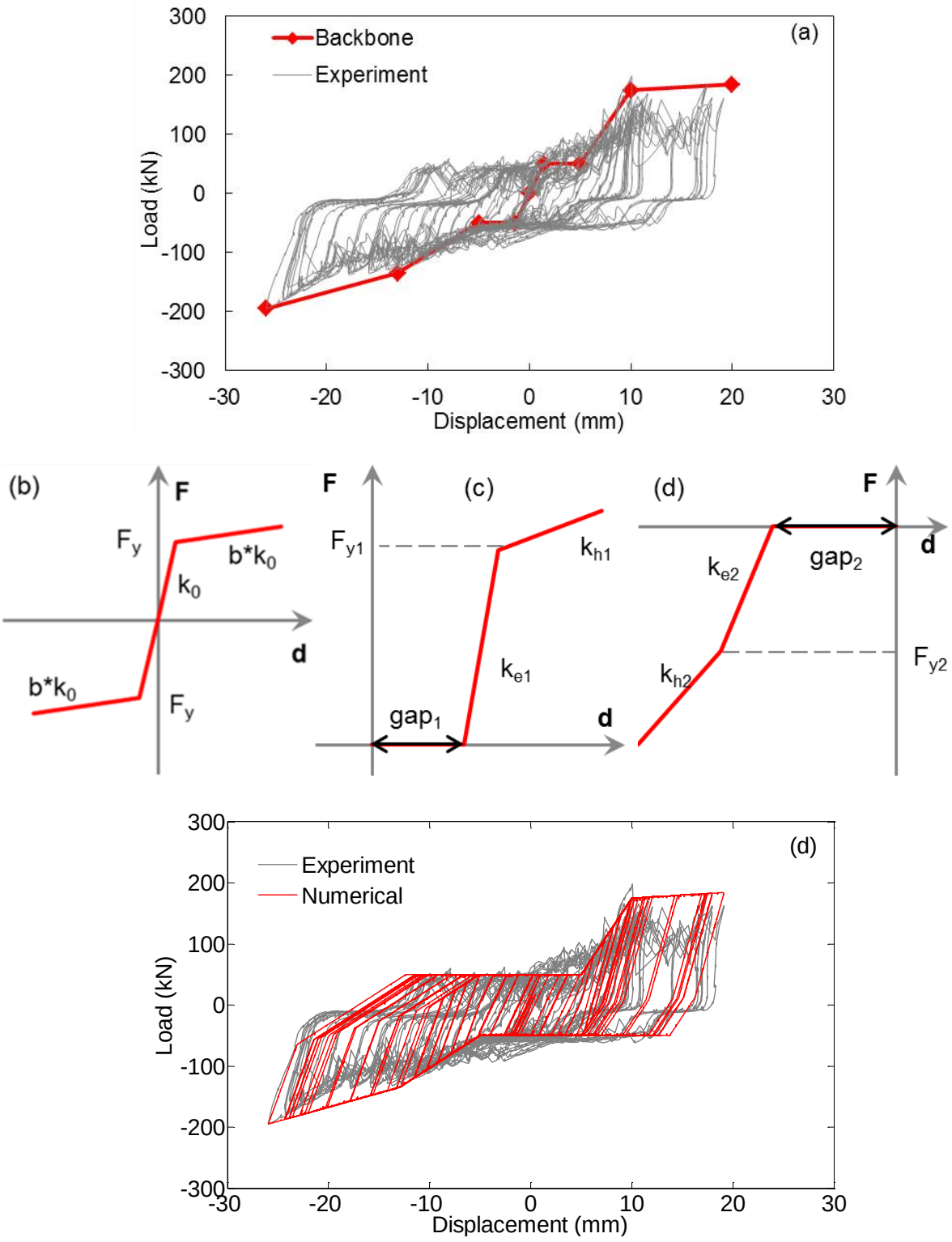

Figure 7.7 Steel rocker bearing with corrosion cleaned transverse behavior model: (a) backbone curve, (b) *Steel01* model used to model friction, (c) *ElasticPPGap* model used to capture positive rocking and yielding, (d) *ElasticPPGap* model for negative rocking and yielding, and (e) comparison between the simulated and experimental responses

7.3.4 Steel bolster bearing model without corrosion

Longitudinal behavior

The longitudinal behavior of the bolster bearing under cyclic loading with increasing displacement magnitudes consists of two main phases that are separated by the occurrence of anchor bolt fracture, which leads to significant strength degradation as shown in Figure 7.8(a). Similar to the rocker bearing models, friction is simulated using the *Steel01* model as shown in Figure 7.8(b). The *ElasticMultiLinear* model is also applied to capture the rocking behavior (Figure 7.8(c)). Yielding, hardening, and eventual fracture of anchor bolts are simulated using the *Hysteretic* model (Figure 7.8(d)). A 5 mm gap exists in both the positive and negative directions of this hysteretic model to account for the clearance around the bolts. A bilinear degradation relationship is assumed in the *Hysteretic* model to better capture the post-fracture experimental hysteretic behavior. Pinching coefficients for displacement and force are determined as 1.0 and 0.0, respectively, which best reproduce the pinching phenomena observed in the bearing load-displacement relationship. The defining load-displacement coordinates are listed in Table 7.8 for the *Hysteretic* model. Finally, the overall constitutive model is symmetric, consistent with the bearing condition, and matches the experimentally observed behavior adequately.

A comparison of the simulated and the experimental responses is shown in Figure 7.8(e). Because the bolster bearing under longitudinal loading does not develop a stable sliding behavior and shows a predominant rocking behavior at larger displacement cycles, this leads to an unloading response that almost follows the loading curve as opposed to returning at a lower load level as is typically seen. At displacement levels of ± 5 mm, the bottom of the bolster bearing is fully in contact with the steel pedestal and friction dominates. At larger displacements, rocking begins to initiate along with sliding. This interdependent behavior of rocking and sliding for the bolster bearing cannot be decoupled and modeled by placing a sliding model and a rocking model in parallel. However, a compromise is made in the bearing model that utilizes a friction model (*Steel01*) and a rocking model (*ElasticPPGap*) placed in parallel to approximate the

bearing behavior. To better account for the observed behavior, only half of the experimental friction resistance (50 kN) obtained during early displacement cycles is applied as the yield force in the *Steel01* model, while the other half is assigned to the rocking model. This approach results in some disparity between the simulated and experimental response at low displacement levels and during unloading at displacement levels larger than 10 mm. However, the overall numerical hysteresis curve envelopes the experimental response with key observed behavior such as bolt fracture and strength degradation well captured.

The maximum bolster bearing strength of 180 kN is achieved at a displacement of ±15 mm in the simulated response, while in the experimental response a maximum strength of 180 kN occurs at 16.5 mm and -25.6 mm. This difference is because the experimental response asymmetry cannot fully be accounted for in the numerical model. The bilinear strength degradation model used in the *Hysteretic* model also works well to capture the degradation associated with bolt yielding and fracture as seen in Figure 7.8(e). The bearing model dissipates a total hysteretic energy of 5718 Joules compared with 5253 Joules for the bearing tested under the same loading protocol. Overall, the bearing model is capable of accurately modeling the longitudinal cyclic behavior of the bolster bearing and incorporating the effect of anchor bolt yielding and fracture.

Transverse behavior

Similar to its longitudinal behavior, the transverse backbone curve for the bolster bearing (Figure 7.9(a)) consists of two distinct behaviors separated by the bolt fracture. The *Steel01* model is adopted to model the friction that steadily develops post-fracture. The sliding resistance is assumed to be 40 kN in the *Steel01* model (Figure 7.9(b)), which yields a good match between the simulated and experimental responses. Yielding and fracture of the anchor bolts are modeled using the *Hysteretic* model (Figure 7.9(c)). Because of the abrupt failure of the anchor bolts, the *Hysteretic* model is constructed to be bilinear with an ascending portion for pre-fracture behavior and a descending portion for post-fracture behavior. The bolster bearing shows a slightly shorter pure sliding plateau during transverse loading than longitudinal loading, thus a 2 mm gap based on the

experimental findings is incorporated into the *Hysteretic* model. The *Hysteretic* model is also assumed to be symmetric with a yield force of 380 kN. The pre-fracture stiffness is taken as 23.8 kN/mm and the post-fracture stiffness is taken as -47.5 kN/mm based on the experimental findings. A displacement pinching coefficient of 1.0 is used, while a force pinching coefficient of 0.5 accounts for the pinching phenomena observed during testing. These coefficient values are derived based on a trial and error study. Additional parameter values used in the models are provided in Table 7.9.

Subjecting the numerical model to the same loading protocol used in the experiment, a comparison of the simulated and experimental response is shown in Figure 7.9(d). A good agreement is observed between the two responses. The initial stiffness and the maximum strength are the same, 60 kN/mm and 380 kN, respectively, for both the simulated and experimental responses. The numerical model is calibrated to produce symmetric response under cyclic loading, while the experimental response is not symmetric due to test setup limitations (rigid slip of the steel pedestal) and the bearing being a little off center, which explains the disparity between the positive responses in the simulation and test results. The negative numerical response matches well with that of the experimental response both pre- and post-fracture of the anchor bolts. Both sets of negative responses peak at -380 kN at a displacement of -18 mm. The capability of the bearing model to recreate the post-fracture sliding behavior is proven (Figure 7.9(d)) where a rectangular response identical to that of the experimental behavior is achieved. An overall 9% difference is found between the cumulative hysteretic energy dissipation of the simulation and the experiment, 9280 Joules and 10177 Joules, respectively. Considering the backbone curve, the pre- and post-fracture response, and the hysteretic energy dissipation, the bearing model developed for simulating the transverse cyclic behavior of the bolster bearing is accurate enough for use in simulating overall bridge response.

The strength of the bolster bearing models (i.e. longitudinal and transverse models) lies in the fact that they are capable of capturing the most critical bearing response, i.e. anchor bolt fracture, under lateral cyclic loading. The models are able to recreate the backbone curve without losing significant resolution in the hysteretic energy dissipation of the

bearing. Considering their wide usage in older bridges throughout the CEUS, these steel bolster bearing models have great potential for application in the seismic assessment of existing bridges.

Table 7.8 OpenSees models and parameters used in the bolster bearing longitudinal model

Friction: *Steel01* Figure 7.8(b)		Rocking: *ElasticMultiLinear* Figure 7.8(c)		Yielding & Fracture: *Hysteretic* Figure 7.8(d)	
Defining parameters	Value	Defining points	Coordinates (mm, kN)	Defining points	Coordinates (mm, kN)
k_0 (kN/mm)	10	*pt1*	-50, -20	*pt1*	-49, 0
F_y (kN)	20	*pt2*	-10, -20	*pt2*	-36, -100
b	0	*pt3*	0, 0	*pt3*	-15, -140
		pt4	10, 20	*pt4*	-3, 0
		pt5	50, 20	*pt5*	3, 0
				pt6	15, 140
				pt7	36, 100
				pt8	49, 0

Table 7.9 OpenSees models and parameters used in the bolster bearing transverse model

Friction: *Steel01* Figure 7.9(b)		Yielding & Fracture: *Hysteretic* Figure 7.9(b)	
Defining parameters	Value	Defining points	Coordinates (mm, kN)
k_0 (kN/mm)	60	*pt1*	-26, 0
F_y (kN)	40	*pt2*	-18, -380
b	0	*pt3*	18, 380
		pt4	26, 0

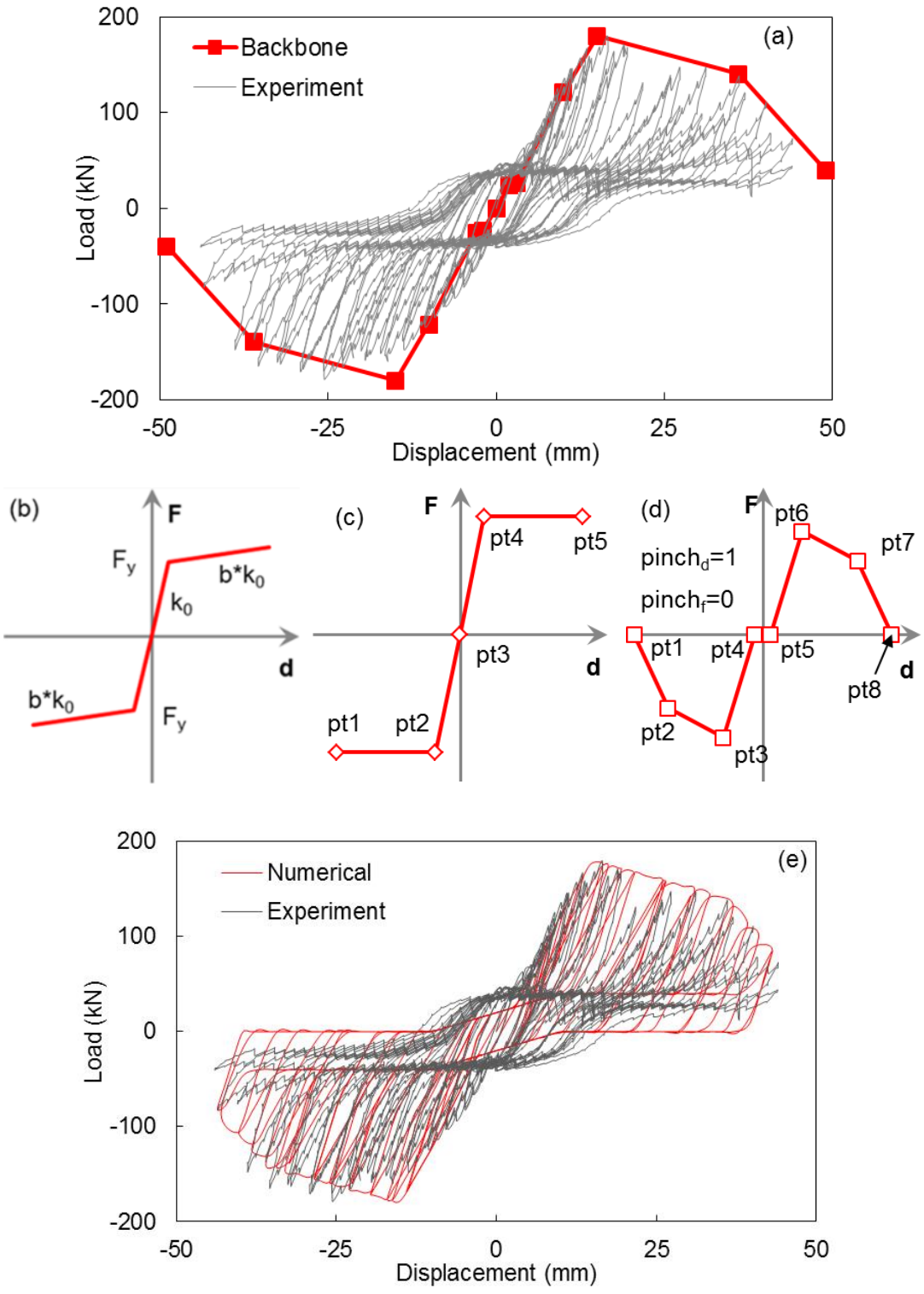

Figure 7.8 Steel bolster bearing longitudinal behavior model: (a) backbone curve, (b) *Steel01* model used to model friction, (c) *Hysteretic* model used to capture yielding and fracture, (d) *ElasticMultiLinear* model used to capture rocking behavior, and (e) comparison between the simulated and experimental responses

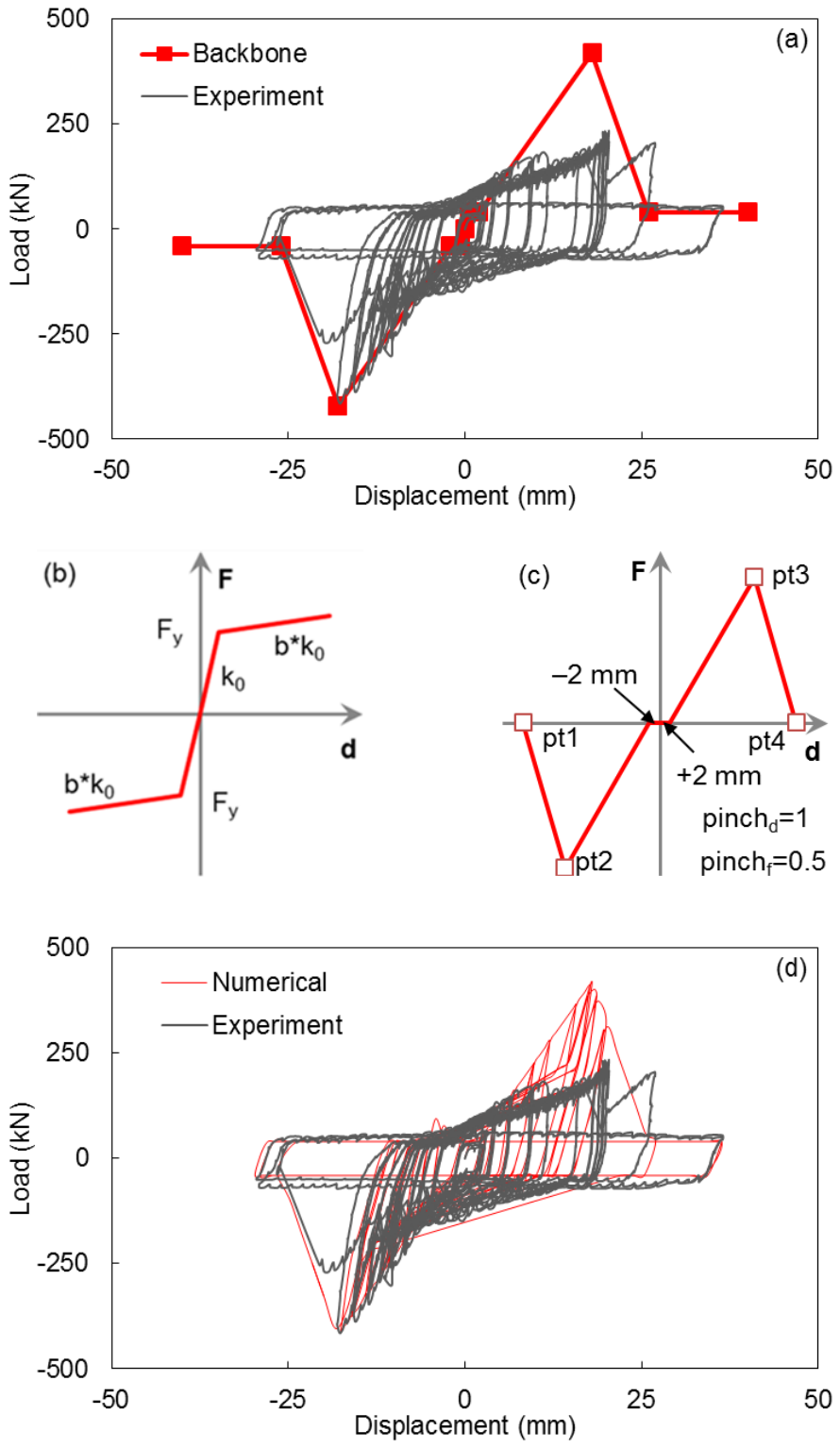

Figure 7.9 Steel bolster bearing transverse behavior model: (a) backbone curve, (b) *Steel01* model used to model friction, (c) *Hysteretic* model used to capture yielding and fracture, and (d) comparison between the simulated and experimental responses

7.4 Analytical Models of the Bridge Members

7.4.1 Superstructure model

The superstructure of the Meridian bridge, Figure 7.10, is modeled using elastic beam-column elements with lumped mass and stiffness. This modeling approach has been widely used in previous studies of the seismic performance of highway bridges, since the bridge superstructure is anticipated to remain elastic under horizontal ground motions (Aviram et al. 2008, Choi et al. 2004, Nielson and DesRoches 2007b, Pan et al. 2010). Assuming lumped mass, nodal masses are only assigned to the superstructure nodes shown in red in Figure 7.10. The blue nodes are artificial nodes defined at the bearing locations to facilitate modeling of the bearings and the connection between the superstructure and substructure. Rigid links are used to connect the artificial nodes to the superstructure nodes allowing the artificial nodes to act as slave nodes to the superstructure nodes (i.e. they undergo the same displacements). Section properties of the composite superstructure are calculated to define the moments of inertia for the elastic superstructure elements.

The steel and concrete material properties for the composite superstructure are obtained from the design drawings of the Meridian bridge. ASTM A36 steel is specified for the steel girders, which has a minimum yield strength of 248 MPa and a Young's modulus of 200 GPa. The specified concrete for the bridge deck has a compression strength of $f'c$ =10 MPa and a corresponding elastic modulus of E_c=4730$\sqrt{f'c}$=15 GPa. The section properties of the superstructure cross-section are calculated using the transformed area method. The RC slab is transformed into an equivalent steel section with the slab width divided by the transformation coefficient and the slab depth maintained the same. The transformation coefficient is determined as the ratio between the steel and concrete elastic moduli. Based on the global coordinate system, the section properties are calculated for the transformed cross-section. The total transformed area is found to be 0.266 m^2. Bending moments of inertia about the global Y and Z axes are 2.69 m^4 and 0.03 m^4, respectively. Moreover, the linear mass density of the composite superstructure is

calculated to be 5610 kg/m and the mass moment of inertia about the longitudinal axis (i.e. the global X axis) is 56.4×10^{6} kg-mm^{2} per unit millimeter length of the superstructure. These values are used to define the nodal masses applied to the superstructure model.

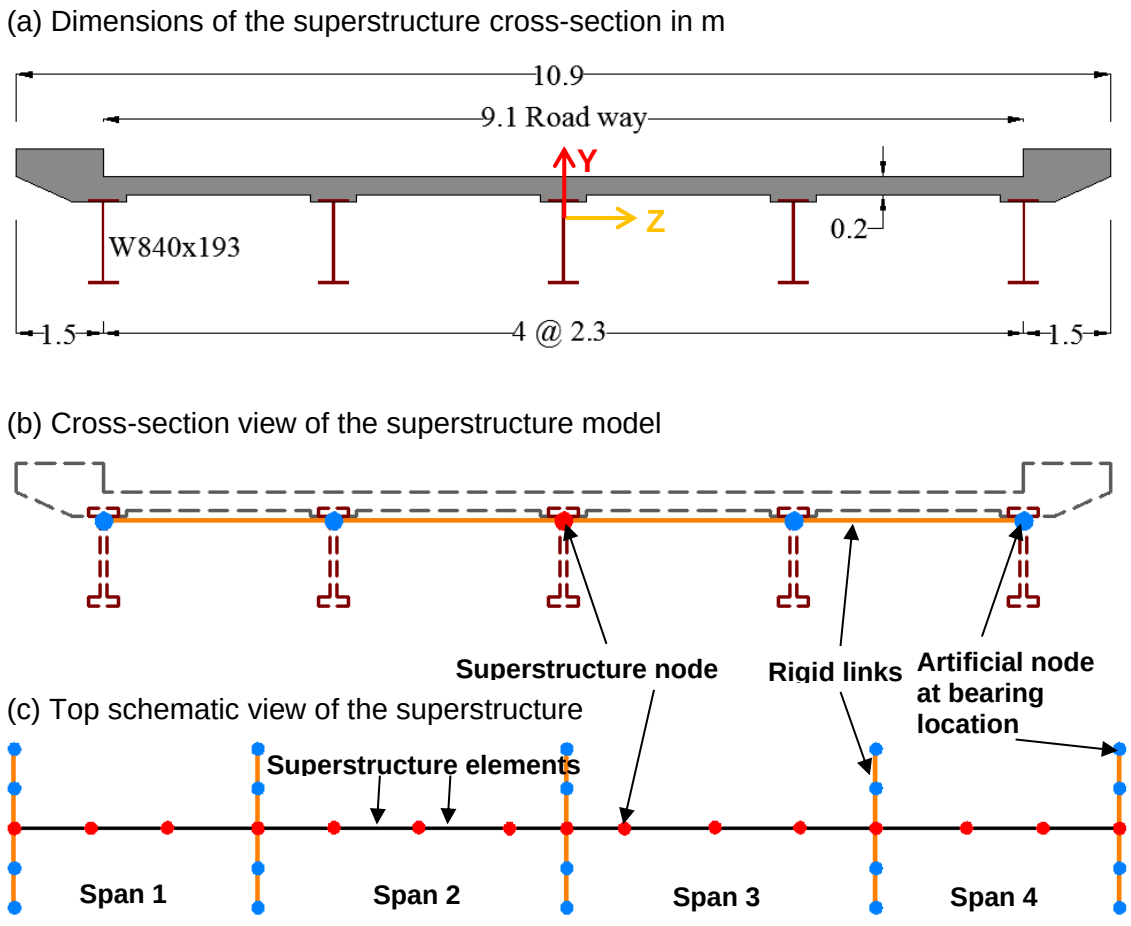

Figure 7.10 Schematic view of the superstructure model

7.4.2 Substructure model

The substructure of the Meridian bridge consists of the cap beam and wall pier as shown in Figure 7.11(a). The cap beam has a tapered cross-section with the depth varying from 0.7 m at the edge to 1.8 m at the interface with the wall pier. It has a constant width of 0.8 m. Ten steel rebars with a diameter of 36 mm (U.S. #11) are placed in two parallel layers and 75 mm apart vertically near the top surface of the cap beam for resisting negative moments developed along the cantilevered portions of the cap beam. Rebar with a

diameter of 16 mm (U.S. #5) are spaced at 210 mm along the perimeter of the cap beam. The wall piers is on average 3.6 m tall, 4.8 m wide, and 0.8 m deep. A total of 36 rebars with a diameter of 16 mm (U.S. #5) are placed vertically along the perimeter of the wall pier with a 305 mm spacing along the longer edge and a 228 mm spacing along the shorter edge of the wall pier cross-section. The depth of the cover concrete is 38.1 mm for the cap beam and wall pier.

Past studies have found that the cap beam generally remains elastic under horizontal ground motions (Aviram et al. 2008) since the cap beam is located at the top of the wall pier where only insignificant bending moments can develop under applied lateral forces minimizing the probability of plasticity. Considering this past finding, elastic beam elements are used to model the cap beam. The tapered cap beam depth is approximated using an average depth of 1.75 m. The section properties of this average section are 0.34 m^4 for the bending moment of inertia about the global X axis, 0.06 m^4 for the bending moment of inertia about the global Y axis, and an area of 1.3 m^2. The cap beam nodes placed at the centroid of the average section are shown in pink in Figure 7.11(b) while the artificial nodes shown in grey are defined at the bearing locations along the top surface of the cap beam. The cap beam nodes and the artificial nodes are connected by rigid links that slave the artificial nodes to the corresponding cap beam nodes. The elastic cap beam elements are shown as the pink line segments spanning between the cap beam nodes in Figure 7.11(b).

Since the wall piers have a high aspect ratio for their cross-section, they mainly undergo flexure about their weak bending axis, i.e. the local y axis or the global transverse axis. As a result, they have performed well in previous experimental studies of their seismic response (Abo-Shadi et al. (2000)). Filipov (2012) shows that a fiber section model implemented in OpenSees can successfully model the behavior of the wall piers under seismic loads. The study compared numerical results obtained using OpenSees to the experimental results of Abo-Shadi et al. (2000) and found good agreement as shown in Figure 7.12. Filipov et al. (2013) further applied a wall pier fiber model in their investigation of the seismic performance of quasi-isolated highway bridges and demonstrated the model's versatility in accurately capturing the wall pier lateral behavior.

The wall pier model developed in this chapter follows these experimental and numerical findings and uses the fiber section mesh procedure outlined in Filipov (2012) to discretize the Meridian bridge wall piers. The fiber size used in discretizing the wall pier cross-section is 19 mm. The wall pier nodes and elements are shown in blue in Figure 7.11(b). The wall piers are discretized with an increasingly denser mesh toward the bottom end of the wall pier. This mesh scheme is used to better capture the nonlinearity, if any, associated with the plastic hinge zone at the bottom of the wall pier. Similar to the cap beam, the tapered wall pier cross-section is approximated using an average cross-section. The concrete material model *Concrete01* in OpenSees is adopted to model the concrete (Figure 7.13(a)). For the unconfined concrete (i.e. cover concrete), a concrete strength of 31 MPa is used in the material model. A confinement ratio of 1.033 is used for the confined concrete (i.e. core concrete) per the recommendation of Nielson (2005). As a result, the confined concrete strenth is 32 MPa and the associated elastic modulus is 26.7 GPa. A yield stress of 455 MPa and a Young's modulus of 200 GPa are used for the rebar which is modeled using the *Steel01* model shown in Figure 7.13(b) with a post-yield modulus of 3.6 GPa (i.e. b=0.018). Rigid elements are used to connect the top wall pier node with the center cap beam node and to connect the bottom wall pier node with the foundation node.

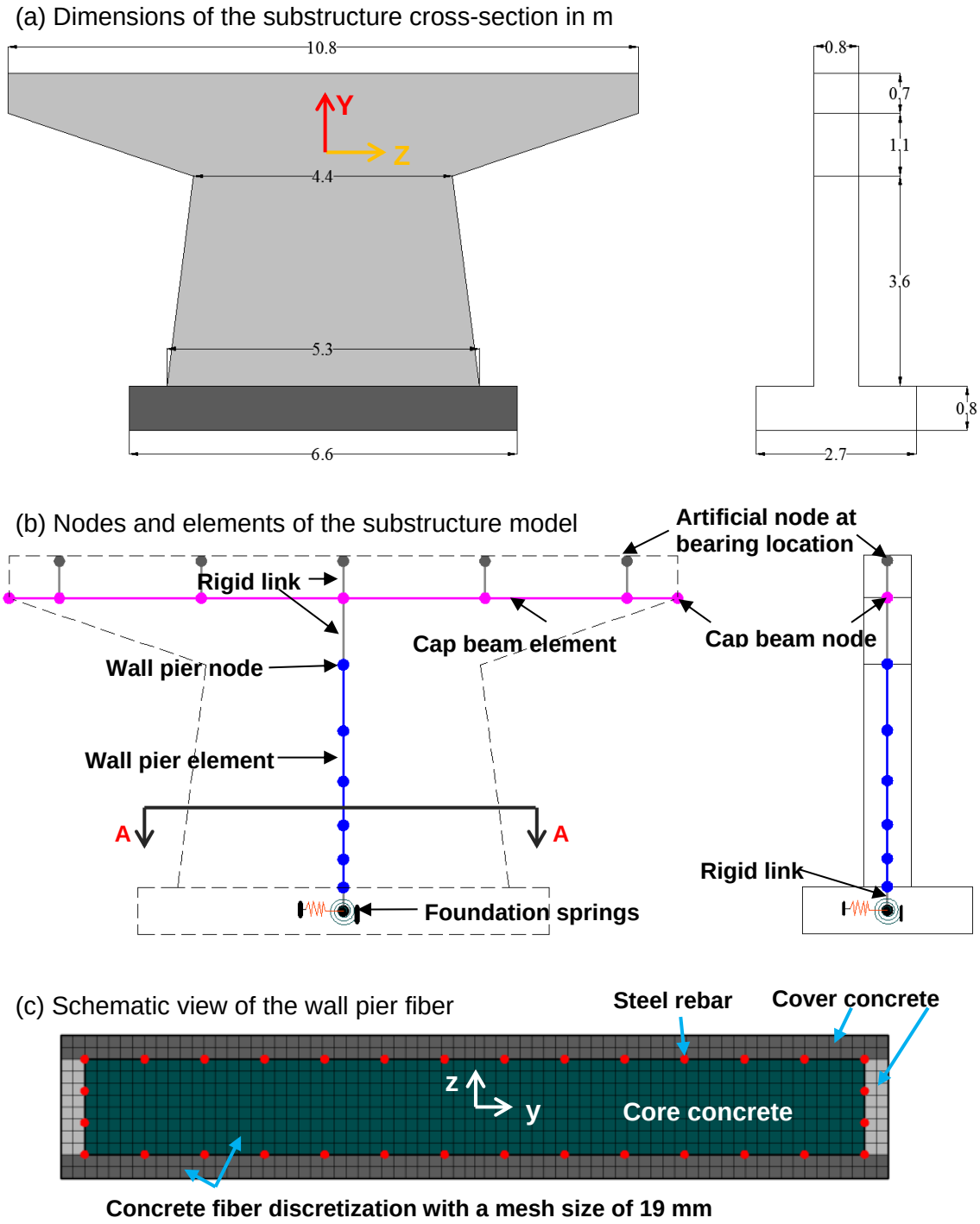

Figure 7.11 Schematic view of the substructure model and fiber section discretization of the cap beam and wall pier

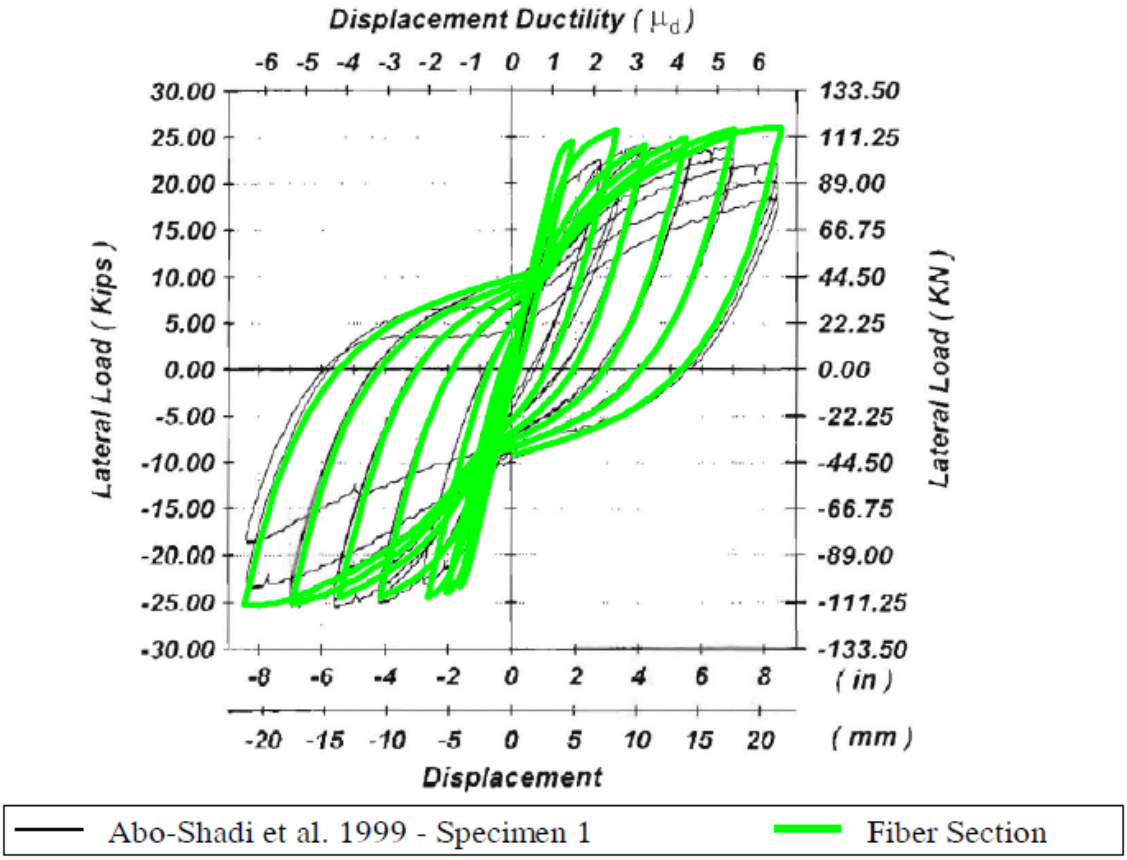

Figure 7.12 Comparison between OpenSees and experimental results of the cyclic behavior of wall piers (Filipov (2012))

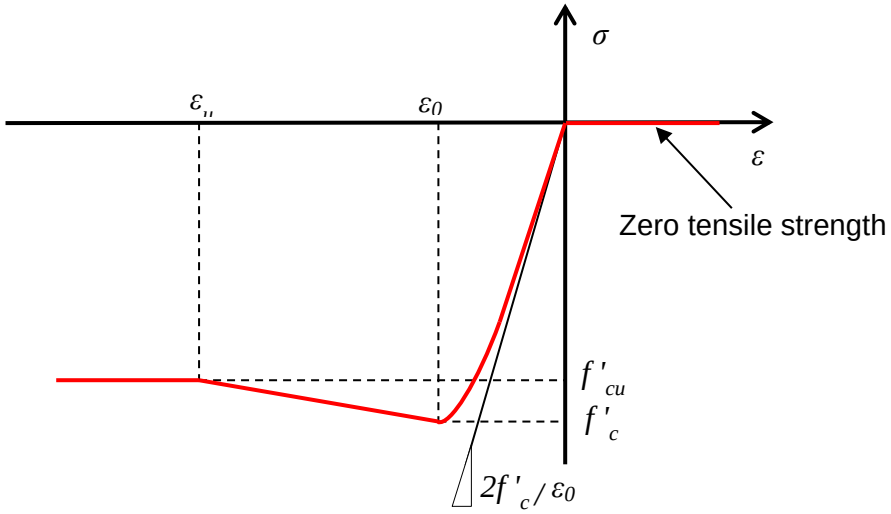

(a) *Concrete 01* material model

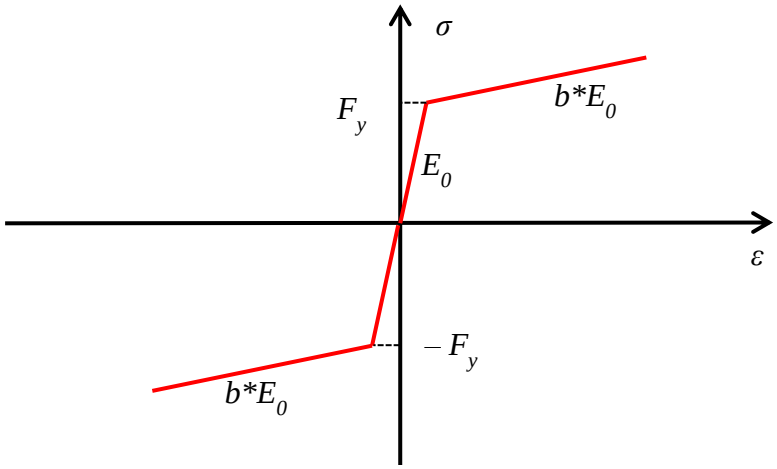

(b) *Steel 01* material model

Figure 7.13 Concrete and steel material models used to model the behavior of the wall pier

7.4.3 Abutment-soil interaction model

The abutment of the Meridian bridge is a typical seat-type abutment supported by a pile group foundation. The abutment has to withstand both vertical loads caused by dead and live loads and horizontal loads induced by vehicular actions (Nielson 2005). The abutment also has to resist the horizontal loading generated during an earthquake. The lateral resistance of the abutment comes from two sources, the resistance of the backfill soil known as passive resistance and the resistance of the foundation piles known as active resistance. The soil resistance is deemed passive because this resistance only initiates when the abutment is being pushed against the backfill and becomes insignificant when the abutment pulls away from the backfill. However, the foundation piles always provide lateral resistance against abutment motion with no regard to the direction of the motion. For this reason, resistance of the foundation piles is considered active (Choi 2002).

In the longitudinal direction of the bridge, when the abutment moves towards the backfill soil (i.e. a negative relative displacement between the abutment and the soil), both the soil and the piles provide resistances against the motion. Meanwhile, when the abutment moves away from the backfill soil (i.e. a positive relative displacement between the abutment and the soil), only the piles are considered to provide resistance against the motion. This leads to an asymmetric abutment-soil interaction model that has significantly larger stiffness due to negative relative displacement than positive. Moreover, in the transverse direction of the bridge, the piles are considered as the sole source of resistance against abutment motion while the passive soil resistance generated behind the wing walls can be conservatively neglected (Nielson and DesRoches 2007a).

Two common types of abutment failure modes are identified in Nielson (2005), which consist of a stability mode and a structural mode. The stability failure mode of the abutment is caused by loss of the soil support or excessive ground deformation, which leads to rigid movements or rotations of the abutment. The structural failure mode is associated with material failure of the abutment itself caused by significant earthen pressure or pounding of the deck. Because of the many incidents of abutment failures

during past earthquakes, the importance of incorporating an abutment-soil interaction model in the overall bridge model has been demonstrated in numerous studies on the seismic performance of highway bridges (Choi et al. 2004, Nielson and DeRoches 2007b, Pan et al. 2007, Filipov et al. 2013, Wang et al. 2012, and Wang et al. 2013). Due to this fact, a detailed abutment model is incorporated into the model of the Meridian bridge used in this study to appropriately capture the nonlinear abutment-soil interaction during a large seismic event.

Passive abutment-soil model

The passive soil model adopted in this study is based on the experimental findings of Shamsabadi et al. (2007) and assumes a hyperbolic load-deformation relationship. This hyperbolic soil model has been validated against experimental results of full-scale abutment tests, including a full-scale abutment test conducted at UC Davis (Maroney et al. 1994), showing its capability for use in modeling all soil types. Figure 7.14 (a) shows the OpenSees *HyperbolicGapMaterial* model that has been developed based on the findings of Duncan and Mokwa (2001), Wilson and Elgamal (2006), and Shamsabadi et al. (2007) on passive soil behavior under lateral loading. Past studies have shown that an initial stiffness (K_{max}) of 20.3 kN/mm can be used for an abutment with a unit length and height of 1.7 m. Given that the Meridian bridge abutment is 2.6 m high, this value needs to be adjusted by a factor of 1.55 (2.6/1.7) which provides an initial stiffness of 31.4 kN/mm (Caltrans 2006). Then, the total initial stiffness considering the full width (11.4 m) of the Meridian bridge abutment is the product of 31.4 kN/mm/m and 11.4 m, which is 357 kN/mm. This total initial stiffness needs to be equally distributed to all of the abutment-soil elements (i.e. 5 in this model) leading to an average initial stiffness of 71.4 kN/mm as indicated in Figure 7.14(a). The ultimate soil resistance for the prototype abutment is 326 kN. Using an approach similar to deriving the initial stiffness for the Meridian bridge abutment, the ultimate soil capacity can also be calculated, 5728 kN. Thus, each of the 5 soil elements has an ultimate resistance of 1146 kN.

Active abutment model

Per the recommendations of Caltrans (2006), the effective lateral stiffness contribution of one 305 mm pile is assumed to be 3.5 kN/mm with a capacity of 89 kN. These values have also been used in Pan et al. (2010) for modeling the active abutment action in their seismic fragility study of steel highway bridges found in New York. Considering that the Meridian bridge abutment is supported by 14-305 mm diameter piles, the total effective lateral stiffness contributed by the piles is 49 kN/mm, while the total ultimate capacity is 1246 kN. However, the lateral pile behavior is nonlinear before reaching the ultimate pile capacity. To account for this, the trilinear load displacement relationship proposed by Choi (2002) is adopted as shown in Figure 7.14(b). This model has been widely adopted (Nielson 2005 and Padgett 2007) and has been proven to effectively capture nonlinearities associated with the lateral behavior of the foundation piles. In this model, the ultimate pile capacity is achieved at a lateral displacement of 25.4 mm and first yielding occurs at a load level that is 70% of the 1246 kN ultimate capacity. This load level occurs when the deformation reaches 30% of the 25.4 mm ultimate deformation leading to an initial stiffness that is 2.3 times larger than the total effective lateral stiffness (Choi 2002). Zero stiffness is assumed after reaching the ultimate capacity. For the Meridian bridge model, these values are equally distributed to the five abutment elements leading to the values provided in Figure 7.14(b).

Abutment longitudinal and transverse response

With the passive and active abutment models established, the longitudinal constitutive model of the abutment is derived by placing the passive and active models in parallel, while the transverse constitutive model of the abutment only consists of the active abutment model. A total of 5 abutment elements are created at the abutment rocker bearing locations. The longitudinal and transverse constitutive models are applied to the abutment elements global X and Z degrees of freedom, respectively, as shown in Figure 7.15(a).

The cyclic behavior of the abutment element developed for this study has been investigated under both longitudinal and transverse loading. The simulated responses are

shown in Figure 7.15(b, c) to illustrate the passive and active abutment behavior in the two orthogonal directions. To show the effect of the initial gap in the passive soil model, a -38.1 mm gap is used in the longitudinal bearing model. As a result, the passive soil model is not engaged until the negative relative displacement exceeds this gap as shown in Figure 7.15(b). Comparing the longitudinal results with the transverse results, it is obvious that the negative longitudinal response shows significantly larger resistance at displacements beyond -38 mm due to the passive soil contribution, while the positive responses are identical for both the longitudinal and transverse results because of the sole contribution from the active abutment model.

7.4.4 Pounding model

Pounding can occur in a bridge system during a seismic event between adjacent decks or between a deck and an abutment because of out-of-phase vibration of adjacent bridge elements and insufficient expansion gap lengths. This behavior has the potential to cause severe structural damage to the superstructure and the abutment (Muthukumar and DesRoches 2006). The superstructure of the Meridian bridge is continuous, which leaves pounding only possible between the deck ends and the abutments. Figure 7.16 illustrates a scenario where the bridge deck impacts the abutment when the relative displacement surpasses the gap length. Muthukumar (2003) found that under moderate to high levels of ground motion, the energy dissipated during pounding between bridge components needs to be properly addressed to avoid over-estimating the response, particularly for stiff structural systems. Muthukumar (2003) proposed a simplified bilinear pounding constitutive model (see Figure 7.17) that can account for the energy dissipation associated with pounding and is shown to be effective in representing impact during pounding.

The complete derivation of the parameters needed to define the bilinear pounding model is provided in Muthukumar (2013). The general theory of the derivation is to first estimate the total energy loss (ΔE) using a stereomechanical model during a pounding event and then equate the hysteretic area enclosed by the bilinear model with the total energy loss estimation so that a relationship can be established between ΔE and the

parameters of the bilinear model. Other assumptions that are required to generate the bilinear model include a maximum penetration depth (d_m) of 25.4 mm and a yield penetration depth (d_y) of 2.54 mm that is 10 percent of the maximum penetration depth. The key parameters, i.e. K_{t1} and K_{t2}, are then determined as 10683 kN/mm and 3678 kN/mm, respectively. The values of the parameters given in Figure 7.17(b) need to be equally divided and distributed to the 5 pounding elements defined at the abutment rocker bearing locations. Further, the initial gap length used in the bilinear pounding model is 38.1 mm based on the design drawings of the Meridian bridge. Figure 7.18 shows the simulated cyclic response of a pounding element defined by the bilinear pounding model. The loading displacements applied to the pounding element have reached over 80 mm, which is not realistic and are only meant for demonstration purposes. The simulated response shows a good bilinear impact response with hysteretic energy being dissipated once yielding occurs at a displacement of 40.6 mm (i.e. sum of the gap length and d_y). The yield force of the pounding element is 5.4 MN, i.e. a fifth of the total yield force.

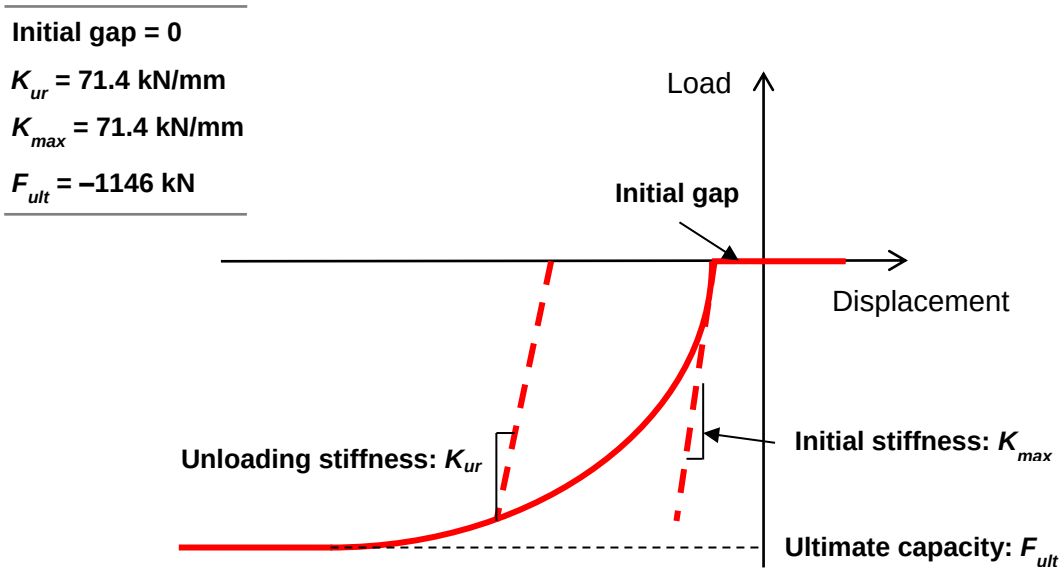

(a) Passive abutment soil model: *HyperbolicGapMaterial*

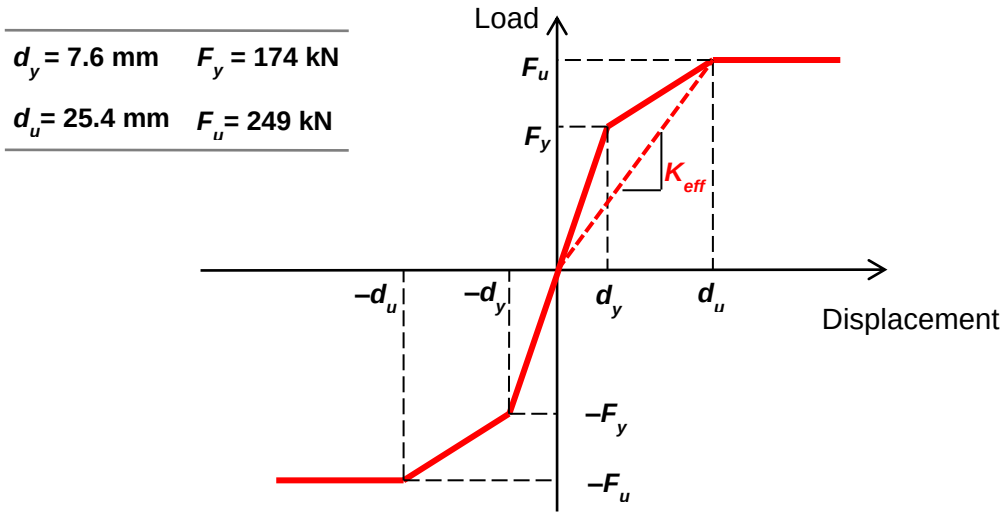

(b) Active abutment model: *Hysteretic* (Choi 2002)

Figure 7.14 Passive and active abutment models

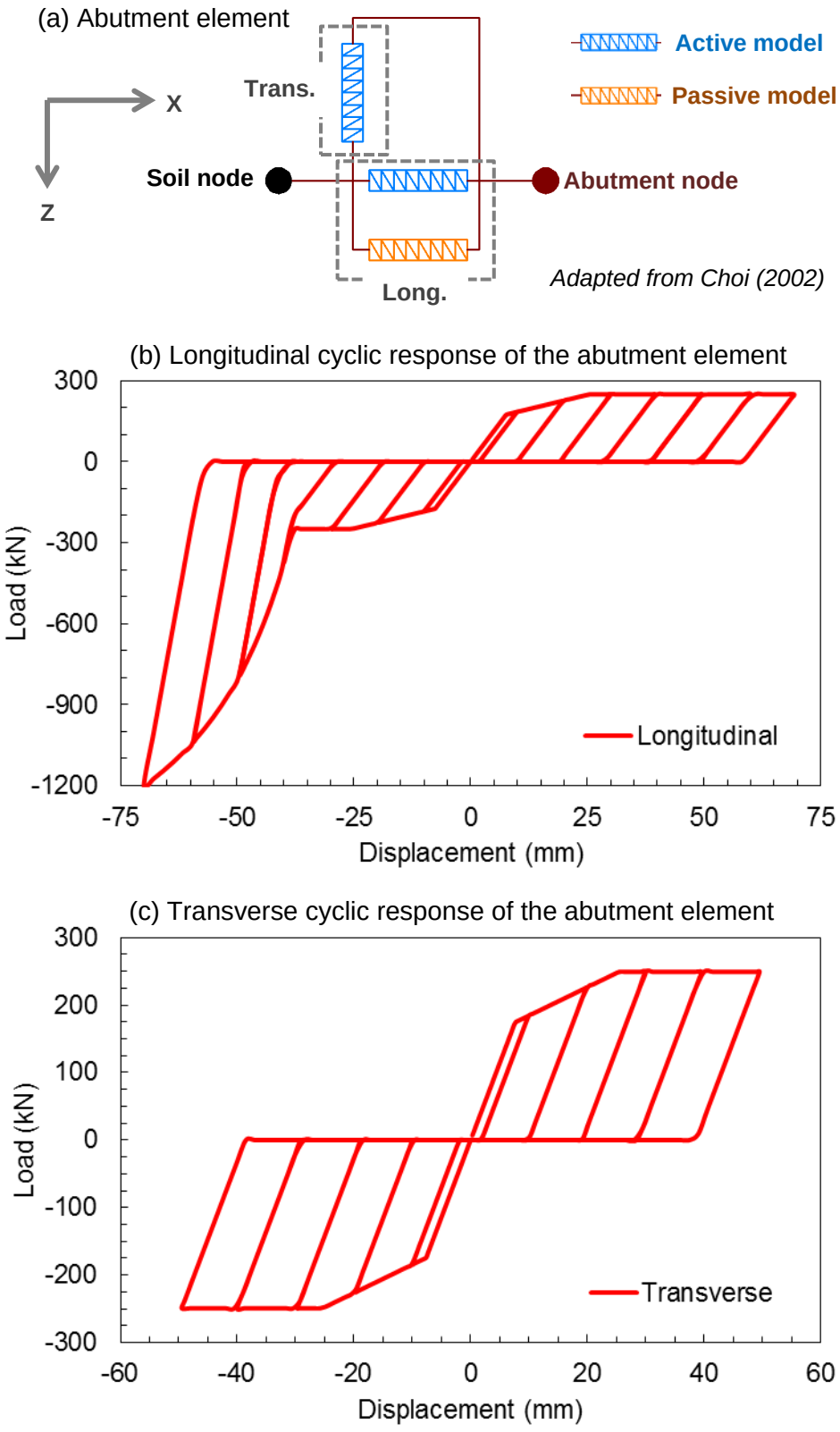

Figure 7.15 Abutment element and its longitudinal and transverse cyclic behavior

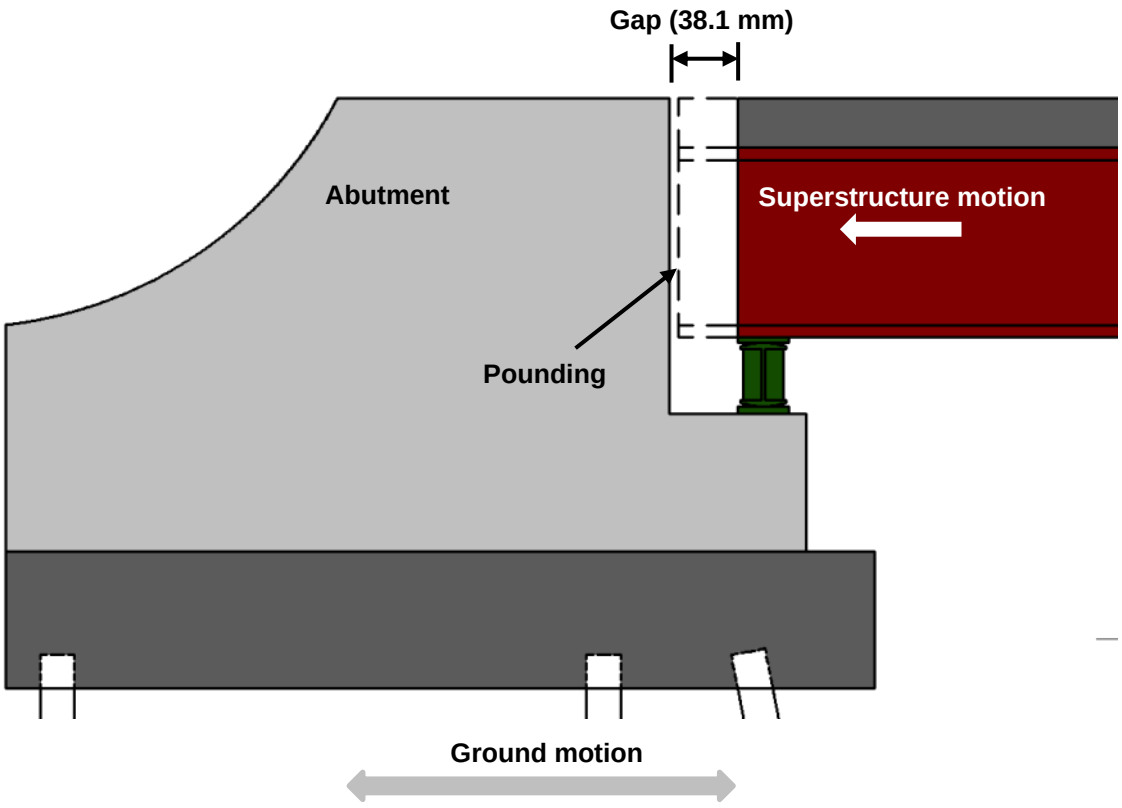

Figure 7.16 Schematic of pounding between the superstructure and abutment under ground motions

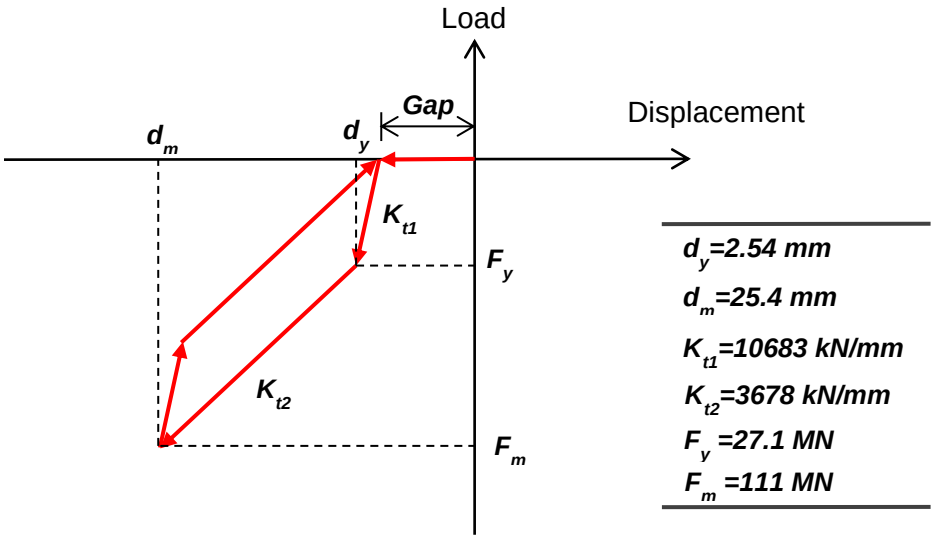

Figure 7.17 Pounding model between the superstructure and abutment (Muthukumar and DesRoches 2006)

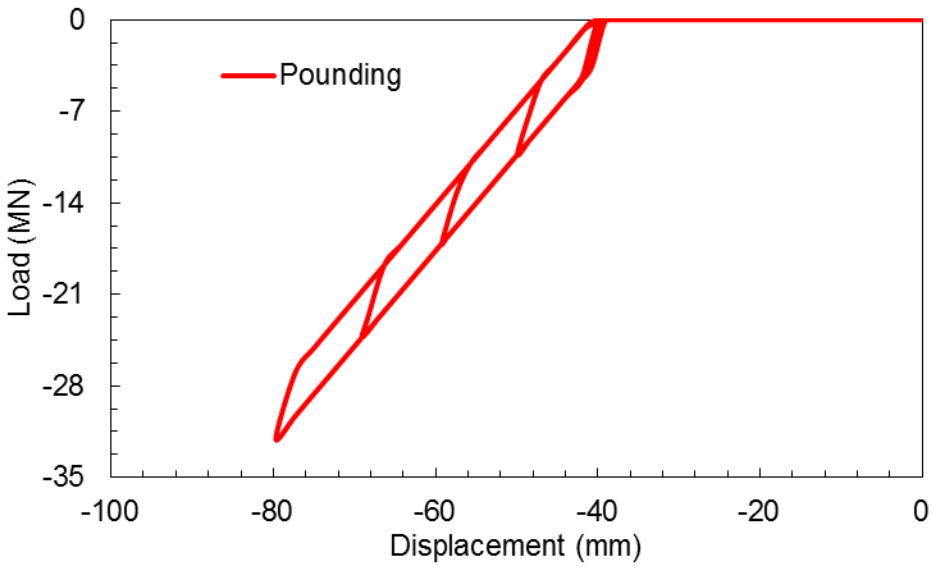

Figure 7.18 Simulated cyclic pounding response using the bilinear pounding model

7.4.5 Foundation model

The pile group foundation of the Meridian bridge utilizes a group of 18 driven concrete piles with diameters of 305 mm and lengths of 5.5 m, 3.0 m, and 4.6 m depending on the pier location. A pile group foundation usually consists of a reinforced concrete pile cap and a group of slender driven piles. The pile group foundation provides a load transfer mechanism between the bridge structure and the ground and has the capability of withstanding large lateral loads. When evaluating the seismic performance of highway bridges, it is important to incorporate the load-displacement relationship of the pile foundation, which is generally simplified in the bridge model to a set of translational and rotational springs (Aviram et al. 2008). The spring constants are determined by the individual pile stiffnesses at the pile top and the geometric configuration of the pile group in the pile foundation (Ma and Deng 2000). Because of the pile group interaction effect, it is often challenging to estimate these spring constants of the pile group foundation.

The foundation modeling methodology for deriving the spring constants adopted in this study is consistent with the one used by Choi (2002) and Nielson (2005), which is outlined in detail in Ma and Deng (2000). The translational degree of freedom (DOF) along the global Y axis (i.e. uplifting DOF) of the foundation is assumed to be fixed

along with the rotational DOF about the Y axis (i.e. torsional DOF). Two identical translational springs are used to model the foundation behavior in the global X and Z directions because all of the piles are engaged in resisting either X or Z movements and two rotational springs with different stiffnesses are adopted to represent the foundation overturning behavior about the global X and Z axes due to the asymmetric layout of the piles.

The horizontal pile stiffness is consistent with the value used in the abutment active model, which is 3.5 kN/mm/pile. The vertical stiffness of a pile is taken as 175 kN/mm, which was first suggested in Choi (2002) for typical piles found in the CEUS and also adopted by Nielson (2005) and Padgett (2007). The pile group effect is addressed using the procedures in Ma and Deng (2000), which is shown in Figure 7.19. The calculated translational stiffness for the X and Z degrees of freedom is 63 kN/mm, while the rotational stiffnesses about the X and Z axes are 1.24×10^{10} kN-mm/rad and 2.14×10^{9} kN-mm/rad, respectively. It should be noted that the rotational stiffness at the top of each pile is neglected in the derivation of the total pile group rotational stiffness, which is conservative since the contribution to the total stiffness from the individual rotational stiffnesses of the piles is negligible compared to the vertical stiffness of the pile (Ma and Deng, 2000). The values for the translational and rotational stiffnesses of the foundation are then applied to the foundation springs as shown in the schematic in Figure 7.19.

Procedure for estimating total stiffness of a pile foundation

Step 1: Configuration and dimensions of the pile foundation (units in mm)

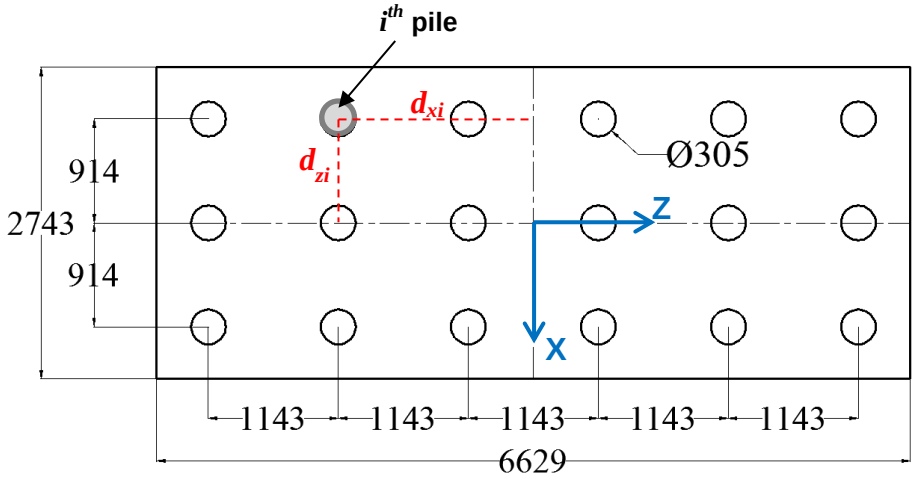

Step 2: Stiffness calculations of a single pile

$K_{hh,i}$ = 3.5 kN/mm/pile

$K_{vv,i}$ = 175 kN/mm/pile

d_{xi} = perpendicular distance from the i^{th} pile to X-axis

d_{zi} = perpendicular distance from the i^{th} pile to Z-axis

N= 18, total number of piles in the foundation

Step 3: Stiffness calculations of the pile group foundation

$K_{G,h} = \sum_{i=1}^{N} K_{hh,i}$ (1) gives the total translational horizontal stiffness for X and Z DOFs

$K_{G,r,X} = \sum_{i=1}^{N} K_{vv,i} \cdot d_{xi}^2$ (2) gives the total rotational stiffness about the X-axis

$K_{G,r,Z} = \sum_{i=1}^{N} K_{vv,i} \cdot d_{zi}^2$ (3) gives the total rotational stiffness about the Z-axis

Stiffness results of the pile group founda

Translational Stiffness (kN/mm)	
X	Z
63	63
Rotational Stiffness (kN-mm/rad)	
X - X	Z - Z
1.24E10	2.14E9

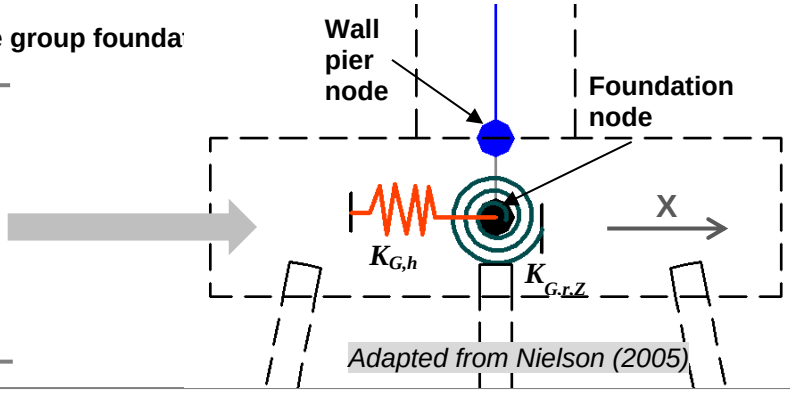

Figure 7.19 Stiffness calculation procedure for modeling the pile group foundation

7.5 Other Simulation Details

7.5.1 Characteristics of the Selected Ground Motions

As a result of the SAC Steel Project, ground motions with given probabilities of exceedence were gathered and developed for Boston, Seattle, and Los Angeles (Somerville et al. 1997). These motions were developed based on both historically recorded ground motions and synthetic time histories. Only the motions developed for the Boston area are used in this study since the focus is on the seismic performance of older bridges with steel bearings typical of the Central and Eastern U.S. The Boston motions consist of two groups: one with a 475 year return period (referred to as 10in50 hereafter) representing a design basis earthquake and the other with a 2475 year return period (referred to as 2in50 hereafter) representing the maximum credible earthquake. These groups correspond to a 10% and a 2% probability of exceedence in 50 years, respectively. Each group is comprised of 10 ground motion pairs with a total of 20 records. Each ground motion pair consists of one fault normal component and one fault parallel component and are developed to represent a stiff soil condition. Table 7.10 and Table 7.11 provide detailed information on the selected Boston ground motions regarding the earthquake magnitude, epicentral distance, and peak ground acceleration. Response spectra (Figure 7.20 through Figure 7.23) for these motions are developed considering a 5% damping ratio. It is clear from these figures that the 2% motions have significantly larger peak spectral accelerations than the 10% motions. Both sets of ground motions show peak spectral accelerations between periods of 0.1 sec. and 0.2 sec. The fault normal and parallel components of each ground motion group also show similar peak spectral accelerations.

The selected Boston ground motions are used to thoroughly investigate the seismic performance of highway bridges using the bridge model discussed previously in this chapter. The fault normal component is applied in the longitudinal direction, while the fault parallel component is applied in the transverse direction. This study mainly focuses on the performance of the steel bearings and how they synergistically interact with the

rest of the structural members of the bridge system under bidirectional ground motion excitations.

Table 7.10 Details of the 10% exceedence in 50 years Boston ground motions

EQ ID	Description	Magnitude	Distance (km)	PGA (cm/sec^2)
bo01	fn Simulation	6.5	30.0	121.97
bo02	fp Simulation	6.5	30.0	72.93
bo03	fn Simulation	6.5	30.0	141.37
bo04	fp Simulation	6.5	30.0	109.65
bo05	fn New Hampshire, 1982	4.3	8.4	564.78
bo06	fp New Hampshire, 1982	4.3	8.4	309.51
bo07	fn Nahanni, 1985	6.9	9.6	86.29
bo08	fp Nahanni, 1985	6.9	9.6	81.18
bo09	fn Nahanni, 1985	6.9	6.1	59.48
bo10	fp Nahanni, 1985	6.9	6.1	72.23
bo11	fn Nahanni, 1985	6.9	18.0	130.69
bo12	fp Nahanni, 1985	6.9	18.0	133.21
bo13	fn Saguenay, 1988	5.9	96.0	196.50
bo14	fp Saguenay, 1988	5.9	96.0	268.44
bo15	fn Saguenay, 1988	5.9	98.0	513.58
bo16	fp Saguenay, 1988	5.9	98.0	243.68
bo17	fn Saguenay, 1988	5.9	118.0	179.47
bo18	fp Saguenay, 1988	5.9	118.0	222.98
bo19	fn Saguenay, 1988	5.9	132.0	172.96
bo20	fp Saguenay, 1988	5.9	132.0	267.23

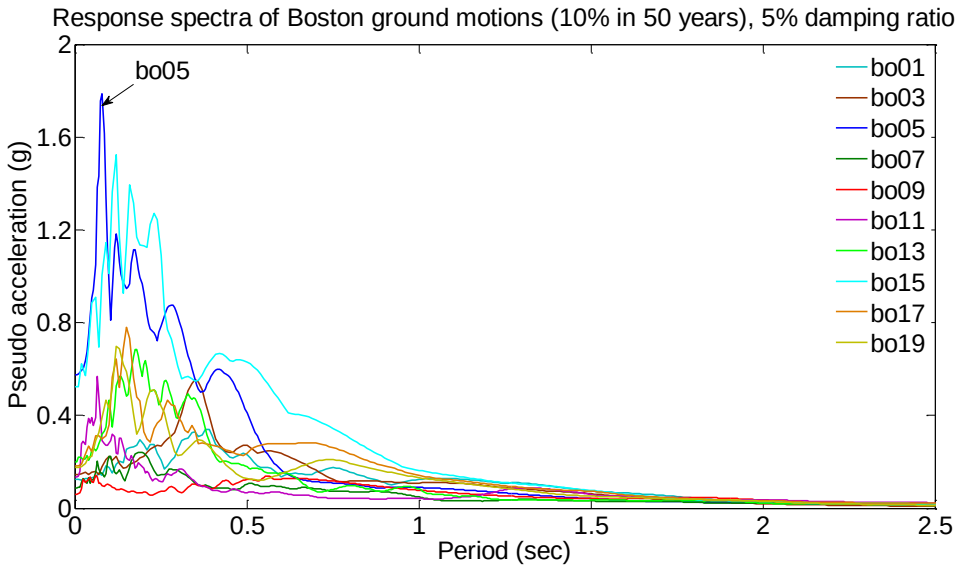

Figure 7.20 Response spectra for the normal (longitudinal) components of the 10 in 50 Boston ground motions

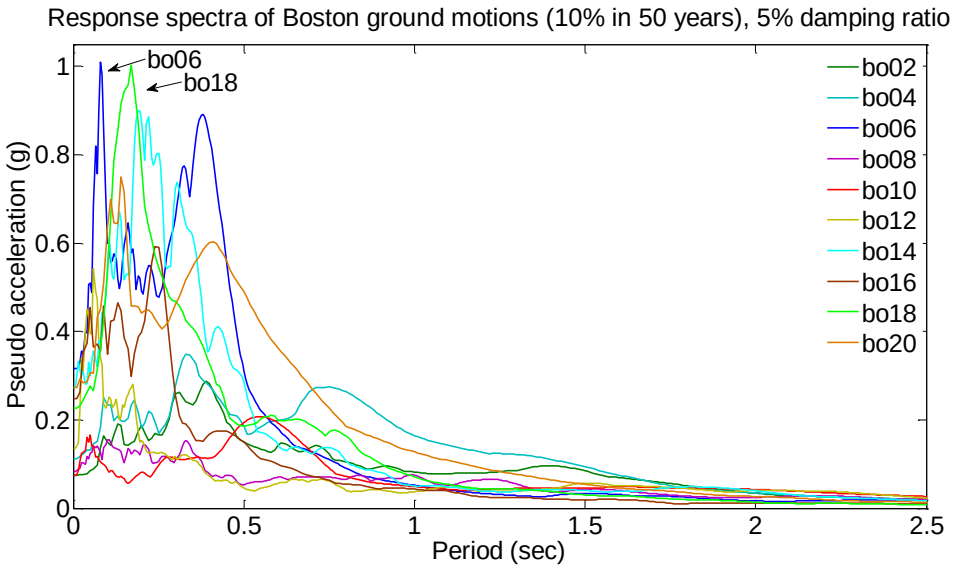

Figure 7.21 Response spectra for the parallel (transverse) components of the 10 in 50 Boston ground motions

Table 7.11 Details of the 2% exceedence in 50 years Boston ground motions

EQ ID	Description	Magnitude	Distance (km)	PGA (cm/sec^2)
bo21	fn simulation, foot wall	6.5	30.0	309.99
bo22	fp simulation, foot wall	6.5	30.0	357.04
bo23	fn simulation, foot wall	6.5	30.0	328.67
bo24	fp simulation, foot wall	6.5	30.0	235.26
bo25	fn simulation, foot wall	6.5	30.0	284.46
bo26	fp simulation, foot wall	6.5	30.0	302.80
bo27	fn Nahanni, 1985 Station 1	6.9	9.6	246.99
bo28	fp Nahanni, 1985 Station 1	6.9	9.6	232.37
bo29	fn Nahanni, 1985 Station 2	6.9	6.1	170.20
bo30	fp Nahanni, 1985 Station 2	6.9	6.1	206.67
bo31	fn Nahanni, 1985 Station 3	6.9	18.0	373.88
bo32	fp Nahanni, 1985 Station 3	6.9	18.0	381.09
bo33	fn Saguenay, 1988	5.9	96.0	562.33
bo34	fp Saguenay, 1988	5.9	96.0	768.21
bo35	fn Saguenay, 1988	5.9	98.0	1475.10
bo36	fp Saguenay, 1988	5.9	98.0	699.90
bo37	fn Saguenay, 1988	5.9	118.0	514.13
bo38	fp Saguenay, 1988	5.9	118.0	638.76
bo39	fn Saguenay, 1988	5.9	132.0	495.52
bo40	fp Saguenay, 1988	5.9	132.0	765.61

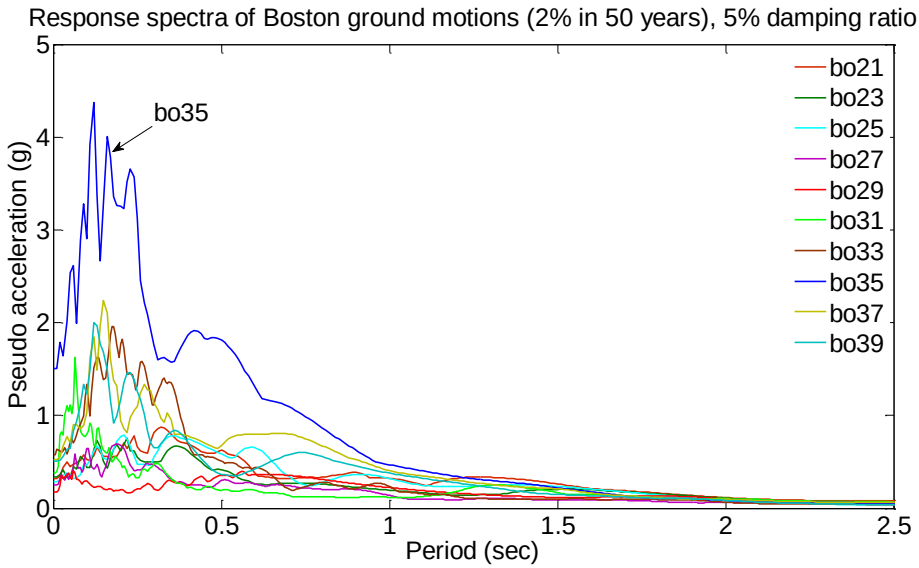

Figure 7.22 Response spectra for the normal (longitudinal) components of the 2 in 50 Boston ground motions

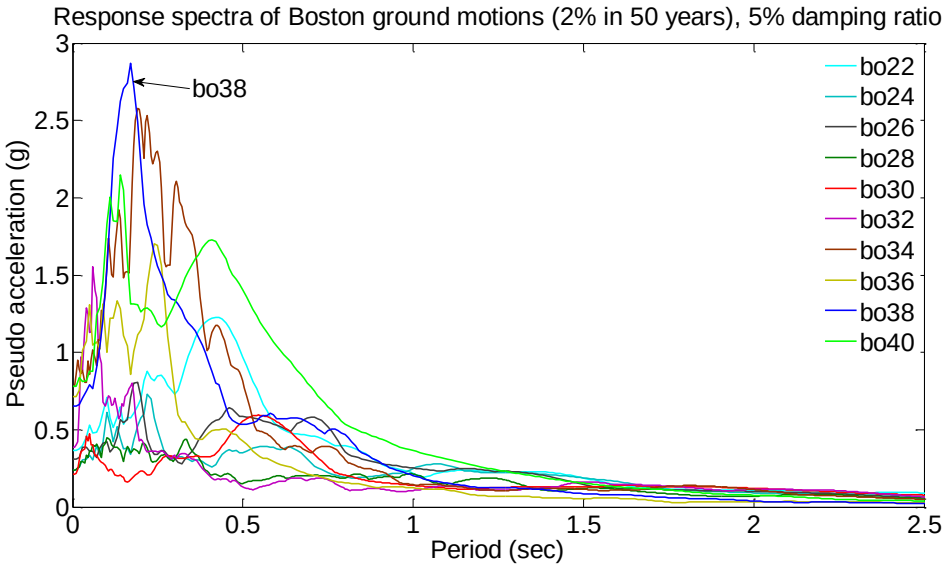

Figure 7.23 Response spectra for the parallel (transverse) components of the 2 in 50 Boston ground motions

7.5.2 Failure criteria of steel bridge bearings

The failure criteria of the steel bridge bearings considered in this study are based on maximum allowable displacements that are determined from the experimental findings and the bridge configuration. The bridge configuration is considered only because the bolster bearing can develop a stable transverse sliding behavior post fracture and its displacement capacity relies on the safety margin permitted by the dimensions of the cap beam before unseating occurs. Using a displacement based failure criterion facilitates the interpretation of the bearing response due to ground motions and also is consistent with past studies (Nielson and DesRoches, 2006).

Table 7.12 Displacement-based steel bridge bearing failure criteria

Steel Bearing Type	Longitudinal Capacity (mm)	Transverse Capacity (mm)
Steel rocker bearing with minor corrosion	74	43
Steel rocker bearing with severe corrosion	70	50
Steel rocker bearing with corrosion cleaned	70	57
Steel bolster bearing with minor corrosion	40	610*

*This value is determined from transverse unseating considerations of the bolster bearing on the cap beam

7.5.3 Scope of the simulation parameters

Figure 7.24 shows a schematic of the bridge model developed based on the component models discussed in the previous sections. A total of two bridge models are developed to be used in this study. The first bridge model considers steel bridge bearings that are in their pristine condition without any major corrosion that could alter the cyclic bearing behavior, which is referred to as *Bridge P* hereafter. The second bridge model reflects the actual condition of the steel bridge bearings after over 4 decades of in-situ service featuring spatially uneven corrosion distribution among the steel bearings. Thus, the second model, referred to as *Bridge C* hereafter, considers corroded abutment rocker bearings while both the pier rocker and bolster bearings are still modeled as in their pristine condition. This condition is selected based on typical inspection reports and the characteristics of the salvaged bearings that were tested. Comparison between the bridge responses of these two models provides a better understanding of the seismic performance of the steel bearings and the influence of corrosion on their behavior and the

overall bridge systems behavior. However, it should be noted that the steel bearing models are based on the behavior of the bearings in each orthogonal direction and do not account for potential decrease in capacity or change in behavior due to simultaneous longitudinal and transverse loading. The probability of exceedence of the ground motions is treated as another parameter in considering the bridge performance, which provides a more thorough assessment of the steel bearing performance and can be used to facilitate performance-based retrofit strategies.

The overall seismic bridge performance is assessed considering: 1) the displacement response of the superstructure, the abutments, and the wall piers; 2) the hysteretic response of the steel rocker bearings, the steel bolster bearings, the abutment-soil interaction, and the abutment-deck impact; and 3) the moment-curvature response of the wall piers. However, due to the large number of ground motion pairs considered in this simulation, only the bridge response under a representative ground motion pair in each ground motion set is discussed in detail as an example to illustrate the impact of that set of ground motions on the overall seismic bridge performance. Distributions of different maximum responses for various bridge components are generated based on the maximum response observed for each ground motion pair. Box plots are used to express these results.

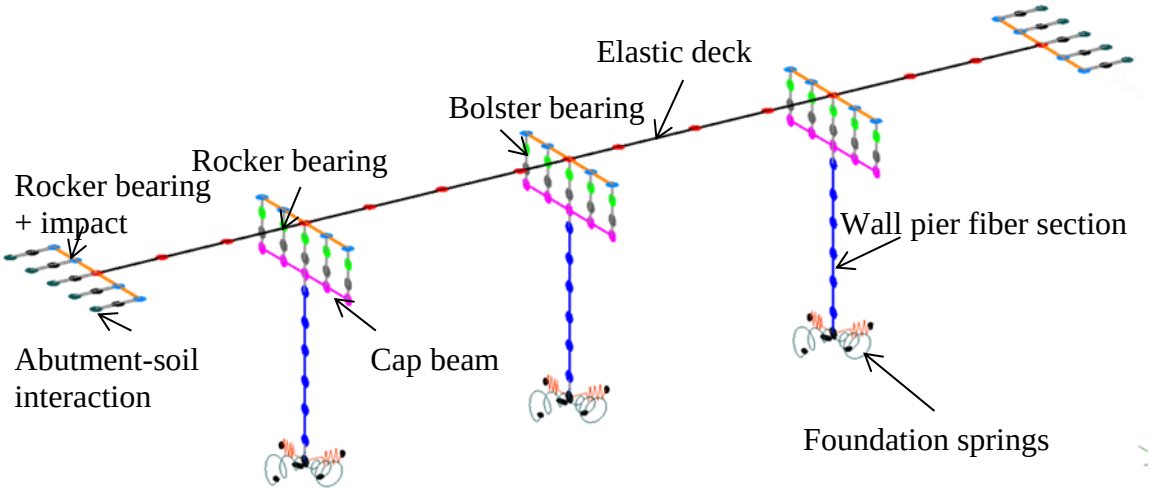

Figure 7.24 Schematic of the bridge model used in the numerical simulations

7.6 Seismic Bridge Performance Subjected to 10in50 Ground Motions

The seismic bridge response is discussed in detail for the ground motion pair consisting of the bo05 (applied in the longitudinal direction) and bo06 (applied in the transverse direction) components. The duration of this motion pair is 19.26 seconds with peak ground accelerations of 0.58g and 0.32g for the normal and parallel components, respectively. Peak spectral accelerations are 1.8g and 1.0g, both recorded at 0.08 seconds, for the normal and parallel components, respectively.

7.6.1 Superstructure displacement time histories

Bridge C

Figure 7.25 provides the absolute displacement time histories of the superstructure and the two abutments of *Bridge C* recorded during the given ground motion pair, bo05 and bo06. The displacement of the superstructure node located above the middle pier is adopted to generate these plots, while the abutment displacement is based on the displacement of the middle abutment node of the left abutment. The superstructure undergoes larger displacements in the longitudinal direction compared to the abutments. The maximum superstructure displacement reaches nearly 20 mm during the first 2

seconds of the ground motion pair. However, this maximum displacement is smaller than the expansion gap length of 38.1 mm between the deck and the abutments, indicating that no impact occurs between them. As a result, the abutments remains elastic in the longitudinal direction with negligible elastic deformation under the given ground motion pair. Both the superstructure and the abutment responses diminish rapidly as the ground motion dissipates.

In the transverse direction, the superstructure also shows larger displacements than the abutments with the maximum displacement also reaching 20 mm. The bridge's transverse response again is largest during the first 5 seconds of the ground motions and then rapidly decreases with time. These large displacements lead to residual displacement of the superstructure indicating potential permanent displacement of the steel bearings. These observations suggest that the overall seismic demand of the motion pair, bo05 and bo06, causes only minor damage to the bridge.

Bridge P

Figure 7.26 shows the displacement time histories obtained for the superstructure and the abutments of *Bridge P*. *Bridge P* experiences much larger displacements of the superstructure compared to the abutments. Since the expansion gap is large enough to accommodate the seismic displacement demand placed on the superstructure, no impact between the superstructure and abutment occurs throughout the duration of the ground motions. Because of this, the abutments remain elastic during the entire loading duration in the longitudinal direction. The longitudinal response of the bridge dissipates quickly after the peak acceleration amplitudes of the ground motion pair passes. The bridge's transverse response also sees superstructure displacements of approximately 20 mm and relatively small abutment movements. As with the longitudinal response, the bridge responses are only significant during the first 5 seconds of the ground motion duration.

Comparison

Figure 7.27 presents the comparison between the superstructure displacements of *Bridge C* and *Bridge P*. In both the longitudinal and transverse loading directions, *Bridge C*

shows a slightly larger maximum displacement than *Bridge P*. The longitudinal superstructure response follows a similar vibration pattern for both bridges, while corrosion effects are visible in the transverse response. *Bridge C* reaches larger transverse displacements and exhibits permanent displacement of the superstructure not seen in *Bridge P*. It is clear that corrosion of steel rocker bearings has an effect on the overall bridge performance, but overall this effect appears to be minor. More in-depth analysis of the hysteretic responses of the various bridge components is required to fully understand and interpret the significance of corrosion in the bearings on the response of the bridge components.

7.6.2 Substructure displacement time histories

Bridge C

The displacement time histories of the three wall piers of *Bridge C* in the longitudinal and transverse loading directions are calculated based on the relative displacement between the pier top and the pier bottom (Figure 7.28). In the longitudinal direction, the left and right piers exhibit identical displacement responses with the maximum relative displacements reaching 5 mm. In comparison, the middle wall pier shows a larger response with the maximum relative displacement close to 10 mm. This difference is due to the fact that the bolster bearings on the middle wall pier resist translational motion leading to larger forces transferred to the middle wall. In the transverse direction, all three of the wall piers show similar relative displacement time histories with the middle wall pier again undergoing slightly larger displacements. The maximum displacement is less than 2 mm for all of the wall piers further suggesting that the wall piers will remain elastic in the transverse direction. No significant permanent deformation in either direction is observed for any wall pier.

Bridge P

The displacement time histories of the wall piers of *Bridge P* are given in Figure 7.29. The left and right piers show identical longitudinal responses similar to the observations

for *Bridge C*. The maximum displacement for the two side piers is less than 5 mm with the largest relative displacements occurring during the first 5 seconds of the ground motions. The middle pier undergoes a larger maximum displacement reaching nearly 10 mm again because this is the location of the bolster bearings. All three wall piers show little to no permanent deformation at the end of the motion duration. In the transverse direction, the middle wall pier shows a response very similar to those of the two side piers with slightly larger displacement magnitudes during the first 5 seconds of the motions. Identical responses are found for the two side piers. Similar to the observation for *Bridge C*, the maximum relative displacement is less than 2 mm for all three wall piers of *Bridge P*. These observations show that the walls of *Bridge P* will essentially remain elastic in both the longitudinal and transverse directions given a 10in50 ground motion pair such as bo05 and bo06.

Comparison

Since the largest demands are placed on the middle wall pier, a comparison is made of its performance in *Bridge C* and *Bridge P* to consider the effects of corroded bearings. Figure 7.30 shows that the overall trend of the two responses in both the longitudinal and transverse directions is similar with only minor differences in the relative displacement magnitudes for the two bridges. Based on the findings, the effect of corrosion of the abutment rocker bearings on the middle pier wall is minor and essentially indiscernible for 10in50 ground motions.

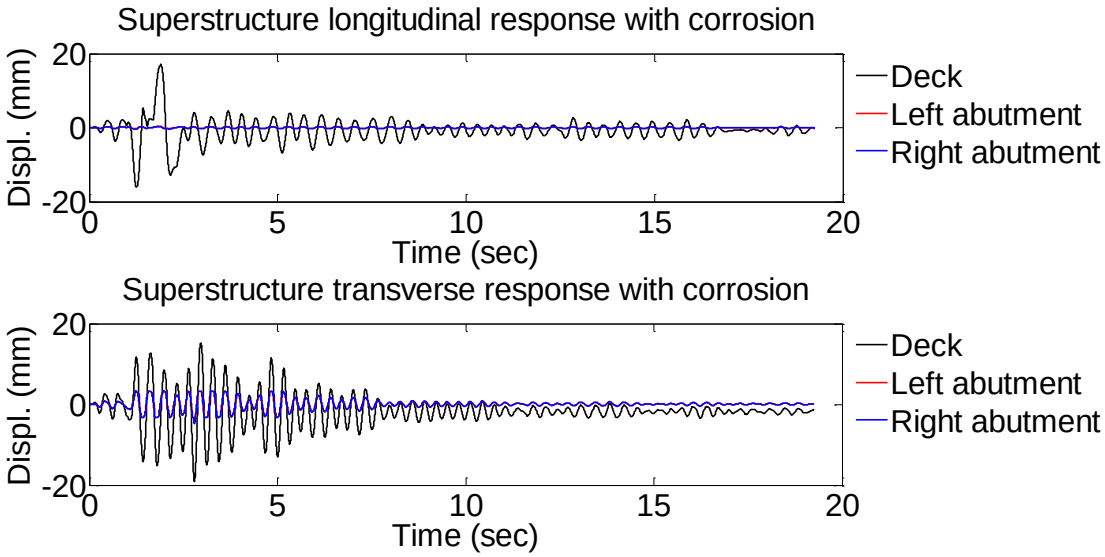

Figure 7.25 Superstructure and abutments displacement time histories of *Bridge C* under bidirectional 10in50 Boston motion pair, bo05 and bo06

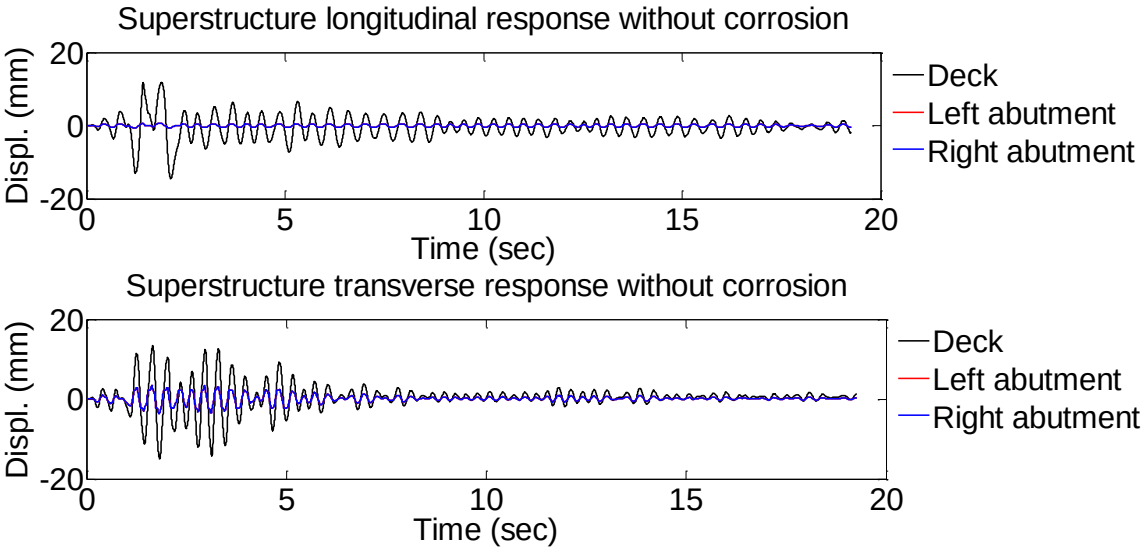

Figure 7.26 Superstructure and abutments displacement time histories of *Bridge P* under bidirectional 10in50 Boston motion pair, bo05 and bo06

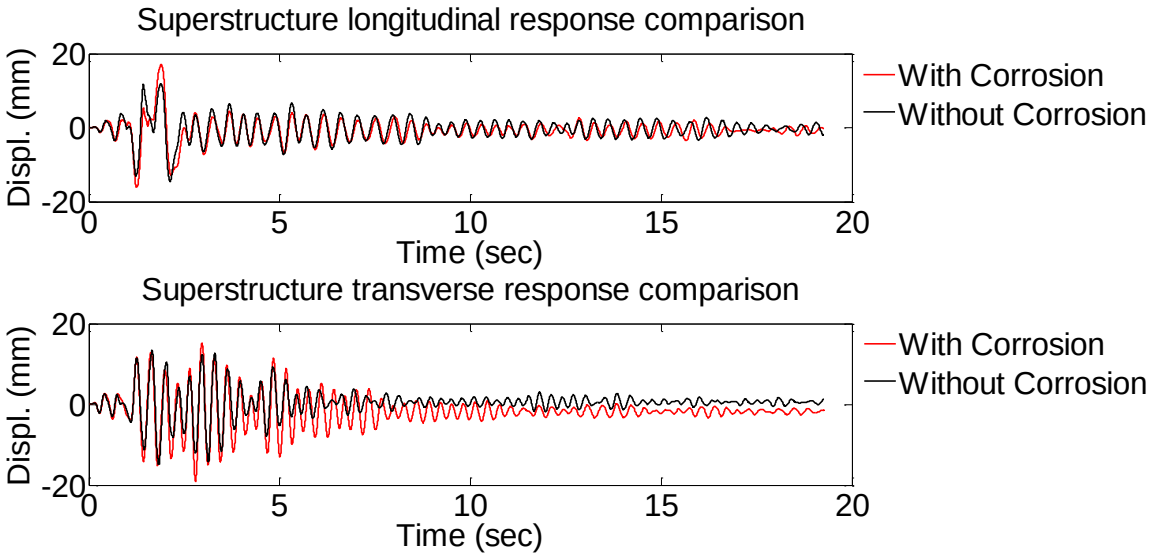

Figure 7.27 Comparison of superstructure displacement time histories under bidirectional 10in50 Boston motion pair of bo05 and bo06 between *Bridge C* and *Bridge P*

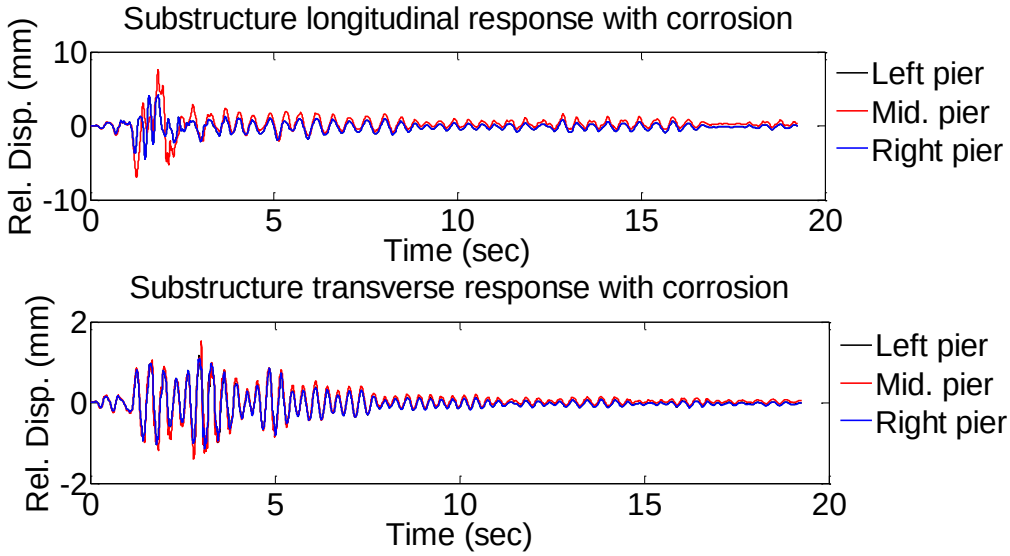

Figure 7.28 Wall pier relative displacement time histories of *Bridge C* under bidirectional 10in50 Boston motion pair, bo05 and bo06

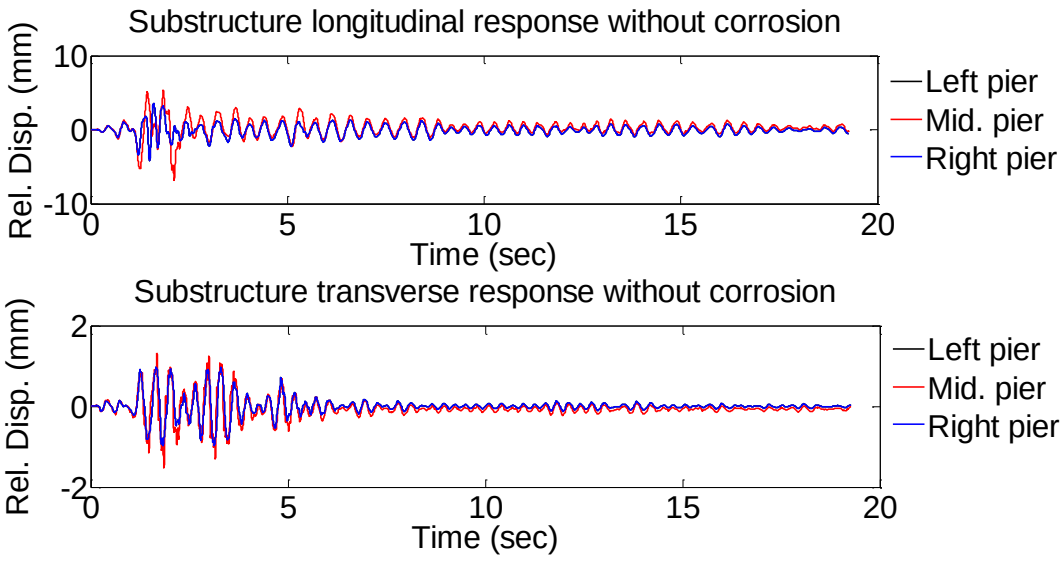

Figure 7.29 Wall pier relative displacement time histories of *Bridge P* under bidirectional 10in50 Boston motion pair, bo05 and bo06

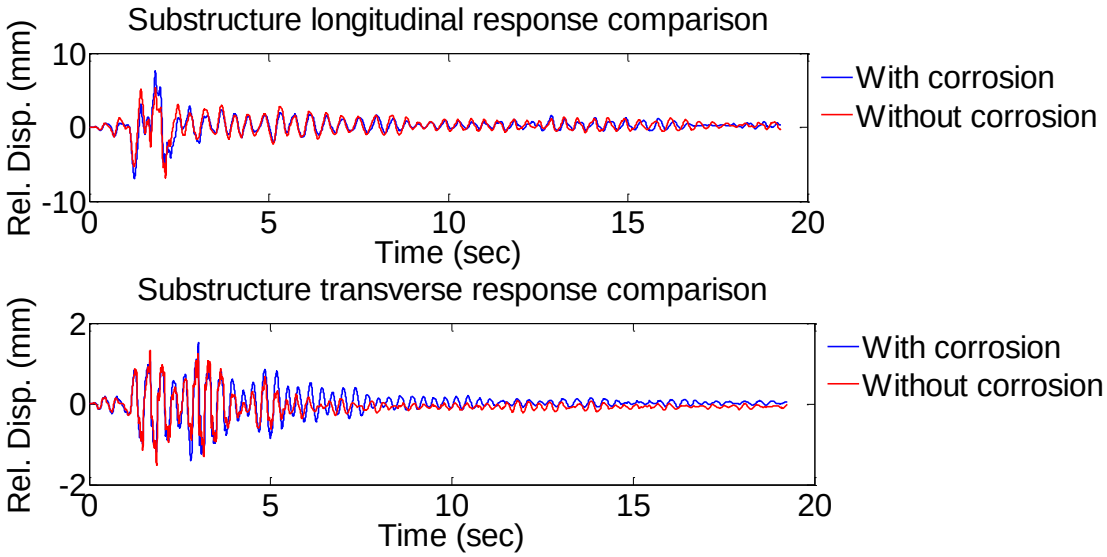

Figure 7.30 Comparison of middle wall pier relative displacement time histories under bidirectional 10in50 Boston motion pair of bo05 and bo06 between *Bridge C* and *Bridge P*

7.6.3 Abutment-soil interaction

The abutment-soil interaction responses of *Bridge C* and *Bridge P* are given in Figure 7.31 and Figure 7.32, respectively. Overall, the abutments in both bridges do not experience large deformations that would lead to significant passive and active actions. The abutment soil response of *Bridge C* remains linear elastic in the longitudinal and transverse loading directions. The maximum active force developed in the longitudinal direction is 20 kN, while the maximum passive force reaches 25 kN at a deformation of -1 mm. The transverse abutment soil response has a maximum force of roughly 60 kN developed at a displacement level slightly above 2 mm. These forces are insignificant compared with either the passive (1146 kN) or active (249 kN) abutment-soil interaction capacity.

In comparison, *Bridge P* undergoes much larger passive forces in the longitudinal abutment-soil interaction response. As shown in Figure 7.32, a maximum passive force of 150 kN is reached at a deformation level of 2.5 mm. The uncorroded rocker bearings located on the abutments in *Bridge P* have a larger secant stiffness than the corroded rocker bearings in *Bridge C* leading to larger forces for a given bearing displacement. However, even at this displacement level, the abutment behavior remains elastic with the nonlinearity due to engaging the passive soil resistance. Conversely, the active response of *Bridge P* is nearly identical to that of *Bridge C* showing a maximum force of 20 kN and a linear-elastic behavior. The transverse abutment responses of *Bridge P* and *Bridge C* are identical with a dominant linear-elastic behavior indicating no yielding of the piles.

7.6.4 Pounding response at the abutment

Figure 7.33 shows the forces due to impact caused by pounding at the abutment of *Bridge C* and *Bridge P*. No pounding occurs due to the ground motion pair bo05 and bo06 in *Bridge C* as the plots show a constant zero impact force. The reason for no impact is that the maximum relative displacement between the deck and abutments is less than the expansion gap length of 38.1 mm. This smaller displacement also helps to explain the low forces observed in the longitudinal abutment response since the abutment only receives forces imparted from the corroded rocker bearings. In contrast, pounding is

observed in the response of *Bridge P* with a maximum impact force of 130 kN when the negative deformation slightly exceeds the expansion gap length. However, the pounding penetration depth is less than 1 mm, which explains the relatively small impact force. This pounding induced impact force provides a further explanation for the large passive abutment forces observed for *Bridge P*.

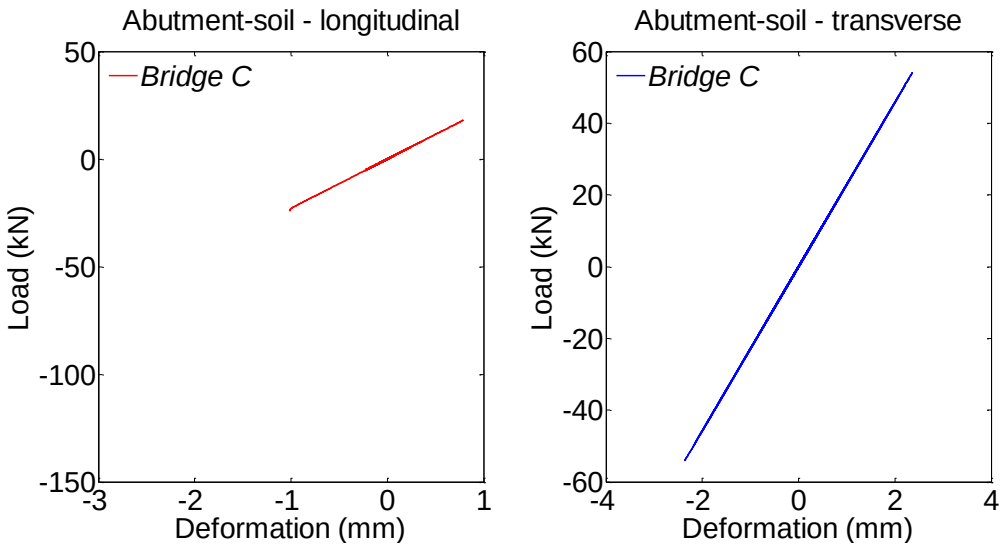

Figure 7.31 Abutment soil interaction response of *Bridge C* under the bidirectional ground motion pair of bo05 and bo06

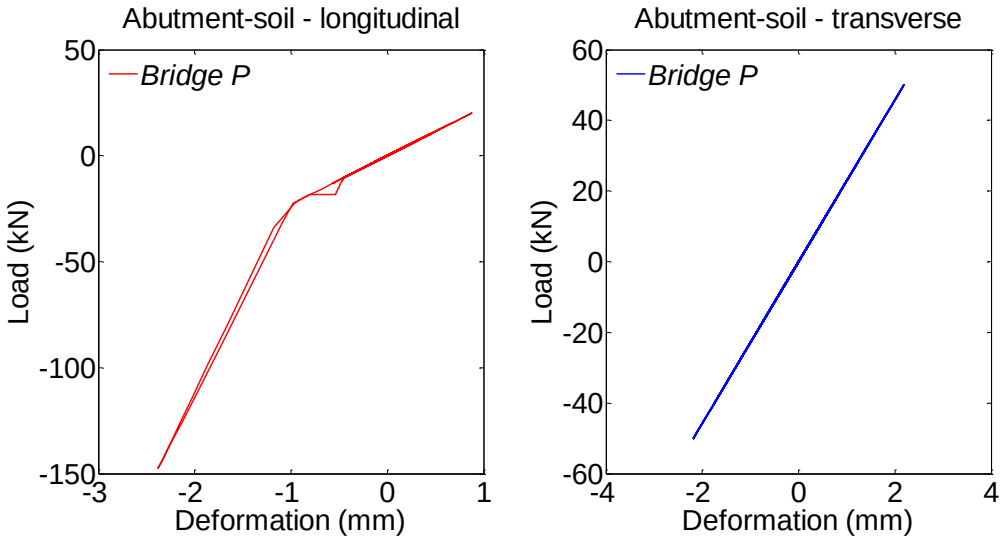

Figure 7.32 Abutment soil interaction response of *Bridge P* under the bidirectional ground motion pair of bo05 and bo06

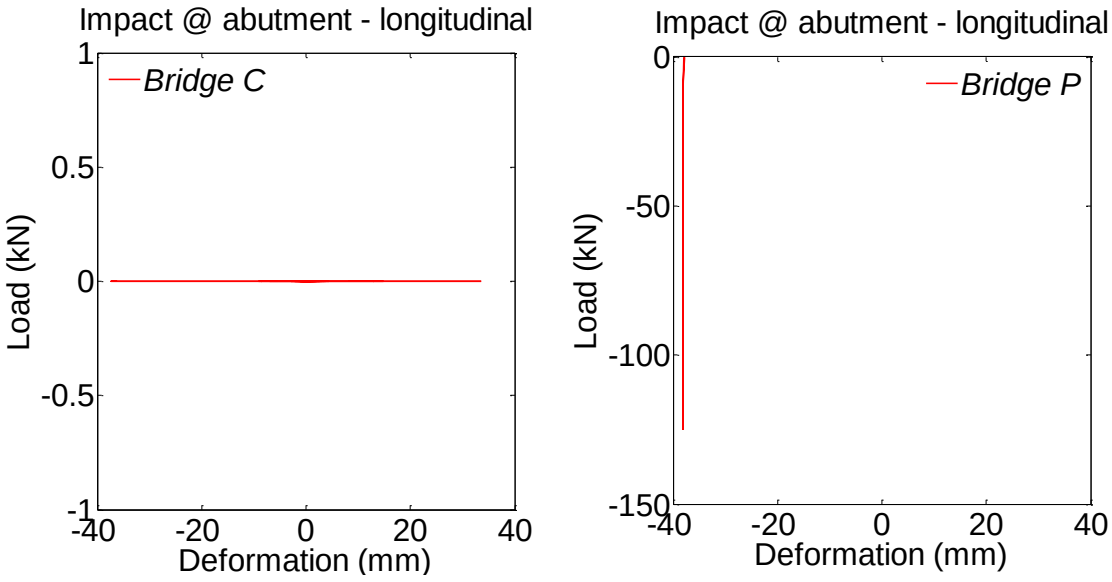

Figure 7.33 Impact responses due to pounding between the deck and abutments for both *Bridge C* and *Bridge P* under bidirectional ground motion pair bo05 and bo06

7.6.5 Steel rocker bearing response at the abutment

The abutment steel rocker bearing response observed for *Bridge C* is given in Figure 7.34. From the plot, the maximum longitudinal displacement of the steel rocker bearing located on the abutment reaches 40 mm in both the positive and negative directions. Rocking of the bearing initiates at these displacement levels leading to a rapid increase in the bearing longitudinal resistance, which reaches 20 kN in both directions. The transverse response of the rocker bearing remains linear-elastic with only small displacement levels reached. However, the larger bearing transverse stiffness leads to a maximum force of 50 kN. The observed maximum longitudinal and transverse displacements are smaller than the displacement capacities of the corroded rocker bearings indicating that the corroded rocker bearings located on the abutments perform well under the bo05 and bo06 ground motion pair.

Figure 7.35 shows the steel rocker bearing response at the abutment for *Bridge P* that has uncorroded rocker bearings at the abutments and piers. The maximum longitudinal displacements are 40 mm in both the positive and negative directions. The maximum bearing resistance again is 20 kN. The maximum transverse displacement is 2 mm, similar to that seen for *Bridge C*. This displacement level is associated with rigid sliding in the transverse direction at a resistance of 50 kN. Compared with the displacement capacities of the tested bearing with minor corrosion, these longitudinal and transverse displacement demands observed for *Bridge P* can be accommodated safely by the steel rocker bearings. The results suggest that the steel rocker bearings located at the abutments can adequately withstand a 10in50 ground motion pair even though the bearings are not designed for seismic loads.

Close examination of the two sets of steel rocker bearing responses show that the corroded and pristine steel rocker bearings have similar force and displacement levels in the longitudinal and transverse directions as a result of the ground motion pair bo05 and bo06. The minor differences between the responses are due to corrosion-induced deformation mode variations in the steel rocker bearings. The performance of both bearings suggests that the longitudinal behavior will likely dictate the failure mode of a

steel rocker bearing whether corrosion is present or not due to the fact that significantly larger longitudinal displacements are induced compared to those in the transverse direction.

7.6.6 Steel rocker bearing response at the pier

Figure 7.36 shows the steel rocker bearing response at the left pier location observed for *Bridge C*. No corrosion effect is considered for the pier rocker bearings because they are located beneath a continuous deck joint. The maximum longitudinal displacement of the bearing reaches 40 mm in the positive and negative directions, leading to a maximum bearing resistance of 20 kN. The transverse response remains linear-elastic under the considered ground motions. The maximum transverse deformation remains small reaching only 0.4 mm indicating that the transverse seismic demand is small. The high stiffness of the bearing in the transverse direction does lead to a maximum force of 30 kN. For both the considered cases, the chance of failure is small with only minor nonlinear longitudinal displacements.

The steel rocker bearing response at the left pier location for *Bridge P* is presented in Figure 7.37. The longitudinal displacement response suggests significant rocking of the steel rocker bearing. The maximum longitudinal displacement of the steel rocker bearing is 30 mm with a maximum resistance of 20 kN. In contrast, the bearing transverse response remains elastic. Maximum bearing transverse displacements are less than 0.5 mm with a maximum bearing resistance of approximately 40 kN. The steel rock bearing performs well in both the longitudinal and transverse directions with the maximum displacements remaining below its capacities indicating that the seismic demand from a design basis earthquake can be accommodated by the steel rocker bearing located on the left pier.

Comparing the steel rocker bearing responses from *Bridge C* and *Bridge P* suggests a similar response with respect to the maximum displacements and resistance for both the longitudinal and transverse directions. This observation indicates that the pier rocker bearing response is not heavily influenced by the corrosion condition of the abutment rocker bearings for this particular ground motion pair. Additionally, the longitudinal

displacements of the steel rocker bearings are much more significant than their transverse displacements, indicating the steel rocker bearings at the piers are more prone to topple in the longitudinal direction than in the transverse direction.

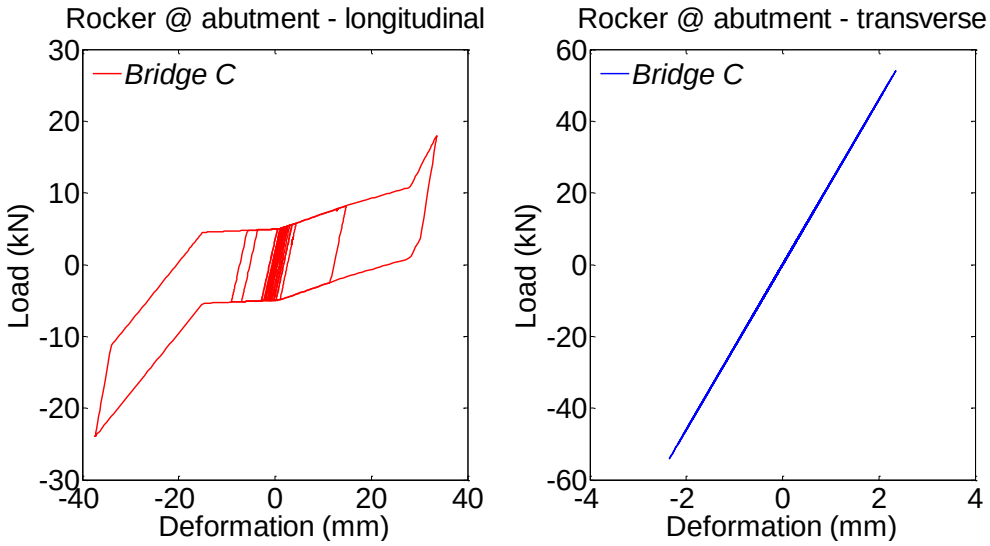

Figure 7.34 Steel rocker bearing response at the abutment of *Bridge C* under the bidirectional ground motion pair of bo05 and bo06

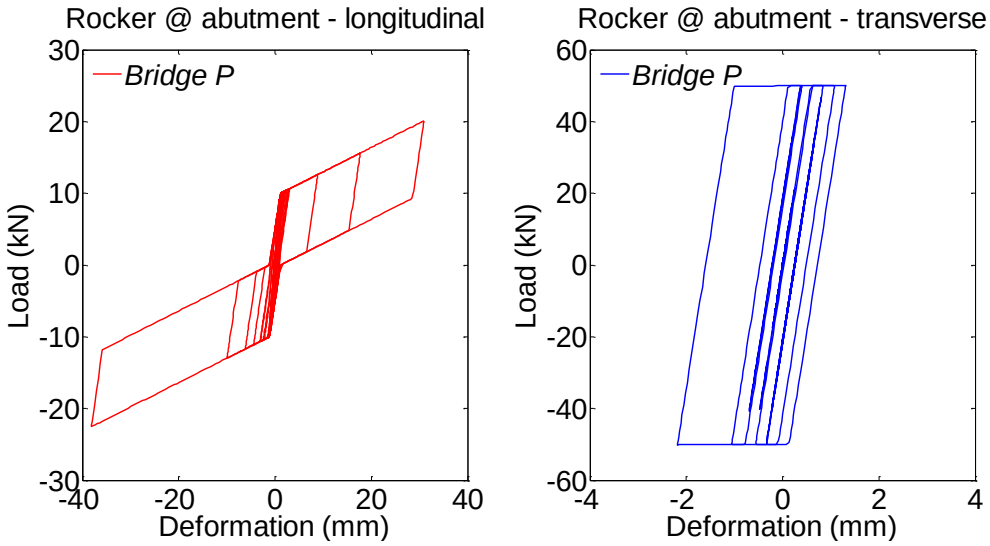

Figure 7.35 Steel rocker bearing response at the abutment of *Bridge P* under the bidirectional ground motion pair of bo05 and bo06

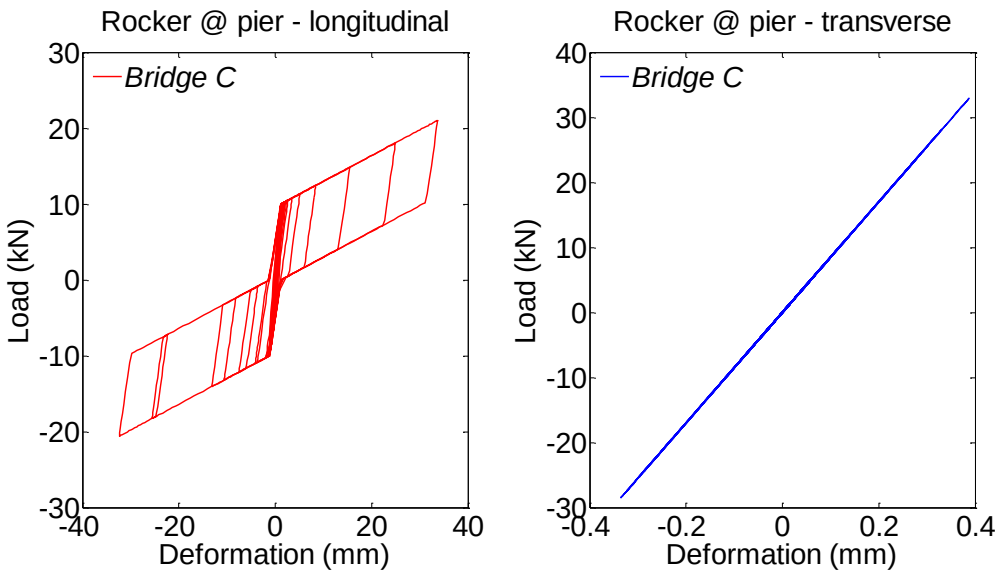

Figure 7.36 Steel rocker bearing response at the pier of *Bridge C* under the bidirectional ground motion pair of bo05 and bo06

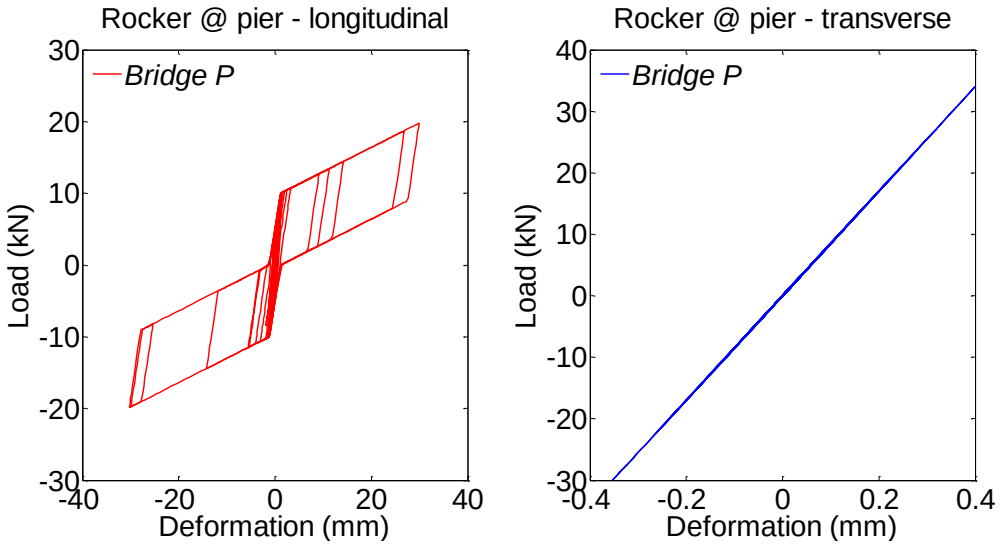

Figure 7.37 Steel rocker bearing response at the pier of *Bridge P* under the bidirectional ground motion pair of bo05 and bo06

7.6.7 Steel bolster bearing response at the pier

The steel bolster bearing response recorded for *Bridge C* under the bo05 and bo06 ground motion pair is shown in Figure 7.38. In the longitudinal direction, the steel bolster bearing undergoes a maximum displacement of roughly 8 mm in both the positive and negative directions. This displacement level engages the anchor bolts in resisting the longitudinal forces imparted to the bolster bearing as is evident by the rapid increase in the bearing resistance. The maximum bearing resistance is 80 kN. As has been seen with other components, the displacement and force levels are not large enough to cause yielding of the anchor bolts and as a result, no strength degradation is observed under the considered ground motion pair. In the transverse direction, the bearing response remains linear-elastic. The maximum displacement is 0.5 mm, which is below that needed to initiate sliding. Likewise, the maximum transverse forces are 40 kN, significantly less than the bearing capacity. These observations indicate that the steel bolster bearing in a bridge with corroded rocker bearings will see minimal damage under a design basis seismic event typical of the CEUS.

Figure 7.39 presents the steel bolster bearing response recorded for *Bridge P*. The maximum longitudinal displacement of the steel bolster bearing is 8 mm, enough to engage the anchor bolts. The maximum bearing resistance reaches 80 kN in both directions. No strength degradation is observed in the longitudinal response indicating that the anchor bolts remain elastic. A much smaller transverse displacement of less than 1 mm is observed for the bearing transverse response. This displacement level is sufficient to initiate a small level of sliding in the bolster bearing with a sliding resistance of 40 kN. The seismic demand in both the longitudinal and the transverse directions is less than the capacities of the steel bolster bearings, suggesting that the steel bolster bearings perform adequately under a design basis earthquake without experiencing severe damage.

Comparing the steel bolster bearing responses obtained for *Bridge C* and *Bridge P*, similar behavior is seen with only minor differences in the transverse responses. These observations suggest that the corroded rocker bearings at the abutments have limited

influence on the seismic performance of the steel bolster bearings. Similar to the observations for the steel rocker bearings, larger longitudinal displacements are observed in the steel bolster bearing response for both bridges. These longitudinal displacements are largely due to the fact that the bridge is much stiffer in the transverse direction than in the longitudinal direction, thus requiring a significantly larger seismic demand to generate a comparable transverse response.

7.6.8 Wall pier base moment-curvature response

Considering that the steel bolster bearings can transfer larger forces into the substructure than the steel rocker bearings, only the middle wall pier response is selected for investigation. The response of the wall pier is measured using the moment-curvature response recorded at the base of the wall pier under the input seismic excitation. For the considered wall pier, the ultimate moment capacities about the two main bending axes are estimated to be 2065 kN-m about the weak (transverse) axis and 14944 kN-m about the strong (longitudinal) axis based on the geometry and reinforcement ratio of the wall pier. The shear developed in the wall pier is not a concern because the shear capacity of the concrete alone for the wall pier is over 4000 kN, much greater than the maximum shear forces (2100 kN) that can be developed in the bolster bearings and transferred to the substructure. These calculated pier capacities are on the same order as past studies with similar reinforced concrete wall piers (Bignell et al. 2005, Filipov et al. 2013). For the purpose of this study, the wall pier response is only discussed from an ultimate moment capacity perspective. Ductility of the wall piers is not addressed.

Figure 7.40 shows the moment-curvature response recorded at the wall pier base of *Bridge C*. This location is chosen because it provides the maximum moment along the wall pier height. The maximum weak-axis bending moments developed are 1650 kN-m and 1997 kN-m for the positive and negative bending responses, respectively. These numbers are slightly lower than the wall pier transverse bending capacity of 2065 kN-m. The maximum strong-axis bending moments are 1834 kN-m and 1399 kN-m for the positive and negative responses, respectively, which are significantly smaller than the wall pier longitudinal bending capacity (14944 kN-m). The results indicate that the wall

pier performs adequately in bending without reaching its ultimate capacity due to bending in either direction under the 10in50 seismic excitation.

Figure 7.41 presents the moment-curvature response for *Bridge P* recorded at the wall pier base. The maximum weak-axis bending moments are 1528 kN-m and 2030 kN-m for the positive and negative responses, respectively. These numbers are also slightly lower than the wall pier ultimate capacity of 2065 kN-m. Moreover, the maximum strong-axis bending moments are 1899 kN-m and 1045 kN-m for positive and negative bending, respectively. The wall pier strong-axis bending capacity is much higher than these recorded bending moments induced by the considered 10in50 ground motion pair, again suggesting the wall pier can withstand the strong-axis bending seismic demand.

A closer inspection of the wall pier responses for the two considered bridges shows a similarity in the response in terms of the maximum experienced bending moments about both bending directions. This observation suggests that the corroded abutment rocker bearing has little influence on the seismic moment demands placed on the middle wall pier for a design basis earthquake. Additionally, the wall pier is more susceptible to experience plastic deformation due to weak-axis bending, while the strong-axis bending capacity of the wall pier is much greater than the applied moments. As a result, care should be directed to investigating the weak-axis bending performance of the wall piers when evaluating wall piers subjected to moderate earthquakes.

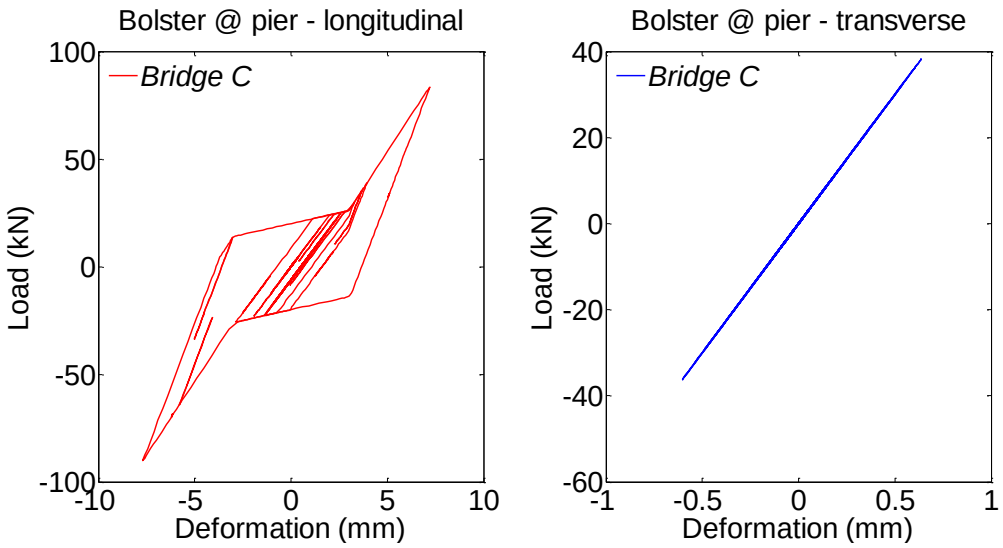

Figure 7.38 Steel bolster bearing response at the pier of *Bridge C* under the bidirectional ground motion pair of bo05 and bo06

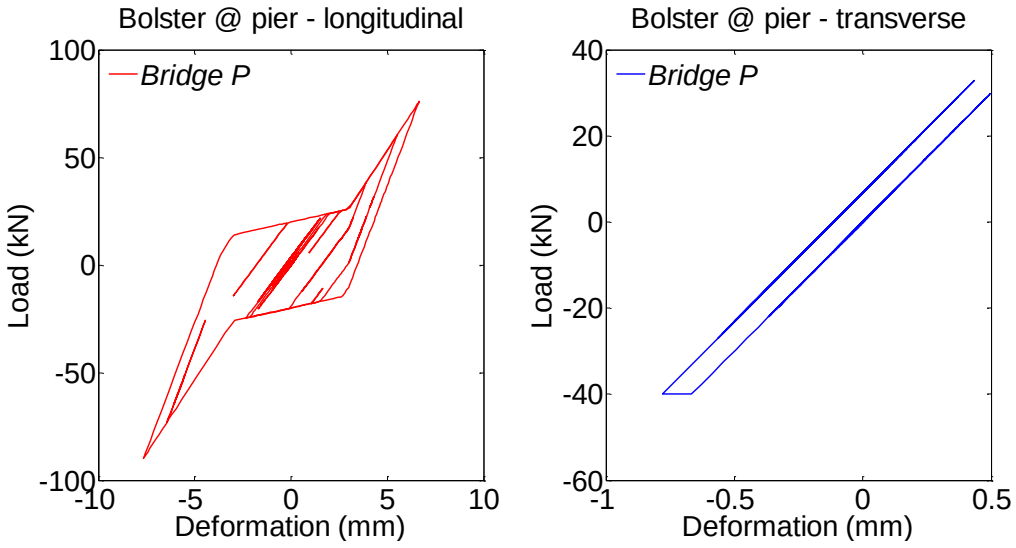

Figure 7.39 Steel bolster bearing response at the pier of *Bridge P* under the bidirectional ground motion pair of bo05 and bo06

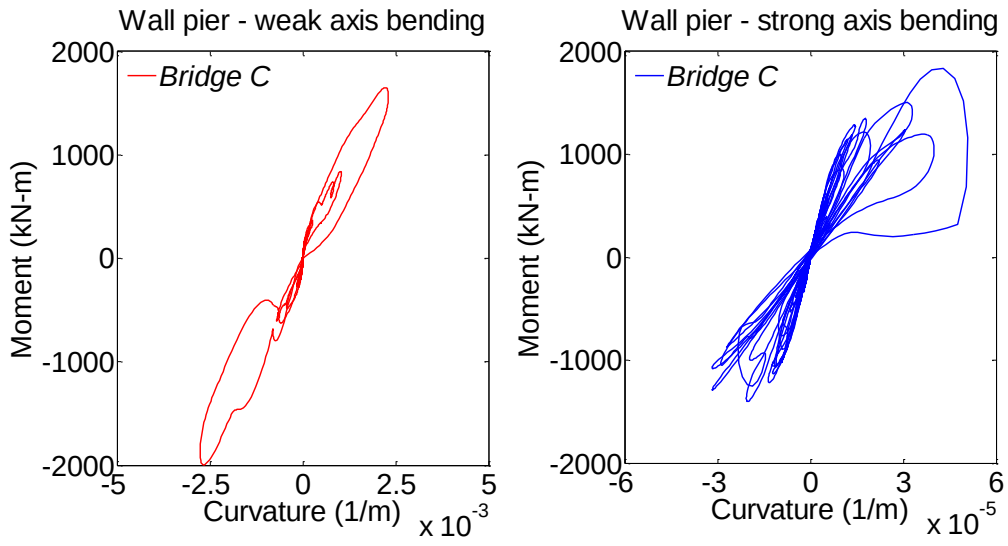

Figure 7.40 The moment-curvature response at the base of the middle wall pier of *Bridge C* under the 10in50 bidirectional ground motion pair of bo05 and bo06

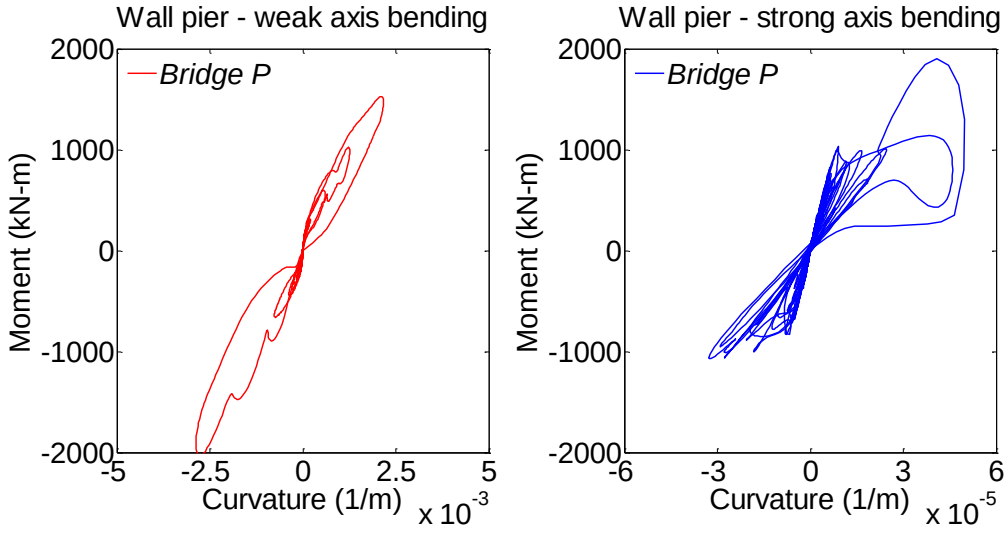

Figure 7.41 The moment-curvature response at the base of the middle wall pier of *Bridge P* under the 10in50 bidirectional ground motion pair of bo05 and bo06

7.7 Seismic Bridge Performance Subjected to 2in50 Ground Motions

The seismic bridge response is discussed in detail for the ground motion pair consisting of the bo35 (longitudinal) and bo36 (transverse) components. The duration of this motion pair is 29.58 seconds with peak ground accelerations of 1.5g and 0.71g for the normal and parallel components, respectively. The peak spectral accelerations are 4.4g at 0.12 seconds and 1.7g at 0.25 seconds for the normal and transverse components, respectively.

7.7.1 Superstructure displacement time histories

Bridge C

The longitudinal and transverse displacement time histories of the superstructure and the two abutments of *Bridge C*, when subjected to the ground motion pair of b035 and bo36, are shown in Figure 7.42. The superstructure undergoes significantly larger displacements than the abutments in the longitudinal direction with a maximum displacement of 80 mm. This displacement level is more than twice the expansion gap length of 38.1 mm indicating severe pounding occurs between the deck and the abutments. As a result of pounding, the abutments undergo large displacements with the maximum deformation reaching 50 mm. The two abutment responses show a 180 degree phase difference due to the fact that pounding only occurs at one side at a time. These observations indicate that significant forces are generated between the abutment backwall and the backfill soil.

In the transverse direction, the deck undergoes larger displacements than the abutments. The superstructure has a maximum transverse displacement of 20 mm, while the maximum abutment displacement is less than 5 mm. Both abutments show an identical response indicating no phase difference between the transverse abutment responses. These observations indicate that the seismic displacement demand of a maximum credible earthquake is greater in the longitudinal direction than in the transverse direction of the bridge with corroded steel rocker bearings.

Bridge P

Figure 7.43 presents the displacement time histories of the superstructure and the abutments for *Bridge P* with no rocker bearing corrosion. The responses observed for *Bridge P* are similar to those of *Bridge C*. The maximum longitudinal displacement experienced by the superstructure is 80 mm, leading to pounding between the deck and abutments. As a result, the abutments also undergo a significant deformation of 50 mm. Over the course of the loading history, multiple pounding events are observed leading to large displacements of the abutments. However, little residual deformation is observed in the abutments compared to the findings for *Bridge C*.

In the transverse direction, the superstructure undergoes a larger response than the abutments. The maximum displacement is 15 mm for the superstructure and roughly 5 mm for the abutments. The small abutment deformation suggests that they remain elastic under the imposed ground motion pair. Overall, the seismic demand of bo35 and bo36 is greater in the longitudinal direction than in the transverse direction for both *Bridge P* and *Bridge C*.

Comparison

Figure 7.44 shows a comparison between the superstructure responses of *Bridge C* and *Bridge P*. In the longitudinal direction, the deck response of the two bridges is nearly identical with respect to the time histories and peak values. Minor differences are observed between 15 and 20 seconds. In the transverse direction, the maximum displacement of *Bridge C* is greater than that of *Bridge P*. Further analyses are needed to look at the force-deformation relationships of the bearings and other bridge components to fully understand the effects that the corroded abutment bearings have on the overall bridge performance.

7.7.2 Substructure displacement time histories

Bridge C

Using the same approach described in Section 7.6.2, the displacement time histories of the three wall piers of *Bridge C* are given in Figure 7.45. For the longitudinal substructure response, an identical response is found for the left and right piers while the middle pier has a larger response. The maximum displacement for the two side piers is 20 mm, which increases to 40 mm for the middle pier. The difference between the pier responses is mainly due to the fact that the bolster bearings on the middle pier can transmit larger forces into the pier than the rocker bearings located on the side piers. On the other hand, the transverse responses of all three wall piers are similar with the middle pier undergoing a slightly larger response than the side piers. The peak responses of all three piers are a little over 1 mm, which leads to only a minor seismic displacement demand placed on the wall piers in the transverse direction.

Bridge P

Figure 7.46 shows the displacement time histories of the wall piers of *Bridge P*. The response of the two side piers is identical, while the middle pier experiences a larger peak response. The maximum displacement for the side piers is 20 mm, which increases to 40 mm for the middle pier. Similar to the observations for *Bridge C*, this difference is due to the bolster bearings at the middle pier having a much larger longitudinal stiffness than the rocker bearings on the side piers. In the transverse direction, the middle pier has a slightly greater response than the side piers that show an identical response. However, the magnitudes of all of the displacement histories are within ±2 mm, indicating a rather insignificant seismic demand.

Comparison

The middle wall pier responses of *Bridge C* and *Bridge P* are used in this comparison as shown in Figure 7.47. The two responses are nearly identical in the longitudinal direction and similar in the transverse direction. A maximum longitudinal displacement of 40 mm is recorded for both bridges. The maximum transverse displacement of both bridges is

less than 2 mm. A larger discrepancy is seen between the transverse bridge responses with *Bridge C* showing a slightly larger response scattered throughout the entire motion duration. These comparisons show that the effect of corroded rocker bearings at the abutment on the substructure response is fairly negligible in terms of wall pier displacements.

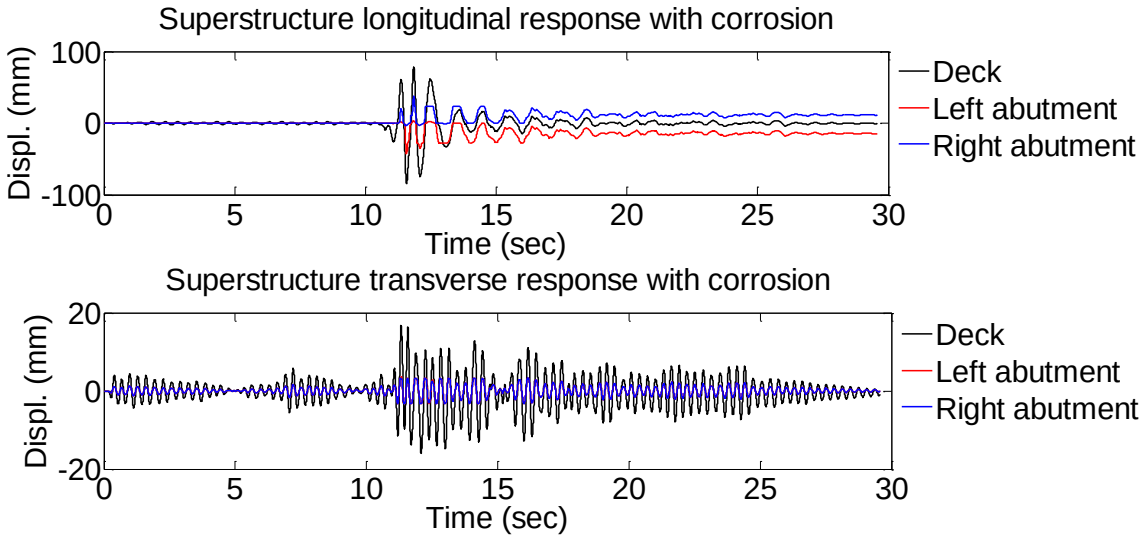

Figure 7.42 Superstructure and abutments displacement time histories of *Bridge C* under bidirectional 2in50 motion pair of bo35 and bo36

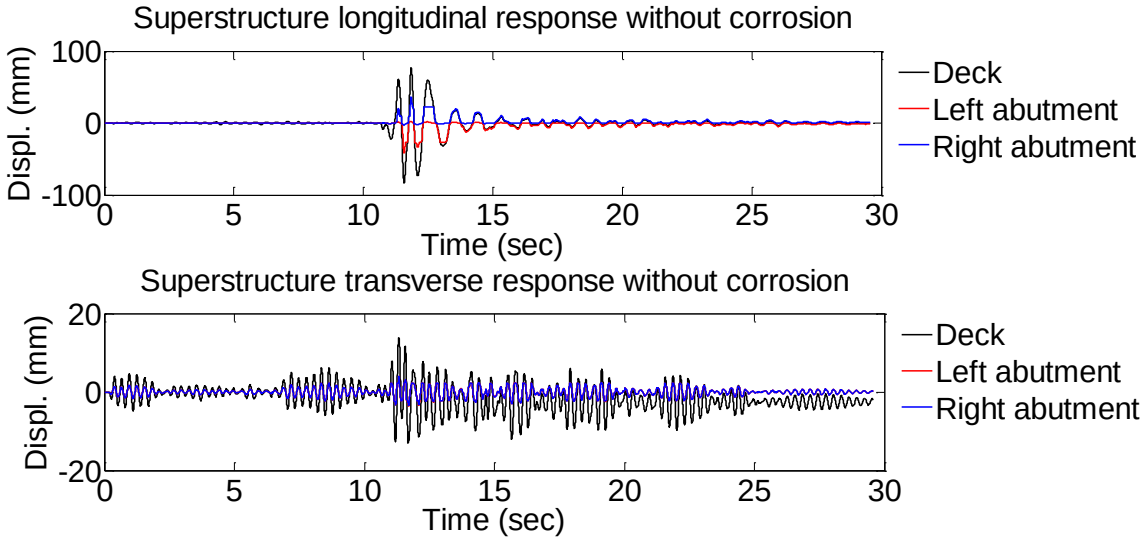

Figure 7.43 Superstructure and abutments displacement time histories of *Bridge P* under bidirectional 2in50 motion pair of bo35 and bo36

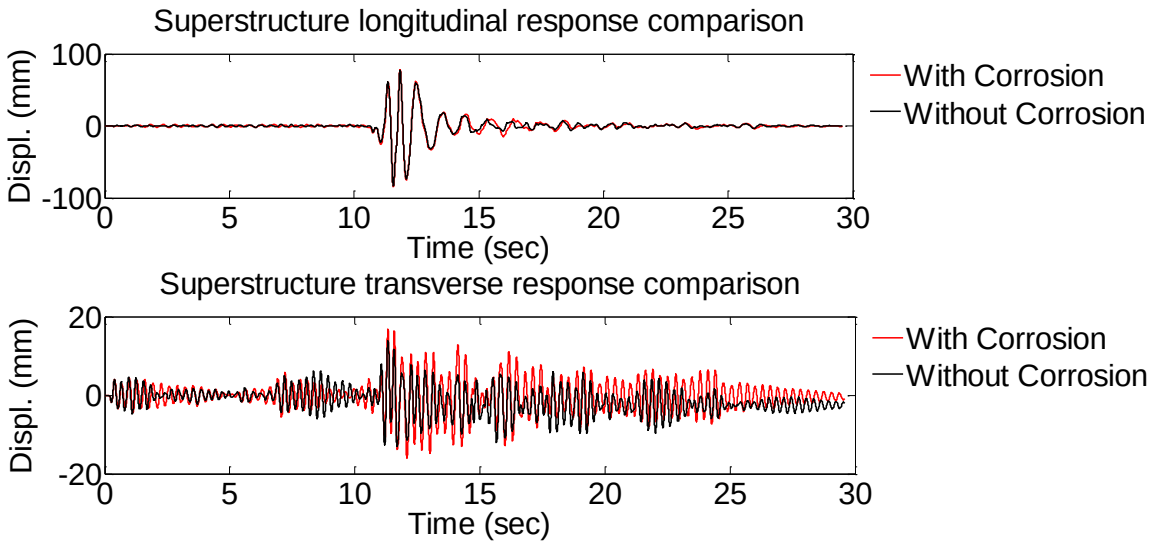

Figure 7.44 Comparison of superstructure displacement time histories under bidirectional 2in50 motion pair of bo35 and bo36 between *Bridge C* and *Bridge P*

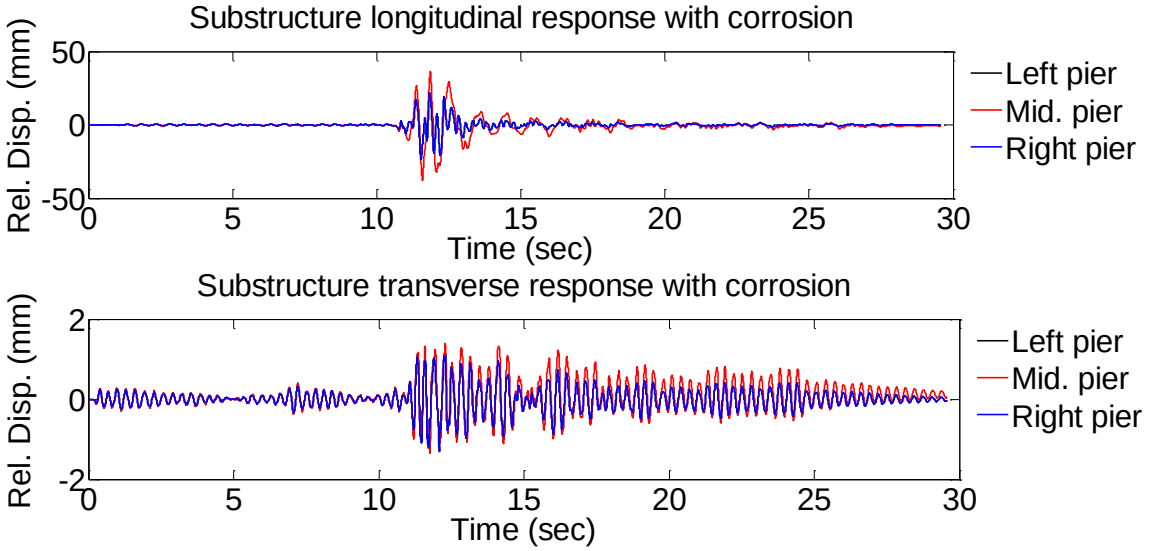

Figure 7.45 Wall pier displacement time histories of *Bridge C* under the bidirectional 2in50 motion pair of bo35 and bo36

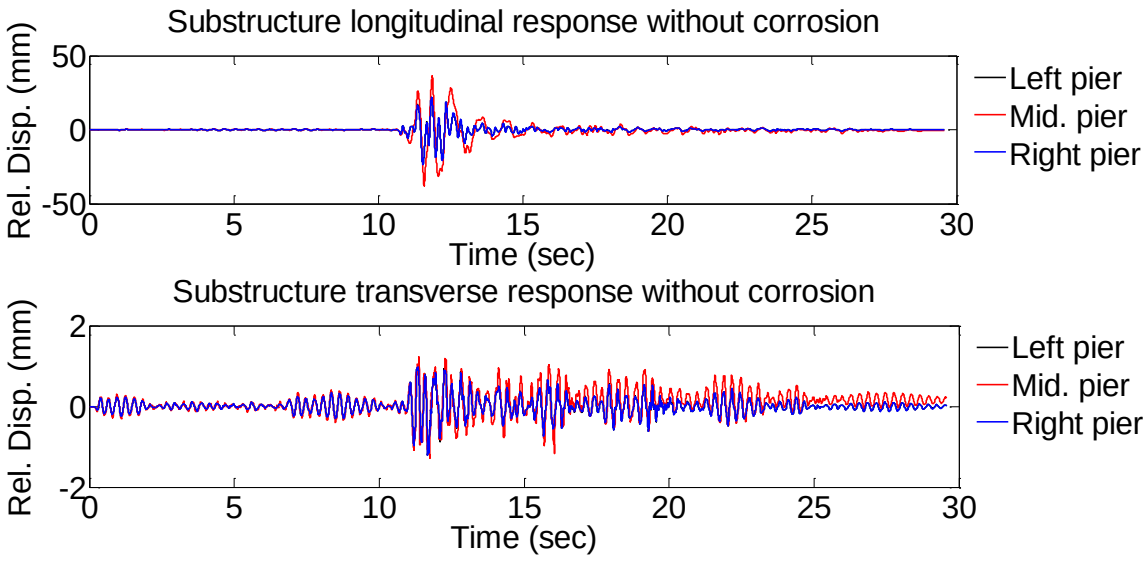

Figure 7.46 Wall pier displacement time histories of *Bridge P* under the bidirectional 2in50 motion pair of bo35 and bo36

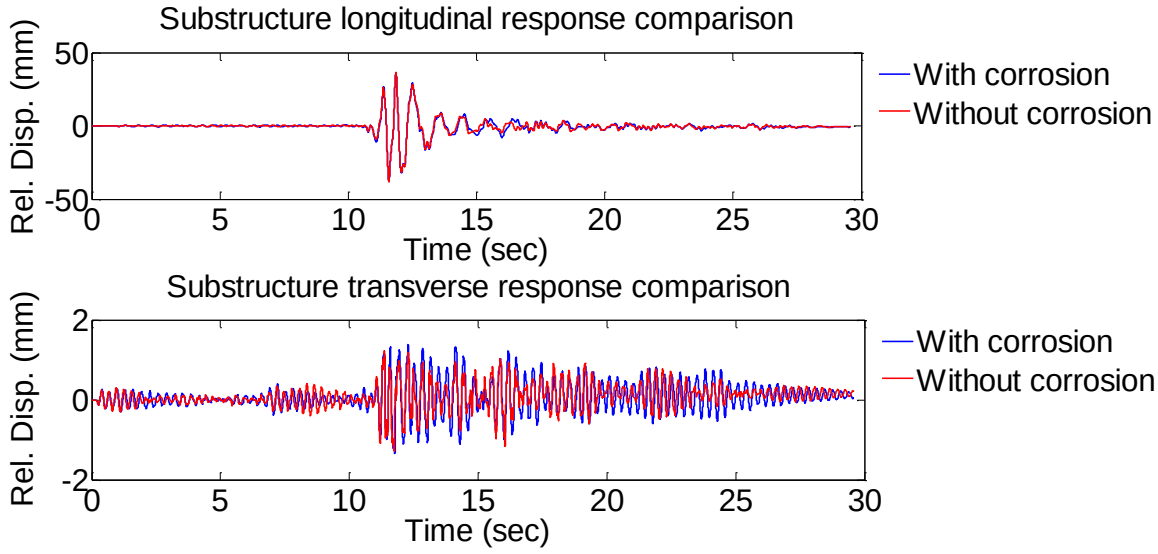

Figure 7.47 Comparison of middle wall pier displacement time histories under the bidirectional 2in50 motion pair of bo35 and bo36 between *Bridge C* and *Bridge P*

7.7.3 Abutment-soil interaction

Figure 7.48 and Figure 7.49 show the abutment soil interaction responses for *Bridge C* and *Bridge P*, respectively. These figures suggest significant inelastic deformation of the passive backfill occurs at both abutments due to longitudinal displacements. As discussed previously, multiple deck-abutment impact incidents occur over the duration of the ground motion. These impact incidents generate significant forces leading to a passive abutment soil response. The passive action is clear from the fact that the maximum resistance developed is around 1300 kN at a deformation of nearly 45 mm. This is a significant force level considering that the total passive abutment soil capacity per an abutment node is 1395 kN, indicating the high magnitude of the generated force and the significance of the soil inelastic deformation. However, the longitudinal active abutment soil interaction response still remains elastic for both bridge systems with a maximum active force of roughly 70 kN at a roughly 3 mm deformation. This relatively small force is due to the fact that the steel rocker bearings, whether corroded or pristine, have a fairly small longitudinal stiffness that limits the load being transferred via the rocker bearing to the abutment.

The responses of the bridges in the transverse direction are also similar. Both bridge abutments undergo only linear-elastic deformations in the transverse direction with similar maximum deformations that are less than 4 mm and maximum forces that are less than 100 kN. These findings suggest that no inelastic deformation of the abutment piles occurs due to transverse displacement. Overall, *Bridge P* experiences a slightly greater deformation and resistance level. This slight difference is due to the transverse stiffness variation between the corroded and uncorroded rocker bearings. The transverse active bridge response is slightly larger than the longitudinal active bridge response because the rocker bearings possess greater stiffness and load carrying capacity in the transverse direction. These observations indicate that a larger seismic demand is generated at the abutment in the longitudinal direction due to impacts between the deck and the abutments. The effect of the corroded rocker bearings at the abutment on the overall abutment-soil performance is minor.

7.7.4 Impact response due to pounding

Figure 7.50 shows the impact responses for *Bridge C* and *Bridge P*, which are nearly identical in terms of deformation and resistance. The maximum impact displacement is around 39 mm for both bridges indicating a penetration depth of roughly 1 mm. However, this penetration depth has not reached the yield depth of the impact model, thus an elastic impact response is observed. The associated impact force at this penetration depth is nearly 1300 kN, which is further transferred to the backfill leading to the observed large passive soil resistance in the abutment-soil interaction response. Based on the similar result for both bridges, it is clear that the effect of steel rocker bearing corrosion on pounding is negligible even under large seismic demands.

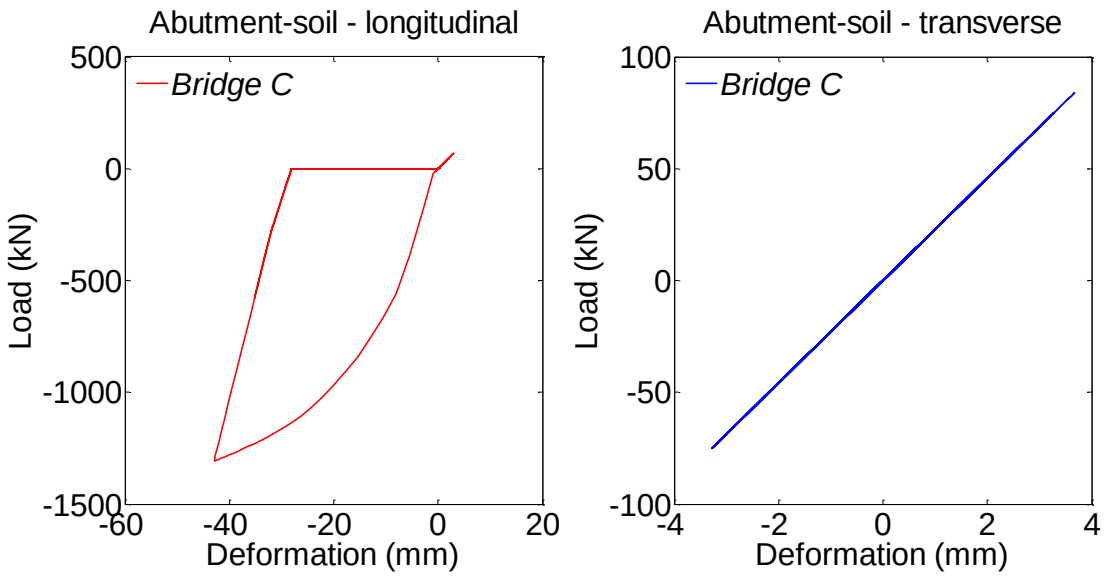

Figure 7.48 Abutment soil interaction response of *Bridge C* under the bidirectional 2in50 ground motion pair of bo05 and bo06

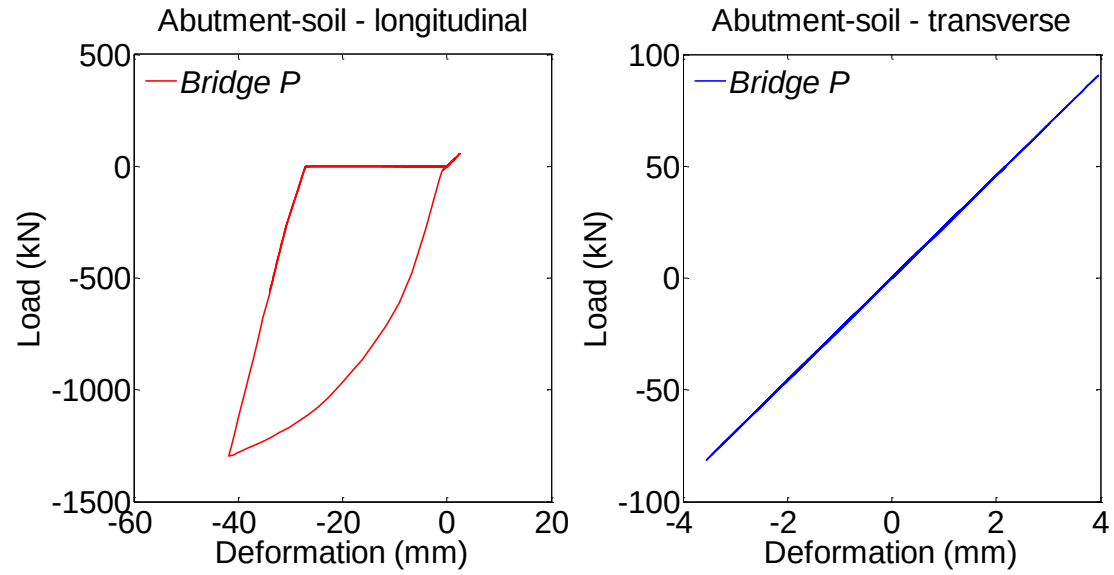

Figure 7.49 Abutment soil interaction response of *Bridge P* under the bidirectional 2in50 ground motion pair of bo05 and bo06

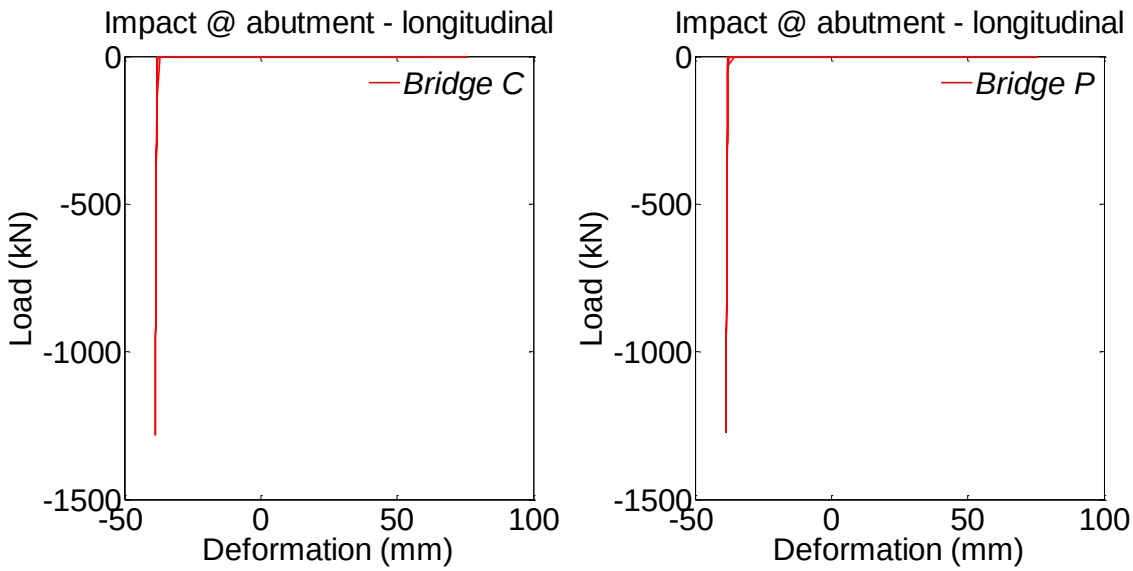

Figure 7.50 Impact responses due to pounding between the deck and abutments for both *Bridge C* and *Bridge P* under the bidirectional 2in50 ground motion pair of bo35 and bo36

7.7.5 Steel rocker bearing response at the abutment

Figure 7.51 shows the response of a corroded rocker bearing for *Bridge C* under a 2in50 ground motion excitation. The maximum longitudinal displacements are 75 mm and 40 mm in the positive and negative directions, respectively, and the corresponding resistances are approximately 72 kN and 24 kN. Rocking occurs under positive displacement due to the magnitude of the motion pair and the flexibility of the bearings in the longitudinal direction. The large disparity between the positive and negative response is due to the occurrence of pounding between the deck and the abutment which limits the displacement of the rocker bearing in the negative loading direction. The 75 mm longitudinal displacement will likely cause toppling of the rocker body based on the previous experimental findings from Chapter 6. The transverse response of the rocker bearing shows maximum displacements of approximately 8 mm and 10 mm in the positive and negative directions, respectively. The deformation mode is predominantly sliding with a constant resistance of 75 kN. This observation indicates that the rocker bearing is capable of accommodating the transverse seismic demand.

Figure 7.52 presents the response of the uncorroded rocker bearings at the abutment of *Bridge P*. The maximum longitudinal positive and negative displacements are 75 mm and 40 mm, respectively. These values are almost identical to those seen for *Bridge C*. The maximum forces associated with these displacements are 60 kN and 20 kN. Rocking behavior is more severe due to positive displacements rather than negative displacements due to that the negative rocker displacement being confined by the expansion gap length. The observed 75 mm positive displacement is fairly large for a steel rocker bearing and will likely lead to toppling of the rocker body. The transverse response of the steel rocker bearing consists of both sliding and rocking deformation modes. The maximum displacements are roughly 8 mm in both directions with a maximum resistance of 100 kN. These values are all significantly less than the transverse capacity of the rocker bearing.

Comparison of the two bearing responses for *Bridge C* and *Bridge P* shows that both sets of bearings undergo similar displacements and forces under the same ground motion pair. The disparity in their hysteresis curves is due to the variation in bearing stiffness,

deformation mode, and capacity caused by corrosion. Both bearings show a strong toppling tendency in the longitudinal direction due to the large displacements induced by the given motions. The transverse performance of the corroded rocker bearing is on par with that of the uncorroded rocker bearing, both demonstrating a potential to withstand a 2in50 seismic event. These findings further show that the abutment rocker bearings, whether corroded or not, may be more susceptible to seismic loads in the longitudinal direction.

7.7.6 Steel rocker bearing response at the pier

Figure 7.53 shows the response of an uncorroded steel rocker bearing at the pier location of *Bridge C* under the ground motion pair, bo35 and bo36. The maximum longitudinal displacements are 75 mm and 100 mm in the positive and negative directions, respectively, while the associated longitudinal resistances are 60 kN and 80 kN. These maximum longitudinal displacements exceed the bearing capacity suggesting a potential for the pier rocker bearing to topple in the longitudinal direction. An unsymmetric response is observed for the rocker longitudinal behavior under the given ground motions with severe rocking observed in both the positive and negative directions. The asymmetry is largely associated with the significant inelastic deformation of the backfill since this deformation leads to excessive superstructure displacement in the negative direction which places further displacement demand on the negative response of the pier rocker bearing. The transverse response of the pier rocker bearing shows maximum displacements of roughly 4 mm and 5 mm for the positive and negative responses, respectively. The transverse response is mainly dominated by rigid sliding with a constant resistance of 50 kN. Minor rocking is initiated in the negative response when the displacement approaches 5 mm.

Figure 7.54 shows the response of the pier rocker bearing for *Bridge P* under the ground motion pair bo35 and bo36. The maximum longitudinal displacements are 72 mm and 100 mm in the positive and negative directions, respectively, and the maximum resistance for the positive and negative responses is 54 kN and 80 kN. The maximum negative displacement of 100 mm is fairly large suggesting instability of the rocker bearing in the

longitudinal direction. The asymmetry between the positive and negative responses is attributed to the same reason as discussed for *Bridge C*. The transverse response of the rocker bearing is predominantly rigid sliding with a constant resistance of 50 kN. The maximum displacements are 3mm and 4 mm in the positive and negative directions, respectively. These displacements are below the transverse capacity of the rocker bearing, indicating the pier rocker bearing performs well under a 2in50 seismic event in the transverse direction.

Comparing the two bearing responses from *Bridge C* and *Bridge P* shows a strong similarity in terms of maximum displacement and resistance, which indicates that the corroded abutment rocker bearings have little effect on the pier bearing response. Additionally, the longitudinal toppling due to excessive displacement is identified as a likely failure mode of the pier rocker bearings under 2in50 bidirectional ground motion excitations.

7.7.7 Steel bolster bearing response at the pier

Figure 7.55 shows the steel bolster bearing response obtained for *Bridge C* under the bo35 and bo36 ground motion pair. The bolster bearing response suggests that rocking and prying are the dominant deformation modes in the longitudinal direction under a maximum credible earthquake. The maximum displacements associated with the longitudinal response are approximately 15 mm for both the positive and negative responses. Rapid increase in bearing resistance is seen in the positive and negative directions with the maximum values being 180 kN and 170 kN, respectively. The maximum positive force of 180 kN corresponds to the capacity of the bolster bearing indicating that the anchor bolts have yielded due to prying of the bolster bearing. However, no further damage would be expected, such as bolt fracture, since no strength degradation is observed in the bearing response. In the transverse direction, the main deformation modes of the bolster bearing based on the response are sliding and prying. The maximum transverse displacements are relatively small and less than 4 mm leading to resistances below 100 kN. These observations suggest that the bolster bearing can

survive a 2in50 seismic event without failure in either the longitudinal or transverse direction. However, the anchor bolts would be expected to see some damage.

Figure 7.56 shows the steel bolster bearing response of *Bridge P* under the bo35 and bo36 ground motion pair. Similar to the response of *Bridge C*, significant rocking and prying is observed in the longitudinal response induced by the 2in50 motion pair. The maximum displacements are approximately 14 mm and 13 mm in the positive and negative directions, respectively. The maximum resistance associated with these displacements is 178 kN and 160 kN. These values are slightly less than the ultimate longitudinal strength of the bolster bearing. No strength degradation is observed suggesting that the anchor bolts do not fully yield. In the transverse direction, the bolster bearing response is dominated by rigid sliding and at larger deformation levels, rocking and prying also occur. Due to the rocking and prying, the bearing resistance quickly increases to over 100 kN in the positive direction and to nearly 90 kN in the negative direction. These transverse force and deformation demands can be easily accommodated by the bearing. From these observations, it is clear that the bolster bearing of *Bridge P* performs well under a potential 2in50 seismic event.

In comparison, the steel bolster bearing response for *Bridge C* and *Bridge P* exhibit a strong resemblance with respect to initial deformation modes and expected maximum displacements and resistances. The effect of the corroded abutment rocker bearings is minimal in terms of the seismic performance and response of the pier bolster bearings under a 2in50 seismic event. Additionally, the seismic demand is larger in the longitudinal direction than in the transverse direction of the bolster bearing for both bridges, suggesting a longitudinal failure of the bolster bearing is more likely during a maximum credible earthquake. However, for this specific motion pair of bo35 and bo36, the bolster bearing in both bridges performs adequately.

7.7.8 Wall pier base moment-curvature response

Figure 7.57 shows the moment-curvature response of the middle wall pier for *Bridge C* recorded at the base of the wall pier. The maximum weak-axis bending moments generated during the seismic excitation are roughly 3800 kN-m for both the positive and

negative bending responses, which is much greater than the weak-axis bending capacity (2065 kN-mm) of the wall pier. This observation suggests extensive damage will be incurred by the wall pier at its base under a 2in50 seismic event. Meanwhile, the maximum strong-axis bending moments are roughly 2300 kN-m and 2900 kN-m for the positive and negative bending responses, respectively. These seismic bending moments are significantly lower than the wall pier moment capacity about the strong axis, suggesting the wall pier performs well in bending about the strong axis even during a 2in50 seismic event.

Figure 7.58 presents the moment-curvature responses for *Bridge P* at the base of the wall pier. The maximum weak-axis bending moments are nearly 3800 kN-m for both the positive and negative bending responses. This moment demand is much larger than the wall pier weak-axis bending capacity, indicating severe plastic deformation in the wall pier. Additionally, the maximum strong-axis bending moments are approximately 2200 kN-m and 2800 kN-m for the positive and negative bending responses, respectively, which are insignificant compared with the strong-axis bending moment capacity of the wall pier. The performance of the wall pier for *Bridge P* is similar to that observed for *Bridge C*, which suggests extensive damage is expected in the wall pier due to weak-axis bending moments incurred by a 2in50 seismic event.

The wall pier moment-curvature responses of both bridges are similar in regards to the maximum bending moments in each direction. This observation suggests that the effect of the corroded abutment rocker bearings is minimal on the overall wall pier seismic performance under 2in50 bidirectional seismic excitations. The wall pier is shown to be more vulnerable to seismic moments about the weak bending axis than about the strong bending axis. Extensive plastic deformation associated with the wall pier plastic hinge region is expected under a 2in50 seismic excitation. However, the strong axis bending performance of the wall pier is not a concern based on the simulation results.

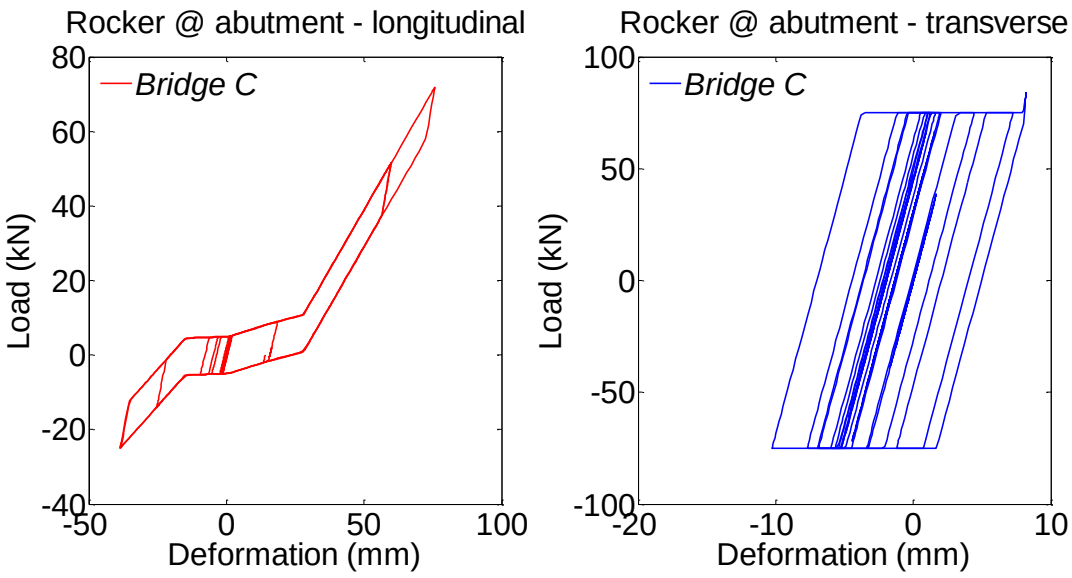

Figure 7.51 Steel rocker bearing response at the abutment of *Bridge C* under the bidirectional 2in50 ground motion pair of bo35 and bo36

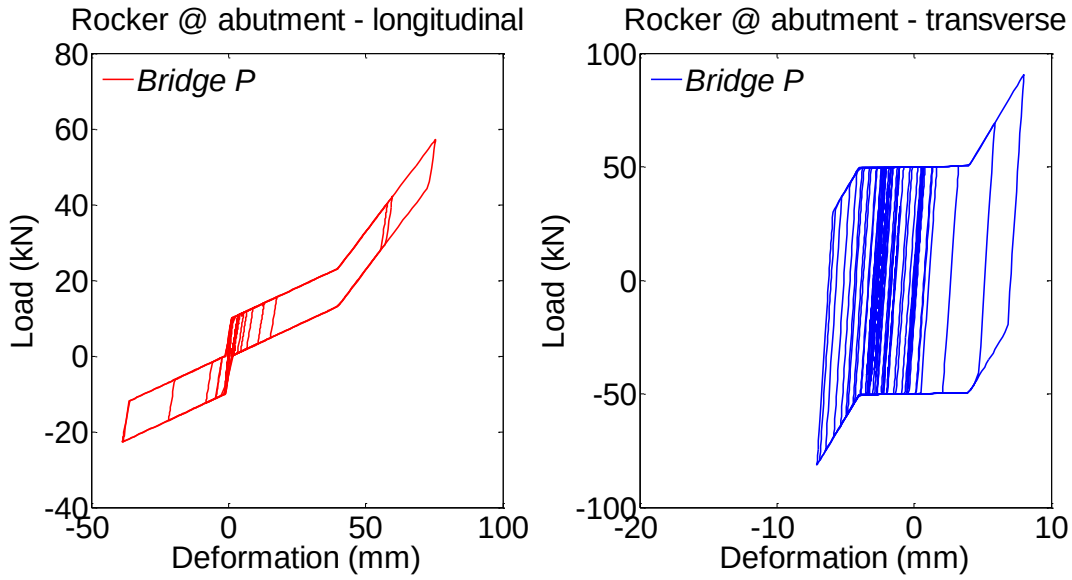

Figure 7.52 Steel rocker bearing response at the abutment of *Bridge P* under the bidirectional 2in50 ground motion pair of bo35 and bo36

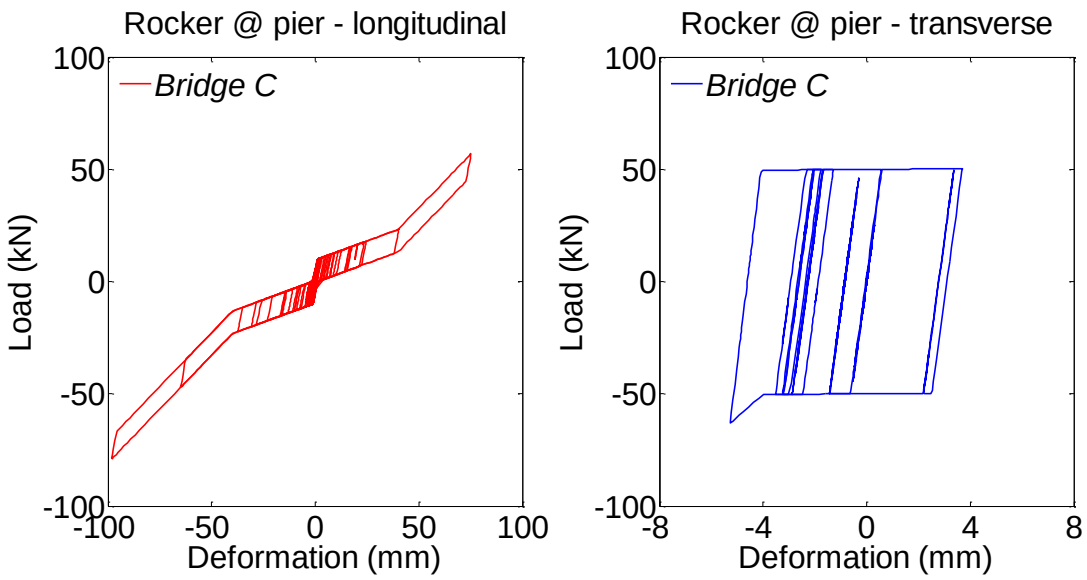

Figure 7.53 Steel rocker bearing response at the pier of *Bridge C* under the bidirectional 2in50 ground motion pair of bo35 and bo36

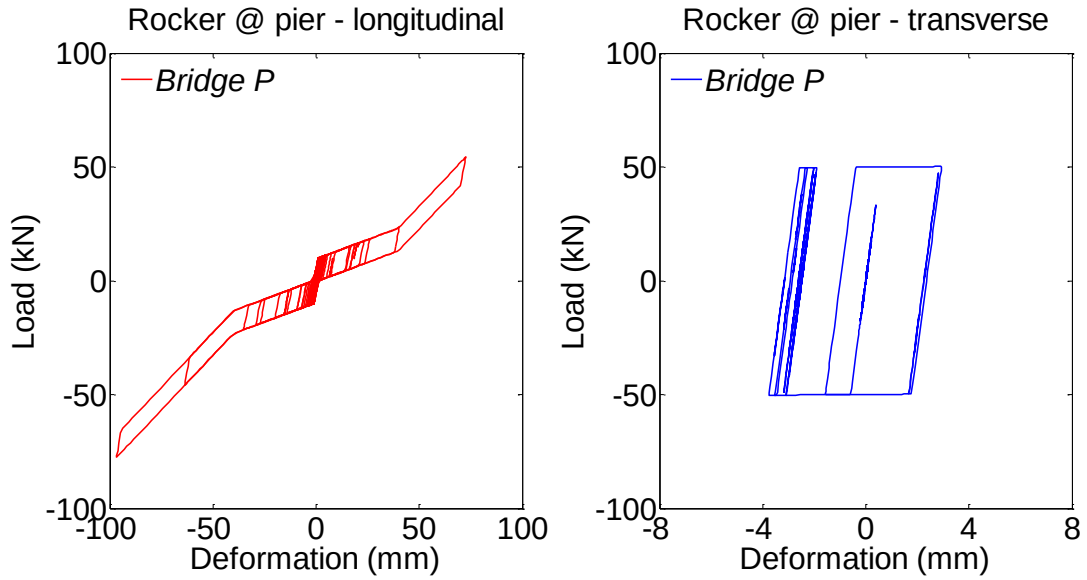

Figure 7.54 Steel rocker bearing response at the pier of *Bridge P* under the bidirectional 2in50 ground motion pair of bo35 and bo36

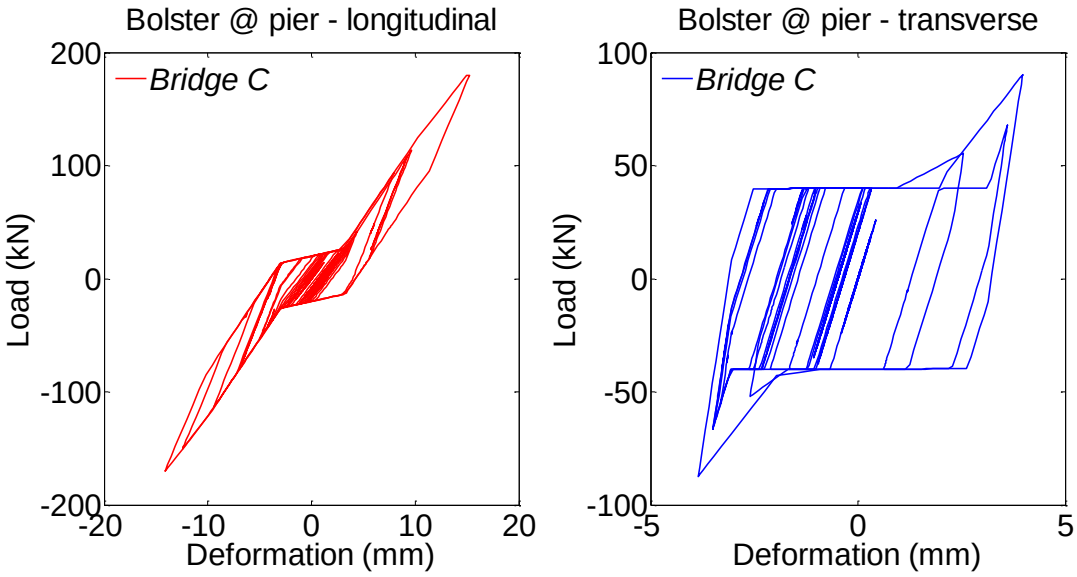

Figure 7.55 Steel bolster bearing response at the pier of *Bridge C* under the bidirectional 2in50 ground motion pair of bo35 and bo36

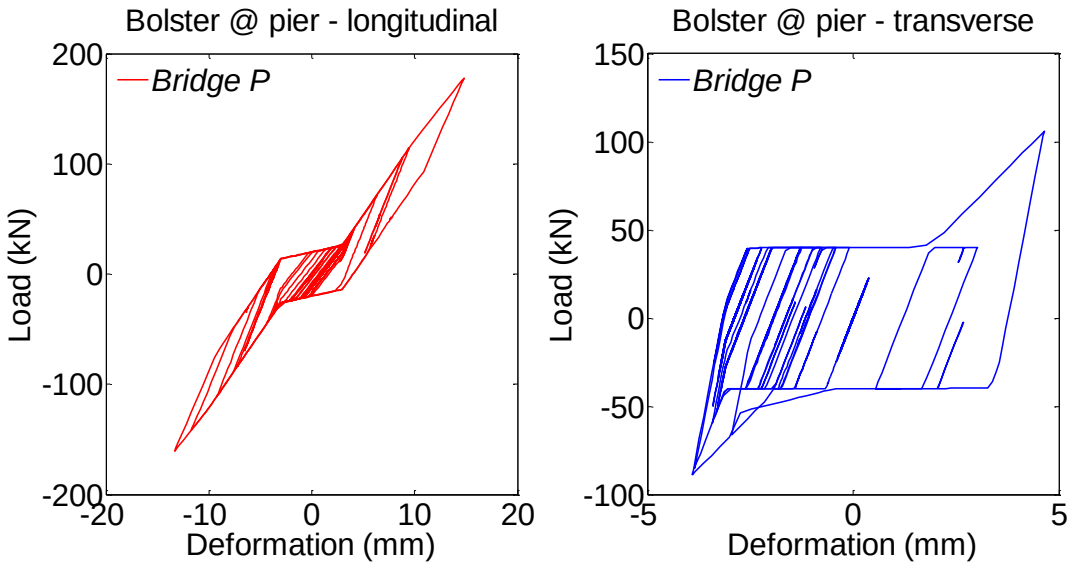

Figure 7.56 Steel bolster bearing response at the pier of *Bridge P* under the bidirectional 2in50 ground motion pair of bo35 and bo36

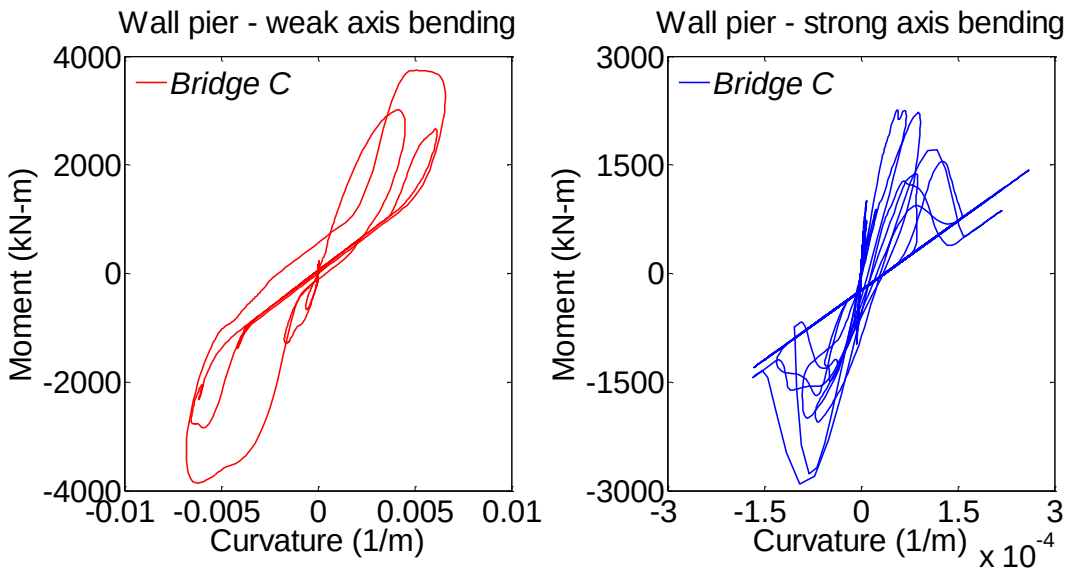

Figure 7.57 The moment-curvature response at the base of the middle wall pier of *Bridge C* under the 2in50 bidirectional ground motion pair of bo35 and bo36

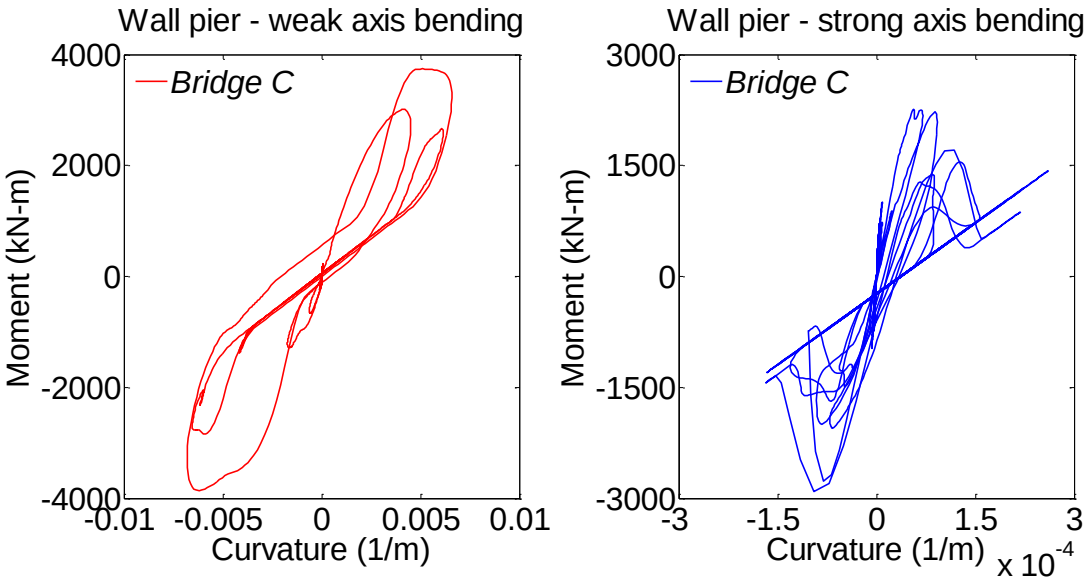

Figure 7.58 The moment-curvature response at the base of the middle wall pier of *Bridge P* under the 2in50 bidirectional ground motion pair of bo35 and bo36

7.8 Distribution of Seismic Response of Bridge Components

The distribution of the response of different bridge components under a given ground motion suite (i.e. 10in50, 2in50) is considered for the absolute peak response (i.e. maximum deformation, force, or moment) generated under each seismic excitation pair in the considered ground motion suite. Specifically, the abutment-soil interaction resistance, the impact force, the abutment steel rocker bearing displacements, the pier steel rocker bearing displacement, the pier steel bolster bearing displacement, and the middle wall pier maximum moment are aggregated and discussed. The distribution of each response for a given ground motion suite is expressed using a boxplot. The top edge of the box represents the 75^{th} percentile response and the bottom edge of the box corresponds to the 25^{th} percentile response, while the red band inside the box shows the median response. The whiskers extend above or below the box to include the furthest responses that are less than 1.5 times the height of the box from either the top or bottom box edge. Responses that are beyond this range are singled out and represented by a red cross and considered as outliers. Due to this definition, the box itself contains 50% of the peak responses for a specific suite of ground motions.

7.8.1 Abutment-soil resistance

Figure 7.59 shows the longitudinal abutment-soil resistance response for *Bridge C* and *Bridge P* under both the 10in50 and the 2in50 ground motions. Under the 10in50 ground motions, the abutment-soil resistance for *Bridge C* has a median value of 8 kN and 50% of the peak responses located between 7 kN and 10 kN. *Bridge P* has a median of 14 kN and 50% of the peak responses located between 11 kN and 16 kN with an outlier response of nearly 150 kN. This outlier is the only response under the 10in50 motions that saw pounding. The comparison between these distributions shows that *Bridge P* with uncorroded steel bridge bearings develops a slightly larger abutment-soil resistance. However, the difference between the two distributions is not significant because under most of the 10in50 motions, no pounding has initiated and as a result only insignificant rocker bearing forces are transferred to the abutment. These findings further show that no

major damage will be incurred by the abutment backfill when subjected to ground motions with a return period of 475 years.

Under the 2in50 ground motions, much larger abutment-soil force distributions are observed for both bridges due to pounding. *Bridge C* shows a 23 kN median value, a 15 kN 25th percentile value, and a 637 kN 75th percentile value while *Bridge P* has a 21 kN median value, a 19 kN 25th percentile value, and a 612 kN 75th percentile value. Both bridges have an extreme peak resistance of around 1300 kN. The plots suggest the performance of the two bridges with respect to the abutment are very similar indicating that the corroded abutment rocker bearings have little influence on the overall longitudinal abutment-soil response. This result is due to the fact that these rocker bearings, whether corroded or not, provide little longitudinal stiffness and pounding between the deck and abutment dictates the abutment longitudinal deformation and the associated abutment-soil required resistance. The 2in50 ground motion results further indicate that significant plastic deformations can occur in the abutment backfill soil leading to increased likelihood of abutment failures when subjected to ground motions with a return period of 2475 years.

The transverse abutment resistance for both bridges are given in Figure 7.60. Under the 10in50 ground motion suite, the transverse abutment resistance of *Bridge C* has a 75 kN median value and 50% of the responses are located between 33 kN and 75 kN. In comparison, the abutment resistance of *Bridge P* has a 50 kN median value and half of the responses contained between 42 kN and 79 kN. *Bridge C* and *Bridge P* show a relatively large variation in the median response. However, half of the responses for both bridges are confined to a similar range roughly between 30 kN and 80 kN. These observations show that the effect of the corroded rocker bearings on the transverse abutment required resistance is rather limited. Further, since the abutment rocker bearings are the only load transfer mechanism between the superstructure and the abutments in the transverse direction, insignificant forces will be generated in the transverse direction due to the relatively low transverse stiffness and load resistance of the abutment rocker bearings.

Under the 2in50 ground motion suite, larger response distributions are shown for both bridges than those under the 10in50 suite. The abutment resistance of *Bridge C* shows a median abutment force of 80 kN with a 73 kN 25th percentile value and 198 kN 75th percentile value, while the abutment resistance of *Bridge P* has a median of 73 kN value with a 52 kN 25th percentile value and 197 kN 75th percentile value. The 75th percentile values exceed the yield force (174 kN) of the transverse abutment model. The similarity between the abutment resistance of the two bridges under the 2in50 suite of motions further confirms that the corroded abutment rocker bearings have limited influence on the overall required transverse abutment resistance. Additionally, the 2in50 ground motion suite does have the potential to cause yielding of the abutment piles that yield at 174 kN. Yet, none of the abutment resistances reach the ultimate transverse abutment capacity of 249 kN for either bridge.

7.8.2 Impact response distributions

The developed impact forces due to longitudinal pounding between the deck and the abutments for *Bridge C* and *Bridge P* are shown in Figure 7.61. Under the 10in50 ground motion suite, the superstructure displacements for *Bridge C* are all accommodated by the expansion gap length (38.1 mm) resulting in no pounding. However, a single pounding incident for *Bridge P* occurs, which results in a minor impact force of roughly 120 kN. Overall, the 10in50 ground motions do not generate a seismic demand on the superstructure that causes pounding.

Under the 2in50 ground motion suite, extensive pounding is observed in both bridges. While the median impact force for both bridges is 0 kN, a 612 kN 75th percentile value is observed for *Bridge C* and a 589 kN 75th percentile value for *Bridge P*. Both bridges also have an extreme pounding incident where the impact force reaches 1300 kN. These observations suggest that each bridge experiences pounding under half of the ground motion pairs in the 2in50 suite. Pounding can cause local damage to the deck and the abutments and further overload the abutment backfill leading to potential abutment failure as discussed in the previous section. In conclusion, the 2in50 ground motions can

generate extensive pounding between the deck and the abutments regardless of whether the abutment rocker bearings are corroded.

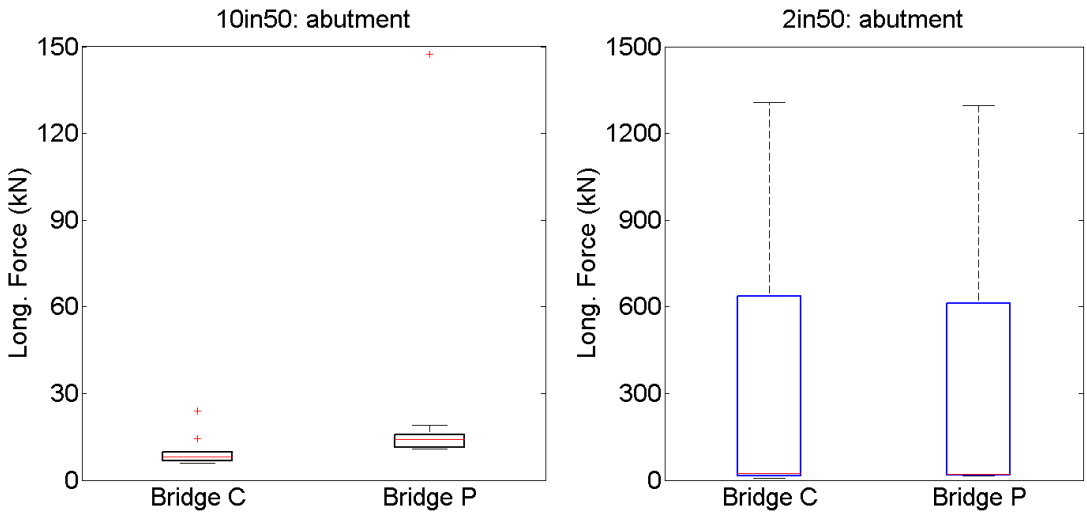

Figure 7.59 Longitudinal abutment-soil force response distributions for *Bridge C* and *Bridge P* under both the 10in50 and 2in50 ground motions

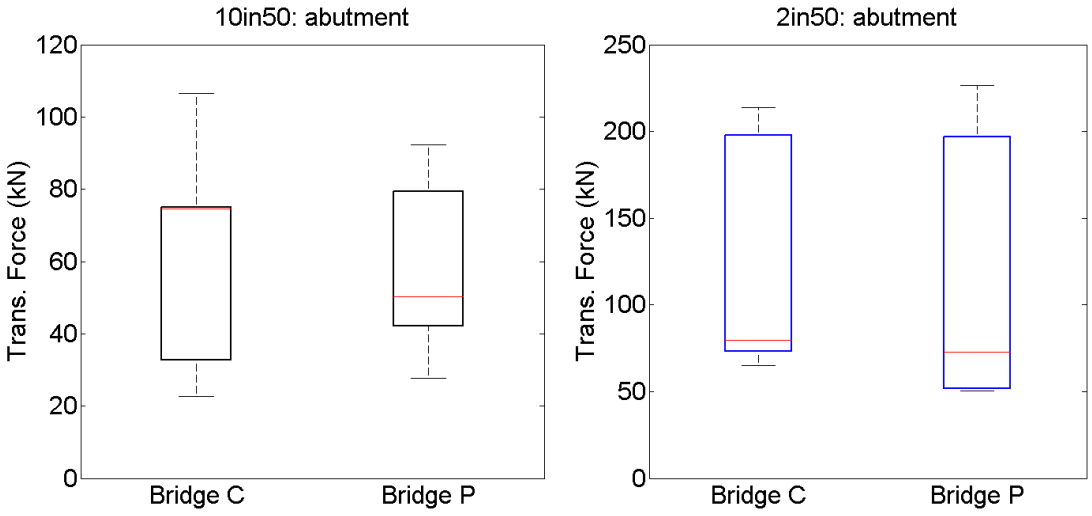

Figure 7.60 Transverse abutment-soil force response distributions for *Bridge C* and *Bridge P* under both the 10in50 and 2in50 ground motions

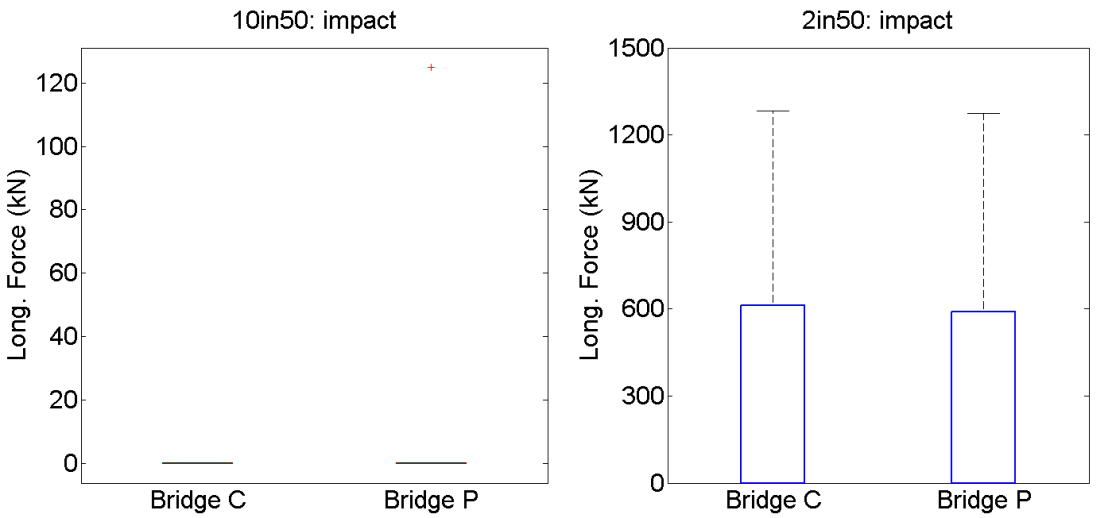

Figure 7.61 Longitudinal impact force response distributions for *Bridge C* and *Bridge P* under both the 10in50 and 2in50 ground motions

7.8.3 Abutment rocker bearing response distributions

Figure 7.62 shows the maximum longitudinal displacement of the abutment rocker bearing for *Bridge C* and *Bridge P*. Under the 10in50 ground motions, the maximum longitudinal displacement of the abutment rocker bearing for *Bridge C* has a median value of 16 mm, a 25th percentile value of 8 mm, and a 75th percentile value of 22 mm, while for *Bridge P*, the deformation distribution shows a 13 mm median value, a 5 mm 25th percentile value, and an 18 mm 75th percentile value. A comparison of the two bridge's responses shows that the uncorroded rocker bearings of *Bridge P* undergo slightly smaller displacements than the corroded rocker bearings of *Bridge C*. This change in longitudinal displacement for the two bridges can be attributed to the fact that the corroded rocker bearing is more flexible than the uncorroded one. The maximum responses of the two rocker bearing distributions are 37 mm and 38 mm, respectively, both of which are lower than their longitudinal displacement capacities. This observation indicates that the abutment rocker bearing, either corroded or pristine, can perform well in the longitudinal direction without toppling under 10in50 ground motions.

Under the 2in50 ground motions, the rocker bearing longitudinal displacements for both bridges are nearly identical. The longitudinal displacements in *Bridge C* show a 36 mm median value and 50% of the responses between 30 mm and 53 mm, while for *Bridge P* a 34 mm median value is observed with 50% of the responses between 26 mm and 52 mm. Both bridges show a maximum rocker displacement of roughly 75 mm, exceeding the displacement capacity of the rocker bearings. These findings suggest that under the 2in50 ground motions, the response difference between the corroded and uncorroded rocker bearings is insignificant, but toppling of the rocker bearing is expected due to excessive seismic displacement demands.

The transverse displacements of the abutment rocker bearing for both bridges are given in Figure 7.63. Under the 10in50 ground motions, the corroded abutment rocker bearing displacements show a median value of 3 mm with 50% of the responses between 1 mm and 8 mm, while the uncorroded abutment rocker bearing transverse displacements have a 2.5 mm median value and 50% of the responses between 0.5 mm and 7 mm. Overall,

Bridge P shows smaller transverse displacements than *Bridge C*. The maximum transverse responses for the corroded and uncorroded rocker bearings are 12 mm and 8 mm, respectively, both lower than their transverse deformation capacities. This finding indicates that whether corroded or not, the abutment rocker bearing can survive ground motions with a 475 year return period. Further, the corrosion effect on the transverse rocker bearing response at the abutment is limited.

Under the 2in50 ground motions, the corroded rocker bearing shows transverse displacements with a larger dispersion than the uncorroded rocker bearing. The corroded rocker bearing's transverse displacements have a median value of 8 mm, a 25^{th} percentile value of 3 mm, and a 75^{th} percentile value of 19 mm, while the uncorroded rocker bearing's transverse displacements have a 6 mm median value, a 4 mm 25^{th} percentile value, and a 15 mm 75^{th} percentile value. The maximum responses of the corroded and uncorroded rocker bearings are 21 mm and 18 mm, respectively, both lower than the bearing transverse displacement capacity. These observations show that under the 2in50 ground motions, corrosion of the rocker bearing results in a slight difference in the bearing transverse displacement response. However, the transverse seismic demands from the 2in50 ground motions can still be accommodated by either the corroded or uncorroded rocker bearings.

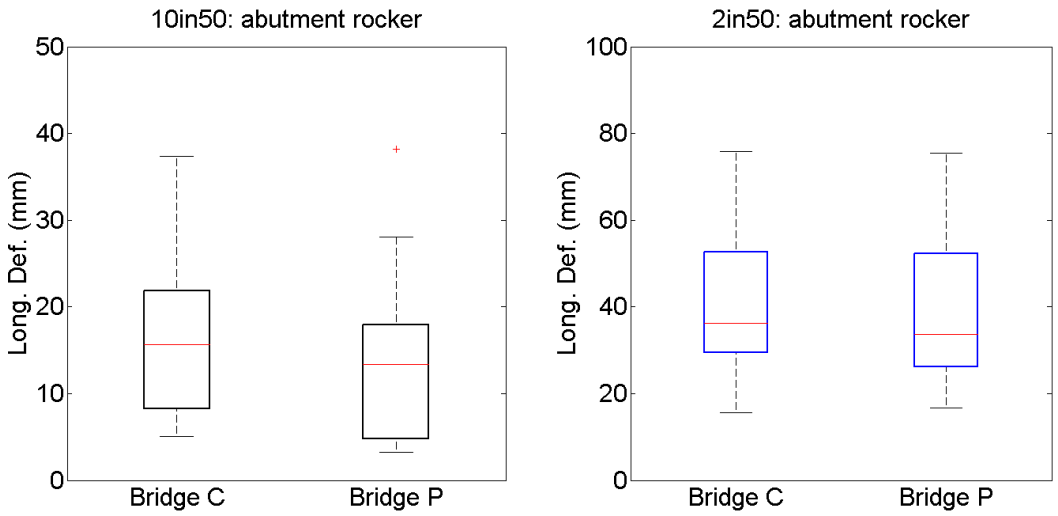

Figure 7.62 Longitudinal abutment rocker bearing deformation response distributions for *Bridge C* and *Bridge P* under both the 10in50 and 2in50 ground motions

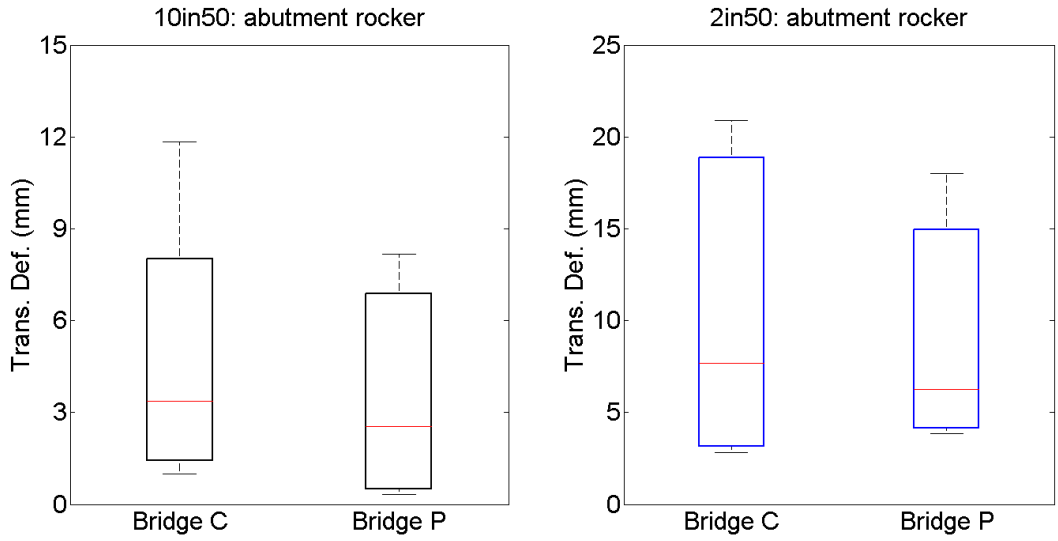

Figure 7.63 Transverse abutment rocker bearing deformation response distributions for *Bridge C* and *Bridge P* under both the 10in50 and 2in50 ground motions

7.8.4 Pier rocker bearing response distributions

Figure 7.64 shows the longitudinal displacements of the pier rocker bearings for *Bridge C* and *Bridge P*. Under the 10in50 ground motions, the displacements of the pier rocker bearing for *Bridge C* have a median value of 16 mm, a 25th percentile value of 7 mm, a 75th percentile value of 21 mm. For *Bridge P* the rocker bearing longitudinal displacements show a 12.5 mm median value, a 2 mm 25th percentile value, and a 20 mm 75th percentile value. The maximum pier rocker bearing displacements are 34 mm and 30 mm for *Bridge C* and *Bridge P*, both less than half of the pier rocker bearing displacement capacity. These findings show that the pier rocker bearing of *Bridge C* generally has a greater longitudinal displacement response than *Bridge P* and that the pier rocker bearings of both bridges perform well under the 10in50 ground motion suite.

Under the 2in50 ground motion suite, the pier rocker bearing longitudinal displacements for the two bridges are very similar. The bearing longitudinal displacements of *Bridge C* have a median value of 36 mm and a maximum value of 98 mm, while for *Bridge P* the median value is 32 mm and the maximum value is 97 mm. The differences between the 25th and 75th percentiles for the two bridges are within 3 mm. Both bridges have one outlier response that exceeds the deformation capacity of the pier rocker bearing. These observations suggest that under 2in50 ground motions, the effect of the corroded abutment rocker bearing on the seismic response of the pier rocker bearings is negligible. Further, the pier rocker bearings of both bridges are capable of accommodating the increased seismic demands of all the motion pairs, but one. This finding indicates that the pier rocker bearings perform well without toppling in the longitudinal direction under strong ground motions with a 2475 year return period.

Figure 7.65 shows the transverse displacements of the pier rocker bearing for *Bridge C* and *Bridge P*. Under the 10in50 ground motions, the pier rocker bearing transverse displacements for both bridges have a similar median value of roughly 0.45 mm and a similar 25th percentile value of roughly 0.2 mm. However, *Bridge C* shows a 3 mm 75th percentile value which is slightly larger than the 2 mm value for the 75th percentile of *Bridge P*. The maximum transverse displacements are 7 mm and 4 mm for *Bridge C* and

Bridge P, respectively. Both of these values are much lower than the transverse capacity of the pier rocker bearing. These findings suggest that the corroded abutment rocker bearings have a slight influence on the transverse response distribution of the pier rocker bearing under the 10in50 ground motions.

Under the 2in50 ground motion suite, a similar trend is observed for the pier rocker transverse displacements of both *Bridge C* and *Bridge P*. The median values are 3 mm and 2 mm, while the maximum values are 20 mm and 19 mm for *Bridge C* and *Bridge P*, respectively. These observations indicate that when subjected to the 2in50 ground motions, the transverse displacements of the pier rocker bearing is negligibly affected by the corrode abutment rocker bearing and the pier rocker bearing is capable of accommodating the transverse displacement seismic demands.

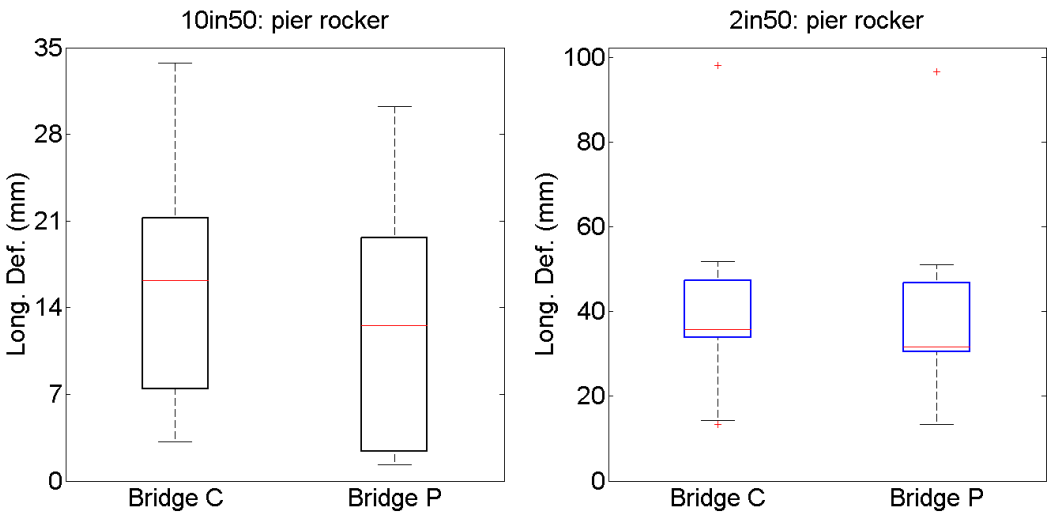

Figure 7.64 Longitudinal pier rocker bearing deformation response distributions for *Bridge C* and *Bridge P* under both the 10in50 and 2in50 ground motions

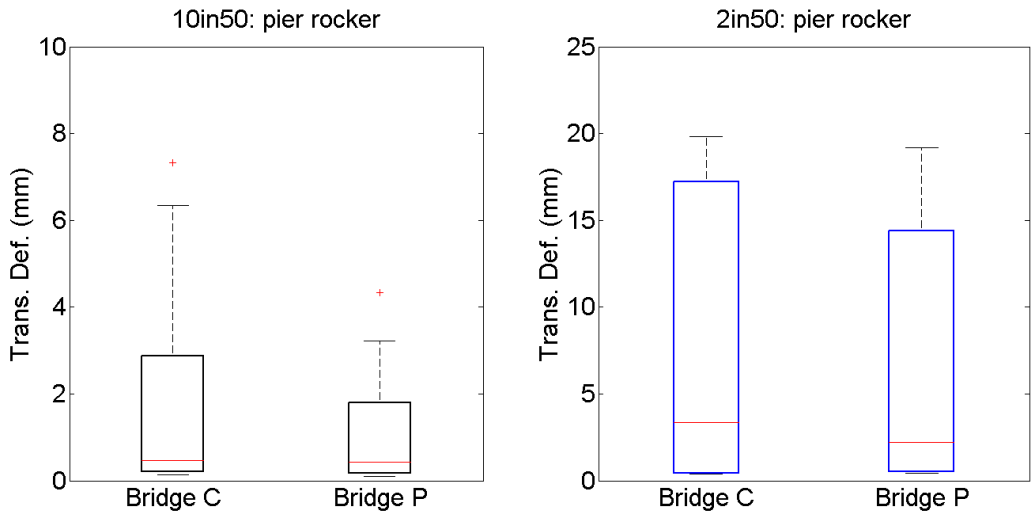

Figure 7.65 Transverse pier rocker bearing deformation response distributions for *Bridge C* and *Bridge P* under both the 10in50 and 2in50 ground motions

7.8.5 Pier bolster bearing response distributions

Figure 7.66 provides the longitudinal displacements of the pier bolster bearing for *Bridge C* and *Bridge P*. Under the 10in50 ground motions, the bolster bearing longitudinal displacements for both bridge are similar. Both bridge's pier bolster bearing longitudinal displacements have median values of around 4 mm, 75th percentile values of roughly 5.5 mm, and maximum values close to 8 mm. The 25th percentiles show a minor difference of just 0.4 mm. These observations indicate that the bolster bearings longitudinal response is negligibly influenced by the corrosion condition of the abutment rocker bearings. The bolster bearings are also capable of accommodating the seismic demands without yielding of the anchor bolts.

Under the 2in50 ground motion suite, the longitudinal responses for both bridges are also similar. The median responses for the two bridges are 7 mm and 6.5 mm, respectively. Both have roughly the same maximum response of 15 mm, while the differences between the 25th percentiles and the 75th percentile values are less than 0.5 mm. Comparing the longitudinal displacements of the two bridges shows that there is little influence from the corroded abutment rocker bearings on the longitudinal displacement response under the 2in50 ground motions. Moreover, the bolster bearings also show the capability of accommodating the seismic demands from ground motions with a 2475 year return period with only minor yielding of the anchor bolts induced under a few ground motion pairs.

Figure 7.67 shows the transverse displacements of the pier bolster bearing for *Bridge C* and *Bridge P*. Under the 10in50 ground motions, the bolster bearing transverse displacements of both bridges are very similar in terms of the 25th and 75th percentiles. The 25th percentile values are roughly 0.4 mm and the 75th percentile values are roughly 4 mm. The median bolster bearing transverse displacement is 1.2 mm for *Bridge C*, which is 0.5 mm larger than that observed for *Bridge P*. The difference between the maximum transverse responses for the two bridges is less than 1 mm. These observations show that the corrosion condition of the abutment rocker bearings has very little influence on the seismic response of the pier bolster bearing under ground motions with a 475 year return

period. The maximum transverse responses also indicate that the bolster bearings can safely accommodate the seismic demands without incurring damage to the anchor bolts.

Under the 2in50 ground motions, minor differences are observed between the bolster bearing transverse displacements from *Bridge C* and *Bridge P*. The two transverse displacement sets have similar median values around 3 mm, similar 25th percentile values of roughly 1 mm, and the same maximum values of 16 mm. The bolster bearing transverse displacements of *Bridge C* have a 75th percentile value of 13 mm while for *Bridge P* it is 12 mm. These observations show that the pier bolster bearing transverse response under the 2in50 ground motions is not affected by the corrosion condition of the abutment rocker bearings. Additionally, the bolster bearing can withstand the seismic demands from ground motions with a 2475 year return period.

7.8.6 Wall pier moment distributions

Figure 7.68 shows the weak-axis bending moment response of the middle wall pier for *Bridge C* and *Bridge P*. Considering the 10in50 ground motions, the maximum moments in the wall pier of *Bridge C* have a median value of 837 kN-m, a 25th percentile value of 596 kN-m, a 75th percentile value of 1086 kN-m, and a maximum value of 1994 kN-m, while *Bridge P* has a 741 kN-m median value, a 381 kN-m 25th percentile value, a 974 kN-m 75th percentile value, and a 2030 kN-m maximum value. Overall, only minor differences are found between the two maximum moment responses indicating that the wall pier moment response is minimally affected by the corrosion condition of the abutment rocker bearings. The similar trend between the wall pier moments and the bolster bearing responses suggests that the maximum moment in the wall piers relies heavily on the forces being transferred from the bolster bearings at the pier top.

Under the 2in50 motion suite, the difference between the maximum wall pier moment of *Bridge C* and *Bridge P* becomes indiscernible. *Bridge C* has a median value of 1710 kN-m, a 25th percentile value of 1493 kN-m, a 75th percentile value of 2664 kN-m, and a maximum value of 3861 kN-m. Correspondingly, these values change to 1605 kN-m, 1435 kN-m, 2548 kN-m, and 3771 kN-m for *Bridge P*. The results confirm that under the 2in50 ground motions, the corrosion condition of the abutment rocker bearings has

minimal influence on the wall pier weak-axis bending moment response. However, considering that the weak-axis bending capacity of the wall pier is 2065 kN-m, extensive wall pier damage is expected due to the seismic moment demands in the pier plastic hinge region under ground motions with a 2475 year return period.

Figure 7.69 shows the strong-axis bending moments of the wall pier for *Bridge C* and *Bridge P*. Under the 10in50 ground motions, the maximum strong-axis moments in the wall pier of *Bridge C* have a median value of 1759 kN-m, a 25th percentile value of 930 kN-m, a 75th percentile value of 2279 kN-m, and a maximum value of 3041 kN-m. These values change to 1591 kN-m, 851 kN-m, 2613 kN-m, and 2948 kN-m for *Bridge P*. Overall, the maximum strong-axis moments in the wall pier are similar with one noticeable difference between the 75th percentile values. This comparison indicates that the strong-axis wall pier moment response is also minimally affected by the corrosion condition of the abutment rocker bearings under the 10in50 ground motions. Further, the observed maximum moments are far less than the moment capacity of the wall pier indicating that the wall pier will perform well in bending about the strong axis.

Under the 2in50 ground motions, the wall pier maximum moments for *Bridge C* have a median value of 2397 kN-m, a 25th percentile value of 1700 kN-m, a 75th percentile value of 7095 kN-m, and a maximum value of 8262 kN-m. These numbers change to 2230 kN-m, 1522 kN-m, 6721 kN-m, and 8596 kN-m for *Bridge P*. Clearly, the differences between the two bridges under the 2in50 motions are negligible indicating the influence of the corroded rocker bearings is minimal on the wall pier performance. Moreover, the maximum observed seismic moments induced under the 2in50 motions are still much smaller than the wall pier moment capacity. This suggests that the wall pier can accommodate the seismic bending moments about the strong axis developed under the 2in50 ground motions without forming plastic hinges at the pier base.

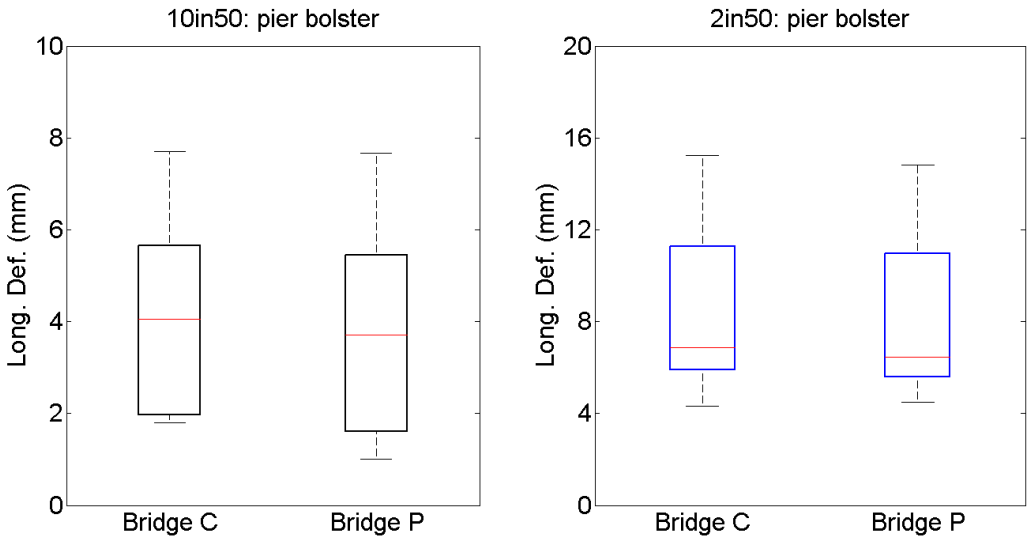

Figure 7.66 Longitudinal pier bolster bearing deformation response distributions for *Bridge C* and *Bridge P* under both the 10in50 and 2in50 ground motions

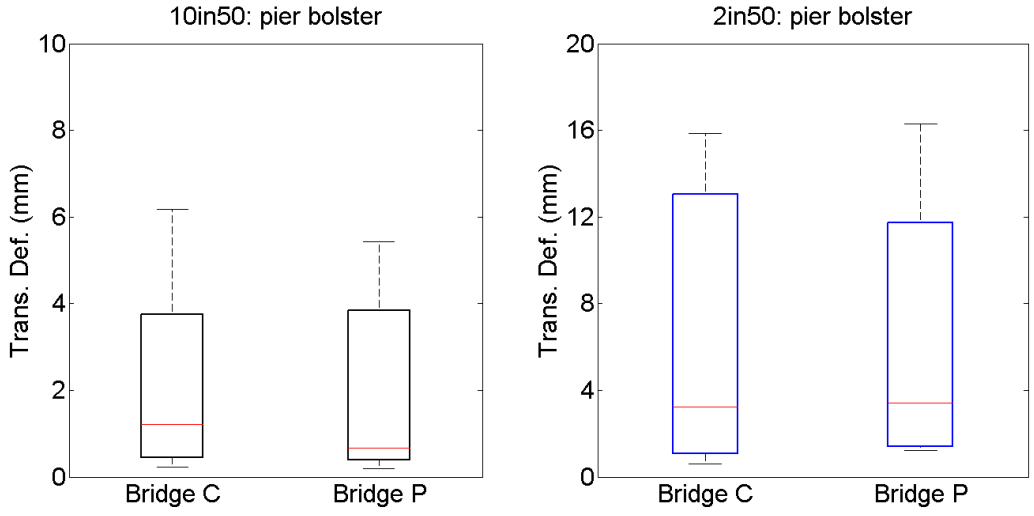

Figure 7.67 Transverse pier bolster bearing deformation response distributions for *Bridge C* and *Bridge P* under both the 10in50 and 2in50 ground motions

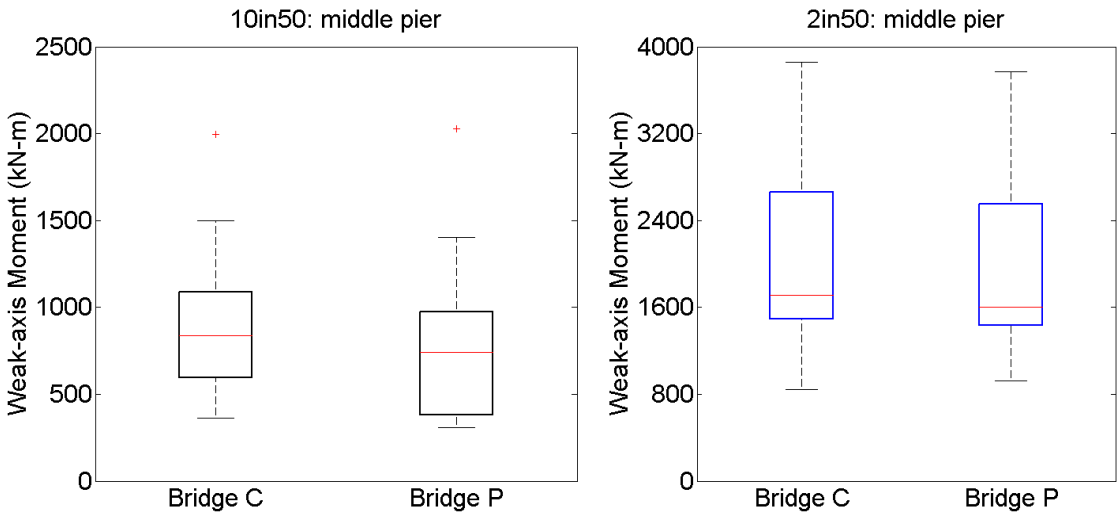

Figure 7.68 Weak-axis bending moment distributions of the middle wall pier for *Bridge C* and *Bridge P* under both the 10in50 and 2in50 ground motions

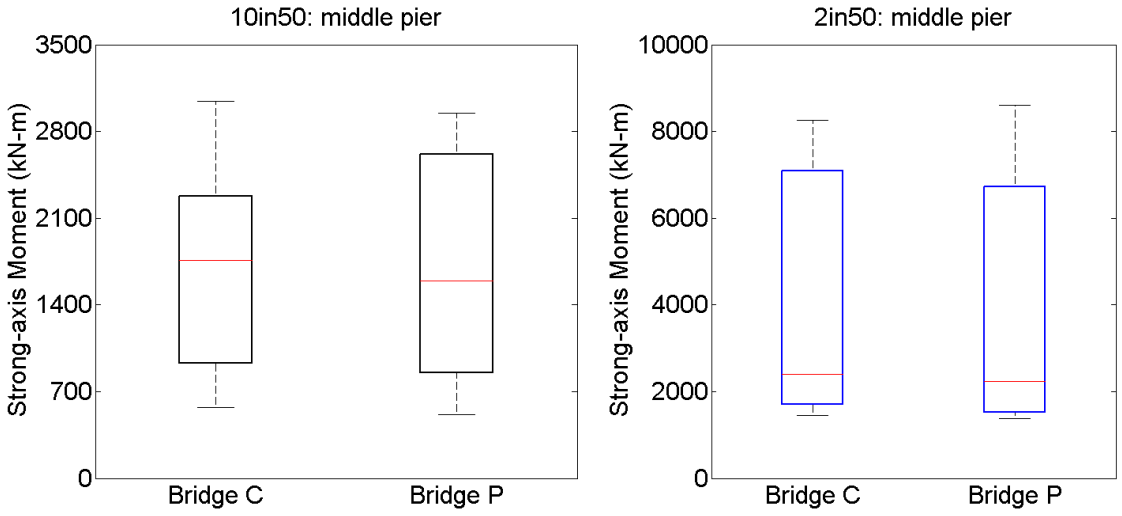

Figure 7.69 Strong-axis bending moment distributions of the middle wall pier for *Bridge C* and *Bridge P* under both the 10in50 and 2in50 ground motions

7.9 Summary

A portfolio of constitutive models that incorporate corrosion effects was developed for steel bridge bearings based on their experimental test results. The constitutive models account for loading in two orthogonal directions, longitudinal and transverse, to allow for simulation of the seismic performance of steel bridge bearings and highway bridges under bidirectional ground motions. Effects of corrosion on the lateral cyclic behavior of steel rocker bearings are implicitly considered in the developed constitutive bearing models by assigning different values to the parameters associated with the deformation modes, lateral stiffnesses and resistances. Fracture of the anchor bolts observed in the steel bolster bearing lateral response is directly modeled considering the hysteretic behavior associated with yielding and fracture of the anchor bolts. Moreover, full bridge models were developed for a 4-span continuous prototype bridge found in Illinois. Nonlinearities associated with soil-abutment interaction, lateral behavior of pile group foundations, pounding, and the behavior of RC wall piers under large lateral loads are accounted for based on the latest research findings.

To better evaluate the seismic performance of a continuous span steel girder bridge when corrosion is considered and to further understand the dynamic interaction between components in this bridge system when subjected to seismic loads, two bridge models, considering an in-situ condition and a pristine condition for the steel bearings, were created. The response of these models was evaluated under a suite of design basis earthquakes and a suite of maximum credible earthquakes to better understand corrosion effects on the bridge performance. The two considered suites of earthquakes, representative of the CEUS, have two orthogonal components, normal/longitudinal and parallel/transverse, for each record, permitting the seismic assessment of the bridges under bidirectional seismic excitation.

The simulation results provided a better understanding of the level of damage that is expected for various bridge components when subjected to ground motions of different magnitudes. According to the findings of these simulations, the two bridges considered in this study performed adequately under the design basis earthquakes. None to minor

inelastic deformation was observed in the abutment-soil interaction response. Insignificant impact forces were developed between the deck and abutment due to pounding. Steel rocker bearings, both corroded and uncorroded, showed the ability to accommodate the seismic displacement demands. Steel bolster bearings did not undergo significant displacement and only minor damage was incurred to the anchor bolts. Additionally, the RC wall piers also exhibited adequate moment capacities to accommodate the seismic moment demands.

On the other hand, extensive failures were observed for the bridges under the maximum credible earthquakes. Extensive pounding events were generated between the deck and the abutment, leading to large inelastic deformations and forces developed in the abutment backfill. Excessive longitudinal displacements were observed for steel rocker bearings with or without corrosion, some of which were above the threshold for toppling indicating that longitudinal failures would occur in the steel rocker bearings. Inelastic deformation to the anchor bolts of steel bolster bearings was caused by the large seismic displacement demands. However, the overall performance of the steel bolster bearings was adequate without complete fracture of the anchor bolts. The seismic moment demands on the wall pier about the weak-axis were significant resulting in extensive damage to the wall pier in its plastic hinge region. Conversely, the seismic moment demands on the wall pier about the strong-axis were lower than the moment capacity of the wall pier, indicating that the wall pier would perform adequately without having major damage due to bending about the strong-axis.

CHAPTER 8 SUMMARY AND CONCLUSIONS

8.1 Summary and Conclusions

Steel bridge bearings, including rocker and bolster bearings, have been widely used in highway bridges throughout the CEUS due to low fabrication cost and ease of installation. They provide a means of transferring loads from the superstructure to the substructure and accommodate rotations and translations of the superstructure induced by thermal and vehicle braking action. Due to lack of routine maintenance and the use of low carbon steel in fabrication, many in-situ steel bearings, in particular those located beneath expansion joints and at abutments, have developed various levels of corrosion over their decades in service. Some steel bearings have sustained such severe corrosion that the mobility of the bearing becomes locked causing larger than expected forces in the substructure. Several bridge failures have occurred in the past due to locked steel rocker bearings leading to expensive repair costs and disruption to local traffic. However, the level of corrosion that can develop on a steel bearing and its effect on the bearing's lateral behavior still lack in-depth research.

Traditionally, steel bridge bearings are not designed to withstand seismic loads and thus little consideration has been put to optimize the performance of steel bearings under large lateral loading such as that from an earthquake. Consequently, poor seismic performance of steel bridge bearings has been demonstrated repeatedly during past seismic events in the United States and Japan. Fracture of bearing components, such as anchor bolts and keeper plates, instability, and anchorage failures, such as concrete breakout and bolt pullout, have been observed as the main failure patterns for steel bearings. Yet, few studies have attempted to provide a better understanding of how steel bridge bearings perform under lateral cyclic loading, why they show a high vulnerability to earthquake-type loading, and what influence they have on the overall performance of bridge systems.

Further, the combined effect of corrosion and seismic on the performance of steel bearings requires consideration given the age of the highway network and bridge infrastructure. To address these needs, the goal of this study has been to characterize the cyclic behavior of salvaged steel bearings and correlate this behavior with their corrosion level allowing for a better assessment of the seismic performance of steel bridge bearings and the bridge systems in which they are installed.

To achieve this goal, a three task study has been undertaken including: analytical and finite element modeling of steel bearings, large-scale experimental testing of salvaged steel bearings and steel bearing-concrete pedestal assemblies, and nonlinear time history analyses of bridge systems with steel bearings under bidirectional ground motions.

8.1.1 Analytical and FE modeling of steel bearings

An analytical study was first carried out to gain a preliminary understanding of the stiffness and strength of steel bridge bearings, in which rigid body kinematics were applied to determine the longitudinal secant stiffness and the critical load to incur transverse instability of steel rocker bearings. An upper bound plastic analysis was conducted to estimate the maximum resistance in the longitudinal and transverse directions for steel bolster bearings.

Finite element models were then created to preliminarily investigate the lateral behavior of steel bridge bearings considering different friction coefficients and vertical loads. This preliminary analysis was important in guiding the design of the experimental test setup and test matrix. The contact and friction behavior between contact surfaces was directly accounted for in the models to capture the deformation modes of the steel bearings. Both the longitudinal and transverse behavior of the steel bearings was considered in the finite element study. Monotonic pushover analyses were conducted for the steel bearings using the models and the results were compared with those determined from the analytical study. Good agreement between the results was found. Further simulations were performed using these models considering two types of cyclic loads, one with an increasing displacement level and the other with a constant displacement level, to gain a

better understanding of the cyclic behavior of steel bridge bearings. A parametric study was also conducted considering the effect of friction and vertical load.

8.1.2 Experimental characterization and testing of salvaged steel bearings

Twenty-five salvaged steel bridge bearings were considered in the experimental study. In addition to corrosion level, the configuration of these salvaged steel bearings has not been considered in past research on the lateral behavior of steel bridge bearings. Four subtasks were completed in the experimental study. First, corrosion level of the salvaged steel bearings was categorized based on visual inspection. Weight measurements, corrosion-induced mass loss, and component geometry loss were then quantified. Second, the lateral behavior of the steel bearings with varying corrosion levels was investigated under monotonic loading. Third, the cyclic behavior of the steel bearings with varying corrosion levels was characterized where uncorroded anchor bolts were connected to a steel pedestal to allow for the evaluation of the full strength of the steel bearings. Lastly, the cyclic behavior of the steel bolster bearing-concrete pedestal assemblies was studied to examine the performance of the anchorage.

The first subtask of this experimental study identified a nonhomogeneous spatial distribution of corrosion for steel rocker bearings located at different locations on the bridge. Steel bearings that were previously installed at the abutments sustained severe corrosion with an average mass loss of 11%, while steel bearings that were located at the piers under the continuous spans experienced none to minor corrosion. Additionally, the distribution of corrosion varied significantly among various components of the abutment rocker bearings. For the abutment rocker bearings, the most severe corrosion occurred to the cylindrical flange (24%) and pintles (73%) located at the bottom cylindrical contact interface.

The second subtask of this experimental study considered the monotonic behavior of steel bridge bearings. Deformation modes and failure patterns of the corroded rocker bearings, uncorroded rocker bearings, and uncorroded bolster bearings were investigated under a laterally applied monotonic loading not considering the effect of anchor bolt corrosion. Effects of bearing corrosion on the lateral behavior of the steel rocker bearings were

studied and discussed. Yielding and fracture of the uncorroded anchor bolts were observed during testing of the steel bolster bearings. Secant stiffness and maximum lateral resistance calculations provided insight into the bearings' lateral behavior under longitudinal and transverse loading.

The third subtask of this experimental study considered an in-depth investigation of the cyclic behavior of the salvaged steel bearings where a steel pedestal was used to provide anchorage to the bearing specimens. The use of a steel pedestal permitted the full strength of the steel bearing assemblages, including the sole plate, bearing body, masonry plate, and anchor bolts, to be evaluated, without experiencing anchorage pullout. Predominant deformation modes and failure patterns were identified for the steel bearings when subjected to lateral cyclic loading. The cyclic behavior of the steel bearings in the longitudinal and transverse directions was obtained and analyzed. Based on these results, a quantitative correlation between corrosion and cyclic behavior was established in regards to deformation modes, secant stiffness, and lateral resistance. To achieve a deeper understanding of the corrosion effects, pack rust was removed from the corroded rocker bearings after the as-received testing and the cleaned rocker bearings were subsequently subjected to the same loading protocol to evaluate the effects of the pack rust on the bearings' cyclic behavior.

The fourth subtask of this experimental study considered the effect that the concrete pedestal and anchorage failure had on the cyclic performance of steel bolster bearings. RC pedestals, designed to mimic the actual cap beam dimension and reinforcement ratio, were fabricated to facilitate this subtask. Two anchor bolt diameters (i.e. 25.4 mm and 34.9 mm) were considered to gain a further understanding of the role of the anchor bolts in determining the deformation mode and failure pattern for the steel bearings. Experimental testing was only performed on the steel bolster bearings since they are the bearing type that is likely to experience anchorage damages under seismic loading as a result of the moment connection between the masonry plate and the bolster bearing body permits large shear forces to be transferred to the substructure.

Conclusions drawn from this experimental program are summarized below:

Monotonic behavior of steel bearings

- The longitudinal behavior of steel rocker bearings consists of two main deformation modes, rolling (at smaller displacements when bearing height change is insignificant) and rocking (at larger displacements when bearing height change is significant). Corrosion has limited influence on the deformation modes of steel rocker bearings, but can significantly change the stiffness and resistance of the lateral response associated with these deformation modes. Additionally, corrosion-induced uneven section loss of the cylindrical surfaces can lead to instability of the bearing body at its upright position, as evident by the observed negative rolling stiffness at relatively low displacement levels.
- The steel rocker bearings with either severe or minor corrosion show significant longitudinal displacement capability; however, the secant stiffness of the load-displacement relationship is fairly insignificant and lower than 1 kN/mm.
- Steel rocker bearings with pack rust removed show identical deformation modes and similar load-deformation relationships to those of the bearings prior to rust removal. However, an increase in the secant stiffness at same maximum displacement is observed due to rust removal.
- The transverse behavior of steel rocker bearings shows disparities in regards to deformation modes and stiffness between the bearings with minor and severe corrosion. Initial stable sliding observed for the bearings with minor corrosion is not seen in the behavior of the bearings with severe corrosion. A much earlier onset of rocking is observed in the corroded bearing response than in the response of the bearing with minor corrosion.
- Both the severe and minor corroded rocker bearings exhibit significantly larger lateral resistances in the transverse direction than in the longitudinal direction. However, the corroded rocker bearing shows a slightly smaller stiffness and lateral resistance than the rocker bearing with minor corrosion at similar displacements.

- The rocker bearing with the pack rust removed shows a response similar to that of the bearing before cleaning. An insignificant increase in the secant stiffness at the maximum applied displacement is observed after rust removal.
- Corrosion shows greater influences on the deformation modes, stiffness, and resistances of the lateral response of steel rocker bearings than on their capability to displace under lateral loads. Cleaning of corrosion byproducts generally results in larger lateral stiffness and resistance for the corroded rocker bearings.
- The longitudinal behavior of steel bolster bearings is governed by the combined rocking and prying deformation mode that subjects the anchor bolts to combined tension and shear. Sliding is also observed at smaller displacement levels due to the clearance around the bolts and pintles. Both bolts fracture during loading, however, at different displacement levels, while the pintles remain intact. Strength degradation occurs in the lateral response as a result of the bolts yielding and fracturing.
- The transverse behavior of steel bolster bearings is governed by masonry plate prying and shearing of the anchor bolts. The anchor bolts are subjected to combined tension and shear with shear being more predominant. The bolts fracture simultaneously leading to a significant load loss at that instant. However, no obvious strength degradation phase is observed in the transverse response, indicating shear failure of the bolts is dominant.
- Steel bolster bearings show a fairly good deformation capability under both longitudinal and transverse loading before loss of both anchor bolts due to fracture. Severe corrosion is not found on any salvaged steel bolster bearing.

Cyclic behavior of steel bridge bearings anchored to a steel pedestal

- The longitudinal cyclic behavior of steel rocker bearings is susceptible to corrosion-induced section losses and other byproducts (i.e. pack rust) in terms of deformation modes, lateral stiffness, and resistance. A symmetric response is obtained for the bearing with minor corrosion, which shows a predominant rolling and rocking deformation mode. In contrast, a highly asymmetric response is found for the corroded bearing with a longer rolling displacement range and a

significant disparity between positive and negative rocking responses, which owes directly to the uneven section loss induced by corrosion at the top and bottom cylindrical contact surfaces.

- Compared to the rocker bearing with minor corrosion, the corroded bearing shows a significant decrease in longitudinal stiffness and resistance, but a comparable capability to accommodate large applied displacements without overturning.
- The cleaned rocker bearing response has a more pronounced rolling displacement range with a smaller rolling resistance than the corroded rocker bearing. Overall, cleaning leads to a reduced stiffness with the same displacement accommodation capability.
- The transverse behavior of steel rocker bearings shows significant differences between bearings with minor and severe corrosion in regards to deformation modes, lateral stiffness, and resistance. Initial sliding observed for the uncorroded rocker bearing is not seen for the corroded rocker bearing due to pack rust that formed at the top and bottom cylindrical surfaces and on the masonry plate. This rust restrains sliding and leads to the onset of rocking at smaller displacements. Sliding of the masonry plate of the corroded rocker bearing initiates after the lateral load increases to 60 kN.
- Large transverse resistances at relatively small displacements are observed for both the uncorroded and corroded rocker bearings compared to those observed in the longitudinal direction.
- Cleaning of the pack rust leads to only minor changes for the transverse cyclic response of the corroded rocker bearing in regards to secant stiffness and sliding resistance. A small reduction in the maximum lateral resistance is also caused by cleaning.
- Corrosion of steel rocker bearings in the form of nonhomogeneous section loss results in asymmetric cyclic responses in the longitudinal and transverse directions. Changes in deformation modes are also induced at relatively small displacements; however, the displacement accommodation capacity of the steel rocker bearings is not significantly compromised.

- The longitudinal cyclic behavior of steel bolster bearings has several deformation modes including sliding of the sole plate and the masonry plate, rocking of the bearing on top of the steel pedestal, and prying of the anchor bolts. These deformation modes lead to a bearing hysteresis featuring a sliding plateau and pinching and strength degradation due to yielding and fracture of the anchor bolts. The maximum longitudinal resistance of the steel bolster bearing is governed by the strength of the anchor bolts because they are weaker compared to the pintles.
- The transverse cyclic behavior of steel bolster bearings also has three deformation modes including sliding of the sole plate and the masonry plate, rocking of the bearing, and prying of the anchor bolts. Fracture of the anchor bolts again dictates the maximum transverse resistance of the bolster bearing. However, only minor pinching and strength degradation are observe in the hysteresis curve due to a more shear-dominant fracture of the anchor bolts. Post-fracture response of the bolster bearing is governed by continuous sliding.

Cyclic behavior of steel bolster bearings anchored to a concrete pedestal

- The steel bolster bearing using 25.4 mm diameter anchor bolts has longitudinal deformation modes similar to those observed for the bolster bearing anchored to the steel pedestal. However, severe anchor bolt pullout occurs at large displacements leading to progressively increasing rocking of the steel bearing. This is evident from the increasing pinching phenomenon observed in the hysteretic response of the bearing. Fracture of the anchor bolts is not observed due to continuous pullout of the anchor bolts. Minor radial cracks are observed in the concrete surrounding the anchor bolts. Maximum longitudinal resistances, comparable to those observed for the steel pedestal-based test, are achieved.
- The steel bolster bearing using 25.4 mm diameter bolts is more flexible and experiences more severe pinching under transverse loading than the behavior of the bearing attached to a steel pedestal. Even though pullout of the anchor bolts occurs during cyclic loading, the anchor bolts still fracture under combined tension and shear. The anchor bolts also damage the surrounding concrete and creates two large craters in the top surface of the concrete pedestal. However, no

significant cracking is observed in the pedestal. Maximum transverse resistances observed in the test are also comparable to those recorded for the bearing test using a steel pedestal.

- The longitudinal cyclic behavior of the steel bolster bearing using 34.9 mm diameter bolts shows a much larger deformation capability than the two tests using 25.4 mm diameters bolts. Pinching and degradation observed in the hysteresis have little to do with yielding or fracture of the anchor bolts, rather they are due to significant rocking. Rocking is the dominant deformation mode observed in this bearing test directly owing to anchor bolt pullout under cyclic loading. Maximum longitudinal resistances that are larger than those for the other two tests are observed.
- The transverse cyclic behavior of the steel bolster bearing using 34.9 mm diameter anchor bolts is very similar to that observed for the steel bolster bearing tested on a steel pedestal with respect to secant stiffness and lateral resistance. At relatively small displacements, the lateral resistance of the bolster bearing undergoes a significant increase indicating that the 34.5 mm diameters bolts have made the connection between the bolster bearing and the concrete pedestal very stiff. Minimal pullout of the anchor bolts has occurred when the test concluded.
- Pullout of the 25.4 mm diameter anchor bolts is significant leading to more flexible cyclic behavior of the steel bolster bearings under longitudinal and transverse loading. Yet, comparable maximum resistances are reached in these tests compared to those using a steel pedestal. However, fracture of the anchor bolts is only observed during transverse testing. Pullout of the 34.9 mm diameter anchor bolts is severe for the longitudinal bearing test and results in a rocking-dominant response featuring increased pinching and degradation of the hysteresis. Moreover, a significantly stiffer transverse response is observed for the bolster bearing using 34.9 mm diameter anchor bolts. Larger secant stiffness and lateral resistance are achieved at relatively small displacements in the transverse loading direction.
- Concrete pedestals cannot provide enough anchorage to the steel bolster bearing to develop enough forces to fracture the anchor bolts in the longitudinal loading

direction. They are capable of providing sufficient anchorage to fracture the anchor bolts when the bearing is loaded in the transverse direction. The use of 34.9 mm diameter anchor bolts will cause larger transverse forces to be transferred to the substructure resulting in potentially more severe damage to the concrete substructure.

8.1.3 Performance evaluation of highway bridges using time-history analyses

Constitutive models were created for the steel bridge bearings considering corrosion effects based on the experimental test results. These models are suitable for implementation in larger numerical bridge models for performing time-history analyses of existing highway bridges under seismic loading. To further assess the seismic performance of the steel bearings and the effects of corroded steel bearings on the overall seismic bridge performance, two bridge models were considered based on the prototype bridge from which the steel bearing specimens were salvaged. These bridge models accounted for nonlinearities associated with abutment-soil interaction, pounding, lateral behavior of RC wall piers, and the pile ground foundation behavior. One bridge model assumed that all steel bearings were in a good condition with minor corrosion, while the other bridge model considered corroded steel rocker bearings only at the abutments, consistent with the observation of the corrosion distribution for the salvaged steel bearings. Two suites of ground motions that are representative of the CEUS were used to excite the considered bridges, one a suite of design basis earthquakes and the other a suite of maximum credible earthquakes. These simulations provide insight into the effects of corrosion on the performance of steel bridge bearings and the overall performance of continuous steel girder bridge systems.

Conclusions drawn from this numerical study are provided below:

- Under the design basis suite of earthquakes, the performance of both bridges is very satisfactory. Corrosion of the steel rocker bearings located at the abutments has limited influence on the seismic performance of the various bridge components.

    - At most, minor pounding incidents occur due to the given ground motion suite and thus minimal inelastic deformation is induced in the abutment backfill.
    - The corroded and uncorroded rocker bearings can accommodate the seismic displacement demands placed on them in both the longitudinal and transverse directions.
    - The steel bolster bearings can withstand the seismic demands without undergoing any inelastic deformation in the anchor bolts.
    - The wall piers also exhibit enough capacity to accommodate the seismic moment demands about both the weak and strong bending axes.
- Under the maximum credible suite of earthquakes, severe damage is induced in several components of both bridges. Again, corrosion of the steel rocker bearings located at the abutments has limited influence on the seismic performance of various bridge components.
    - Extensive pounding occurs between the deck and the abutment, leading to larger longitudinal forces imparted to the abutment backfill. Meanwhile in the transverse direction, the seismic abutment force demands remain less than the capacity of the abutment resistance.
    - Larger seismic displacement demands are placed on the steel rocker bearings in the longitudinal direction, leading to increased likelihood of toppling in the longitudinal direction. Larger seismic displacement demands are also observed on the steel rocker bearing in the transverse direction; however, they are less than the transverse displacement capacity of the steel rocker bearing.
    - Greater seismic displacement demands are placed on the steel bolster bearing in both the longitudinal and transverse directions. However, the steel bolster bearing still can accommodate these demands without incurring fracture to the anchor bolts.
    - Extensive wall pier damage is observed due to seismic moment demands in bending about the weak axis, while the strong-axis bending capacity of

the wall pier is capable of accommodating seismic moment demands placed on it.

- The seismic demands generated by the maximum credible suite of earthquakes can pose serious threat to the steel bearings, whether corroded or not, and the bridges that employ them. This can potentially lead to extensive damage of various bridge components ranging from the abutment backfill, steel bearings, and wall piers. Care needs to be directed to evaluate the seismic performance of existing bridges under a potential 2in50 seismic event.

8.2 Impact

An experimental study has been undertaken to characterize the cyclic behavior of salvaged steel bearings with various corrosion levels and the results are used to develop high-fidelity and efficient constitutive bearing models for implementation in assessing seismic bridge performance of existing highway bridges. The significant contributions resulting from this study include the following:

- Simplistic theoretical formulations and accurate finite element models have been developed for the considered steel bearings, which enable a fast and reliable preliminary evaluation of the mechanical behavior of such bearings. The modeling approach has potential to be used for bearings with a variety of configurations.
- Corrosion and its effects are quantified leading to a previously non-existent understanding of how corrosion distributes among bearing components and affects the lateral behavior of steel bridge bearings, allowing for a better evaluation of in-situ steel bearing conditions.
- The cyclic behavior of steel bridge bearings commonly found in the CEUS is established for various levels of corrosion. This understanding can be used to better evaluate the vulnerability of existing highway bridges.

- Performance of the anchorage provided by existing RC cap beams is also evaluated under large cyclic loads, enabling an evaluation of the interaction between the steel bearing and the cap beam under seismic loading. However, corrosion of the cap beam or anchor bolts is not considered, but may be present in actual bridges.
- A portfolio of constitutive models, each consisting of one longitudinal model and one transverse model, are developed for the steel bearings considered in this study. These constitutive models incorporate corrosion effects and can be readily applied to bridge system models for performing time-history analyses for existing bridges that use steel bearings and have sustained corrosion.
- The simulations of the bridge systems under seismic loads that adopt the constitutive bearing models show that steel bearings may be adequate under a design basis earthquake. It is also shown that corrosion of the steel rocker bearings at the abutments has limited impact on the performance of the other bridge components of the prototype bridge, such as the abutments, wall piers, and steel bolster bearings.

8.3 Limitations and Future Recommendations

Some of the inherent limitations of this work are provided below to provide a better context in which to view the findings:

- The finite element models for the steel bearings do not explicitly model fracture, such as fracture of the anchor bolts.
- Corrosion is only considered for steel bridge bearings salvaged from a continuous span, steel girder highway bridge located in an urban area and cold region where high chloride concentration and other pollutants are often present. Thus, the characteristics of the discussed corrosion distribution are applicable to steel bearings in bridges of similar configuration and location. However, based on inspection reports, a similar corrosion distribution is often found under expansion joints and at the abutments of other types of bridges.

- Corrosion effect on the steel anchor bolts is not addressed in this work due to the fact that only the bearings were salvaged from the prototype bridge. Additionally, deterioration of the reinforced concrete pedestal is not explicitly considered.
- The numerical simulation considers biaxial loading. However, the steel bearing models are based on the behavior in each orthogonal direction individually. Potential loss in strength to simultaneous longitudinal and transverse loading is not accounted for in simulating the bridge performance. The bearing models in Chapter 7 do not account for the coupled effect of biaxial loading.
- The bridge models developed in this work only consider a specific multi-span, continuous bridge and thus are not necessarily applicable to other bridge configurations, such as multi-span simply-supported bridges.

Several potential future research directions are identified as the following:

- With a better understanding of the cyclic behavior of older steel bridge bearings with various levels of corrosion, a study of viable and sustainable retrofit solutions is needed considering the number of aging highway bridges in the U.S.
- RC wall piers considered in this study show a vulnerability to earthquakes with a 2475-year return period due to substantial seismic moment demands placed on the wall pier in bending about its weak axis. One possible solution would be to replace the steel bolster bearings that are capable of transferring large shear forces into the wall pier with aseismic devices that can cap the shear forces being transferred to the substructure.
- Many in-situ steel rocker bearings are not resting in their upright position due to various reasons such as installation error and thermal expansion or contraction. The effect of this predisposed rotation on the seismic performance of the steel rocker bearings in regards to toppling needs further investigation.
- This study only considers the seismic performance of multi-span continuous highway bridges with steel bearings. However, there are many other types of highway bridges, such multi-span simply-supported bridges, which also need to be investigated for their seismic performance considering corroded steel bearings.

REFERENCES

Abo-Shadi, N., Saiidi, M., and Sanders, D. (2000). Seismic response of reinforced concrete bridge piers walls in the weak direction, Technical Report MCEER-00-0006, Multidisciplinary Center for Earthquake Engineering Research, Buffalo, NY.

Albrecht,P. and Naeemi, A.H. (1984). Performance of weathering steel in bridges, Report 272, National Cooperative Highway Research Program, Washington, D.C.

American Association of State Highway and Transportation Officials (AASHTO). (2005). Grand Challenges: A Strategic Plan for Bridge Engineering, AASHTO Highway Subcommittee on Bridges and Structures.

American Association of State Highway and Transportation Officials (AASHTO). (2008). Bridging the Gap, American Association of State Highway and Transportation Officials.

American Association of State Highway and Transportation Officials (AASHTO). (2009). Guide Specifications for LRFD Seismic Bridge Design, Washington, D.C.

American Association of State Highway and Transportation Officials (AASHTO). (2010). LRFD Bridge Design Specifications with 2010 Interim Revisions, American Association of State Highway and Transportation Officials, Washington, D.C.

American Concrete Institute(ACI). (2005). Building code requirements for structural concrete and commentary, ACI 318-05 and ACI 318R-05, ACI Committee 318, Detroit.

American Society of Civil Engineers (ASCE). (2011). Failure To Act: The Economic Impact of Current Investment Trends in Surface Transportation infrastructure, American Society of Civil Engineers.

American Society of Civil Engineers (ASCE). (2013). Reprot Card for America's Infrastructure, American Society of Civil Engineers: Reston, VA.

Aviram, A., Mackie, K.R., and Stojadinovic, B. (2008). Guidelines for nonlinear analysis of bridge structures in California, Technical Report No. 2008/03, Pacific Earthquake Engineering Research Center, Berkeley, CA.

Balassone, F. (2010). "Rocker bearing issues", Northeast bridge preservation conference, Hartford, CT.

Barker, M.G. and Hartnagel, B.A. (1998). "Longitudinal restraint response of existing bridge bearings", Transportation Research Record, Issue 1624: 28-35.

Basoz, N.I., Kiremidjian, A.S., King, S.A., and K.H. Law (1999). "Statistical analysis of bridge damage data from the 1994 Northridge, CA, earthquake", Earthquake Spectra, 15(1): 25-53.

Bignell, J.L., LaFave, J.M., and Hawkins, N.M. (2005). "Seismic vulnerability assessment of wall pier supported highway bridges using nonlinear pushover analyses", Engineering Structures, 27: 2044-2063.

Bruneau, M., Wilson, J.C., and Tremblay, R. (1996). "Performance of steel bridges during the 1995 Hyogo-ken Nanbu (Kobe, Japan) earthquake", Canadian Journal of Civil Engineering, 23: 678-713.

Bursi, O.S. and Jaspart, J.P. (1998) "Basic issues in the finite element simulation of extended end plate connections", Computers and Structures, 69: 361-382.

California Department of Transportation (Caltrans). (2006). Seismic Design Criteria, Sacramento, CA.

Center of Earthquake Research and Information (CERI). (2011). New Madrid Earthquake Catalog Search, University of Memphis: http://folkworm.ceri.memphis.edu/catalogs/html/cat_nm.html

Chen, W-F. and Duan, L. (2003). Bridge Engineering: Substructure Design, CRC Press, Boca Raton, FL.

Choi, E. (2002). Seismic analysis and retrofit of mid-America bridges, Ph.D. Thesis, Georgia Institute of Technology, Atlanta, GA.

Choi, E., DesRoches, R., and Nielson, B. (2004). "Seismic fragility of typical bridges in moderate seismic zones", Engineering Structures, 26(2): 187-199.

Citipitioglu, A.M., Haj-Ali, R.M., and White, D.W. (2002). "Refined 3D finite element modeling of partially-restrained connections including slip", Journal of Constructional Steel Research, 58: 995-1013.

Cramer, S.D., Covino, B.S., Bullard, S.J., Holcomb, J.R., Russell, J.H., Nelson, F.J., Laylor, H.M., and Soltesz, S.M. (2002). "Corrosion prevention and remediation

strategies for reinforced concrete coastal bridges", Cement and Concrete Composites 24(1): 101-117.

Czarnecki, A.A. (2006). System reliability models for evaluation of corroded steel girder bridges, PhD Thesis, Univeristy of Michigan, Ann Arbor, MI.

Czarnecki, A.A. and Nowak, A.J. (2008). "Time-variant reliability profiles for steel girder bridges", Structural Safety, 30: 49-64.

DesRoches, R., Choi, E., Leon, R.T., Dyke, S.J., and Aschheim, M. (2004). "Seismic response of multiple span steel bridges in central and southeastern United States. I: As built", Journal of Bridge Engineering, 9(5): 464-472.

DesRoches, R., Leon, R.L., and Dyke, S. (2003). Response modification of bridges, Mid-America Earthquake Center Research Report.

Dicleli, M. and Bruneau, M. (1995a). "Seismic performance of multispan simply supported slab-on-girder steel highway bridges", Engineering Structures, 17(1): 4-14.

Dicleli, M. and Bruneau, M. (1995b). "Seismic performance of single-span simply supported and continuous slab-on-girder steel highway bridges", Journal of Structural Engineering, 121(10): 1497-1506.

Dicleli, M. and Mansour, M.Y. (2003). "Seismic retrofitting of highway bridges in Illinois using friction pendulum seismic isolation bearings and modeling procedures", Engineering Structures, 25(9): 1139-1156.

DS-Simulia, (2008). ABAQUS version 6.8-1Documentation, Providence, RI

Duncan, J. M. and Mokwa, R. L. (2001). "Passive earth pressures: theories and tests", Journal of Geotechnical and Geoenvironmental Engineering, 127(3):248-257.

Earthquake Engineering Research Institute (EERI) (2011). Bridge performance in the Mw 9.0 Tohoku, Japan, earthquake of March 11, 2011, EERI Special Earthquake Report.

Eggert, H. and Kauschke, W. (2002). Structural bearings. Berlin, Germany: Ernst and Sohn.

Fan, X. and McCormick, J. (2014). "Characterization of the behavior of steel bridge bearings under cyclic load reversal", Structure and Infrastructure Engineering, in press.

Federal Highway Adminstration (FHWA). (2010). National Bridge Inventory Data, Federal Highway Adminstration.

Filipov, E.T. (2012). Nonlinear seismic analysis of quasi-isolation systems for earthquake protection of bridges, M.S. Thesis, University of Illinois, Urbana-Champaign, IL.

Filipov, E.T., Fahnestock, L.A., Steelman, J.S., Hajjar, J.F., LaFave, J.M., and Foutch, D.A. (2013a). "Evaluation of quasi-isolatied seismic bridge behavior using nonlinear bearing models", Engineering Structures, 49(14): 168-181

Filipov, E.T., Revell, J.R., Fahnestock, L.A., LaFave, J.M., Jajjar, J.F., Foutch, D.A., and Steelman, J.S. (2013b). "Seismic performance of highway bridges with fusing bearing components for quasi-isolation", Earthquake Engineering and Structural Dynamics, 42(9): 1375-1394.

Fontana, M.G. and Greene, N.D. (1967). Corrosion Engineering, McGraw-Hill: New York.

Garlock, M.E. and Selamet, S. (2010) "Modeling and Behavior of Steel Plate Connections Subject to Various Fire Scenarios", Journal of Structural Engineering, 136(7): 897-906.

Ghobarah, A. and Ali, H.M. (1988). "Seismic performance of highway bridges", Engineering Structures, 10(3): 157-166.

Ghosh, J. and Padgett, J.E. (2010). “Aging Considerations in the Development of Time-Dependent Seismic Fragility Curves”, Journal of Structural Engineering, 136(12): 1497-1511.

Hindi, R. and Dicleli, M. (2006). "Effect of modifying bearing fixities on the seismic response of short-to-medium-length bridges with heavy substructures", Earthquake Spectra, 22(1): 65-84.

Hite, M.C. (2007). Evaluation of the performance of bridge steel pedestals under low seismic loads, Ph.D. Thesis, Georgia Institute of Technology, Atlanta, GA.

Hite, M.C., DesRoches, R., and Leon, R.T. (2008). "Full-scale tests of bridge steel pedestals", Journal of Bridge Engineering, 13(5): 483-491.

Housner, G.W. and Thiel, C.C. (1995). "The continuing challenge: report on the performance of state bridges in the Northridge earthquake", Earthquake Spectra, 11(4): 607-636.

Housner, G.W., Penzien, J., Agbabian, M.S., Arnold, C., Dickinson, L.V., Elsesser, E., Idriss, I.M., Jennings, P.C. Podolny, W., Scordelis, A.C., Wallace, R.E., and Thiel, C.C. (1990). Competing against time, report to Governor George Deukmejian from the Governer's Board of Inquiry on the 1989 Loma Prieta Earthquake, CA.

Johnston, A.C. and Schweig, E.S., (1996). "The enigma of the New Madrid earthquakes of 1811-1812", Annu. Rev. Earth Planet. Sci., 24: 339-384.

Kawashima, K. (2012). "Damage of bridges due to the 2011 Great East Japan earthquake", Proceedings of the International Symposium on Engineering Lessons Learned from the 2011 Great East Japan Earthquake, Tokyo, Japan.

Kayser, J.R. (1988). The effects of corrosion on the reliability of steel girder bridges, Ph.D. Thesis, University of Michigan, Ann Arbor, MI.

Kayser, J.R. and Nowak, A.S. (1989a). "Capacity loss due to corrosion in steel girder bridges", Journal of Structural Engineering, 115(6): 1525-1537.

Kayser, J.R. and Nowak, A.S. (1989b). "Reliability of corroded steel girder bridges", Structural Safety, 6: 53-63.

Komp, M.E. (1987). "Atmospheric corrosion rating of weathering steels: Calculation and significance", Material Performance, 26(7): 42-44.

Kulak, G.L., Fisher, J.W., and Struik, J.H. (2001). Guide to Design Criteria for Bolted and Riveted Joints, 2nd Edition, American Institute of Steel Construction, Inc., Chicago, IL.

Lindquist, L. (2008). Corrosion of steel girder anchor bolts, Master Thesis, Georgia Institute of Technology, Atlanta, GA.

Lindquist-Hoeke, L.J., Moser, R.D., Singh, P.M., Kahn, L.F., and Kurtis, K.E. (2009). "Degradation of steel girder bridge bearing system by corrosion", Corrosion 2009: NACE Conference and Expo., Atlanta, GA.

Ma, Y. and Deng, N. (2000). "Deep Foundations", Bridge Engineering Handbook, CRC Press, Boca Raton, FL.

Makris, N. and Zhang, J. (2004). "Seismic response analysis of a highway overcrossing equipped with elastomeric bearings and fluid dampers", Journal of Structural Engineering, 130(6): 830-844.

Mander, J.B., Kim, D-K., Chen, S.S., and Premus, G.J. (1996). Response of Steel Bridge Bearings to Reversed Cyclic Loading, Technical Report NCEER-96-0014, National Center for Earthquake Engineering Research.

Maroney, B., Kutter, B., Romstad, K., Chai, Y.H., and Vanderbilt, E. (1994). "Interpretation of large scale bridge abutment test results", 3rd Annual Seismic Research Workshop, Caltrans, Sacramento, CA.

Mazroi, A., Wang, L.R-L., and Murray, T.M. (1983). "Effective coefficient of friction of steel bridge bearings", Transportation Research Record, (903): 79-86.

McCormick, J., Nagae, T., Ikenaga, M., Zhang, P-C., Katsuo, M., and Nakashima, M. (2009). "Investigation of the sliding behavior between steel and mortar for seismic applications in structures", Earthquake Engineering and Structural Dynamics, 38: 1401-1419.

McKenna, F., Fenves, G.L., Scott, M.H., and Jeremic, B. (2000). Open System for Earthquake Engineering Simulation (OpenSees). Pacific Earthquake Engineering Research Center, Berkeley, CA.

Merino, M., Stein, S., Liu, M., and Okal, E.A. (2010). "Comparison of seismicity rates in the New madrid and Wabash Valley seismic zones", Seismological Research Letters, 81(6): 951-954.

Mitchell, D., Bruneau, M., Williams, M., Anderson, D., Saatcioglu, M., and Sexsmith, R. (1995). "Performance of bridges in the 1994 Northridge earthquake", Canadian Journal of Civil Engineering, 22: 415-427.

Modjeski and Masters Inc. (2008). Birmingham Bridge Forensic Inspection Final Report Summary.

Mosqueda, G., Whittaker, A.S., and Fenves, G.L. (2004). "Characterization and modeling of friction pendulum bearings subjected to multiple components of excitations", Journal of Structural Engineering, 130(3): 433-442.

Muthukumar, S. (2003). A Contact Element Approach with Hysteresis Damping for the Analysis and Design of Pounding in Bridges, Ph.D. thesis, Georgia Institute of Technology, Atlanta, GA.

Muthukumar, S. and DesRoches, R. (2006). "A Hertz contact model with non-linear damping for pounding simulation", Earthquake Engineering and Structural Dynamics, 35: 811-828.

Nielson, B. and DeRoches, R. (2007a). "Analytical seismic fragility curves for typical bridges in the Central and Southeastern United States", Earthquake Spectra, 23(3): 615-633.

Nielson, B. and DeRoches, R. (2007b). "Seismic fragility methodology for highway bridges using a component level approach", Earthquake Engineering and Structural Dynamics, 36(6): 823-839.

Nielson, B.G. and DesRoches, R. (2006). "Influence of modeling assumptions on the seismic response of multi-span simply supported steel girder bridges in moderate seismic zones", Engineering Structures, 28(8): 1083-1092 .

Nielson, B.G. (2005). Analytical fragility curves for highway bridges in moderate seismic zones, Ph.D. Thesis, Georgia Institute of Technology, Atlanta, GA.

New Madrid Seismic Zone Expert Panel. (2011). Report of the Independent Expert Panel on New Madrid Seismic Zone Earthquake Hazards, USGS.

National Surface Transportation Policy and Revenue Study Commission (NSTPRSC). (2008). Report of the National Surface Transportation Policy and Revenue Study Commission.

National Transportation Safety Board (NTSB). (2008). Highway Accident Report: Collapse of I-35W Highway Bridge, Minneapolis, Minnesota.

New York State Department of Transportation (NYSDOT). (2005). Structural Forensic Investigation Report: BIN 109299A, Ramp AC, Dunn Memorial Bridge Interchange, Albany, NY.

Padgett, J. (2007). Seismic vulnerability assessment of retrofitted bridges using probabilistic methods, Ph.D. Thesis, Georgia Institute of Technology, Atlanta, GA.

Pan, Y., Agrawal, A.K., Ghosn, M., and Alampalli, S. (2010). "Seismic fragility of multispan simply supported steel highway bridges in New York State. I: Bridge modeling, parametric analysis, and retrofit design", Journal of Bridge Engineering, 15(5): 448-461.

Park, C-H. (1999). Time-dependent reliability models for steel girder bridges, PhD Thesis, University of Michigan, Ann Arbor, MI.

Park, C-H. and Nowak, A.J. (1997). "Lifetime reliability model for steel girder bridges", In: Das PC, editor. Safety of bridges. London: Thomas Telford Publishing.

Park, K., Jung, H., and Lee, I. (2002). "A comparative study on aseismic performances of base isolation systems for multispan continuous bridge", Engineering Structures, 24(8): 1001-1013.

Pond, W.F. (1972). "Performance of bridges during San Fernando earthquake", PCI Journal, July-August: 65-75.

Ramberger, G. (2002). Structural Bearings and Expansion Joints for Bridges, Int'l Association for Bridge and Structural Engineering, Austria.

Rashidi, S. and Saadeghvaziri, M.A. (1997). "Seismic modeling of multi-span simply-supported bridges using ADINA", Computers and Structures, 64(5/6): 1025-1039.

Saadeghvaziri, M.A. and Rashidi, S. (1998). "Effect of steel bearings on seismic response of bridges in eastern United States", 6th U.S. National Conference on Earthquake Engineering, Seattle, WA.

Sarraj, M., Burgess, I.W., Davison, J.B., and Plank, R.J. (2007). "Finite element modeling of steel fin plate connections in fire" Fire Safety Journal: 42: 408-415.

Sato, Y., Sakai, M., and Ohtomo, K. (2008). "Effects of steel bearing performance on global seismic response of a bridge", 14th World Conference on Earthquake Engineering, Beijing, China.

Shamsabadi, A., Rollins, K.M., and Kapuskar, M. (2007). "Nonlinear soil-abutment-bridge structure interaction for seismic performance-based design", Journal of Geotechnical and Geoenvironmental Engineering, 133(6): 707-720.

Somerville, P., Smith, N., Punyamurthula, S., and Sun, J. (1997). "Development of ground motion time histories for Phase 2", Report No. SAC-BD-97-04, SAC Joint Venture.

Splitstone, D.E., Stonecheck, S.A., Dodson, R.L., and Fuller, J.A. (2010). "Birmingham bridge emergency repairs: Micropile foundation retrofit", Proceedings of the GeoFlorida 2010 Conference, Florida

Steelman, C., Filipov, E.T., Fahnestock, L.A., Revell, J.R., LaFave, J.M, Hajjar, J.F., and Foutch, D.A. (2014). “Experimental Behavior of Steel Fixed Bearings and Implications for Seismic Bridge Response”, Journal of Bridge Engineering, in press (published online July 29, 2013)

Su, L., Ahmadi, G., and Tadjbakhsh, I.G. (1989). "A comparative study of performance of various base isolation systems, part I: shear beam structures", Earthquake Engineering and Structural Dynamics, 18(1): 11-32.

Swanson, J.A., Kokan, D.S., and Leon, R.T. (2002). "Advanced finite element modeling of bolted T-stub connection components", Journal of Constructional Steel Research, 58: 1015-1031.

Tobias, D.H., Anderson, R.E., Hodel, C.E., Kramer, W.M., Wahab, R.M., and Chaput, R.J. (2008). "Overview of earthquake resisting system design and retrofit strategy for bridges in Illinois", Practice Periodical on Structural Design and Construction, 13(3): 147-158.

Townsend, H.E. and Zoccola, J.C. (1982). "Eight-year atmospheric corrosion performance of weathering steel in industrial, rural, and marine environments", Atmospheric Corrosion of Metals, ASTM STP 767, Pittsburg, PA.

Tuttle, M.P., Schweig, E.S., Sims, J.D., Lafferty, R.H., Wolf, L.W., and Haynes, M.R. (2002). "The earthquake potential of the New Madrid seismic zone", Bulletin of the Seismological Society of America, 92(6): 2080-2089.

United States Geological Survey (USGS). (2006). Earthquake Hazard in the Heart of the Homeland, U.S. Geological Survey Fact Sheet 2006-3125.

United States Geological Survey (USGS). (2008). U.S. Geological Survey Hazard Map, http://earthquake.usgs.gov/hazards/products/

Van der Vegte, G.J. and Makino, Y. (2004). "Numerical simulations of bolted connections: the implicit versus the explicit approach", AISC-ECCS, Amsterdam, Netherlands.

Wang, Z., Padgett, J.E., and Duenas-Osorio, L. (2012). "Seismic response of a bridge-soil-foundation system under the combined effect of vertical and horizontal ground motions", Earthquake Engineering and Structural Dynamics, 42(4): 545-564

Wang, Z., Padgett, J.E., and Duenas-Osorio, L. (2013). "Influence of vertical ground motions on the seismic fragility modeling of a bridge-soil-foundation system", Earthquake Spectra, 29(3): 937-962.

Wardhana, K. and Hadipriono, F.C. (2003). "Analysis of recent bridge failures in the United States", Journal of Performance of Constructed Facilities, 17(3): 144-150.

Wheeler, A.T., Clarke, M.J., and Hancock, G.J. (2000). "FE modeling of four-bolt, tubular moment end-plate connections", Journal of Structural Engineering, 126(7): 816-822.

Wilson, P. and Elgamal, A. (2006). "Large scale measurement of lateral earth pressure on bridge abutment back-wall subjected to static and dynamic loading", Proceedings of the New Zealand Workshop on Geotechnical Earthquake Engineering, University of Canterbury, Christchurch, New Zealand: pp 307-315.

Xie, F. and Levinson, D. (2009). "Evaluating the E ects of I-35W Bridge Collapse on Road-Users in the Twin Cities Metropolitan Region", 88th Transportation Research Board Conference, Washington , DC.